UNCLASSIFIED

AD NUMBER

AD325217

CLASSIFICATION CHANGES

TO: **unclassified**

FROM: **secret**

LIMITATION CHANGES

TO:

Approved for public release, distribution unlimited

FROM:

Distribution: No Foreign

AUTHORITY

Group-4 DoDD 5200.10, 26 Jul 1962; AFSC ltr., 24 Apr 1992

THIS PAGE IS UNCLASSIFIED

AD 325 217

PYE WACKET
Feasibility Test Vehicle Study
(Configurations and Autopilot Control)

(TITLE UNCLASSIFIED)

VOLUME III

Prepared by

Convair/Pomona
General Dynamics Corporation
Pomona, California

for

AIR PROVING GROUND CENTER

EGLIN AIR FORCE BASE, FLORIDA

Qualified Requesters

MAY OBTAIN COPIES OF THIS REPORT FROM

Armed Services Technical Information Agency

Document Service Center
Arlington Hall Station
Arlington 12, Virginia

SECRET

PYE WACKET
Feasibility Test Vehicle Study
(Configuration and Autopilot/Control)

CR 341 377 001
AFSC Project 3811
Contract AF 08(635)-1168

15 February 1961

Convair/Pomona
Convair Division of General Dynamics Corporation
Pomona, California

Prepared for

Detachment 4
HEADQUARTERS, AERONAUTICAL SYSTEMS DIVISION
Air Force Systems Command
United States Air Force
Eglin Air Force Base, Florida

SECRET

FOREWORD

This report was prepared under Air Force Contract Number AF 08(635)-1168, Project 3811, (U) "Lenticular Rockets." The work was administered initially under the direction of the Directorate of Development, APGC, and completed under the guidance of Detachment 4, Hq Aeronautical Systems Division at Eglin Air Force Base, Florida.

This document, except the title, is classified SECRET in accordance with AFR 205-1, paragraph 10b, because of the nature and potential military application of the research work and data described herein, and NOT RELEASABLE TO FOREIGN NATIONALS in accordance with AFDCMI 56.

ABSTRACT

Feasibility studies were conducted
of a circular planform, modified lenti-
cular cross section vehicle. The results
of these studies form the basis for the
ultimate fabrication and flight test of
the vehicles to prove the omnidirectional
launch, stability and control, and maneuver-
ability aspects of the basic concept.

The main propulsion, basic vehicle
configuration, material, dimensions and
fabrication techniques were developed for
the Feasibility Test Vehicle. A detailed
study was conducted of the problems associ-
ated with stabilizing and controlling the
missile. From these studies the autopilot
and reaction control system parameters
were developed. The adequacy of the final-
ized system was demonstrated by simulated
flights on a time-varying three-dimensional
analog simulation.

The complete task is reported in
three volumes: Volume I -- Summary, Volume
II -- Aerodynamics, and Volume III --
Configuration and Autopilot/Control.

iii

CONTENTS

TABLE   PAGE

                                              SECRET

Section 1.0
FEASIBILITY TEST VEHICLE CONFIGURATION STUDIES

1.1 INTRODUCTION

The design was established for a Feasibility Test Vehicle (FTV)
which could later be implemented and flight tested from a high-speed
rocket-sled to prove that the circular planform, blunted lenticular
cross-section configuration represents a significant advance in airborne
weaponry. This proof-of-concept dictates the necessity for stabilized
and controlled flights to demonstrate the omnidirectional launch and
maneuverability of the vehicle.

The circular planform, lenticular cross section concept originated
with the Technical Planning Group, formerly of the Directorate of Develop-
ment of the Air Proving Ground Center, now of Detachment 4 of Wright
Air Development Division, Target and Armament Development Directorate,
Eglin Air Force Base, Florida. This effort was further advanced by an
experimental program conducted in Tunnel E-1 of the Gas Dynamics Facility,
Arnold Engineering Development Center. Convair/Pomona continued the
developmental work under a six-month study contract entitled "Lenti-
cular Rocket," AF 08(635)-542, awarded in June 1959. During this Phase
I study contract a general aerodynamic evaluation and a vehicle feasi-
bility study were conducted and reported in the "PYE WACKET Feasibility
Study, Summary Technical Report" (Reference 4.1). One of the important
results of this effort was the origination of the blunted lenticular
cross-section configuration. This modified lenticular shape displays
a significant increase in feasibility over the symmetrical vehicle
previously considered.

Volume III comprises the configuration studies and the Autopilot/
Control analyses. It is important to note that the wind-tunnel data
obtained during this study was not available until near the end of the
contract period. It therefore was imperative that estimates be made
of the omnidirectional aerodynamic characteristics for use during the
preliminary studies. Many of the intermediate results presented in this
report are based on these aerodynamics. Although these estimates are
reasonably accurate, a detailed examination of the intermediate results
may reveal some small discrepancies. Throughout this study, a maximum
effort was directed toward the use of highly reliable, low cost items
consistent with the ultimate purpose of proving the feasibility of the
concept as an airborne weapon.

Section 2.0 of the report deals with the study of the structural
development of an FTV. As in any airborne vehicle, a structural configu-
ration must be designed which is capable of accomodating the guidance,

1.1

control, and main propulsion hardware, and which is also capable of withstanding the environment associated with the ultimate mission. The final structural design was developed in a stepwise sequence beginning with the definition of the outside vehicle dimensions. This choice was necessarily preceded by the definition of the aerodynamic characteristics, the main propulsion unit configuration and the weight-space allocations for the missile control hardware. The studies were then directed toward the selection of the main load bearing structural members with the appropriate attention being applied toward the distribution of the thrust loads. The remaining structures were then designed for aerodynamic and handling loads in conjunction with the design layouts.

1.2 BASIC FTV CONFIGURATION

The basic FTV configuration consists of a main propulsion unit and a main load bearing structure. To initiate the design, it was first necessary to find a compatible main propulsion system. This selection was greatly influenced by the control system and aerodynamic considerations. The final choice then dictated the outside vehicle dimensions and hence provided the inputs necessary for the main structural design.

1.2.1 BOOSTER MOTOR INVESTIGATION

The PYE WACKET FTV requires a single stage main propulsion system to boost the vehicle to its maximum velocity. In order to differentiate between this main propulsion system and the attitude and directional control system of the vehicle (which also utilize rocket motors), the main propulsion system is generally termed the booster in this report. The design objective was a booster which would provide a vehicle burnout Mach number of approximately 2.0 for an 800 ft per sec forward launch. This objective, however, is subject to the following limitations on vehicle design:

a.   maximum vehicle acceleration of 50 g's,
b.   maximum use of off-the-shelf components,
c.   maximum vehicle diameter of 60 inches for the blunted lenticular design, and
d.   maximum t/c (thickness-to-chord ratio) of 21%.

1.2.1.1 Booster Motor Evaluation

Because of the above restriction, the evaluation of boosters for the FTV application was limited to liquid and solid propellant rocket systems. Air-breathing systems were not considered feasible for the reasons outlined in the Phase I report (Reference 4.1). The principal disadvantages inherent in an air-breathing system are decrease in vehicle omnidirectional launch capability and problems associated with the design of an inlet for the lenticular configuration. Also, the availability of acceptable air-breathing propulsion systems is more limited than that of the rocket systems.

1.2

To adhere to the vehicle t/c and the approximate Mach 2 burnout requirements, it was necessary to investigate clustered packaging of available solid and liquid propellant motors. A survey of available motors in the size and impulse class applicable to the FTV resulted in the list of motors shown in Table 1.2.1. A detailed investigation of the applicability of each motor resulted in the selection of M58A2 motors (Falcon) in a cluster of three as the most suitable choice for the flight test vehicle. The detailed reasons supporting this conclusion are contained in the following sections.

Solid Propellant Rocket Motors   The 1.12-KS-10200 and the 2-KS-8600 motors shown in Table 1.2.1 were eliminated from consideration because of the vehicle size limitations previously discussed. The characteristics of the remaining six solid motors are compared in Table 1.2.2. Values of rated thrust, impulse, propellant fraction, and impulse-to-total-weight ratio are shown in this table with the vehicle diameter required to house the particular motor.

A preliminary analysis was made of vehicle performance using the Model 227-A motor in clusters of both three and four. The resulting performance was then compared to that obtained using similar clusters of M58A2 motors. The results of this comparison indicate that the M58A2 motors are superior to the Model 227-A for use in the FTV. This conclusion was based on the following considerations:

1. the additional length of the Model 227-A would create serious packaging problems for a 60-in. diameter FTV,

2. the thrust level of the Model 227-A would cause acceleration loads 33% higher than those obtained with the M58A2 for the same burnout velocity, and

3. the higher total weight of the Model 227-A would add 60 to 80 lb to the launch weight of the FTV.

After eliminating the Model 227-A motor from further consideration, the performance of the remaining five solid propellant motors was compared (Figures 1.2.1 and 1.2.2). The preliminary aerodynamic drag data used in the comparison is presented in Figure 1.2.3. It can be seen in Figure 1.2.2 that smaller diameter vehicles utilizing either the 1.95-KS-614 or the 6.0-KS-260 appear to be inadequate for the FTV. The low thrust of these motors is the major factor accounting for the low vehicle terminal velocities of 1230 ft per sec (30 in. diameter, 1.95-KS-614) and 1500 ft/sec (48 in. diameter, 6.0-KS-260). The difficulty of scaling down the size of the other components in the vehicle and the potential problem of scale factor in relating small FTV characteristics to a full-size

1.3

Table 1.2.1 Available Motors for the FTV

Manufacturer	Motor Designation	Propellant	Length, in.	Diameter, in.	Missile Application
Thiokol	TD-174	Liquid	51.65	8.00	Sparrow III
Thiokol	TD-187	Liquid	40.47	12.04	Bullpup
Talco	2.0-KS-3000	Solid	33.4	6.00	Pima I
Thiokol	XM46	Solid	28.46	6.405	Falcon
Thiokol	M58A2	Solid	30.75	5.775	Falcon
NOTS	Model 227-A	Solid	42.50	5.00	Sidewinder
Aerojet	1.95-KS-614	Solid	33.40	2.75	Aeronite
ARC	6.0-KS-260	Solid	24.00	2.75	Redeye
Thiokol	1.12-KS-10200	Solid	66.87	5.25	Cherokee
Aerojet	2-KS-8600	Solid	52.0	8.0	Sparrow

Table 1.2.2. Solid Propellant Engine Performance

	1.95-KS-614	6.0-KS-260	Model 227A	2.0-KS-3000	XM46	M53A2
Thrust, lb	614	260	5650	3000	4584/c10	4250
Impulse, lb-sec	1190	1560	6500	6000	5420	6600
Duration, sec	1.95	6.0	1.2	2.0	0.61/4.25	1.42
Total wt,lb	19.3	9.0	65.2	49	42.96	45.85
Propellant wt, lb	5.95	6.2	29.5	38	26.41	31.02
Specific Impulse, sec	200	251	219	214	205	213
Propellant Fraction*	0.308	0.689	0.453	0.571	0.614	0.676
Impulse/Total Wt, sec	61.6	173	99.2	122	126	144
Minimum vehicle dia, in.	48	36	60	60	60	60

* Propellant fraction is the ratio of propellant weight (excluding igniter and augmentation charge) to total weight.

FIGURE 12 V

BURNOUT VELOCITY VS LAUNCH WEIGHT

CONDITIONS:
1. FWD LAUNCH @ 800 FPS
2. 0° ANGLE OF ATTACK
3. t/c = 21%
4. ALT. 2000 FT, STD DAY
5. 3 MAIN MOTORS IN CLUSTER
6. MISSILE DIAMETER 40 IN.

BURNOUT VELOCITY ~ FPS

3000

2000

1000

0

M58A2
2.0 KS 30,0 0
XM46

0   100   200   300   400   500
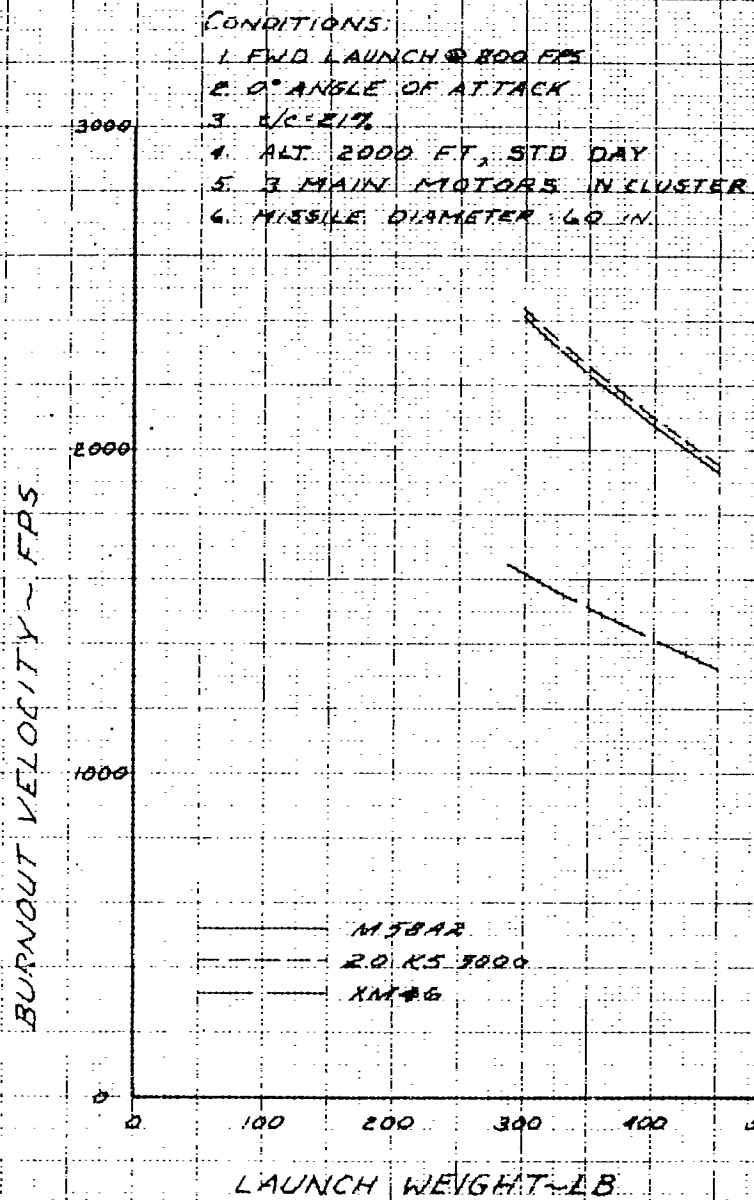
LAUNCH WEIGHT ~ LB

FIGURE 12.2

BURNOUT VELOCITY VS LAUNCH WEIGHT

CONDITIONS:
1. FWD LAUNCH @ 800 FPS
2. 0° ANGLE OF ATTACK
3. t/c 21%
4. ALT - 2000 FT STD DAY
5. 4 MAIN MOTORS

A	————	M58A2 (60" DIA MISSILE)
B	— — — —	2.0 KS 3000 (60" DIA MISSILE)
C	————	XM 46 (60" DIA MISSILE)
D	— · — · —	1.95 KS 614 (48" DIA MISSILE)
E	— — — —	6.0 KS 260 (36" DIA MISSILE)

BURNOUT VELOCITY ~ FPS.

LAUNCH WEIGHT ~ LB
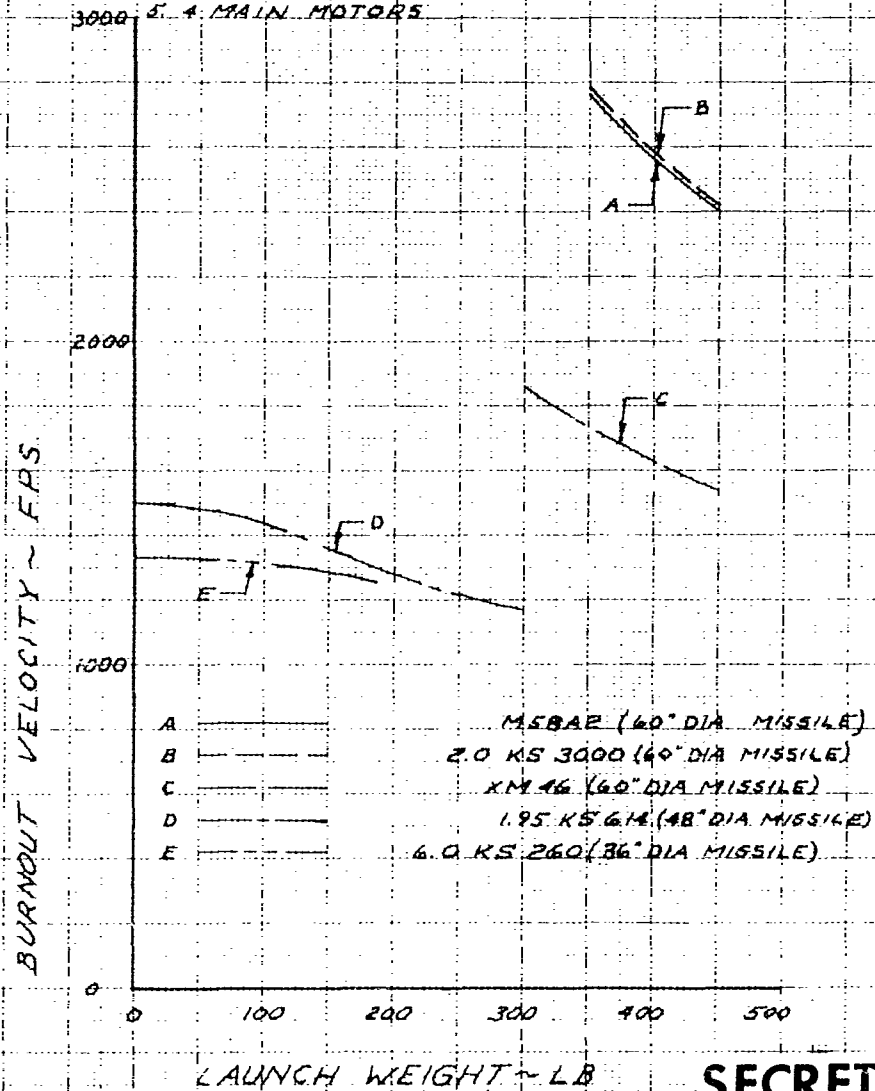
FIGURE 123

DRAG VS VELOCITY

CONDITIONS:
1. $\beta = 0°$ ANGLE OF YAW
2. $\alpha = 0°$ ANGLE OF ATTACK
3. 2000 FT ALT.
4. STANDARD DAY
5. 21 ft/c VEHICLE
6. BASED ON EST. AERO DRAG
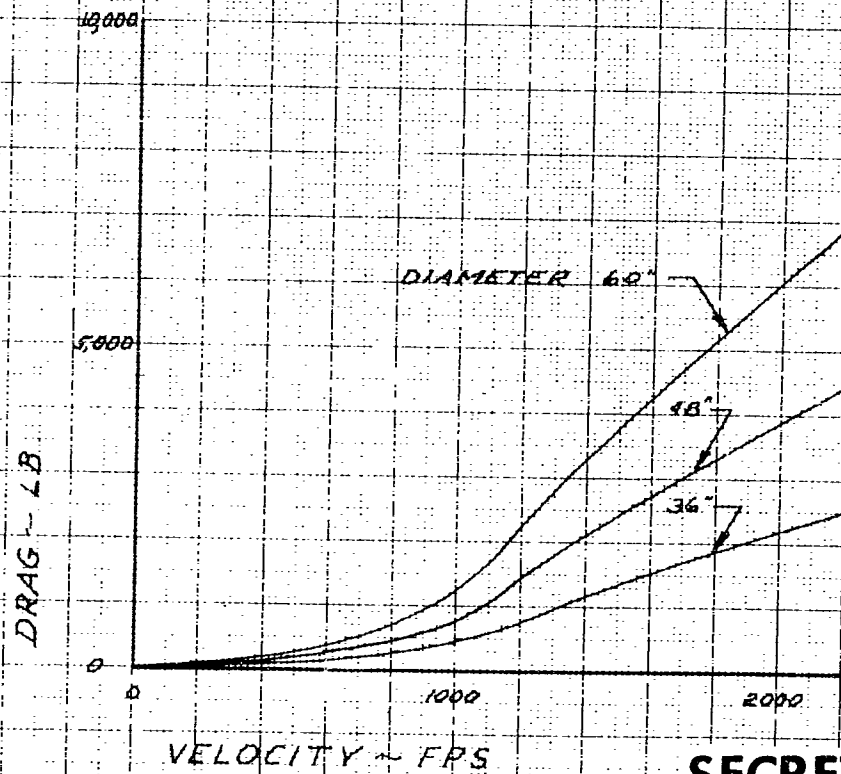
SECRET

prototype count against vehicles smaller than 60-in. diameter.

The XM-46 is a dual-thrust, booster-sustainer type motor, and could be expected to offer some advantage in vehicle velocity during flight coast-down. Vehicle performance obtained using clusters of the XM-46 motors was again compared to performance with the M58A2. For purposes of this comparison, a launch weight of 390 lb was selected, although the relative magnitude of the performance values obtained are valid over a range of launch weights from 300 to 450 lb. As shown in Figures 1.2.4 and 1.2.5 (clusters of four and three motors, respectively), the dual-thrust XM-46 motor produces a higher vehicle coast velocity though the M58A2 motor offers a much higher vehicle burnout velocity. However, since coast velocity is not a major consideration for the FTV, the reduction in maximum velocity obtained with the XM46 would not be warranted. On this basis, it is concluded that the M58A2 would be superior to the XM-46 for the purposes of the flight test program.

The remaining two motors to be evaluated, the M58A2 and the 2.0-KS-3000, offer almost identical vehicle performance for clusters of either three or four motors (Reference Figures 1.2.1 and 1.2.2). Therefore, other considerations must determine the selection of the most suitable motor. The M58A2 has been operational since 1956 in the GAR-1 and GAR-2 Falcon missiles, and because of its high production rate and long service life, represents a highly reliable, low-cost system consistent with FTV objectives. On the other hand, the 2.0-KS-3000 motor has been used only with the Pima I sounding rocket and does not have an extensive background in production and service use. The greater experience level of the M58A2 therefore makes it the most desirable solid propellant motor for the FTV booster.

Liquid Propellant Rocket Motors   In order to use either of the two liquid propellant motors listed in Table 1.2.1, a modification of the 60-in. diameter, 21% t/c vehicle is required. This modification would be necessary to prevent the extension of the forward motor head outside the missile envelope. The 12.04-in. diameter of the TD-187 motor is approximately equal to the maximum allowable vehicle thickness (12.6 in.).

The performance characteristics of the two liquid propellant motors are shown in Table 1.2.3. Based on the rated thrust level of the motors and acceleration limitations on the vehicle, two TD-174 motors or one TD-187 motor could be used for the FTV booster. However, a 21% t/c, 75-in. diameter vehicle would be required to house the two TD-174 motors, resulting in a 50% increase in drag over that of a 21% t/c, 60-in. diameter vehicle. In addition, a comparison of the vehicle performance using two TD-174 motors with the performance obtained with solid propellant M58A2 motors indicated no significant advantages for the liquid propellant system. A comparison of one TD-187 with a cluster of three M58A2 motors also gave similar results.

1.9

FIGURE 12.4

MISSILE VELOCITY VS TIME

CONDITIONS
1. FWD LAUNCH
2. 0° ANGLE OF ATTACK
3. t/c = 21%
4. ALT 2000 FT STD DAY
5. 4 MAIN MOTORS
6. LAUNCH WEIGHT 390 LB

MISSILE VELOCITY ~ FPS

3000

2000

M 5BA2

XMAG

1000

0

0   5   10

TIME ~ SECONDS
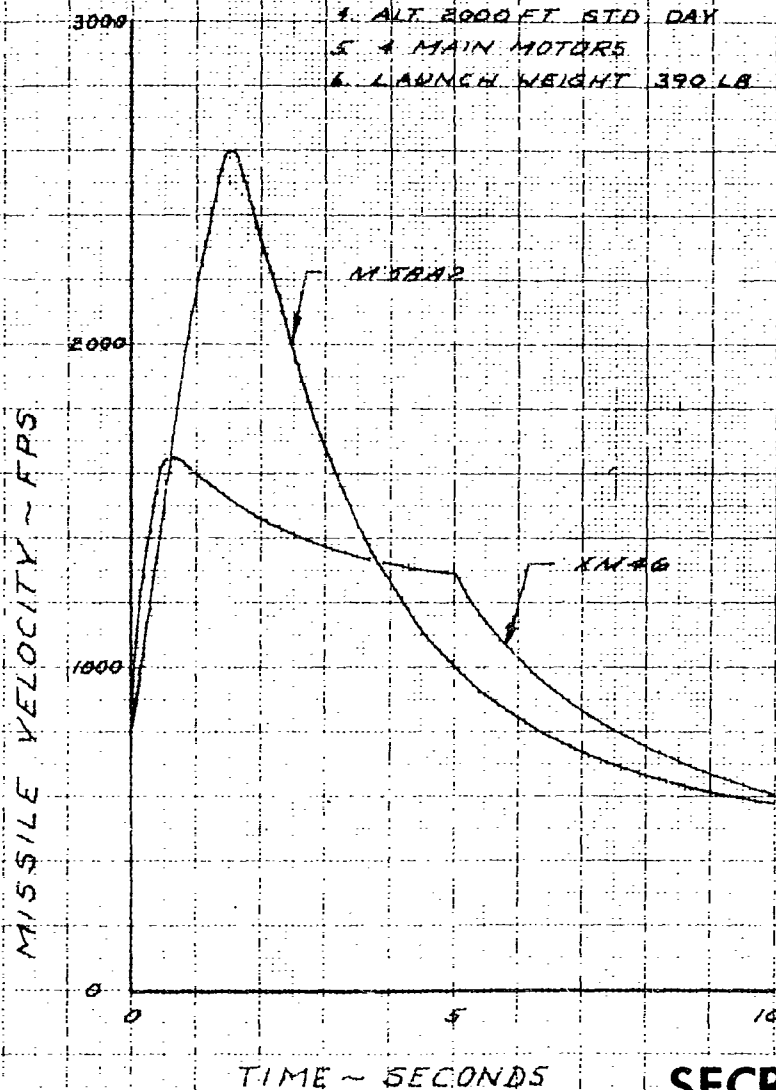
Figure 1.2.5

MISSILE VELOCITY VS TIME

CONDITIONS:
1. FWD LAUNCH @ 800 FPS
2. 0° ANGLE OF ATTACK
3. t/c = .21%
4. ALT. 2000 FT. STD. DAY
5. 3 MAIN MOTORS
6. LAUNCH WEIGHT 390 LB.

MISSILE VELOCITY ~ FPS

TIME ~ SECONDS
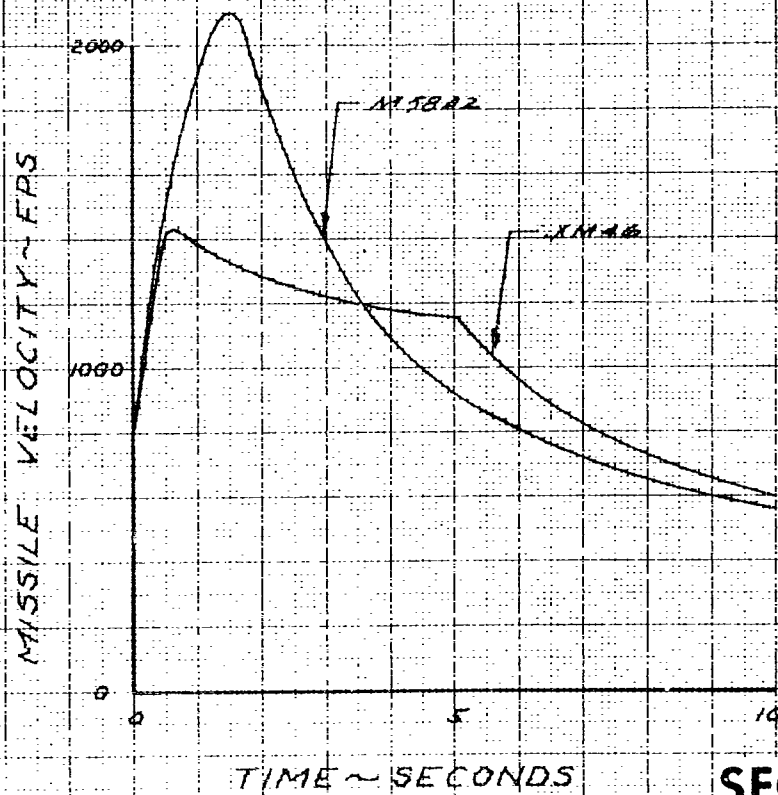
Table 1.2.3 Liquid Propellant Engine Performance

	TD-174	TD-187
Thrust, lb	8,005	12,000
Impulse, lb-sec	16,325	24,200
Duration, sec	1.75	2.04
Total wt, lb	128.3	196.8
Propellant wt, lb	71.70	112.10
Specific Impulse, sec	228	216
Propellant fraction*	0.56	0.57
Impulse/total wt, sec	127	122.9

* Propellant fraction is the ratio of liquid propellant weight to total weight.

From the foregoing discussion, off-the-shelf liquid propellant rocket motors do not appear to satisfy the requirements for the FTV. In addition to several disadvantages in packaging, liquid propellant motors tend to have long ignition intervals (approximately 0.138 sec compared to 0.007 sec for solid propellant motors) which could result in large thrust misalignment moments if one motor is ignited before the other. Therefore, since liquid propellant motors do not offer any significant advantages to overcome their limitations, no further investigation appeared warranted.

Propulsion System Configuration   The information shown on Figures 1.2.1 and 1.2.2 indicates that a cluster of either three or four M58A2 motors will satisfy the required FTV burnout velocity. On the basis of velocity, acceleration, moments due to misalignments and starting transients, and cost (see Table 1.2.4), the three-motor system has a decided advantage over the four-motor system.

The maximum velocities shown in Table 1.2.4 are theoretical values based on drag data at zero angle of attack and forward launch at 800 ft/sec initial velocity. As such, these values are somewhat optimistic, and actual values would probably result in a burnout velocity on the order of Mach 1.8 for the three-motor system and Mach 2.2 for the four-motor system. Therefore, although the four-motor configuration has the higher burnout velocity, both systems produce satisfactory FTV velocity histories.

The investigation of the thrust misalignment in the main propulsion system is discussed in detail in Section 1.2.1.3. Table 1.2.4 summarizes the results of this investigation for yaw, pitch, and roll moments and indicates that thrust misalignment moments for a four-motor configuration are almost twice those obtained with a three-motor system. Since the reaction control system thrust requirements are determined by a combination of aerodynamic and misalignment moments, any increase in the amount of misalignment moment will require an increase in control system thrust. Such an increase would also result in a decrease in total flight time for a fixed propellant volume. Again the three-motor propulsion system is preferred.

The relative costs shown in Table 1.2.4 indicate the potential savings which could be anticipated if three M58A2 motors were used for the FTV propulsion system. In addition, a reduced cost of related components could be anticipated because of less stringent acceleration levels and lower required reaction control thrust.

From the foregoing discussion, it appears that a cluster of three M58A2 motors would be the most suitable booster system for the FTV. This system meets the requirements for the FTV and offers significant advantages

1.13

Table 1.2.4 Comparison of Three and Four M58A2 Motor Clusters

	Three M58A2 Motors	Four M58A2 Motors
Maximum Velocity, ft/sec	2140**	2480**
Maximum Acceleration, g's	+36 -16	+44 -20
Average thrust Misalignment Yaw Moment, ft-lb	220	393
Average Thrust Misalignment Pitch Moment, ft-lb	122	189
Average Thrust Misalignment Roll Moment, ft-lb	22	44
Relative Cost*, per cent of cost of three M58A2 Motors	100	159

* Including modifications necessary to house four M58A2 motors.

**Based on a total vehicle weight (without main motors) of 240 pounds.

in reliability, availability, performance, cost, and/or compatibility
with associated components. Therefore, three M58A2 solid propellant
motors will be utilized for the FTV.

1.2.1.2 M58A2 Motor Characteristics   The M58A2 motor is a high-
thrust, short-duration, cylindrical solid propellant motor having an
internal burning, five-pointed-star grain configuration. As outlined
in References 4.2 and 4.3, the performance of the motor is characterized
by a 1.42 sec nominal burning time and a 4250 lb nominal thrust. The
motor provides a total impulse of approximately 6600 lb-sec, with a
propellant specific impulse of approximately 213 lb-sec/lb at 70°F.

The nominal dimensions of the motor are 36.75-in. overall length,
5.848-in. diameter at the forward alignment surface, 6.185-in. diameter
at the thrust flange, and a 5.775-in. diameter case. The nozzle is
uncanted and has a 30° expansion cone angle with a 1.70-in. diameter
throat and 5.06-in. diameter exit, yielding an expansion ratio of 8.85.

The weight of the complete rocket motor, including the igniter,
is 46.41 lb. The grain is comprised of an ammonium perchlorate/polysulfide
propellant formulation, TRX-237, and weighs 31.02 lb. Some of the im-
portant ballistic properties of the propellant are presented in Table
1.2.5.

A "Jelly-Roll" type igniter, designated M50A1, is incorporated in
the M58A2 motor. The igniter consists of 50 gm of composition X-359
dispersed in a petroleum distillate solvent, spread on a cellulose
acetate sheet and formed into a cylinder with a squib at both ends.

Structurally, the motor case is a one-piece, deep-drawn 4130 steel
shell, necked down and threaded at the aft end. A nozzle adapter incor-
porating a thrust flange to transmit loads produced by the motor is
attached to the chamber. The nozzle is a convergent-divergent cone-type,
made of Type 1020 steel, with a graphite throat section. The internal
surface of the rocket motor chamber is lined with a "Thiokol" polymer
composition, which serves as a heat shield for the chamber during operation.
The propellant is cast into the motor chamber and cured with a core to
form the internal configuration. The configuration and overall dimensions
are shown in Figure 1.2.6.

Both availability and reliability of the M58A2 motor are excellent;
it is currently in a production program status and has been extensively
used in the Falcon GAR-1 and GAR-2 missiles. There have been at least
200 static firings and a great many missile flights using this motor
(Reference 4.2).

Table 1.2.5 M58A2 Ballistic Characteristics

Temperature coefficient of pressure	$0.165\%/^{\circ}F$
Flame temperature	$4500^{\circ}F$
Characteristic exhaust velocity	4500 ft/sec
Firing temperature limits (minimum)	$-50^{\circ}F$
(maximum)	$150^{\circ}F$
Initial surface-to-throat area ratio	253
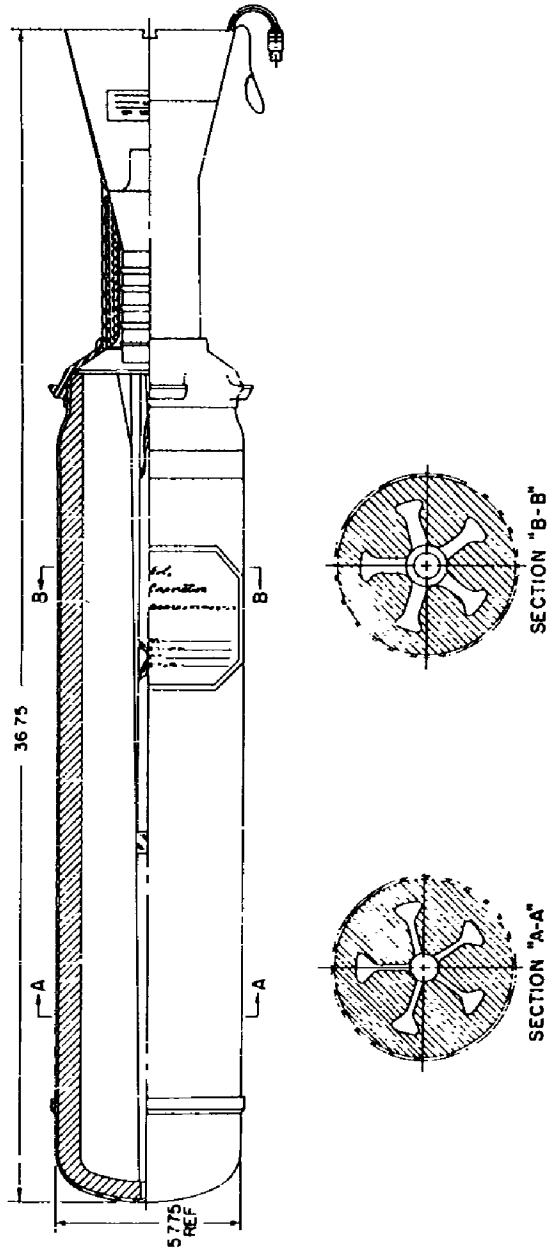
PROPELLANT

Type	T-21
Web Thickness, Average, in.	0.73
Loading Density, Volumetric, %	.75
Port Area, Average/Throat Area	0.55
Burning Rate at 1218 psia and 70°F, in./sec . . .	0.38
Burning Rate Exponent	0.062
Specific Weight, lb/in.^{3}	0.165
Temperature Coefficient of Pressure, %°F	1.24
Ratio of Specific Heats	
Specific Impulse, lb-sec/lb	234

NOZZLE

Material, Body	SAE 1020
Material, Insert	Graphite
Exit Area/Throat Area	
Throat Area, in.^{2}	2.27
Thrust Coefficient, Theoretical, S. L., 70°F . .	

CASE

Material	SAE 4130
Minimum Yield Strength, psi	180,000
Nominal Thickness, in.	0.054

Figure 1.2.6 M5842 Motor Configuration

1.2.1.3 <u>Tolerance Effect on Vehicle Performance</u>   Production tolerances arising in the manufacture of a rocket motor can cause a displacement and/or a rotation of the motor thrust vector. Since the use of such a rocket motor in the FTV can produce eccentric moments, an investigation of the various production tolerances associated with the M58A2 motor was conducted. The potential tolerance effects of the rocket motor can result from the following sources:

A. Misalignment

    1. Angular
        a. between the vehicle longitudinal axis and the rocket motor longitudinal axis,
        b. between the rocket motor longitudinal axis and the nozzle axis, and
        c. between the nozzle axis and the thrust vector.

    2. Linear

        a. between the vehicle center of gravity and the rocket motor longitudinal axis, and
        b. between the thrust vector and the rocket motor longitudinal axis.

B. Thrust level variation of each rocket motor.

C. Ignition lag or starting thrust buildup differences.

The accumulation of tolerances from the above sources that would produce the most severe disturbing moments on the vehicle was determined for the roll, pitch, and yaw aspects of flight. In order to study the tolerance effects, estimates were made of maximum realistic values for motor displacement (0.0625-in. linear, 15 minutes angular), thrust level variation ($\pm 2\%$), and motor ignition lag (15 millisec). These estimates were based on the motor firings and production experience of Thiokol, and in all cases, two-sigma values of the various tolerances were assumed.

<u>Tolerance Effect, Vehicle Roll</u>   The maximum thrust vector misalignment, thrust level variation, and ignition lag between the motors of the boost assembly were assumed in order to assure a conservative maximum roll moment. As presented in Figure 1.2.7, the maximum roll moments produced by both three-motor and four-motor booster systems are shown as a function of time from the initial signal to full booster thrust. A four-motor assembly produces a maximum roll moment of 55 ft-lb, i.e., almost twice the moment produced by a three-motor booster.

<u>Tolerance Effect on Vehicle Pitch</u>   A combination of tolerances which would create the maximum misalignment moment about the vehicle pitch axis was also assumed. The maximum misalignment moment in the

1.18

FIGURE 12.7

MAXIMUM MISALIGNMENT
MOMENT

ROLL

NOTE:
MOTORS ARE IN SCALE

1.10
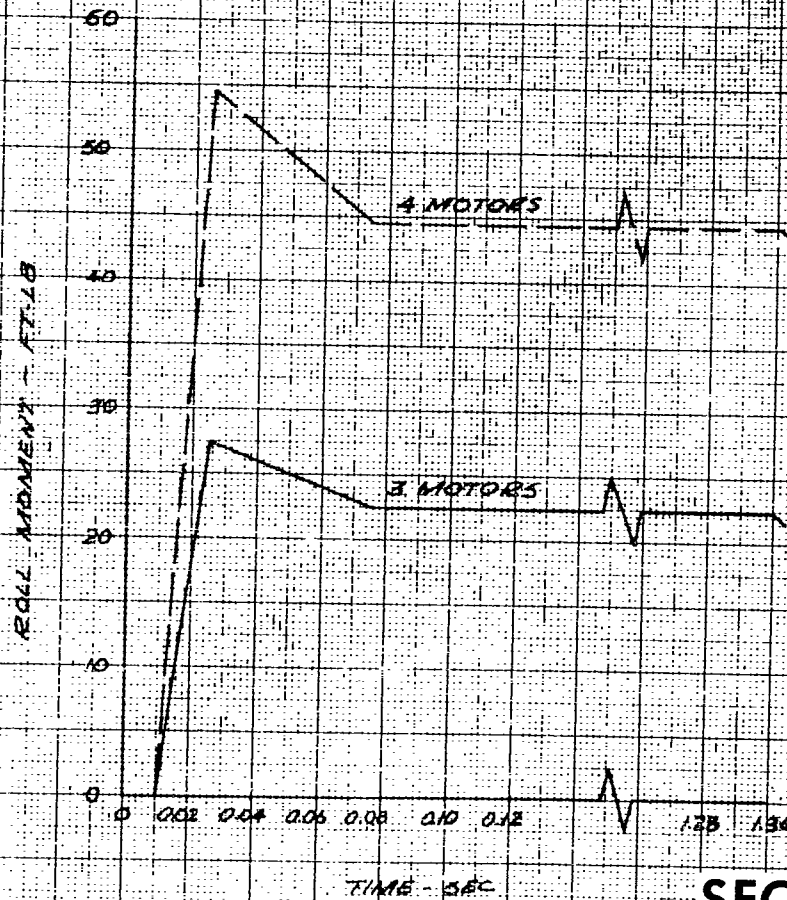
pitch axis (Figure 1.2.8) is also affected by the vehicle center-of-gravity location. The pitch moment decreases as the center of gravity of the vehicle is moved aft toward the rocket nozzles. For example, a 5% aft displacement of the vehicle c.g. produces approximately a 14 ft-lb pitch moment decrease with a three-motor assembly. A similar 5% displacement with a four-motor booster results in approximately a 19 ft-lb decrease.

Tolerance Effect on Vehicle Yaw   As in the cases of pitch and roll, the maximum vehicle yaw moment due to the booster was obtained by adding the tolerance effects. The dependency of this yaw moment on vehicle center-of-gravity location and the moment difference between three-motor and four-motor boosters, are shown in Figure 1.2.9. An extremely large yaw moment "spike" occurs immediately at rocket motor ignition. This spike is a transient effect with a duration of approximately 40 milliseconds. However, due to its large magnitude, it must be compensated during vehicle launch.

Similar to the pitch-moment results, a 5% movement of the vehicle center of gravity produces a 10% change in yaw moment. The steady-state yaw moment associated with a four-motor assembly is also nearly twice that of a three-motor assembly.

1.2.2   SPACE ALLOCATION AND ARRANGEMENT   The initial space envelopes were allocated during the booster motor investigation. For each booster motor and associated vehicle dimensions, several space allocations and arrangements were studied. The 21% t/c, 60-in. diameter vehicle incorporating the three M58A2 motor configuration, as chosen in the previous section, does permit a practical packaging arrangement.

1.2.2.1   Rocket Motor Arrangement   The booster motors, the largest single item, were considered first in the component layout designs (see Figure 1.2.10 for booster installation). Figure 1.2.11 shows the cross sectional profiles of the basic blunted-lenticular configuration and the FTV configuration. The aft end "cutout", as shown for the FTV, allowed the booster motors to be located as far forward as possible to aid the placement of the missile center of gravity (c.g.) at the 43% chord (measured from the leading edge). In the spanwise direction, the boosters are arranged symmetrically about the longitudinal axis with the resultant thrust vector passing through the missile c.g. The center-line distances between the boosters are minimal to reduce the transient yawing moment resulting from possible ignition delay, thrust level variation, and unequal burning time.

The motor supports, which also align the booster cases with respect to the missile center-line, are a part of the main structural weldment. Since these supports will be machined as a unit, maximum parallelism and alignment are achieved. The booster thrust, transmitted from the

Figure 1.28
Maximum Misalignment Moment

PITCH

FIGURE 12.9

MAXIMUM MISALIGNMENT
MOMENT

YAW

NOTE:
MOTORS ARE M15UA2
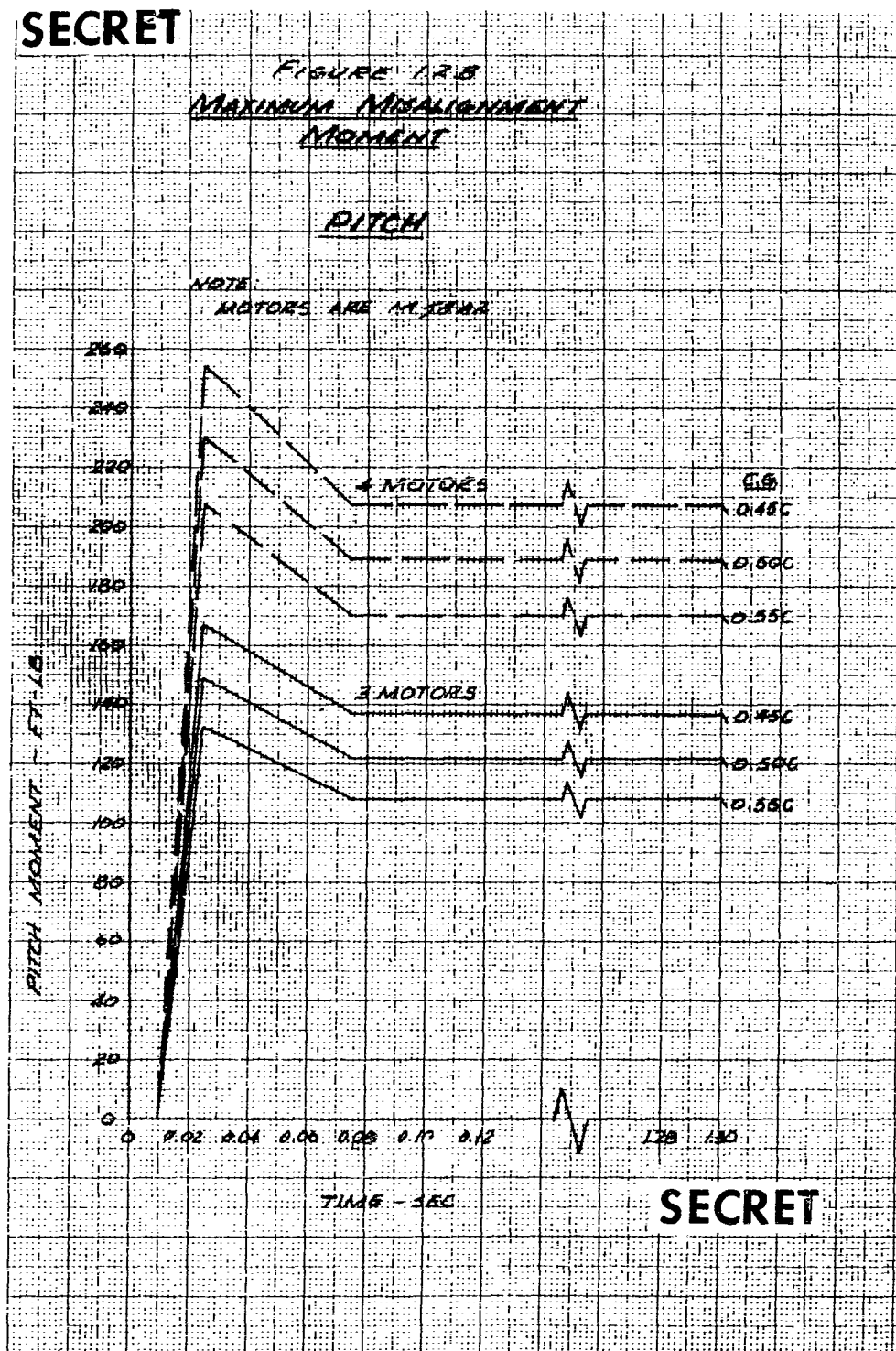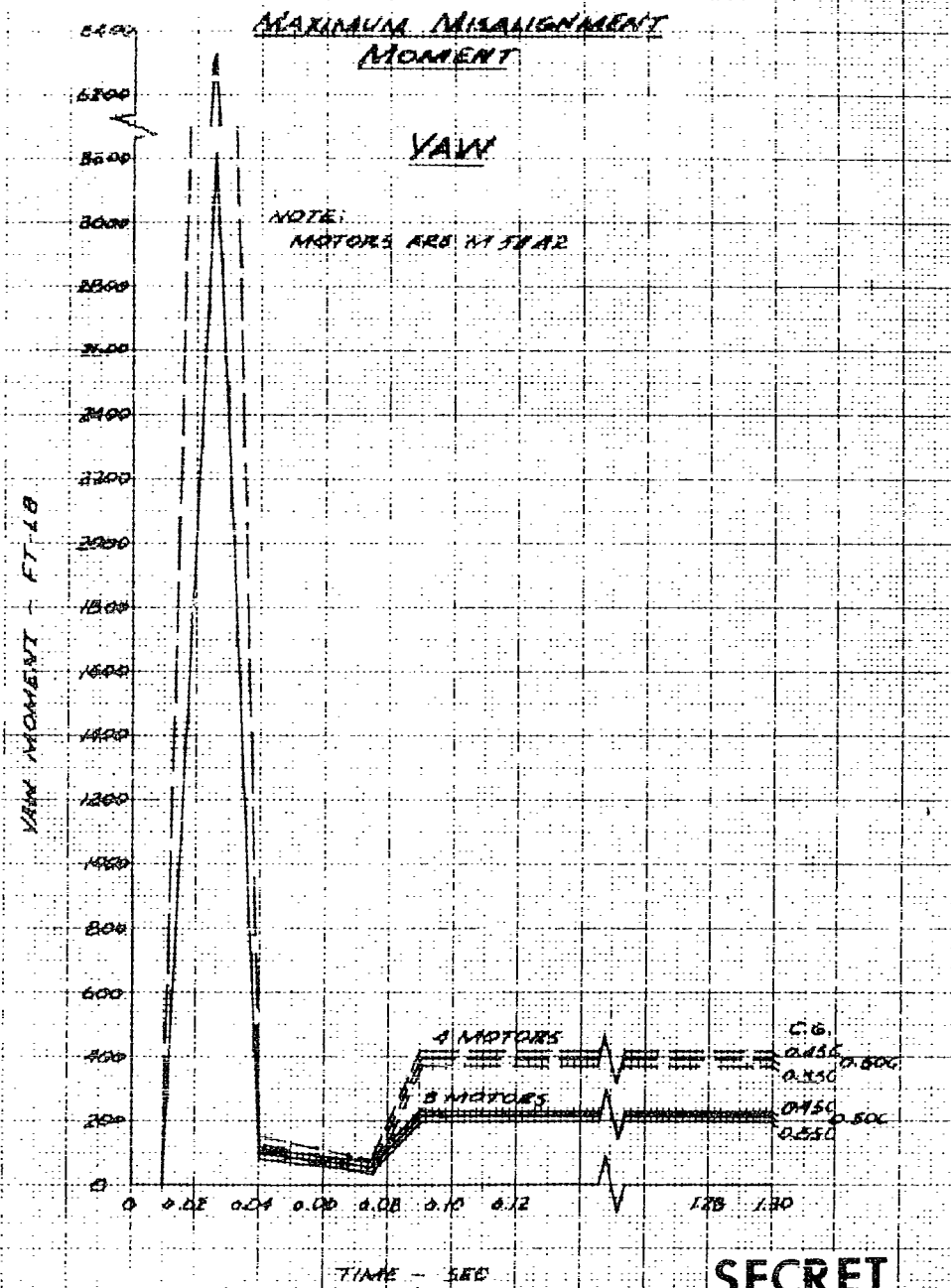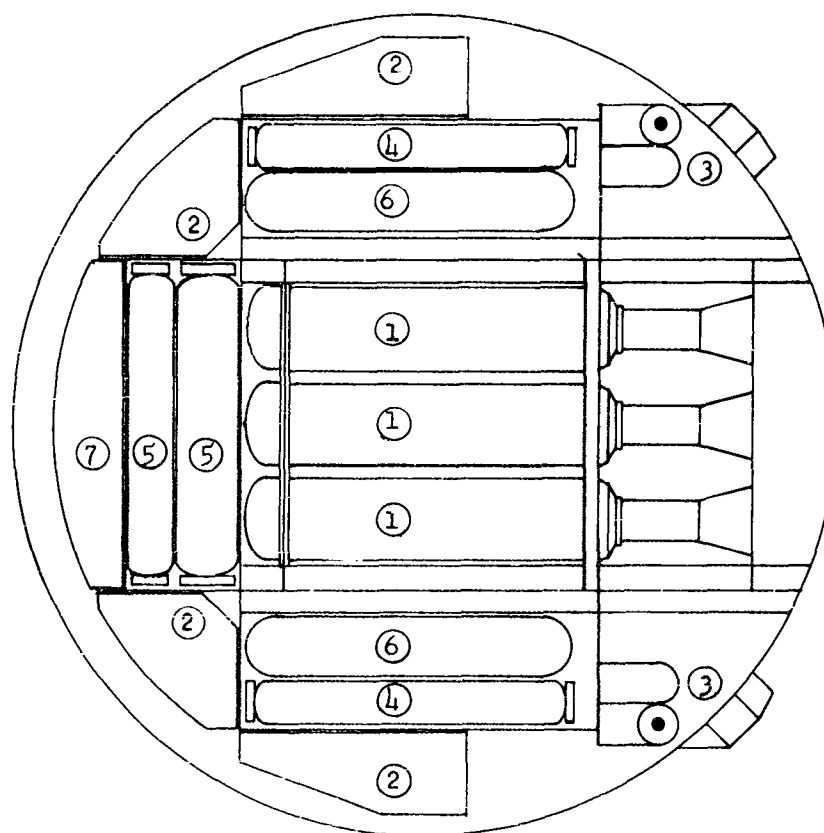
①	Propulsion Motors	⑤	Oxidizer
②	Electronics	⑥	Pressurizing Gas
③	Control Motors	⑦	Ballast
④	Fuel		

Figure 1.2.10 Component Arrangement

1.23
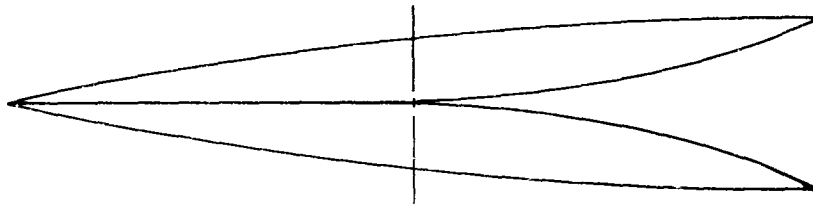
Basic Blunted Lenticular Configuration
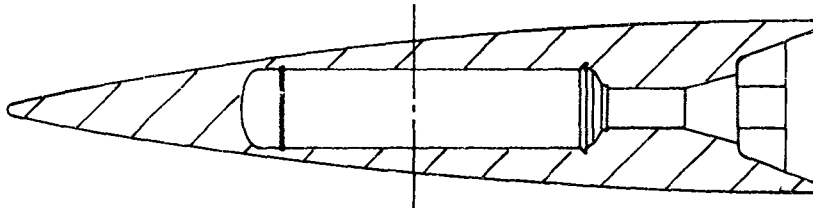
FTV Configuration
(Booster Location)
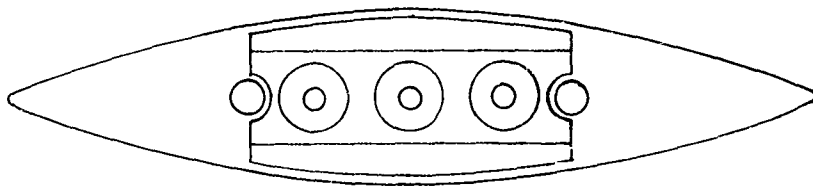
FTV Aft View

Figure 1.2.11 Booster-Motor Location

motor thrust ring to the aft cross member, is transferred into adjacent longitudinal members for distribution to the skin structure and components.

1.2.2.2 **Main Structure** The main structure (weldment), shown in Figure 1.2.12, consists of two longitudinal members and two cross members which, when coupled with the missile skin, provide structural rigidity in all planes. These members also provide attachments for both the skin and subsystem assemblies. The FTV is designed to permit removal of the missile skin from the main structure for access to all components for assembly, test, checkout and service operation.

1.2.2.3 **Control System** The layout of the FTV control system elements is shown in Figure 1.2.10. The four jets which provide the pitch and roll control are located on the top and bottom surfaces, in the aft region of the missile. The two yaw control jets are located on the periphery of the missile planform in the aft region. The control system auxiliary equipment such as fuel and oxidizer tanks, pressurizing gas tanks, pressure regulator, check valves, fill ports, etc., are located in the forward region and are arranged symmetrically with respect to the longitudinal axis to maintain accurate roll balance.

The initial component layouts included a compact control system located in the aft region near the exhaust nozzles. This philosophy was advantageous because of the short fuel lines and hence small fuel transport delays (important from a controls standpoint). However, to ease the control requirement imposed by the body aerodynamics, it is important that the center of gravity of the vehicle be located as far forward as possible for the FTV. The additional penalties assigned to the controls as the center of gravity moves aft is exemplified by the graph of FTV pitching moment as a function of c.g. location (Figure 1.2.13). This compact arrangement of the control system forced the c.g. to move aft and consequently increased the aerodynamic pitch moment. This, in turn, imposed a higher thrust level requirement and hence an increase in propellant weight. At this point a separate propellant system design layout was established.

The propellant tank arrangement, shown in Figure 1.2.10, was designed to maintain the center of gravity on the longitudinal center-line at all times. The two forward tanks store the oxidizer while the two outboard tanks store the fuel. The pressurizing charges are contained in the two large inboard tanks. The longitudinal c.g. shift as a function of propellant consumption is reported in Figure 1.2.14. Since the shift is negligible, no attempt was made to compensate for "fuel sloshing" in this phase of the work.

1.2.2.4 **Electronics** The electronics section, consisting of the autopilot and the telemetry units, is located in the forward section of the missile. The transistorized sections of these units display the greatest flexibility for packaging purposes; subsequently these
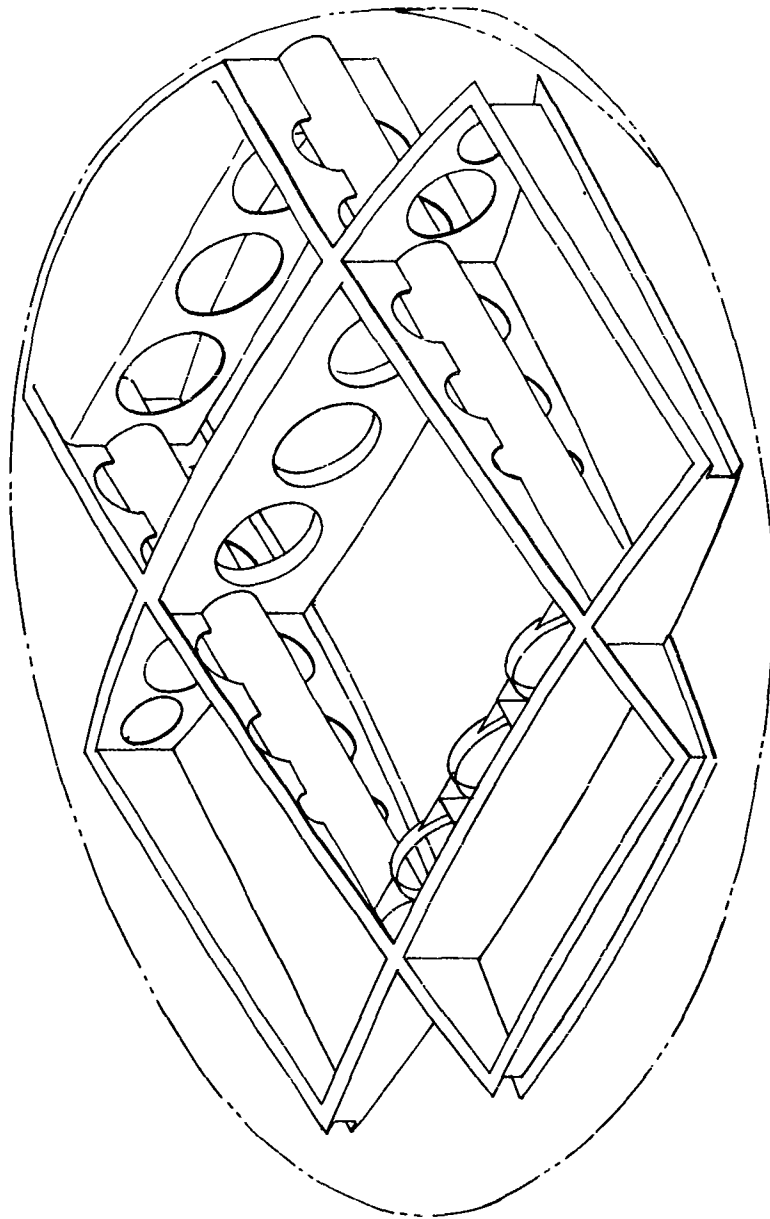
Figure 1.2.12 Main Structure Weldment
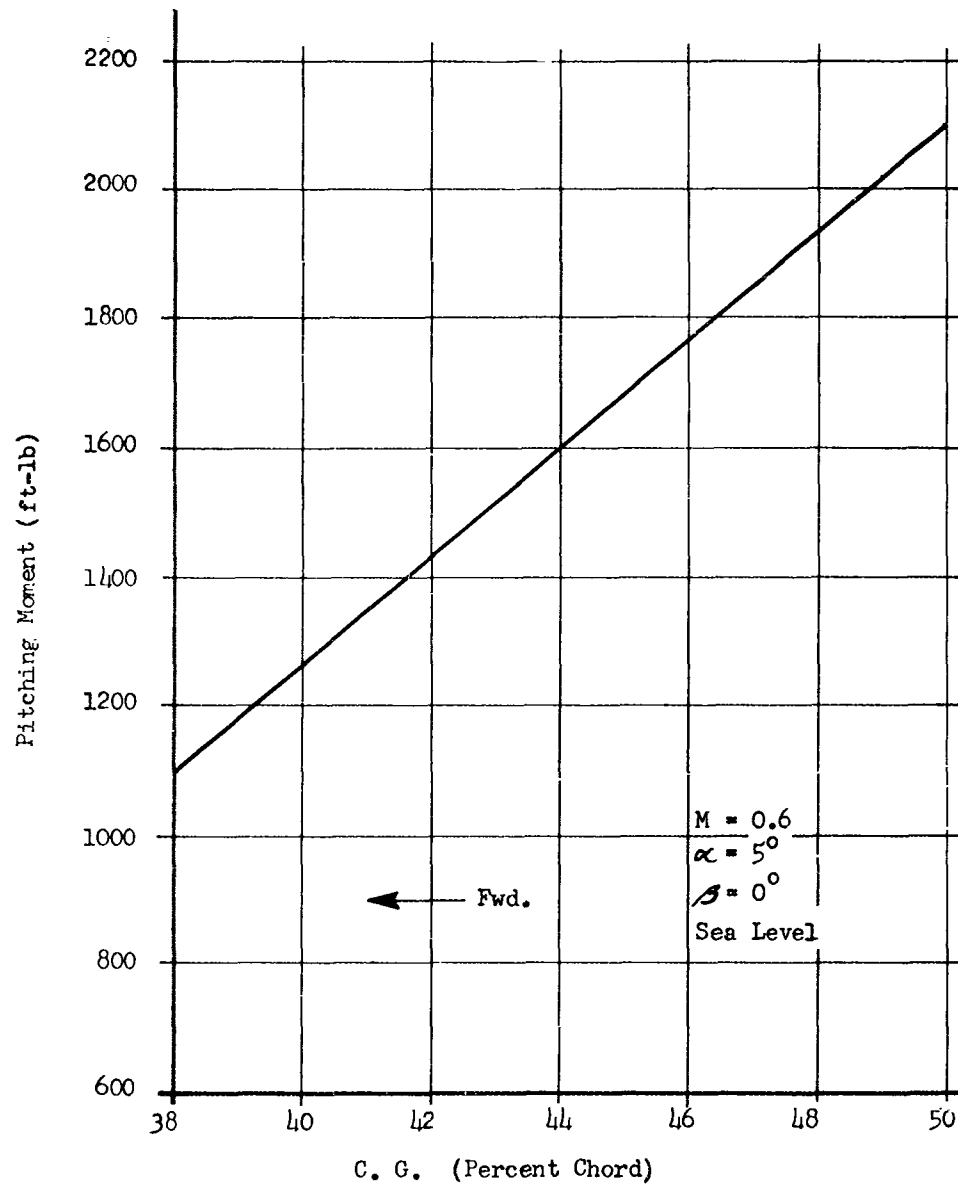
Figure 1.2.13 Pitching Moment vs Center of Gravity Location

S = shift due to longitudinal slosh of propellant
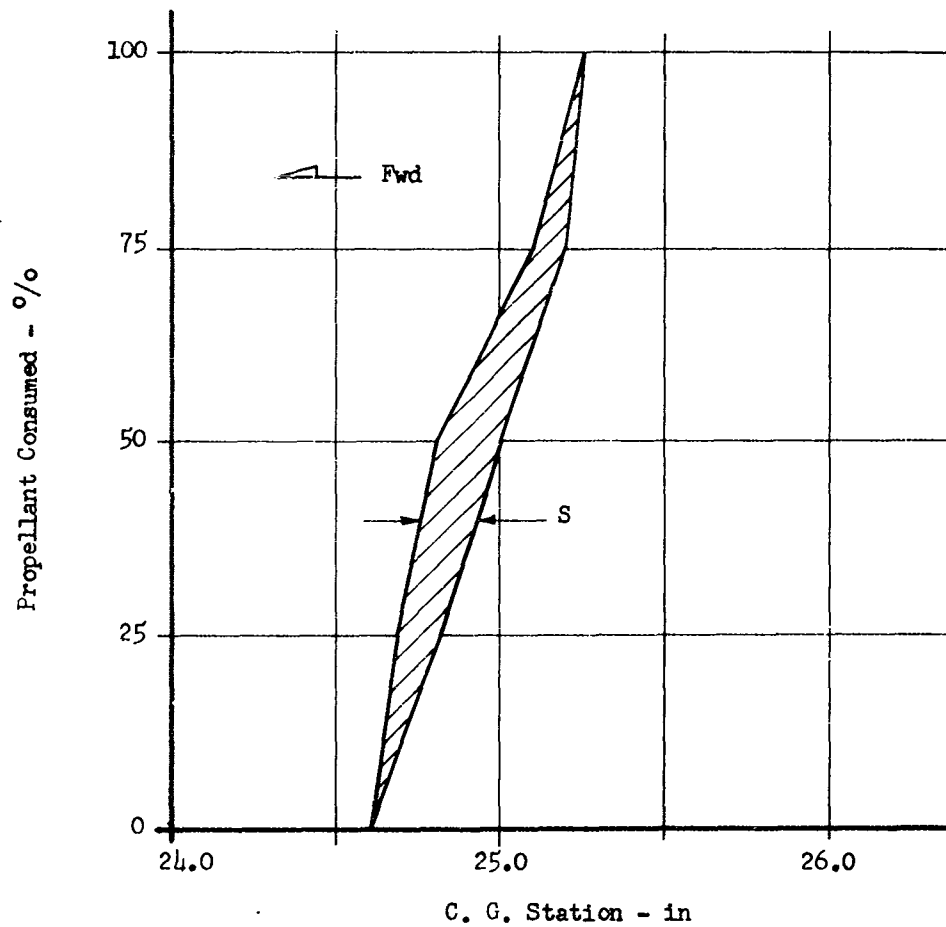
Figure 1.2.14   Control Propellant C G Shift

have been adapted to utilize the thin sections and if necessary the unorthodox-shaped spaces available throughout the missile. The electronic components such as critical sensing elements transducers, gyros, etc., will be located for best performance. The electrical power supply, which consists of batteries and associated circuitry, is located adjacent to the oxidizer tank.

1.3 FTV STRUCTURAL DESIGN

The structural requirements of the main load bearing members are evaluated in this section. Preliminary structural and aeroelastic analysis were conducted on the critical areas to prove the adequacy of the design for the FTV conditions.

To facilitate the design and to allow maximum freedom within the design, the results of the analyses have been plotted and tabulated as a function of several variables. This design philosophy permits easy evaluation of the inherent "trade-offs" resulting from variations in the design parameters.

The initial parameters utilized in the design analyses are listed below:

flight

vertical	20 g's
lateral	20 g's
longitudinal	50 g's

handling

vertical	10 g's
lateral	10 g's
longitudinal	10 g's

main propulsion motor

thrust per motor	5,000 lb

control motors

thrust per jet	600 lb (100% safety factor for the initial estimate of 300 lb per jet)

missile center of gravity 0.43 chord(measured from leading edge)

1.29

The internal configuration used throughout this analysis is shown in Figure 1.2.10. The layout was established to locate the center of gravity at the 43% chord. The ballast shown here is strictly for the Feasibility Test Vehicle and is required to facilitate the use of "off-the-shelf" components in the control system.

The weight distribution of the major components and the corresponding missile center-of-gravity location were calculated for the launch, boost termination and flight termination conditions (see Table 1.3.1). The span- and chordwise weight distribution is illustrated in Figures 1.3.1 and 1.3.2 respectively. The normal air loads are shown in Figures 1.3.3 and 1.3.4.

Moments of inertia for the pitch, roll and yaw phases at these flight conditions are listed in Table 1.3.2.

<div align="center">
Table 1.3.2
FTV Moments of Inertia
</div>

Condition	Weight (lb)	Inertia (slug-ft^2)	
Launch	425	31.7 11.6 21.4	Yaw Roll Pitch
Burnout	330	28.7 10.1 19.8	Yaw Roll Pitch
Empty	295	26.7 9.8 18.9	Yaw Roll Pitch

The conditions noted in the above table are:

    launch ----- basic missile with propulsion propellant and reaction
                 control propellant,
    burnout ---- basic missile plus reaction control propellant, and
    empty ------ basic missile only.

1.3.1 MAIN STRUCTURE   The main structure, illustrated in Figure 1.2.12 consists of four basic members criss-crossing the missile planform. These members are fabricated of magnesium alloy with the web section extending the full depth of the missile cross section. The chordwise shear and moment distributions and the chordwise net loading

<div align="center">1.30</div>

TABLE 1.3.1 WEIGHT AND BALANCE

COMPONENT	WEIGHT			MOMENT		
	LAUNCH	BURNOUT	EMPTY	LAUNCH	BURNOUT	EMPTY
STRUCTURES	66	66	66	2112	2112	2112
REACTION CONTROL SYSTEM	37	37	37	938	938	938
CONTROL PROPELLANT	35	18	--	632	348	---
CONTROL MOTOR	30	30	30	1500	1500	1500
ELECTRONICS	40	40	40	640	640	640
BOOSTER	137	42	42	4450	1605	1605
MISC.	11	11	11	279	279	279
BALLAST	69	69	69	408	408	408
TOTALS	425	313	295	10959	7830	7482

Center of Gravity	(in)	25.8	25.0	25.3
	%	43	41.6	42.0
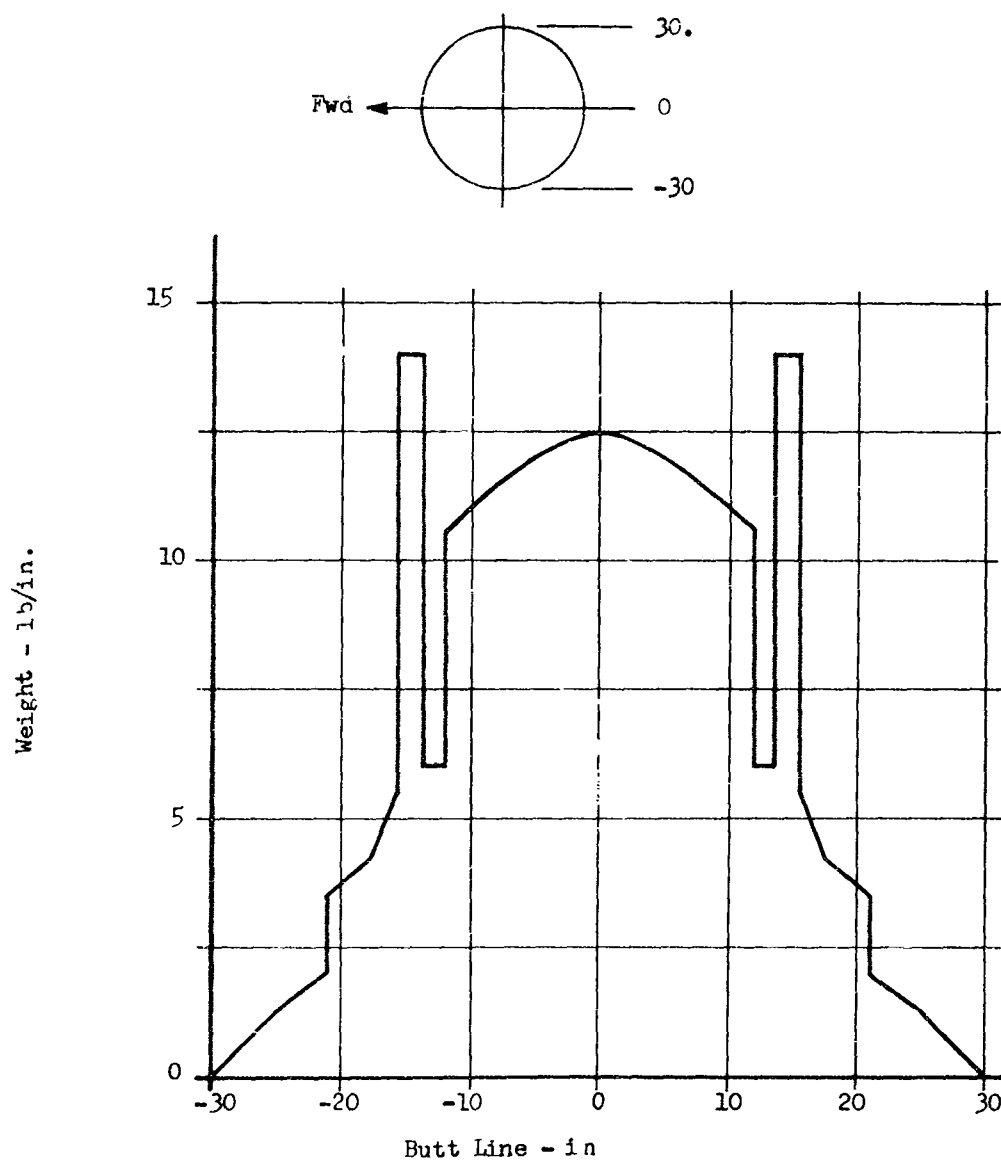
Figure 1.3.1   Spanwise Weight Distribution

SECRET
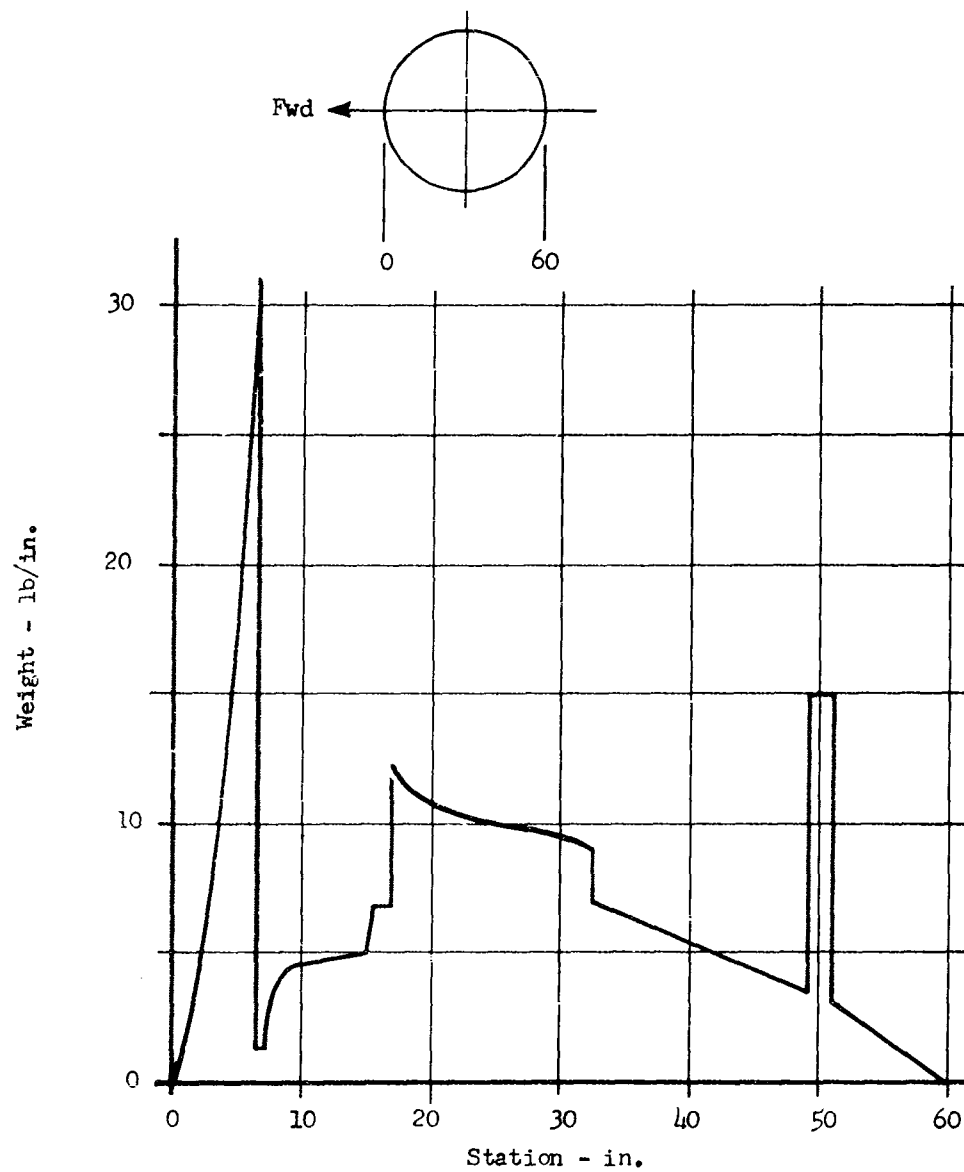
Figure 1.3.2 Chordwise Weight Distribution
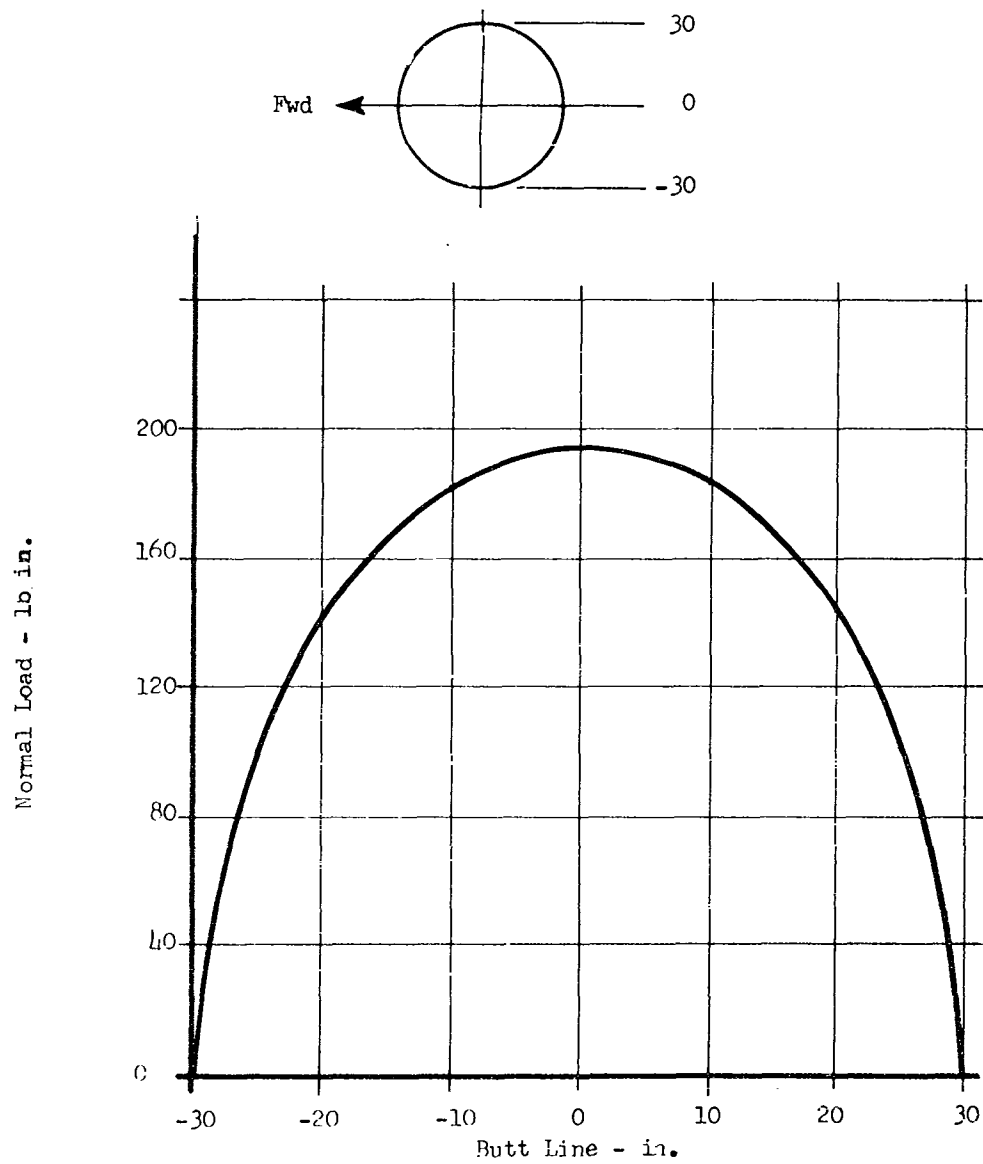
Figure   1.3.3   Spanwise Air Load Distribution

Figure 1.3.4 Chordwise Air Load Distribution

1.35

imparted to the main structure are illustrated in Figures 1.3.5 and
1.3.6 respectively. The bending moments are primarily absorbed by the
skin structure and therefore were not included in the analysis of the
main structure. However, a cursory study of the local web buckling for
body bending has established a minimum web thickness of 0.010 in.

The web section adds stiffness to the bending modes, distributes
booster thrust, maintains and separates the missile skin, and supports
the internal missile components. The critical forces on the webs,
caused by the attached components under missile dynamic environment,
establish the loads for determining the structural stiffness of the web
and of the web attachments for the missile hardware. The analyses of
the web were not completed because of the lack of detailed attachment
hardware information; however, studies have indicated that a suitable
web design is possible within the space allocated.

1.3.2 BOOSTER THRUST-PLATE   Two methods were devised for trans-
ferring the thrust to the body structural members. In the first method,
a thrust plate was designed to absorb the thrust through the forward
head of the rocket motors. This philosophy, although normally not used,
does tend to move the center of gravity in the desired forward direction.
The second design transfers the load from the thrust collar located on
the aft section of the motors. This is the normal practice and as such
has the important inherent reliability associated with it. Figure 1.3.7
illustrates the location of the thrust plates relative to the booster
motors.

For the discussion and analysis of the forward thrust plate refer
to Figure 1.3.8. To simplify the analysis, the thrust was considered
to be a uniformly distributed load over the shaded area. The outside
dimensions of the plate were chosen on the basis of the available space.

For the condition in which all edges are simply supported, the unit
stress (f_t) at the surface of the plate becomes:

$$f_t = \frac{BW}{t^2} \qquad (1.3.1)$$

where B = 0.4, interpolated from Reference 4.4. Therefore;

$$f_t = \frac{6000}{t^2} \qquad (1.3.2)$$
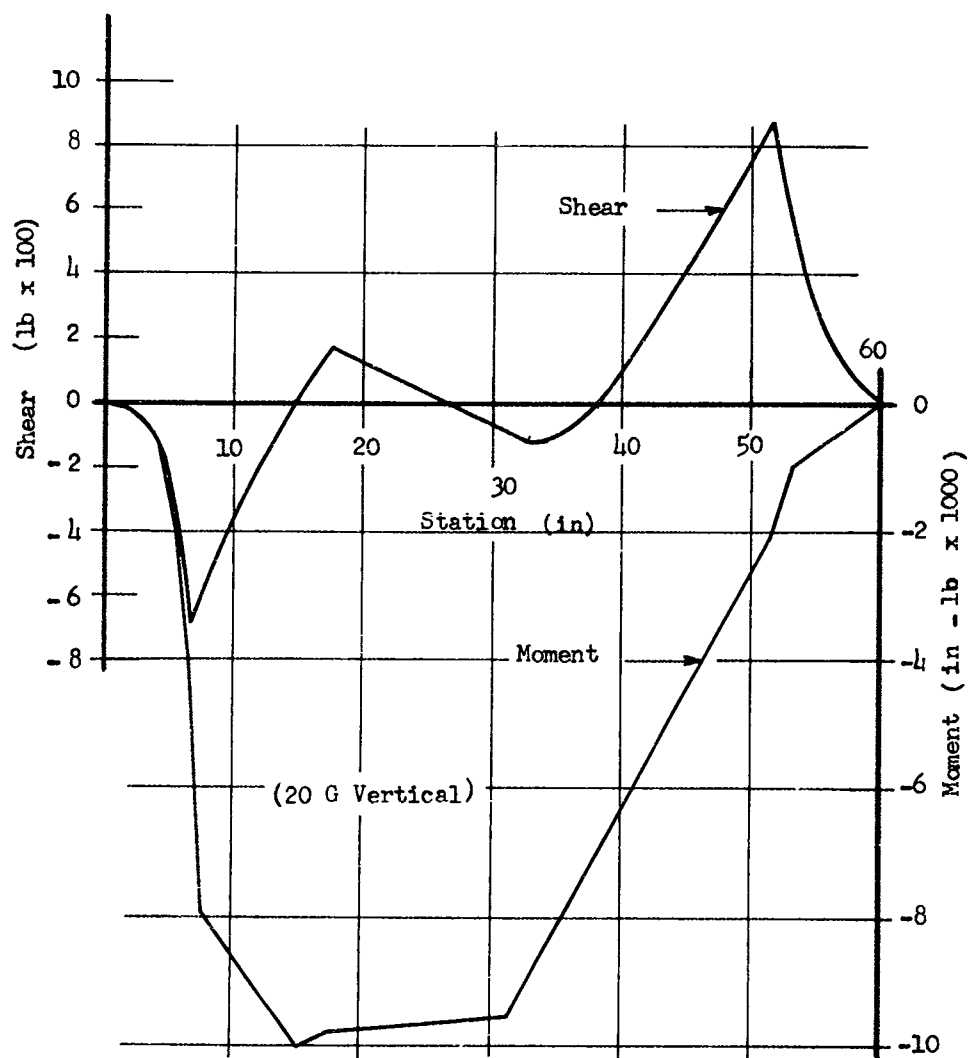
Figure 1.3.5 Shear & Moment Distribution

1.37
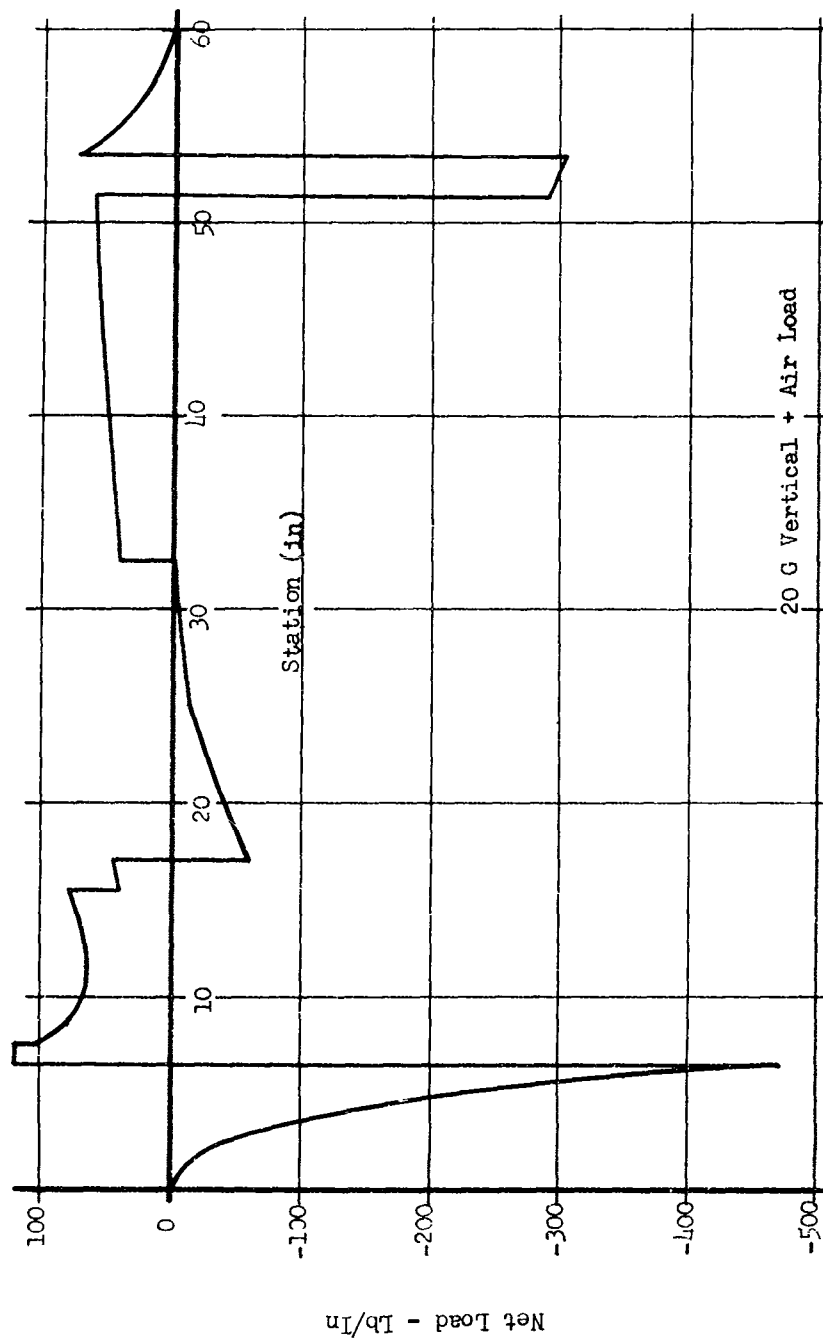
Figure 1.3.6   Chordwise Net Load

1.38

Forward Thrust Plate

Rocket Motor
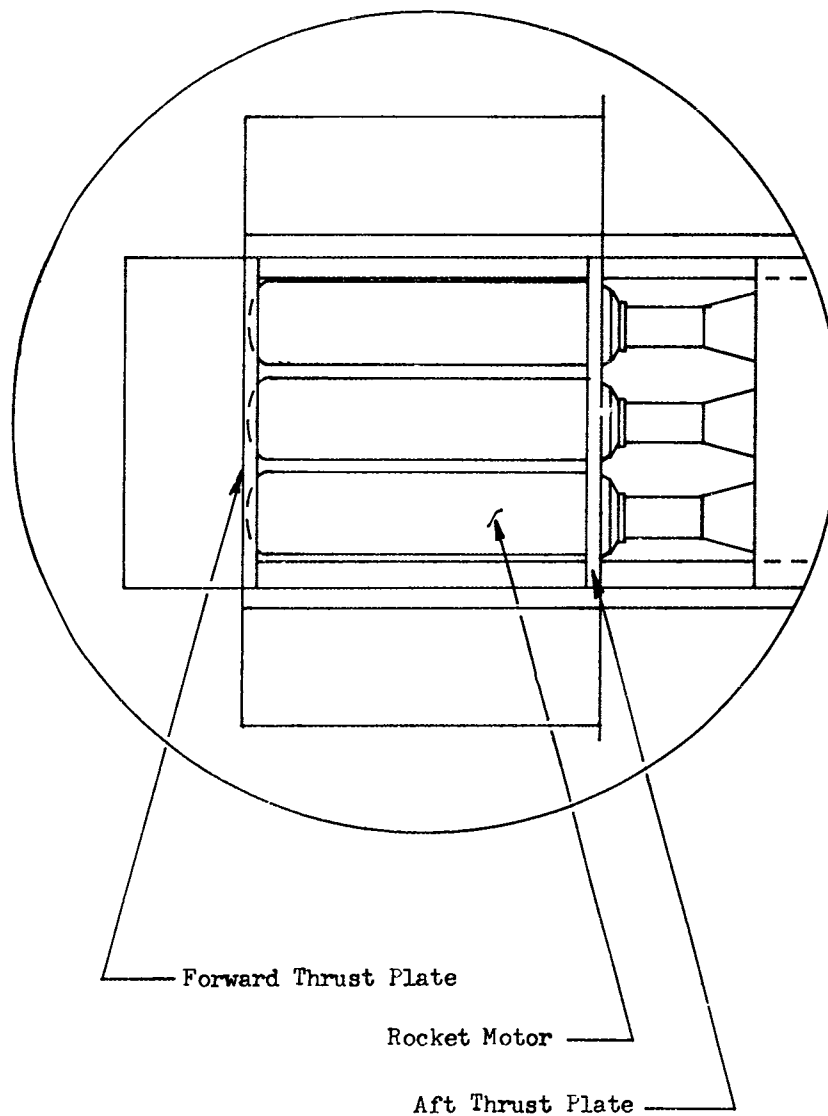
Aft Thrust Plate

Figure   1.3.7   Forward vs Aft Thrust Plate Locations

1.39
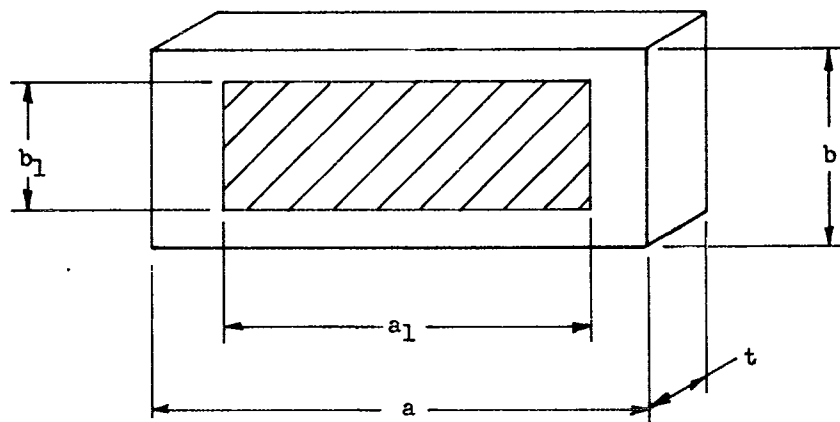
a = 24 in.

b = 5.84 in.

a_1 = 18 in.

b_1 = 4 in.

W = 15000 lb = total applied thrust

w = 200 lb per $in.^2$ = assumed uniform load

t = thickness of the plate (in)

Figure 1.3.8 Forward Thrust Plate

To obtain the minimum thickness in terms of the yield tensile strength of the material, the surface unit stress was equated to the tensile yield stress (F_{ty}). Solving for the plate thickness yields,

$$t = \sqrt{\frac{6000}{F_{ty}}} \qquad (1.3.3)$$

The plate thickness was also computed for fixed edge conditions in terms of the yield stress.

$$F_{ty} = \frac{0.5 w b^2}{t^2 \left[1 + 0.623 (\frac{b}{a})^6\right]} \qquad (1.3.4)$$

from which,

$$t = \sqrt{\frac{3475}{F_{ty}}} \qquad (1.3.5)$$

For various degrees of edge constraint (K), the plate thickness becomes,

$$t = \sqrt{\frac{3475 + 2525 (1-K)}{F_{ty}}} \qquad (1.3.6)$$

The plate thickness as a function of yield stress is plotted for various degrees of constraint in Figure 1.3.9.

<center>1.41</center>
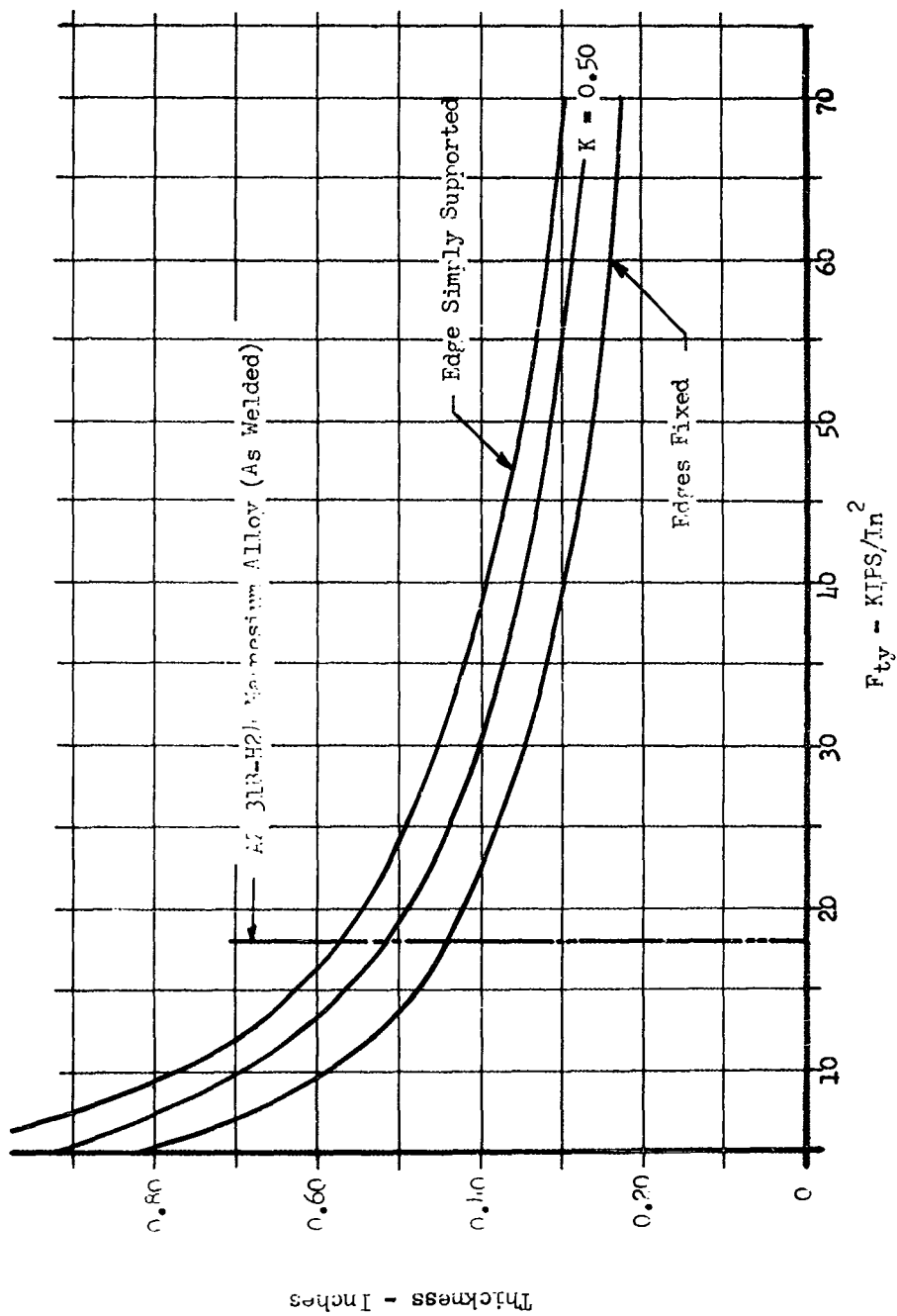
Figure 1.3.9   Forward Thrust Plate Thickness vs. F_{ty}

The aft thrust plate analysis was greatly simplified by assuming that the force (5000 lb per motor) acts at the center of the mounting holes (see Figure 1.3.10). The studies were then conducted for the simply supported and fixed end conditions illustrated in Figure 1.3.11. Since this analysis was conducted for the extreme conditions, the results yield the range of required thickness as (Table 1.3.3). The final choice of the plate thickness requires a detailed analysis of the adjacent structure to determine the exact moment distribution for the thrust loads. However, since a thrust plate having a thickness within the indicated range can be readily packaged into the FTV, the analysis was not pursued further.
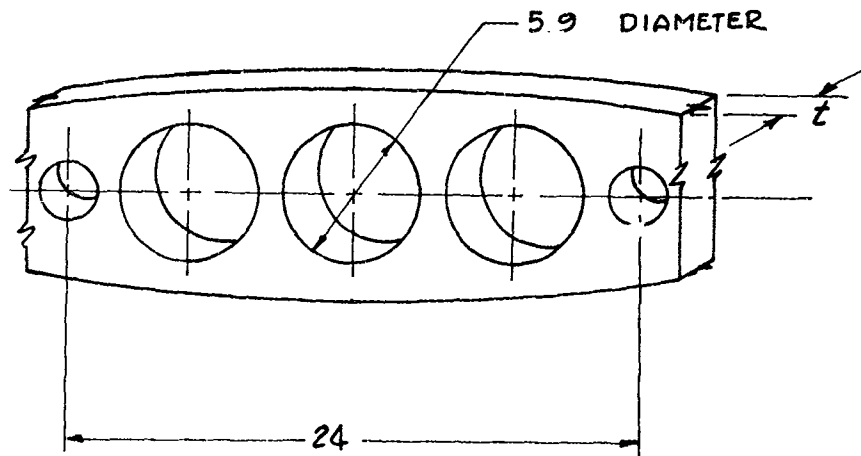
Figure 1.3.10 Aft Thrust Plate

1.43
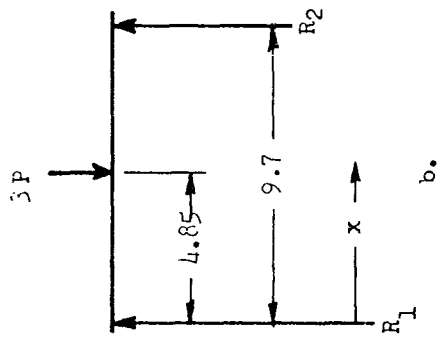
b.
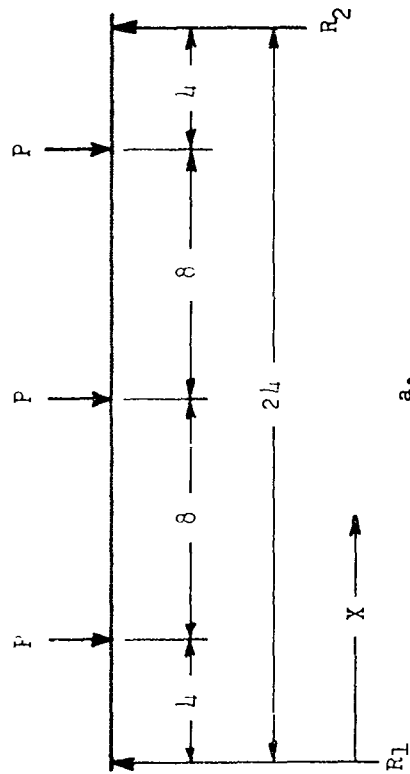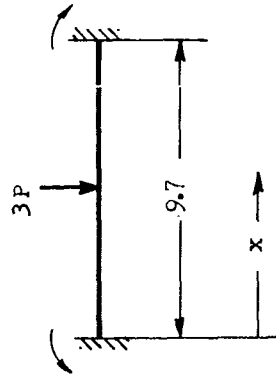
a.

Side & End Views of Simply Supported Plate
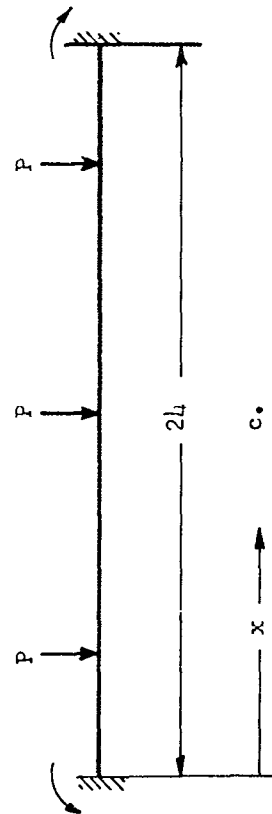
c.

Side & End Views of Plate with Fixed Ends

Figure 1.3.11 Aft Thrust Plate Load Conditions

1.44

Table 1.3.3 Aft Thrust Plate Thickness versus End Conditions

Condition	Thrust	$R_1 = R_2$ (lb)	Moment		t (in.)
			X	in-lb	
a	5000	7500	12	50,000	2.010
b	5000	7500	4.85	36,400	1.320
c	5000	7500	0	31,680	1.015
d	5000	7500	0	18,260	1.216
			4.85	12,200	0.933

Material = AZ31B-H24 Magnesium Alloy, Fcy = 18000 psi (as welded)

t = thickness of member (in.)

R_1, R_2 = reaction at support (lb)

P = rocket motor thrust (lb)

1.3.3 SKIN STRUCTURE   The major portion of the design effort ex-
pended on the PYE WACKET FTV structural hardware studies was directed
toward the skin design. The investigation was conducted on several con-
figurations of the rib and sandwich construction families. In each case,
the designs were studied in the areas of weight, stress, cost and pro-
ducibility. The latter two items, cost and producibility, are discussed
in FTV Fabrication Studies, Section 1.4.

A maximum skin temperature of 325°F (conservative) was calculated
for the leading edge and considerably lower values elsewhere (see FTV
Aerodynamic Heating, Section 1.6). Because of the relatively short FTV
flight times, the temperature effects on the structure are not severe
and have therefore been neglected throughout this analysis.

The general approach to the skin design problem consists of first
determining the panel sizes and rib sections to satisfy the structural
requirements and then performing a preliminary aeroelastic analysis of
the flutter characteristics to ensure overall design adequacy. Initially
the skin thicknesses (see Table 1.3.4) for the various panel sizes shown

Table 1.3.4 Skin Thickness vs Panel Size

Panel	a (in)	b (in)	α (b/a)	α^3	$1+(1.61\alpha^3)^{0.75}$	$\frac{w}{f_b}$	t^2 (in^2)	t (in)
A	24	24	1.0	1.0	2.61	88.3×10^{-6}	1.94×10^{-2}	0.139
B	12	12	1.0	1.0	2.61	88.3×10^{-6}	4.87×10^{-3}	0.069
C	8	12	0.666	0.296	1.477	88.3×10^{-6}	3.81×10^{-3}	0.062
D	8	8	1.0	1.0	2.61	88.3×10^{-6}	2.13×10^{-3}	0.046
E	6	12	0.5	0.125	1.2	88.3×10^{-6}	2.65×10^{-3}	0.051
F	6	8	0.75	0.423	1.68	88.3×10^{-6}	1.89×10^{-3}	0.044
G	6	6	1.0	1.0	2.61	88.3×10^{-6}	1.22×10^{-3}	0.035

w = 2.0 psi uniform aerodynamic load

f_b = 17,000 psi allowable surface stress in direction of b

t = skin thickness

in Figure 1.3.12 were designed to structurally withstand the aerodynamic loads. These panel sizes were then arranged to fit the geometry of the missile skin (see Figure 1.3.13). To facilitate the manufacturing process, the design utilizes a constant thickness (1/16-in. magnesium alloy) as determined by the minimal requirements of the largest panel.

The following analysis of the rib sections is based on the assumption that the body moments are structurally absorbed solely by the skin. The rib sections were analyzed to ensure sufficient stiffness to prevent buckling, sufficient strength to prevent failure in bending, and sufficient stiffness to limit the deflection within the aerodynamic tolerance (0.03 inches).

Since the properties of the rib and panel sections are inseparable, the panel stress for the most critical section in body bending was combined with the equivalent rib stress (Figure 1.3.14). These calculations assumed a uniform 2 psi aerodynamic load (a 20 g maneuver results in approximately 1.6 psi loading).

The unit stress (f_t) was calculated from the following relation (Reference 4.4):

$$f_t = \frac{0.75w\,b^2}{t^2(1 + 1.61\alpha^3)} \qquad (1.3.7)$$

where

f_t = stress, lb per in.^{2},
w = uniform load of 2.0 psi,
b = panel length, 6.5 in.,
a = panel width, 8.0 in., and
α = b/a = 0.813.

By substituting the numerical values into Equation (1.3.7), f_t was found to be -8730 psi.

The detailed analysis of the rib design was primarily concerned with the bending and buckling restrictions. The calculations were performed for the section with the smallest radius of curvature since this represents the most critical area. The rib span was assumed to be under a uniform load with the appropriate end loads (see Figure 1.3.15).

1.47
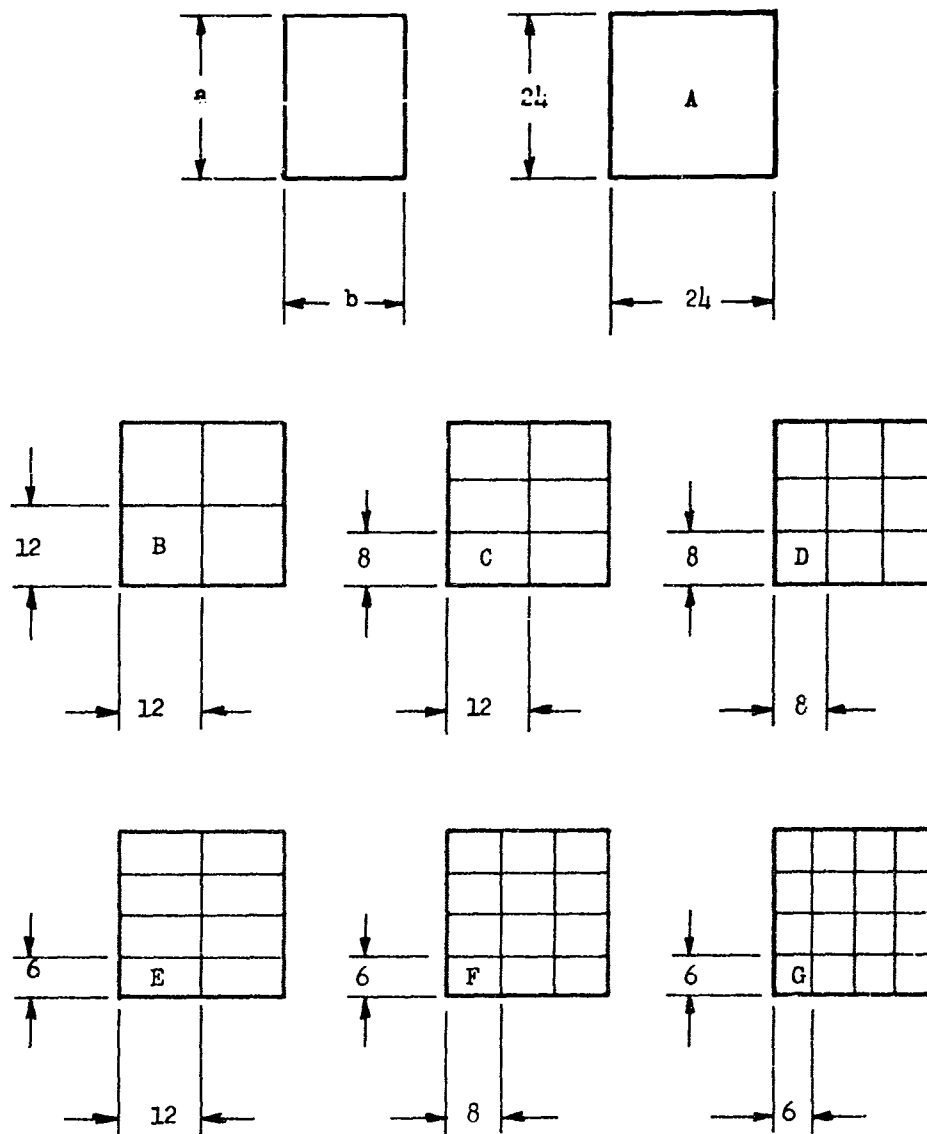
Figure 1.3.12 Panel Sizes

Fwd
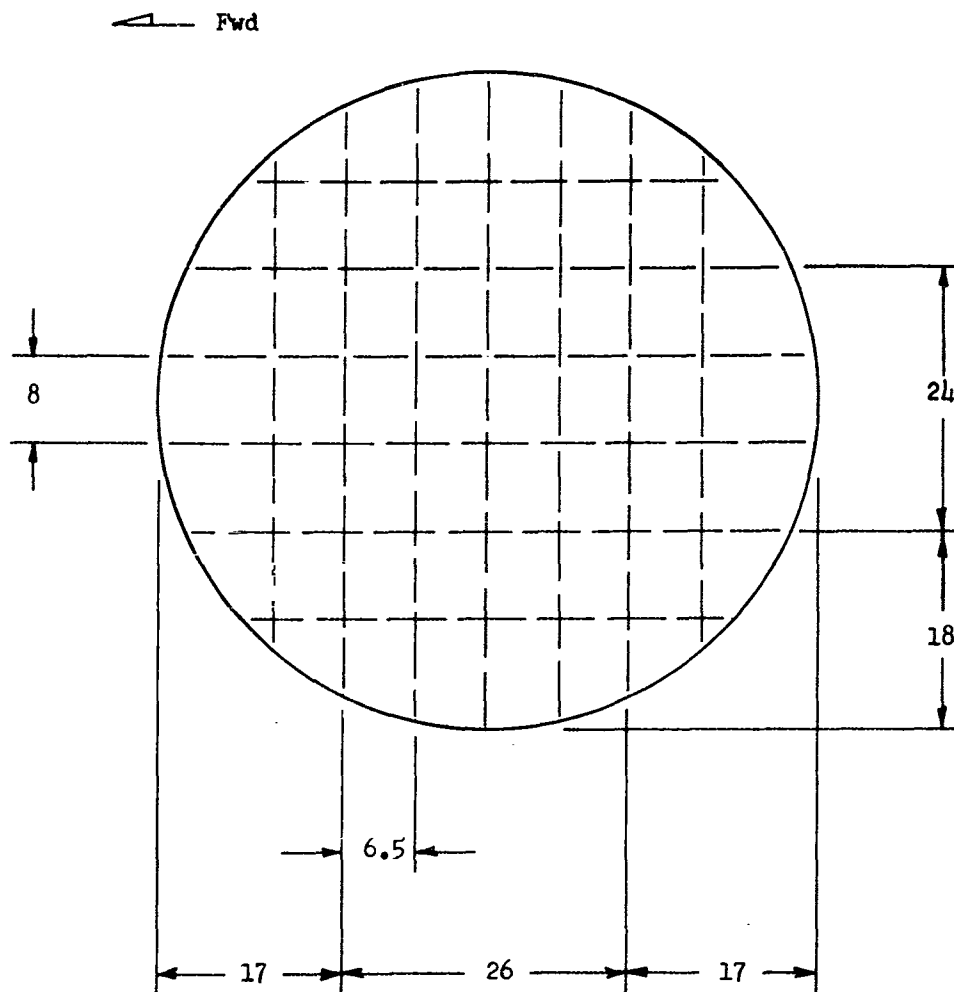
Figure 1.3.13   FTV Skin Rib Configuration
Analyzed for Stress

1.49
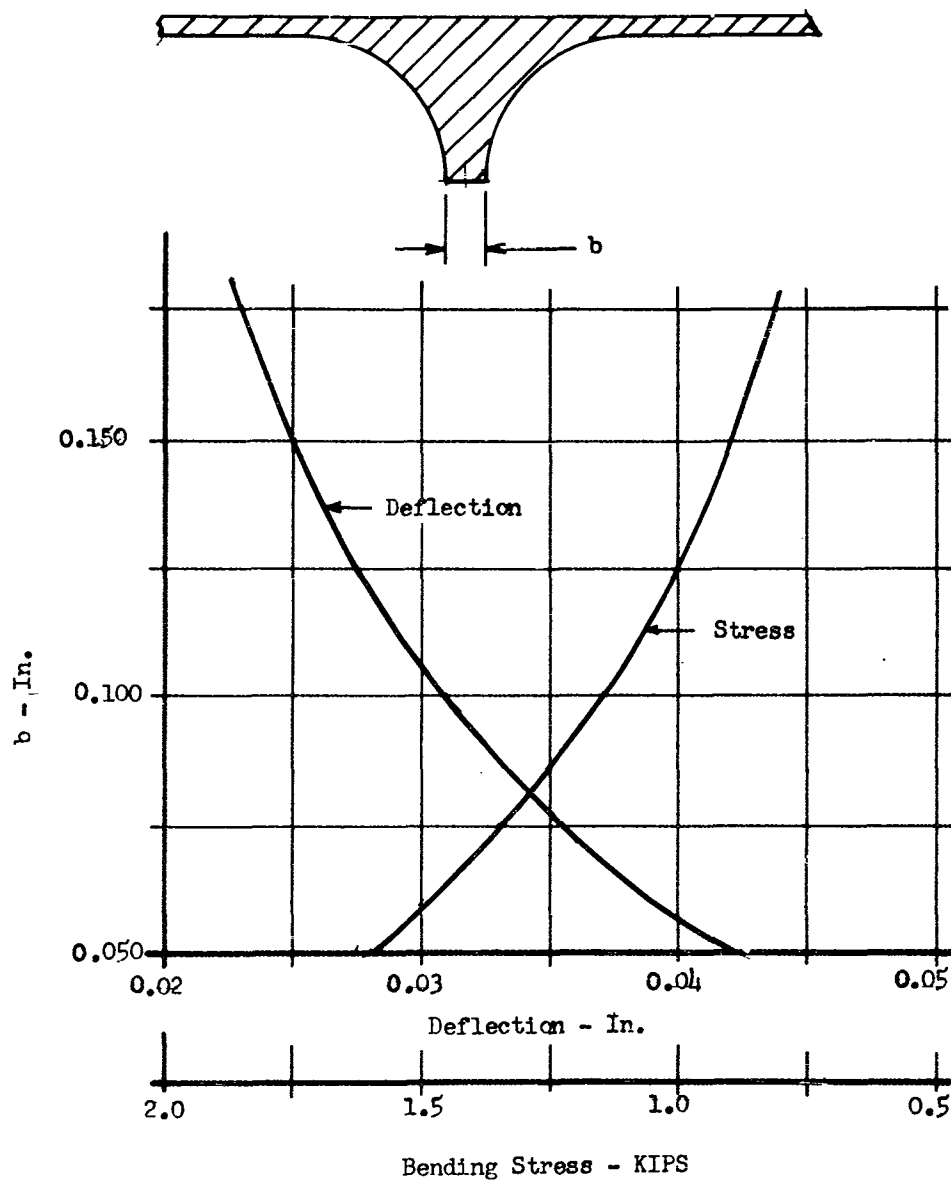
Figure **1.3.14** Skin Rib Deflection & Bending Stress
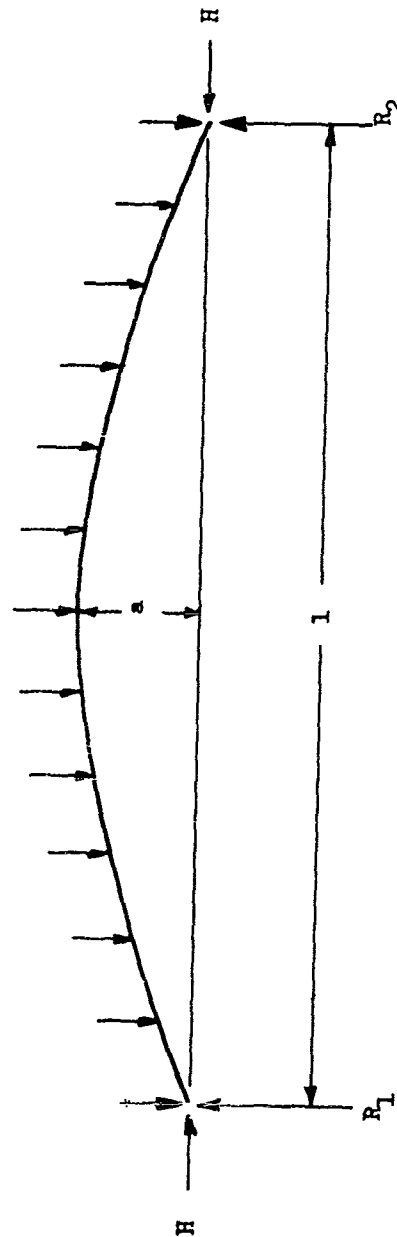
Figure 1.3.15   Skin Rib Loading Diagram

For stability in the buckling mode,

$$M = \frac{4 I_o}{A a^2} \geq 1,$$

and $\quad \dfrac{I_o}{A} \geq \dfrac{a^2}{4} \geq 0.0144 \text{ in.}^2$

where

a = curvature height, in.,
A = rib cross sectional area, in.^{2},
A = $0.4375b + 0.332$,
b = rib width, in.,
H = resultant axial load from body bending, lb, and
I = rib inertia, in.^{4}

For an I_o/A of less than 0.0144 in.^{2}, the rib may be critical in both the bending and buckling modes. However, for an I_o/A greater than 0.0144 in.^{2}, the rib may be critical in bending only. The rib dimensions are shown in Figure 1.3.16.
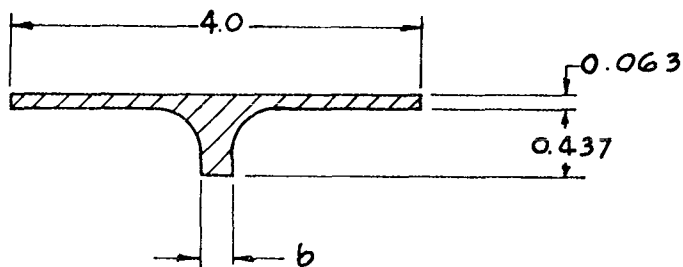
Figure 1.3.16 Rib Section

The minimum rib width (b) will be determined for the rib section based on the stability criteria previously established. The rib moment of inertia,

$$I_o = \frac{(211.1 + 2793b + 945.4 b^2) 10^{-4}}{0.4375b + 0.332} \qquad (1.3.8)$$

By substituting the expression for I_o in the equation $I_o/A \geq 0.0144$ in.^{2}, the minimum rib width (b) which satisfies the buckling requirement was found to be $b \geq 0.0744$ in. A rib width (b) of 0.125 in. is required to maintain the rib deflection to less than 0.030 in. This exceeds the 0.0744 in. and satisfies the stability requirement.

The minimum FTV honeycomb structural requirements are listed in Table 1.3.5 for both aluminum and stainless steel skin configurations. The tabulated thickness represents minimum structural requirements excluding the aeroelastic considerations.

Table 1.3.5 Minimum Honeycomb Sandwich Requirement

Type	Core Thickness in.	Skin Thickness in.	Total Thickness in.
301 stainless Steel-3/4 Hard	0.1	0.003	0.106
5052 Aluminum	0.19	0.004	0.198

The results indicate that a very thin gage sheet is required to resist the imposed aerodynamic load. However, consideration must be given to the handling, the impact of small objects and other abuses. Therefore an aluminum skin at least 0.012 inches thick would be required. Further analysis of the skin will be required to establish a minimum core thickness for the aeroelastic requirements.

1.3.4 AEROELASTIC ANALYSIS   Preliminary aeroelastic studies of the FTV configuration were conducted on a few critical areas. A complete and detailed analysis of the aeroelastic characteristics was not possible due to the task reduction specified at the start of Phase II.

A cursory examination of the estimated physical properties of structural sections with respect to the FTV flight trajectory was conducted. On the basis of this examination, the critical areas were selected for limited aeroelastic analyses.

Estimates of complex body modes and frequencies of the body structure require a complicated procedure and a complete description of the internal hardware. Since these hardware details were not available, an aeroelastic analysis of the body was not warranted in this phase. However, serious control-elastic coupling problems are not anticipated for the FTV body configuration.

Preliminary flutter analysis was conducted on the panels identified and shown in Figure 1.3.17. The flutter analysis for the configuration shown was based on a skin thickness of $h = 0.0625$ in. Dimensions of the
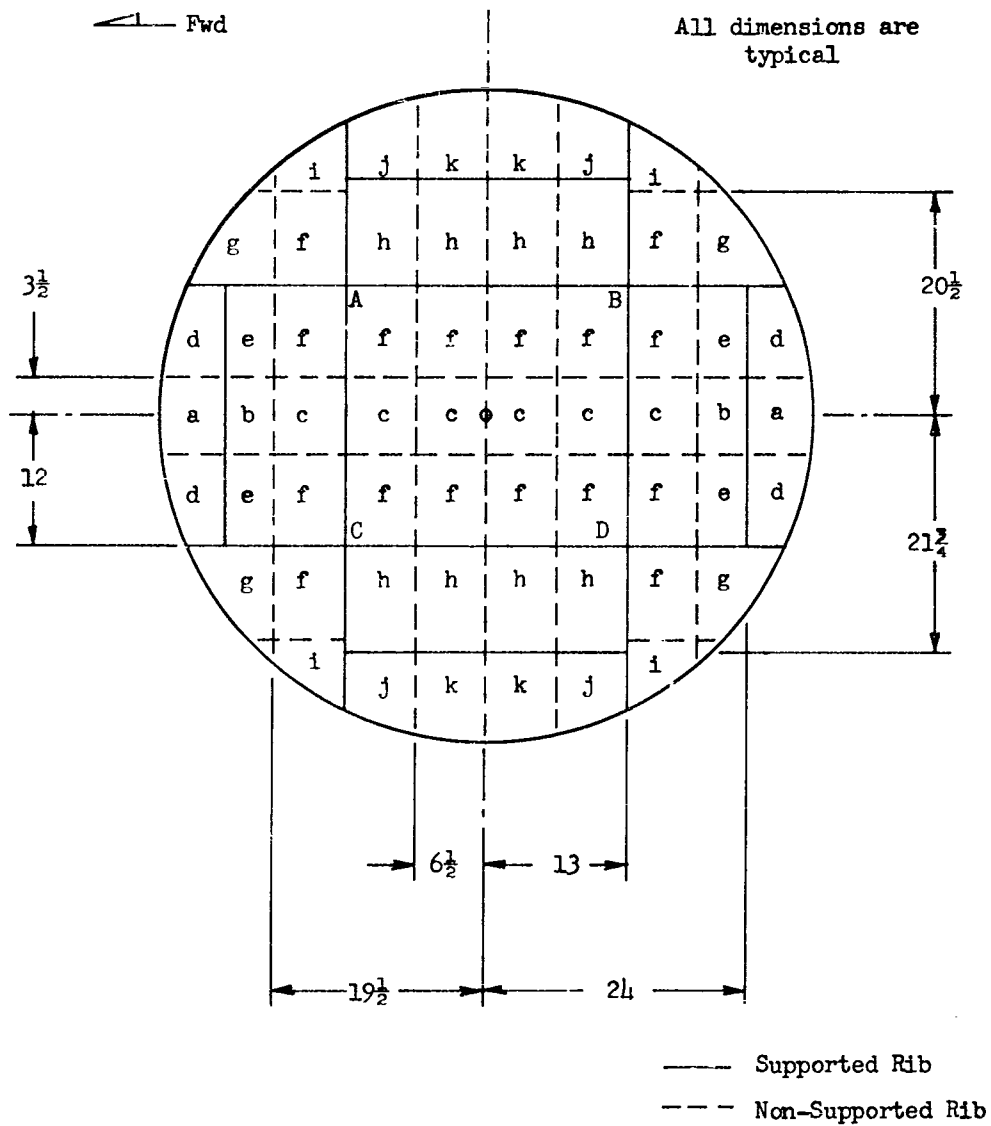
Figure 1.3.17 FTV Skin Rib Pattern Analyzed for Flutter

1.54

panels are listed in Table 1.3.6 and the flutter boundaries given in Figure 1.3.18.

Table 1.3.6 Panel Size and Aspect Ratio

Panel	Length (in.)	Width (in.)	Aspect Ratio
a	6.0	7.0	1.17
b	4.5	7.0	1.55
c	6.5	7.0	1.08
d	5.0	8.4	1.68
e	4.5	8.4	1.87
f	6.5	8.4	1.29
g	6.5	7.5	1.15
h	6.5	9.8	1.51
i	6.5	4.5	0.695
j	6.5	6.6	1.02
k	6.5	8.1	1.25

The critical Mach number for panel flutter was determined as a function of altitude. Figure 1.3.18 shows that the surfaces are all stable with respect to panel flutter up to at least Mach 4.

1.3.5 SKIN FASTENING This analysis determines the minimum number of "tie-down" screws necessary to fasten the skins to the body. Both flight and handling loads were analyzed with the "worst-case" governing the final choice.

The flutter predictions for these panels were based on a worst-case envelope of a collection of panel flutter data presented in Reference 4.5*. These data were taken during tests using various panel edge fixities,

* This is given as a plot of

$$\left(\sqrt{M_{CR}^2 - 1} \;\; \frac{E}{q_{CR}}\right)^{1/3} \;\; \frac{h}{\ell} \quad vs \quad (AR)^{-1}$$

where

ℓ = streamwise panel length,
AR = panel aspect ratio = w/l,
h = skin thickness,
w = panel width,
E = modulus of elasticity (6.06×10^6)
q_{CR} = critical dynamic pressure, and
M_{CR} = critical Mach number
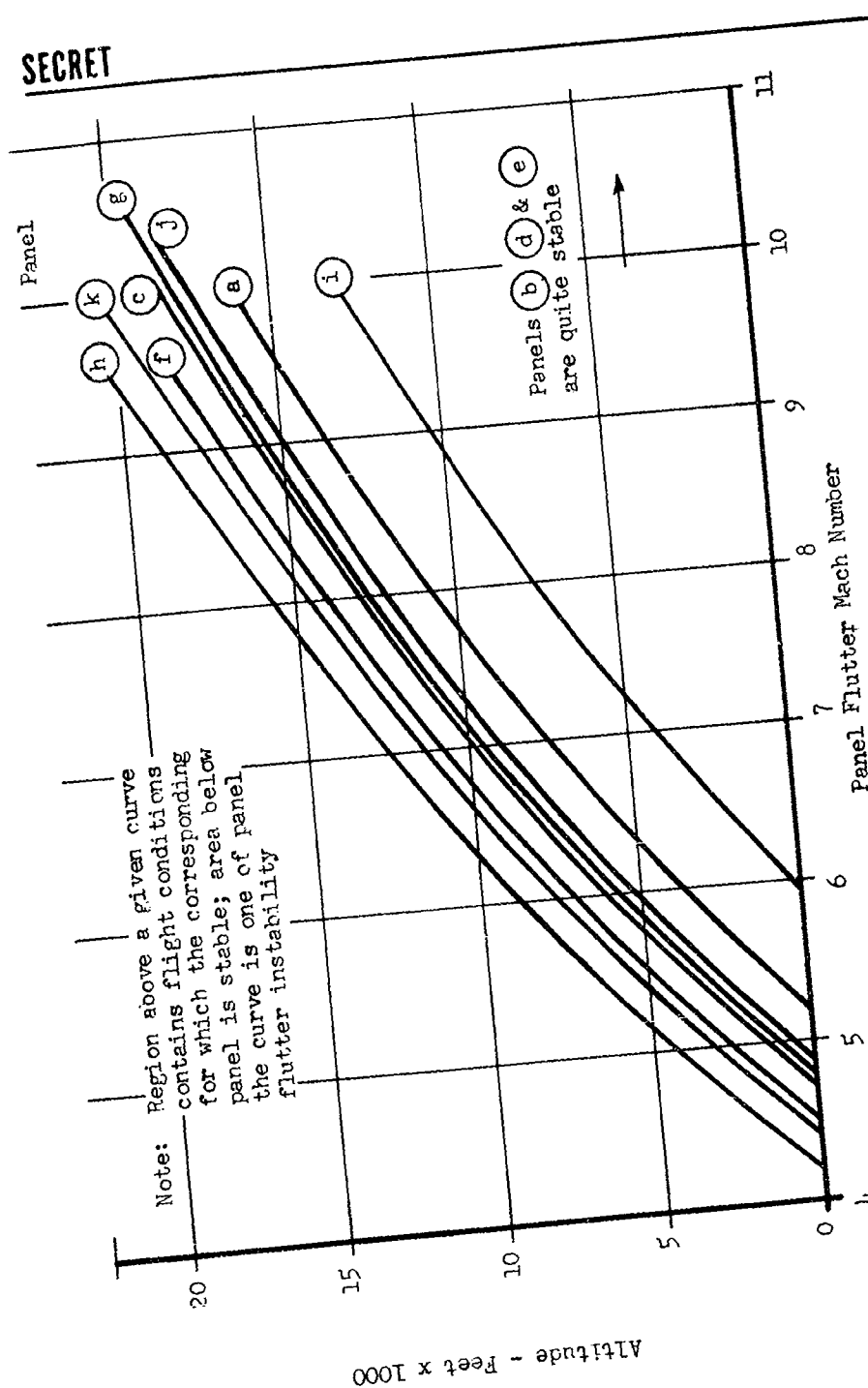
Figure 1.3.18   Panel Flutter Boundaries

Note: Region above a given curve
contains flight conditions
for which the corresponding
panel is stable; area below
the curve is one of panel
flutter instability

Panel

Panels (b) (d) & (e)
are quite stable

Panel Flutter Mach Number

Altitude — Feet x 1000

1.56

differential pressures and mid-plane stress conditions. Use of the worst-case envelope implies some conservatism in this analysis. A further degree of conservatism arises from the assumption that panels in the FTV skin are initially flat; both theory and experiment indicate that initial curvature increases panel flutter stability.

The loads acting on the skin are:

(a) 2 psi aerodynamic pressure uniformly distributed, and
(b) 10 g's handling.

The aerodynamic loads on the four internal main structures and the ring were based on the surface area distribution shown in Figure 1.3.19.

The calculated unit loads on the structure are given in Table 1.3.7.

Table 1.3.7 Air Load Distribution

Structure	Load
a, d, e, h	15.28 lb/in
b, c, f, g	15.98 lb/in
k, i	22.48 lb/in
j, l	23.18 lb/in
m, s, o, q	5.28 lb/in
t, p	10.00 lb/in
n, r	10.00 lb/in

The following tabulated results were calculated to determine the shear forces at periphery of the skin. The values of Q (Σ AY), I and V are listed in Table 1.3.8. Substituting the values from Table 1.3.8 into $q = \frac{VQ}{I}$, yields the unit shear force (q) at the periphery of the missile. These forces are tabulated in Table 1.3.9 and are located by Θ (radians) with respect to the longitudinal axis as shown in Figure 1.3.19.

The unit load combination which showed the smallest screw spacing was 5.28 lb per in (normal load), for q = 462 lb per in (shear load) at Θ = 1.11 radians.

The interaction equation for combining these two units loads is:

$$\frac{f_{sy}^3}{F_{sy}^3} + \frac{f_{ty}^2}{F_{ty}^2} = 1 \qquad (1.3.9)$$

1.57   SECRET

Fwd

B.L

n 30

m

θ

①   b   ④   c   ⑦   o

a   j   d   12

②   i   ⑤   k   ⑧   p   0

h   l   e   -12

③   g   ⑥   f   ⑨

S   q

r   -30

Sta   0   17   43   60
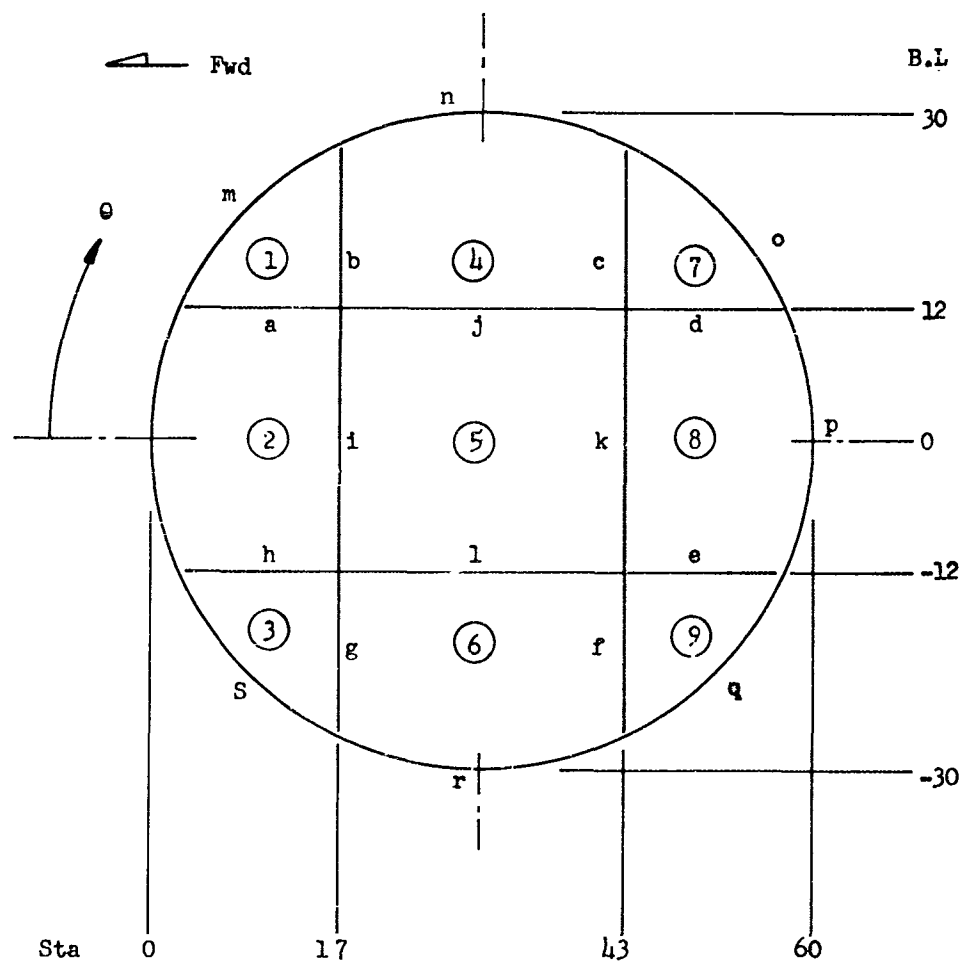
Figure 1.3.19 FTV Skin Surface Area Distribution

1.58

SECRET

Table 1.3.8   Calculated Values of Q, I & V.

Station	Buttline	Moment of Area Q (in³)	Moment of Inertia I (in⁴)	Shear Force V (lb) ⟨airload⟩	Shear Force V (lb) ⟨10 G⟩
00.0		0.00	0.00		
17.0		14.44	48.50	-380	1425
20.0		18.57	66.00	-1200	
29.7		24.15	121.31	-1100	
42.0		28.10	169.80	-648	
60.0		0.00	0.00	0	0
	30.0	0.00	0.00	0	0
	12.0	32.53	155.29	-962	1429
	00.0	42.47	228.68	0	0
	-12.0	32.53	155.29	-962	1429
	-30.0	0.00	0.00	0	0

1.59

Table 1.3.9   Calculated Shear Flow q

Ω radians		Lateral (lb/in)	Longitudinal (lb/in)	Combined (lb/in)
10 G Handling	0	0	0	0
	0.42	258	299	395
	1.11	424	182	462
	$\pi/2$	178	0	178
	2.03	84	182	200
	2.72	51	299	303
	π	0	0	0
Flight	0	0	0	0
	0.42	69	204	215
	1.11	113	124	168
	$\pi/2$	219	0	219
	2.03	108	124	164
	2.72	66	204	214
	π	0	0	0

where

$$f_{sy} = q\,\ell \quad , \quad f_{ty} = w\,\ell$$

and

$$\ell = \text{screw spacing}$$

AN-3 screw properties are:

$$F_{tu} = 2210 \text{ lb,} \qquad\qquad F_{ty} = \frac{103}{125} \times 2210 = 1820 \text{ lb}$$

$$F_{su} = 2126 \text{ lb, and} \qquad F_{sy} = \frac{61.8}{75} \times 2126 = 1750 \text{ lb}$$

Substituting the above values in the interaction equation

$$\left(\frac{462\,\ell}{1750}\right)^3 + \left(\frac{5.28}{1820}\right)^2 = 1$$

and reducing,

$$0.01838\,\ell^3 + 0.0000245\,\ell^2 = 1$$

Since the second term would be very small in the ranges of spacing considered in this case,

$$\ell^3 = \frac{1}{0.01838} = 54.5 \text{ in}^3$$

and

$$\ell = 3.8 \text{ in } \text{maximum.}$$

1.61

Since the determining factor in establishing ℓ = 3.8 inches was the large shear force, shear pins may be substituted for every other screw provided the buckling stability is not exceeded. Substitution of aluminum shear pins results in fewer thread inserts and reduced weight.

The investigation of the skin buckling between "tie-down" points has not been conducted. This decision was based on the high buckling stability exhibited in the previous panel analysis.

1.4 SKIN FABRICATION STUDY

Several methods of fabricating the honeycomb sandwich and rib skins were investigated and compared on the basis of the following criteria:

(a) manufacturing complexity,
(b) final skin weight,
(c) cost,
(d) tooling, and
(e) fabrication time.

The FTV skin type was finalized by choosing the configuration which proved most desirable from both the structural and manufacturing aspects.

1.4.1 RIB-SKIN FABRICATION TECHNIQUES   The rib construction can normally be placed in one of two categories, i.e., a riveted construction consisting of a stretch-formed skin with riveted rib-stiffeners or a one-piece construction fabricated from either a plate or cast material. The rivet construction requires little study since this method has been proven by experience. The one piece construction, however, requires special forming and machining operations.

For the purpose of discussing the application of the fabrication methods to rib-skin construction, these techniques have been grouped and are shown below.

Type	Forming	Finish
A	cast	hand finish
B	cast	profile machining
C	explosive	chemical etching
D	explosive	profile machining

1.4.1.1 Forming   For the integral rib-construction, some method is required to form the exterior or interior surface contour of the skin. In the case of formed plate, the inside surface is processed

to make the integral ribs. For the cast skin, the ribs are cast with the skin and the final operation is performed on the exterior surface.

Of the various forming methods available, only explosive, stretch, and press forming have been considered. The selections were further reduced when investigation indicated that the hydropress capacity for magnesium alloy is 1/4-inch thick plate, and the stretch forming process is limited to even thinner stocks. Only the explosive method is capable of handling the required thickness and size. This technique, however, seems to be limited only by the lack of experience in forming heavier magnesium plate.

Another suitable method is sand casting. Magnesium sand casting can be obtained in a variety of sizes and shapes of uniform quality. The FTV rib-skin structure is simple but it does have relatively large areas of thin skin sections. Recently techniques have been developed for producing thin-walled castings usually made in sand molds as replacements for complicated fabrication. Walls as thin as 1/8 in. can be cast in small parts with good pattern equipment under favorable conditions. For the FTV castings, minimum cast thickness of 0.150 in. has been recommended with a nominal tolerance of ± 1/32 in.

Such important factors as microporosity or microshrinkage, scum or dross inclusions, etc., are dependent on the foundry practice and on the individual experience of the foundry. Therefore, the relative soundness of the casting requires careful design coordination with the prevailing practice of a particular foundry. A local survey has indicated that experience and skill are available, and that similar applications of cast products have been made for missiles.

1.4.1.2 <u>Finish Operation</u>   This operation consists of either chemical etching, machining, sanding, filing or other processes for cleaning or removing materials to produce the desired end product.

<u>Chemical Etching</u>   With this technique, the mechanical milling process is replaced with a chemical etching process to form the raw material into the finished shape. Although this process is applicable to magnesium alloy, the present "know-how" favors the use of aluminum alloy. Because magnesium is very reactive and does not etch evenly, several "in-process" checks are required to maintain acceptable skin thickness tolerances. A different degree of accuracy and evenness in the etching rate is possible by using different chemical compounds. The FTV rib-skin construction requires removal of approximately 0.43 inches of material in forming the skin and ribs from a 0.50-inch thick formed plate. This "cut" presents problems for chemical removal in view of the ± 0.010 tolerance required for the skin.

Machining Operation   The mechanical machining of the ribs on the inside surface of a preformed stock can best be accomplished by an automatic profile machine. This process requires a duplicate model of the end product for the tracer to follow in guiding the cutting tool. The final finish and tolerance capability of this type of machine has been proven and is acceptable for the FTV design. The degree of surface finish will be dependent on the cross feed and the selected tool radius. The maximum tool radius which would always be tangent to the skin surface will produce the best result.

Handwork   This consists of filing, scraping or grinding operations usually sufficient to give the castings the desired smooth finish. The main disadvantage of this method is that it requires an ex sive precision casting. Also, the casting tolerances are expected to produce large variations of weight and in most cases result in a heavier skin casting. Therefore, for the FTV's, this operation can be best used in the final polishing operation for the finish machined skins.

1.4.2 SANDWICH CONSTRUCTION   Many of the obvious advantages of honeycomb sandwich structures added impetus to the investigation of applying this construction to the PYE WACKET FTV. The high strength-to-weight ratio is one of the very important advantages. From an aerodynamic standpoint, the relative smoothness of the surface is very desirable. The surface smoothness is related here to that of the thin gage conventional paneling which often has surface irregularities associated with spot welds and rivet heads. For a given weight, the sandwich construction is normally stiffer than the conventional types. This tends to decrease the surface deflection in the presence of aerodynamic loads.

Forming a honeycomb structure into a compound curve such as the PYE WACKET skin, presents some difficulty because of the cross coupling effect of the honeycomb core. To overcome this problem, the core could be cut into wedge shapes and then assembled. In some cases, the aluminum core can be crushed into shapes to match the curved surfaces.

The honeycomb construction is at a disadvantage if any major structural repairs are required. Only minor alterations are convenient, even when fibre glass cores are employed.

The temperature of a sandwich part fabricated with an epoxy-phenolic adhesive should be limited to 260°F. However, since short time exposures to 500°F or higher are permissible, this does not constitute a limitation for the FTV application.

A sandwich skin for the FTV then seems to be the logical choice in view of the structural advantages and smooth aerodynamic surfaces.

However, there has been little previous fabrication of honeycomb into a compound surface such as required for the FTV skin; some developmental work will be required to prove this capability. The time schedule associated with the proposed flight test program enhances the desirability of having greater flexibility of insert location to meet possible design changes.

1.4.3 SKIN SELECTION Due to the unique surface configuration of the PYE WACKET missile, the preference factor for producibility was heavily weighted in the final FTV skin selection. The cost including lead time, etc., also received a relatively heavy weighting factor. This rule was adopted in view of the difficulties which could be encountered in forming the large surface composed of several compound radii.

The combinations of skin types and fabrications techniques are grouped and presented in Table 1.4.1, along with their relative rating in regards to the criteria employed in this study. The ratings are alphabetical with the A's designating first choice.

Table 1.4.1   Skin Type and Fabrication Comparison

TYPE	FABRICATION	PRODUCIBILITY	COST
Rib Skin Mag. Alloy	Explosive Forming and Machining	E	E
Rib Skin Mag. Alloy	Cast Forming and Machining	A	C
Rib Skin (Rivet) (Mag-Alloy)	Hydro-Forming Stretch-Forming, and Rivet-Assy.	A	D
Sandwich Al. Face Al. Core	Stretch-Forming and Crush-Core with Adhesive Bond	D	B
Sandwich Laminate Skin Al. Core	Crush-Core and Laminate Skin	C	A

The producibility of each combination was primarily based on the current demonstrated capabilities in the field of forming a configuration equivalent to the FTV skin.

Considering the requirements discussed previously, the cast magnesium alloy rib skin as shown in Figure 1.4.1 is the first choice for the FTV skin configuration; second choice is the sandwich laminate skin configuration. It is possible that shrinkage voids may occur in the casting, however these flaws can be easily detected by 100% X-ray examination. The imperfections can then be readily corrected with repair welds even in the thin sections. Dross inclusions in the top surface will be removed during the finish machining operation. The finish operation will be performed on a three-dimensional profile machine. To assure accuracy during this operation, close attention must be directed toward the selection of the proper cutters and machine adjustments.

1.5 FTV LAUNCH SYSTEM

Though not a major part of the study, a brief analysis of the launcher configuration was necessary since the launch technique to be employed has a direct bearing on the FTV design. Therefore, this portion of the PYE WACKET Phase II task was directed toward an investigation of the design feasibility of a launching system which would be compatible with the Feasibility Test Vehicles. The word compatible implies the following design rules:

1. high reliability,
2. mountable on a high-speed rocket-sled,
3. minimum vibration transfer from the sled to the missile,
4. minimum of twelve feet missile-to-ground clearance, and
5. low cost.

In addition, it would be desirable if the FTV launching system could be later adapted to the prototype missile and its aircraft launching platform. However, a cursory study indicated that the most feasible launching technique applicable to a bomber defense system is a downward ejection scheme. The background studies required for such a design include the following major items:

1. loads on the missile due to ejection,
2. effect of firing delay of one ejector (assuming three ejectors required),
3. effect of unbalanced ejector forces,
4. effect of ejector force gradient,
5. effect of sled body and launcher, and
6. effect of ejection acceleration on the reaction control jets.

The extensiveness of such a program renders the ejection launching system unfeasible for the FTV from the standpoint of time and minimum program cost.
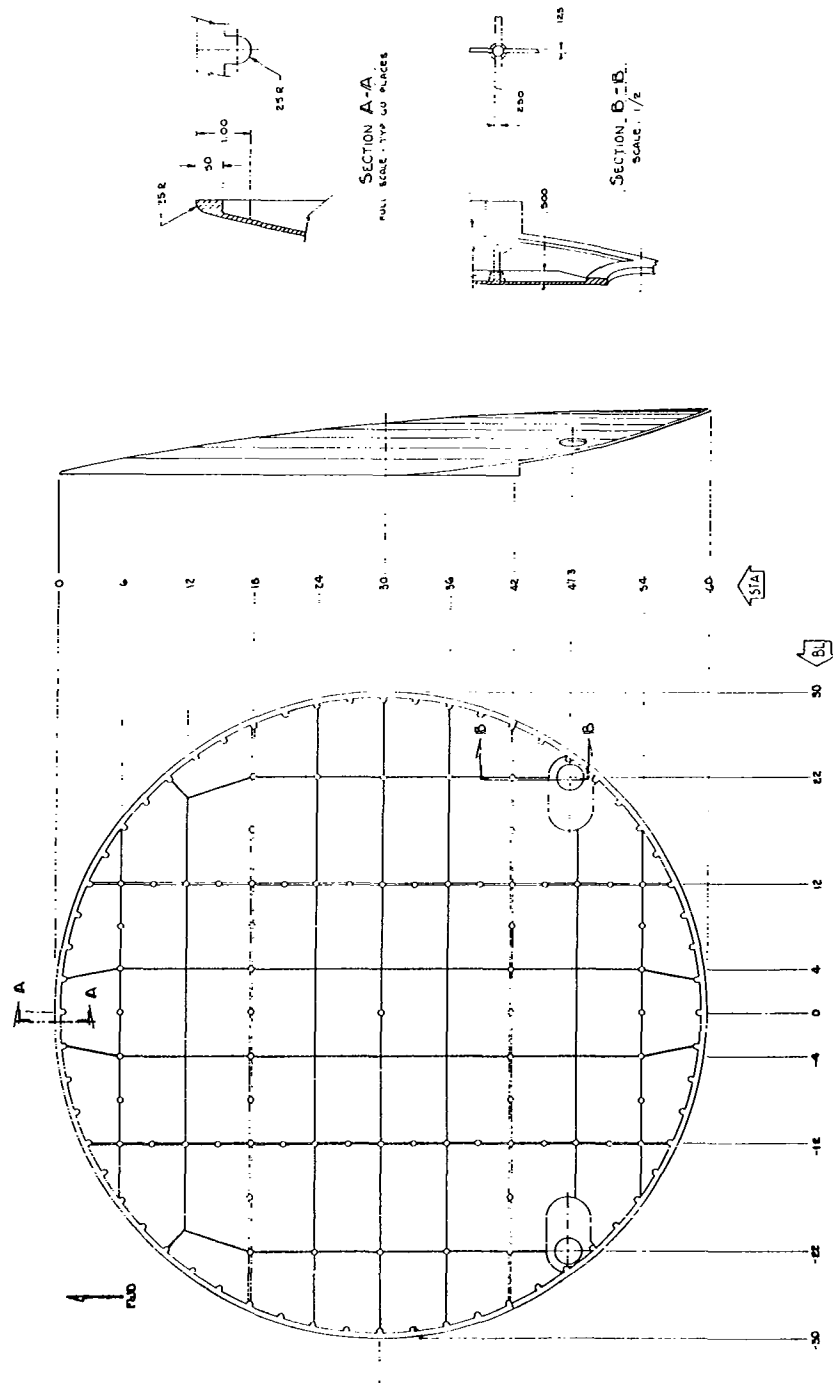
FIGURE 1.4.1 LAYOUT OF CAST MAGNESIUM SKIN

SECRET

The investigation of numerous possible launching systems indicates that the launch-rail system shown in Figures 1.5.1 and 1.5.2 will meet the required FTV conditions. The launcher is a twin-rail system capable of 360 degree rotation in the horizontal plane and 90 degrees in the vertical plane. Vernier adjustments are incorporated for accurate missile alignment.

The launcher rails slide into the two longitudinal cylinders located on either side of the missile booster-motor cluster. A simple locking device to hold the missile prior to launch will be designed into the system. The device will consist of a parallel arrangement of two actuators linked to a single locking mechanism. The redundancy of double actuators provides a simple but highly reliable system. The release mechansim will be in the igniter-circuit interlock. In the case of booster misfire, a simple shear pin prevents the loss of the missile. The pin will be designed for a shear strength greater than the aerodynamic drag force but less than a single booster-motor thrust.

The launching rail elevation above the ground is governed by the aft launch flight parameters of the FTV (see Figure 1.5.3). In addition to providing ground missile clearance, the added height decreases the ground and sled aerodynamic turbulence imposed upon the missile during the launching phase of the flight.

The external envelope of the entire system and the internal structural members under consideration are shown in Figures 1.5.1, 1.5.2, and 1.5.4 respectively. The skin enclosure was introduced to reduce the aerodynamic drag and to prevent buffeting. The preliminary structural analysis of the tower was based on the following loads (see Figure 1.5.4). For the aft launch condition with an assumed 5 degree nose-down angle-of-attack:

$$F_{DM} = 1465 \text{ lb} \quad \text{missile drag (maximum)},$$

$$F_N = 1194(5) = 5790 \text{ lb} \quad \text{normal aerodynamic load (maximum)},$$

$$F_I = 2420(10) = 24200 \text{ lb} \quad \text{inertial load (maximum), and}$$

$$F_{DT} = 3000 \text{ lb} \quad \text{tower drag (maximum)}.$$

Summing the vertical forces for an equilibrium state yields,

$$R_F + R_A + F_N = 0 \quad\quad (1.5.1)$$

1.68
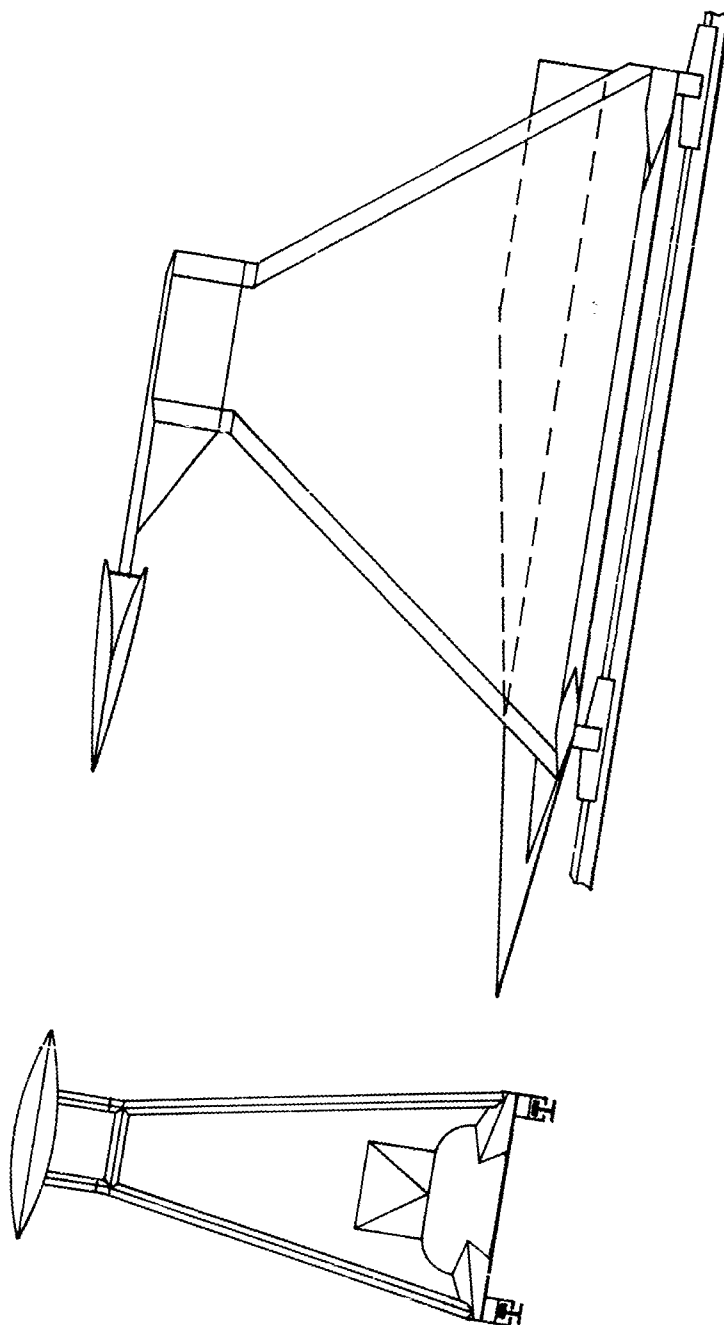
SECRET

Figure 1.5.1   FTV Forward Launch Configuration

1.69
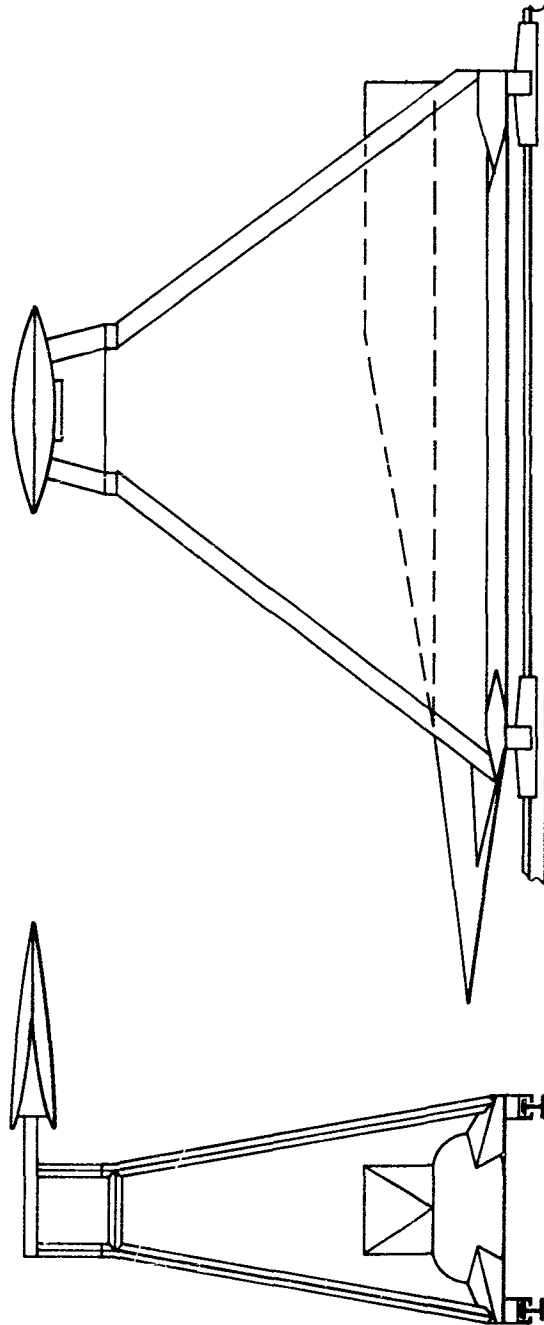
Figure 1.5.2   FTV Side Launch Configuration

Conditions =

    Reaction Jets Off
    Aerodynamics Based on Power Off Condition
    Missile Weight = 425 lb

Missile Vertical Drop (Zero Lift Assumed)

Missile Velocity

One 'G' Maneuver

Missile Trim Angle of Attack Required for Level Flight

Time from Launch - Seconds
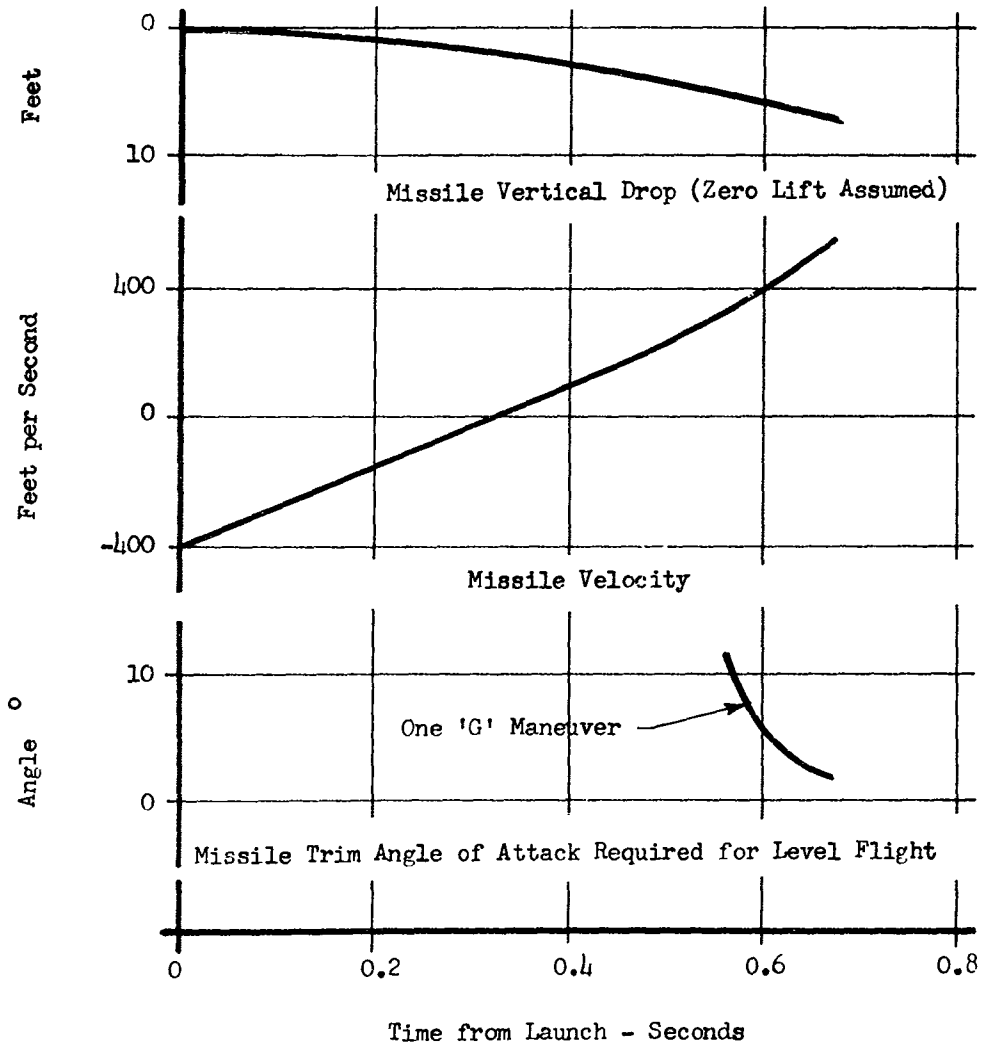
Figure 1.5.3   Estimated FTV Aft Launch Parameters
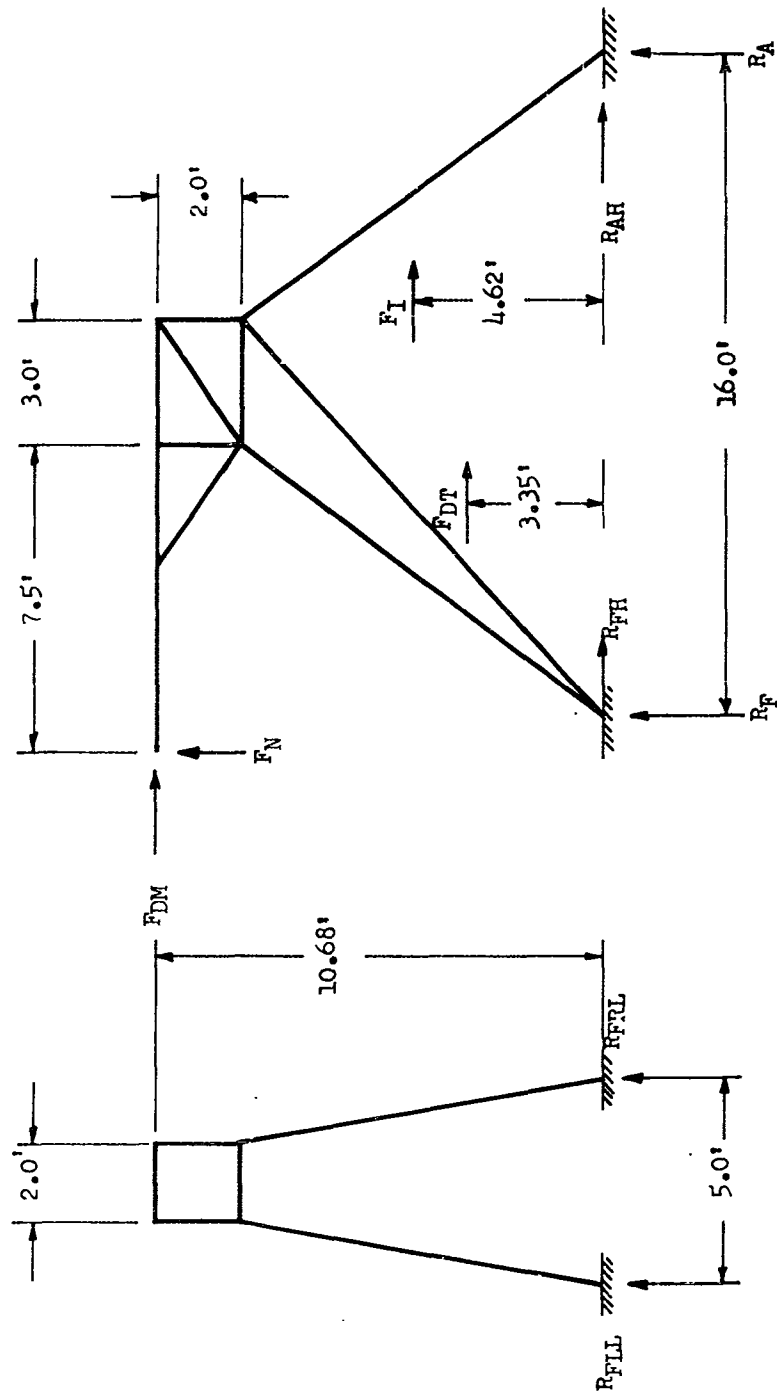
Figure 1.5.4   Launcher Structural Configuration

and hence,

$$R_F + R_A + 5970 = 0.$$

Summing the moments about R_F yields,

$$(6.48 - 7.50)F_N + 15.95R_A - 10.68F_{DM} - 3.35F_{DT} - 4.62F_I = 0 \qquad (1.5.2)$$

from which

$$R_A = 9110 \text{ lb.}$$

The remaining unknown vertical force is:

$$R_F = -9110 - 5970 = -15080 \text{ lb.}$$

But

$$R_{FL} = R_{FR} = R_F/2 = -7540 \text{ lb,} \qquad (1.5.3)$$

$$R_{AL} = R_{AR} = R_A/2 = 4555 \text{ lb, and} \qquad (1.5.4)$$

$$R_{FLL} = R_{FRL} = 0 \qquad (1.5.5)$$

The vertical reactions R_{FL}, R_{FR}, R_{AL}, and R_{AF} will be transferred directly into the structural members located over each sled slipper for maximum rigidity and strength.

The Edwards Air Force Flight Test Center (AFFTC) track capacity is shown in Figure 1.5.6.

Throughout the detailed solution for the axial force (F_c) in strut C (see Figure 1.5.5) a compression force is considered positive.
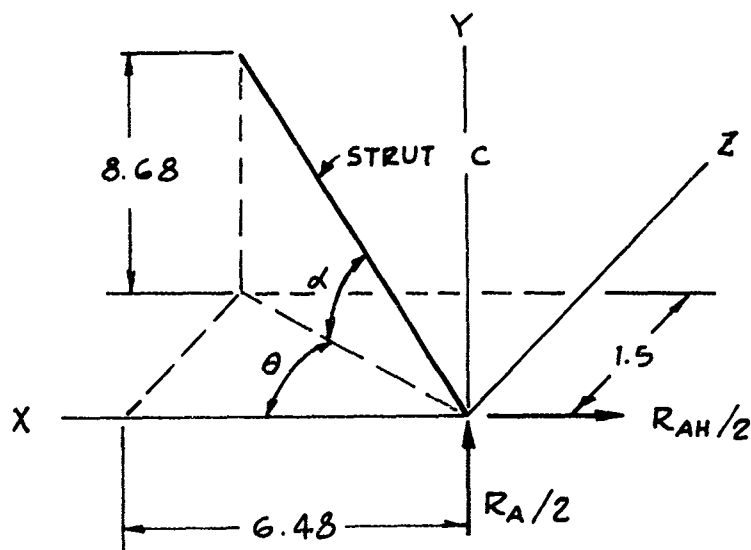
Figure 1.5.5 Strut "C" Analyses

$$F_C \sin \alpha = R_A/2 \qquad\qquad (1.5.6)$$

where

$$\sin \alpha = \frac{8.68}{\left[(8.68)^2 + (1.5)^2 + (6.48^2)\right]^{1/2}} = 0.794$$

Therefore

$$F_C = \frac{4555}{0.794} = 5730 \text{ lb COMPRESSION.}$$

The geometry of the strut C arrangement indicates that

$$\cos \theta = \frac{6.48}{\left[(1.5)^2 + (6.48)^2\right]^{1/2}} = 0.975,$$

1.74

Notes =

1. Curve for point load on one rail.

2. Min. distance between load applications along rail = 3' -0".

3. Curve assumes no axial load on rail i.e., rail temp = 115°F.

Ellipse =
$$\frac{Y^2}{(81K)^2} + \frac{X^2}{(22K)^2} = 1$$

Ellipse =
$$\frac{Y^2}{(108K)^2} + \frac{X^2}{(22K)^2} = 1$$

all scales in lbs x 1000

Upload

Download

Sideload ← → Sideload
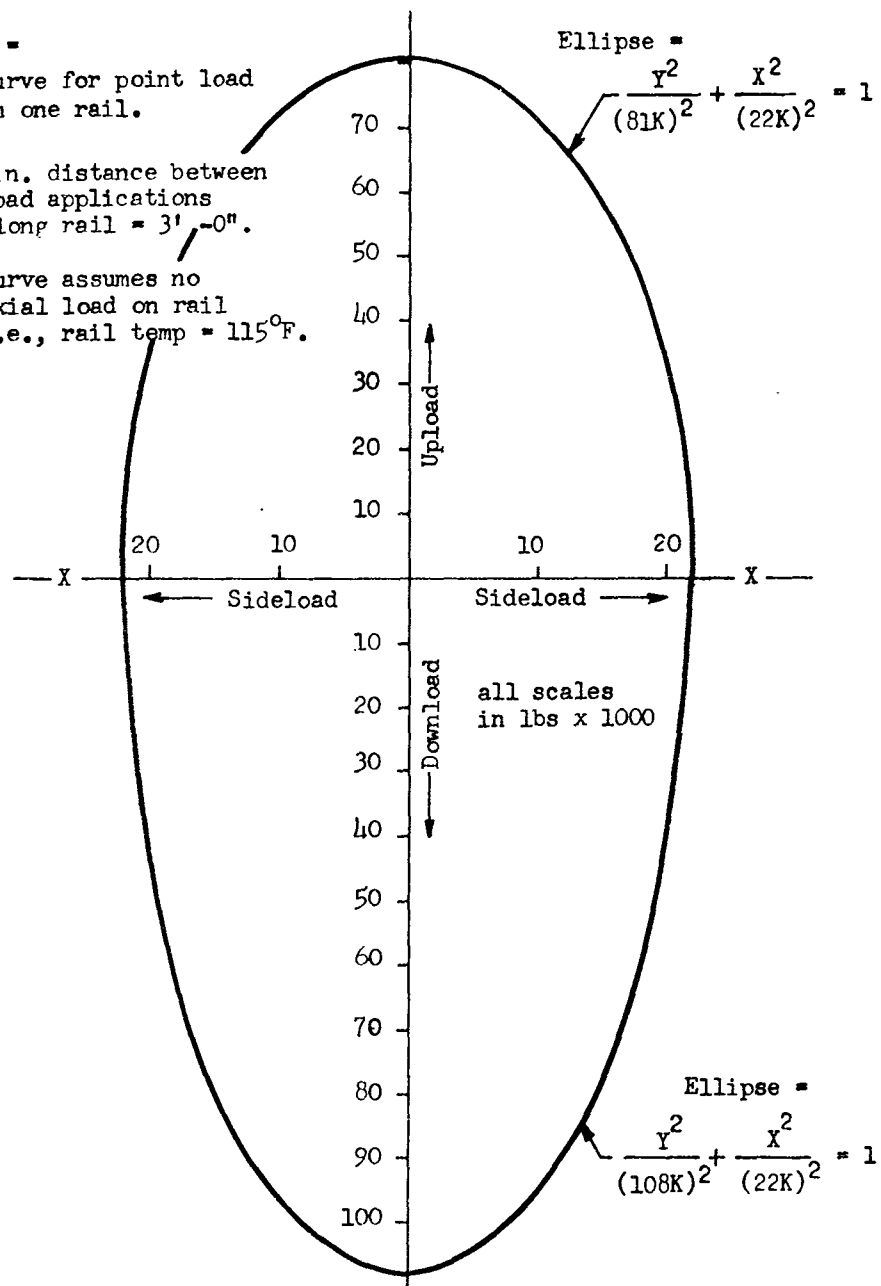
Figure 1.5.6
AFFTC 20,000. Foot High Speed Track Loading Limitations

1.75

SECRET

and

$$\cos\alpha = 0.607$$

But

$$-F_c \cos\alpha \cos\Theta = R_{AH}/2 . \qquad (1.5.7)$$

Therefore

$$R_{AH}/2 = -5730(0.607)(0.975),$$

from which

$$R_{AH} = -6780 \text{ lb} .$$

Since

$$R_{FH} + R_{AH} + F_I + F_{DT} + F_{DM} = 0, \qquad (1.5.8)$$

from which

$$R_{FH} - 6780 + 24200 + 3000 + 1465 = 0$$

then

$$R_{FH} = -21885 \text{ lb} .$$

The following detailed solution for the axial force in struts a and b (considered positive for tension) refers to Figure 1.5.7.

FIGURE 1.5.7   STRUT "a" AND "b" ANALYSES

$$F_a SIN \angle AOC + F_b SIN \angle BOD - R_F/2 = -7540 \, lb \qquad (1.5.9)$$

and

$$F_a COS \angle AOC \, COS \angle COE + F_b COS \angle BOD \, COS \angle DOF = R_{FH}/2 = -10943 \, lb \quad (1.5.10)$$

since

$$SIN \angle AOC = 0.794, \; COS \angle AOC = 0.607, \; COS \angle COE = 0.975,$$

$$SIN \angle BOD = 0.672, \; COS \angle BOD = 0.740 \text{ and } COS \angle DOF = 0.986,$$

then

$$0.794 F_a + 0.672 F_b = -7540$$

and

$$0.592 F_a + 0.730 F_b = -10943 ,$$

from which

$$F_a = 10160 \quad \text{(tension)}$$

and

$$F_b = -23220 \quad \text{(compression)}.$$

This indicates that the maximum strut load is 23,220 lb compression. To obtain a 200% safety factor, the critical buckling load (P_{cr}) is considered to be 46,440 lb. To derive the required inertia (I) of the strut,

$$P_{CR} = \frac{E I}{\ell^2} \tag{1.5.11}$$

where

$$E = 29 \times 10^6 \; PSI \; (STEEL)$$

and

$$\ell = 131 \; inches$$

Therefore, the minimum $I = 2.79$ in^4 which is less than the selected I of 7.233 in^4 of a 4 in. standard pipe. The additional stiffness was designed into the tower to assure launch tower stability under dynamic environments.

The aeroelastic study was performed for the FTV launcher shown in Figure 1.5.1. Because of the unknowns within the limits of this analysis, a qualitative type of investigation was conducted to explore the possibility of adequate separation of the fundamental vibration modes from that of the disturbance spectrum.

Table 1.5.1 shows the launcher-body frequencies and the divergence Mach number. The calculated frequencies show adequate spread for this basic configuration. Since an accurate description of the sled disturbing forces would be difficult to predict, the values in Tables

1.5.1 and 1.5.2 represent aeroelastic properties of preliminary config-
urations which could be fabricated, instrumented, and field tested for
vibration. The divergence Mach number and natural frequencies are
sufficiently high in all three configurations; therefore, sufficient
latitude is available in the space allocated to design a system detuned
from the critical input.

The five degrees of freedom representing the rigid body pitch, roll,
yaw, vertical translation and lateral translation were considered in a
modal study. Conventional methods using influence coefficients were
employed in the calculation of the fundamental frequencies. Figure
1.5.8 illustrates the degrees of freedom and the parameters considered
herein.

The matrix of elastic influence coefficients is defined as:

$$
\left[C_{ij}\right] =
\begin{bmatrix}
C_{\delta\delta} & C_{\delta\theta} & C_{\delta\phi} & C_{\delta h} & C_{\delta\gamma} \\
C_{\theta\delta} & C_{\theta\theta} & C_{\theta\phi} & C_{\theta h} & C_{\theta\gamma} \\
C_{\phi\delta} & C_{\phi\theta} & C_{\phi\phi} & C_{\phi h} & C_{\phi\gamma} \\
C_{h\delta} & C_{h\theta} & C_{h\phi} & C_{hh} & C_{h\gamma} \\
C_{\gamma\delta} & C_{\gamma\theta} & C_{\gamma\phi} & C_{\gamma h} & C_{\gamma\gamma}
\end{bmatrix}
= \frac{\ell^3}{EI}
\begin{bmatrix}
\tfrac{1}{3} & \tfrac{1}{2}\ell & 0 & 0 & 0 \\
\tfrac{1}{2}\ell & \tfrac{1}{2}\ell^2 & 0 & 0 & 0 \\
0 & 0 & \tfrac{4}{3}d^2 & 0 & 0 \\
0 & 0 & 0 & \tfrac{1}{2} & 0 \\
0 & 0 & 0 & 0 & \tfrac{1}{4}\ell^2
\end{bmatrix}
\quad (1.5.12)
$$

The fundamental frequencies are found from the expression:

$$
\begin{Bmatrix}
\delta \\ \theta \\ \phi \\ h \\ \gamma
\end{Bmatrix}
= \omega^2 \left|C_{ij}\right|
\begin{bmatrix}
M & MX_{C.G.} & 0 & 0 & 0 \\
MX_{C.G.} & I_\theta & 0 & 0 & 0 \\
0 & 0 & I_\phi & 0 & 0 \\
0 & 0 & 0 & M & M_{C.G.} \\
0 & 0 & 0 & MX_{C.G.} & I_\gamma
\end{bmatrix}
\begin{Bmatrix}
\delta \\ \theta \\ \phi \\ h \\ \gamma
\end{Bmatrix}
\quad (1.5.13)
$$
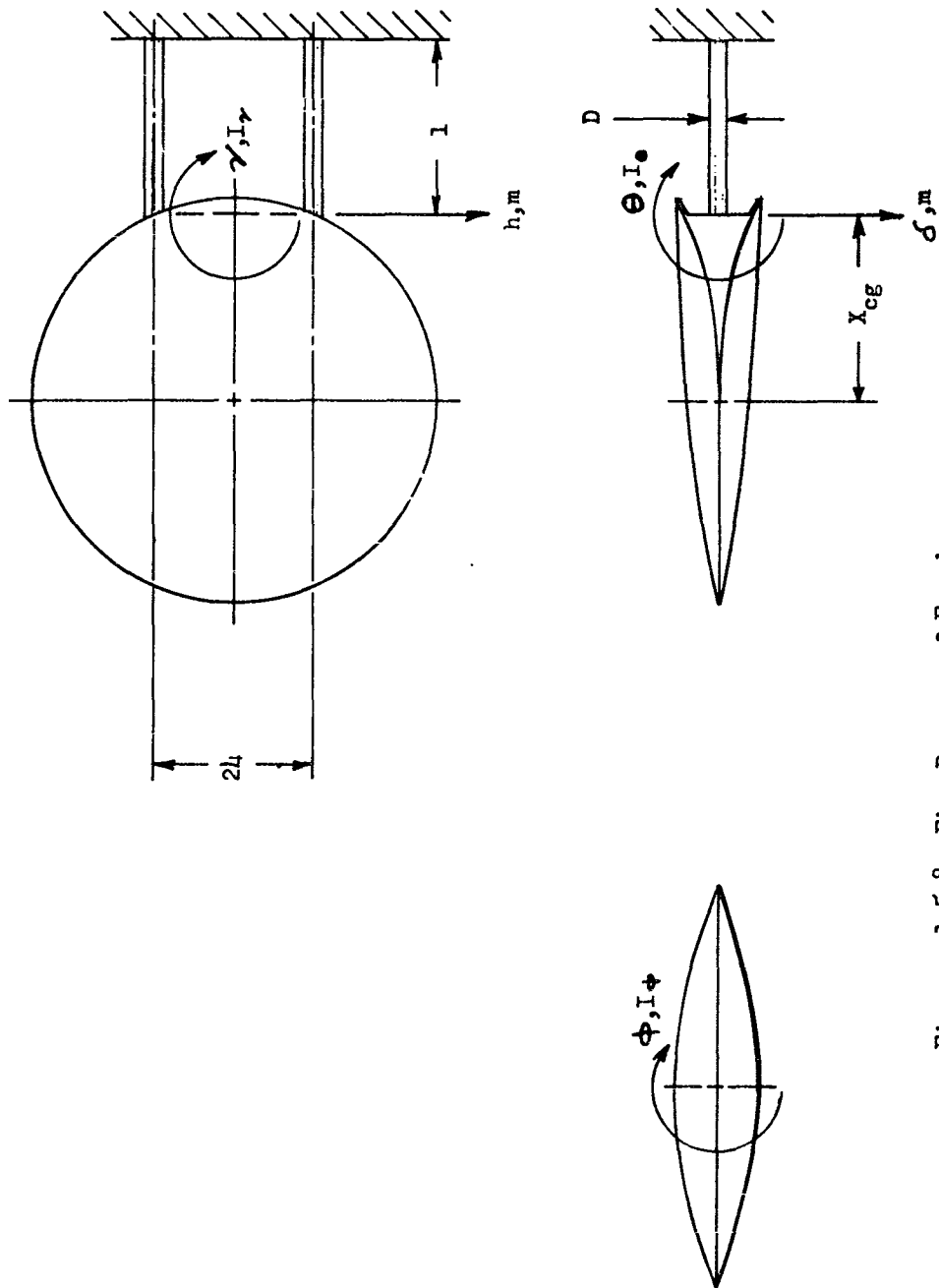
Figure 1.5.8 Five Degrees of Freedom

1.80

The restoring force at the end of the elastic support is:

$$F_s = \frac{EI\alpha}{\ell^2\left(\frac{x_{c.p.}}{\ell} + \frac{\ell}{2}\right)} \qquad (1.5.15)$$

By equating this with the aerodynamic force, an expression for the divergence Mach number is obtained:

$$M^2 = \frac{EI}{1481\lambda \, S \, C_{\ell\alpha} \, \ell^2\left(\frac{x_{c.p.}}{\ell} + \frac{\ell}{2}\right)} \qquad (1.5.16)$$

The results of this equation for sea level conditions are tabulated in Table 1.5.1

Table 1.5.1 Launcher-Body Characteristics

| Configuration Number | Resonant Frequencies CPS | | | | | Divergence Mach No. |
| | Coupled Pitch and Vertical Translation | | Roll | Coupled Yaw and Lateral Translation | | |
	first mode	second mode		first mode	second mode	
I	14.2	337	75.8	30.8	253	2.35
II	16.9	402	90.3	36.8	301	2.79
III	19.8	472	106.0	43.2	355	3.28

Table 1.5.2 Configuration Dimensions

Conf. No.	ℓ (in.)	D (in.)
I	12.0	2.75
II	12.0	3.00
III	12.0	3.25

The above expression shows that the rigid body pitch and vertical translation are affected by both mass and spring coupling. The rigid body

lateral translation and yaw modes are mass coupled while the roll modes remain uncoupled. The results obtained from the above operations are tabulated in Table 1.5.1.

The aerodynamic force caused by the deflection of the support (see Figure 1.5.9) was used to derive the moment equation:

$$M_a(x) = F_a(X_{c.p.} + X) = 1481 \lambda M^2 S C_{l\alpha} (X_{c.p.} + X)\alpha \qquad (1.5.14)$$
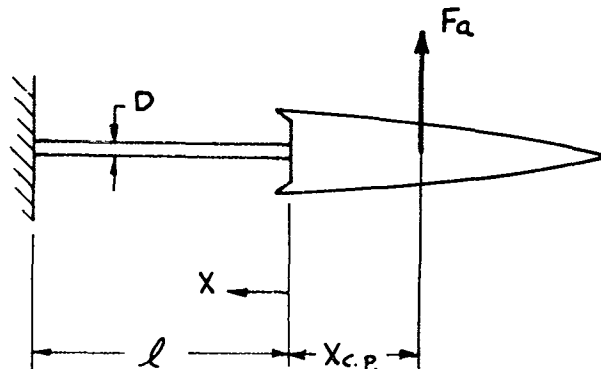
Figure 1.5.9 Aerodynamic Force Caused by Support Deflection

Parameter Definition for Analysis

λ = pressure ratio
M = Mach number
S = reference area 19.6 ft^2
δ = vertical translation
θ = pitch angle
ϕ = roll angle
γ = yaw angle
h = lateral translation
E = modulus of elasticity
α = angle of attack, degree
D = diameter of support, inch

$C_{\ell\alpha}$ = lift coefficient derivative, 1/degree

X_{cp} = center of pressure location

1.6 AERODYNAMIC HEATING

1.6.1 INTRODUCTION Since the aerodynamic heating problem was considered minor, only a cursory study was conducted. Aerodynamic heating of the FTV was determined for a specific flight trajectory in which a maximum vehicle Mach number of 1.71 was reached 1.5 seconds after launch. In determining the structural temperature response of the vehicle under these conditions, forward launch of the vehicle was used since it would yield the most severe aerodynamic heating. Structural temperatures were computed at the leading edge of the vehicle and at two other locations (two and thirty inches aft of the leading edge). In the analysis, magnesium was used as the leading edge insert material, and both magnesium and polyester resin with a honeycomb core were considered for the skin material.

1.6.2 AERODYNAMIC HEATING ANALYSIS

1.6.2.1 Initial and Flight Conditions The initial temperature of the vehicle was assumed to be 140°F, and the USAF Proposed Standard Hot Atmosphere was used for the ambient air temperature during flight (Reference 4.6). Since higher vehicle Mach numbers are of primary interest in an aerodynamic heating analysis, the forward launch condition was used as a basis for the study. Therefore, a maximum vehicle velocity of Mach 1.71, occurring 1.5 seconds after an 800 ft per sec forward launch, was used in the analysis.

1.6.2.2 Boundary Conditions During vehicle flight, the free stream air is decelerated from flight velocity to zero velocity on the vehicle surface. This change in kinetic energy of the ambient air stream is thereby transformed into internal energy with a resulting rise in the boundary layer air temperature. In order to determine the rate of heat transfer from this boundary layer to the vehicle skin, it is then necessary to compute both the boundary layer air temperature (recovery temperature, T_R) and the heat transfer coefficient (h). In this analysis, a modified Colburn turbulent flow heat transfer coefficient (Reference 4.7) was used for the vehicle surface aft of the leading edge. This coefficient was corrected by a reference-temperature (T') factor (Reference 4.8) to extend the incompressible flow correlation to compressible flow conditions. Stagnation-point heat-transfer coefficients were determined from an empirical laminar flow correlation by Sibulkin (Reference 4.9).

1.6.2.3 Structural Temperature Response to Boundary Conditions
The basic equation which governs the transfer of heat from the airstream to the vehicle structure is shown by Equation (1.6.1):

$$q = h A (T_R - T_W) \qquad (1.6.1)$$

The flow of heat throughout a solid is given by the general heat diffusion equation:

$$\frac{\partial T}{\partial t} = \alpha \frac{\partial^2 T}{\partial x^2} \qquad (1.6.2)$$

Since a simplified form of the above diffusion equation is not readily solved when time-variable boundary conditions are applied, it was necessary to use the finite-difference method in the analysis. With this technique, the structure is subdivided into a discrete number of volumes and integration is performed in small increments of time. A numerical solution of the resulting structural-temperature equations was obtained on a Datatron 204 digital computer.

1.6.3 RESULTS OF AERODYNAMIC HEATING ANALYSIS

1.6.3.1 Leading Edge Temperature The temperature history of the 0.25 inch radius magnesium leading edge is shown in Figure 1.6.1, and indicates a peak temperature of 275°F.

1.6.3.2 Skin Temperature Skin temperature histories were computed at two locations aft of the leading edge (two inches and thirty inches). Both a polyester resin skin with a honeycomb core, and a magnesium skin (two different thicknesses) were also considered in the analysis.

Figures 1.6.1, 1.6.2, and 1.6.3 give the calculated temperature histories of the 0.040 and 0.0625 in. magnesium skins at the two locations considered. Maximum temperatures of 275°F and 250°F were obtained at the location nearest the leading edge, for the two thicknesses of magnesium.

The temperature histories calculated for the exposed layer of polyester resin skin are shown in Figure 1.6.3 and 1.6.4, for the two inch and thirty inch locations, respectively. Since this material has a low thermal conductivity, temperature histories at various depths through the skin were determined. Figure 1.6.3 shows that a maximum surface temperature of 320°F is obtained with the polyester resin and that the temperature decreases considerably toward the inner face of the skin.
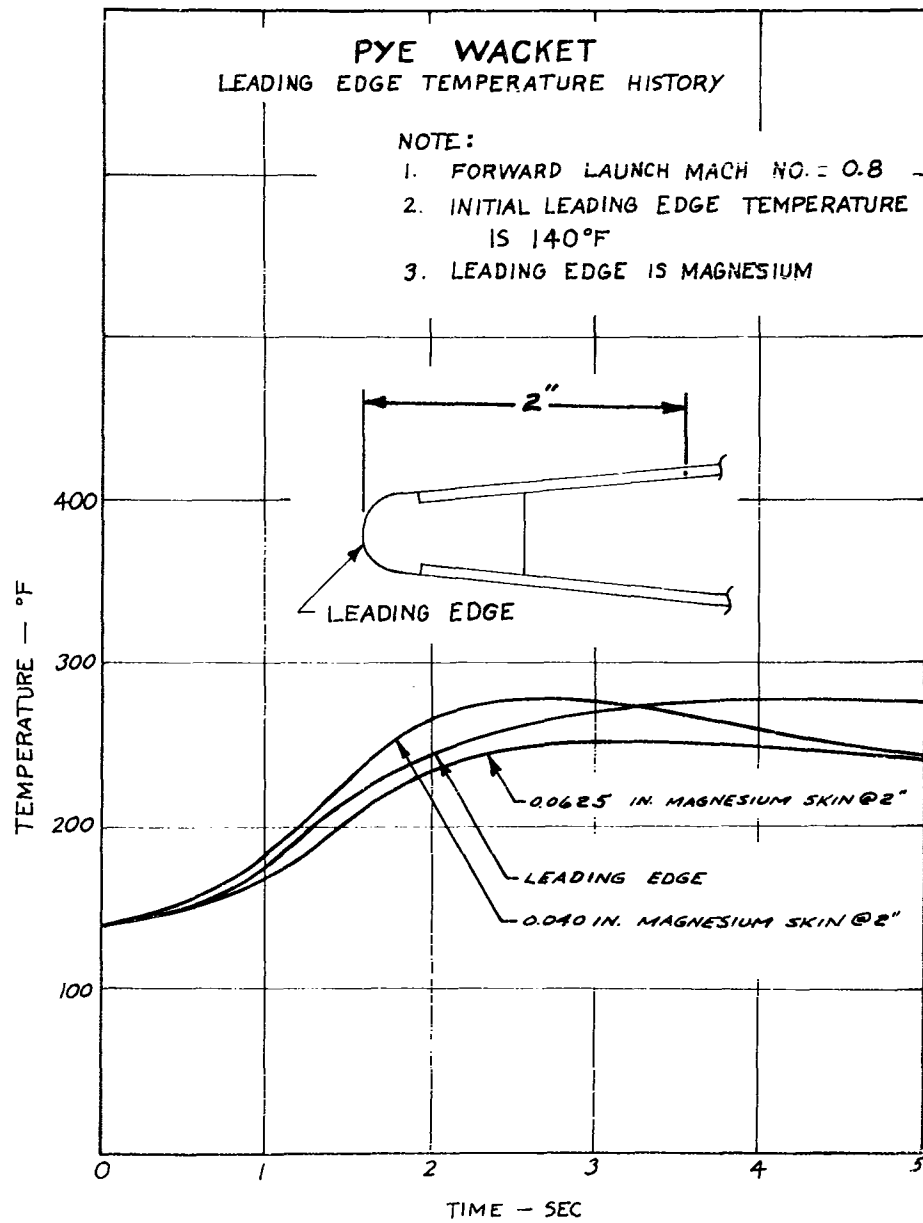
Figure 1.6.1 Temperature History - leading edge, mag. skin

PYE WACKET
SKIN TEMPERATURE HISTORY

NOTE:
1. FORWARD LAUNCH MACH NO.- 0.8
2. INITIAL SKIN TEMPERATURE = 140°F

3. TEMPERATURE LOCATION IS 30 iN.
FROM LEADING EDGE
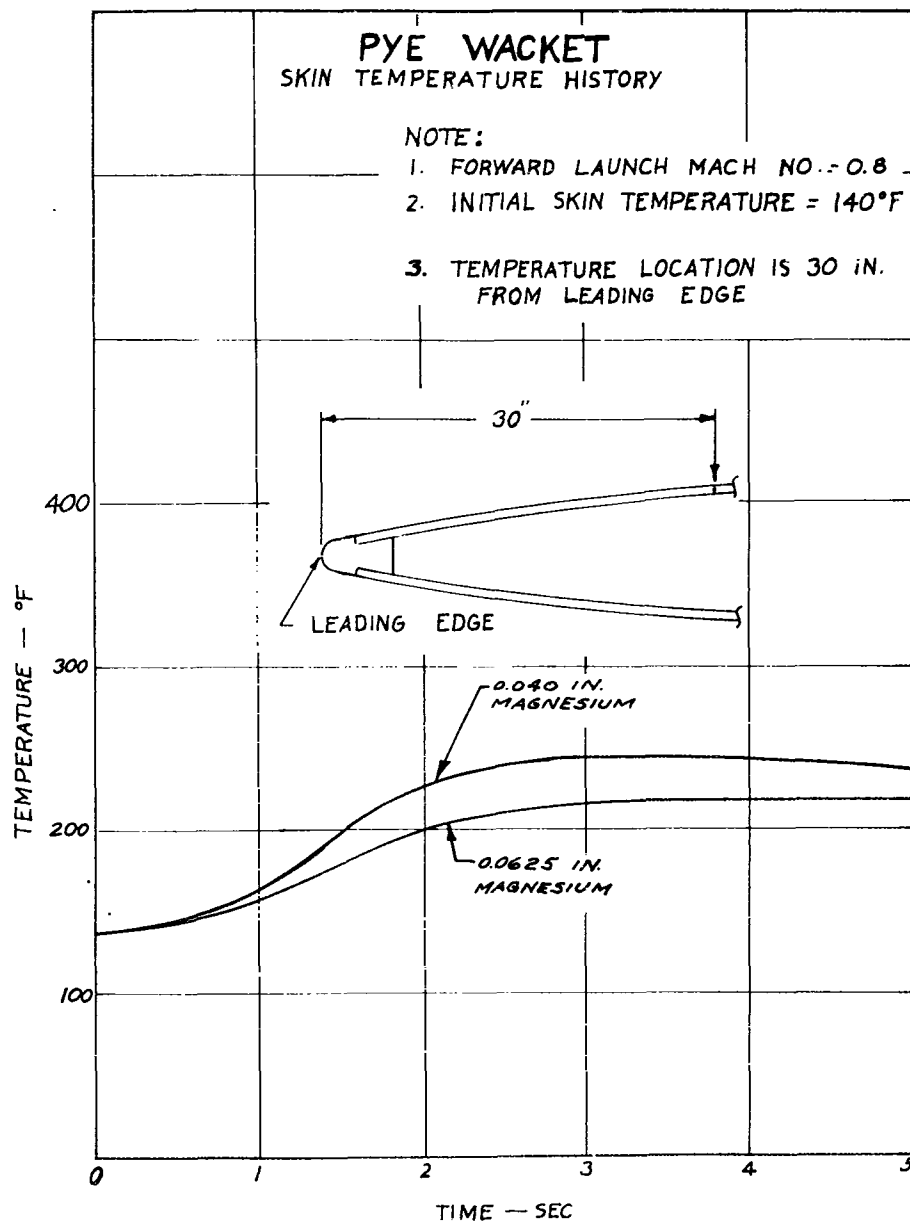
Figure 1.6.2 Temperature History - at Midchord, mag. Skin

PYE WACKET
SKIN TEMPERATURE HISTORIES

NOTE :
1. FORWARD LAUNCH MACH NO. = 0.8
2. INITIAL SKIN TEMPERATURE = 140°F
3. SKIN IS POLYESTER RESIN WITH HONEYCOMB CORE
4. TEMPERATURE LOCATIONS ARE 2.0 IN. FROM LEADING EDGE
5. TEMPERATURE LOCATIONS ARE EQUALLY SPACED
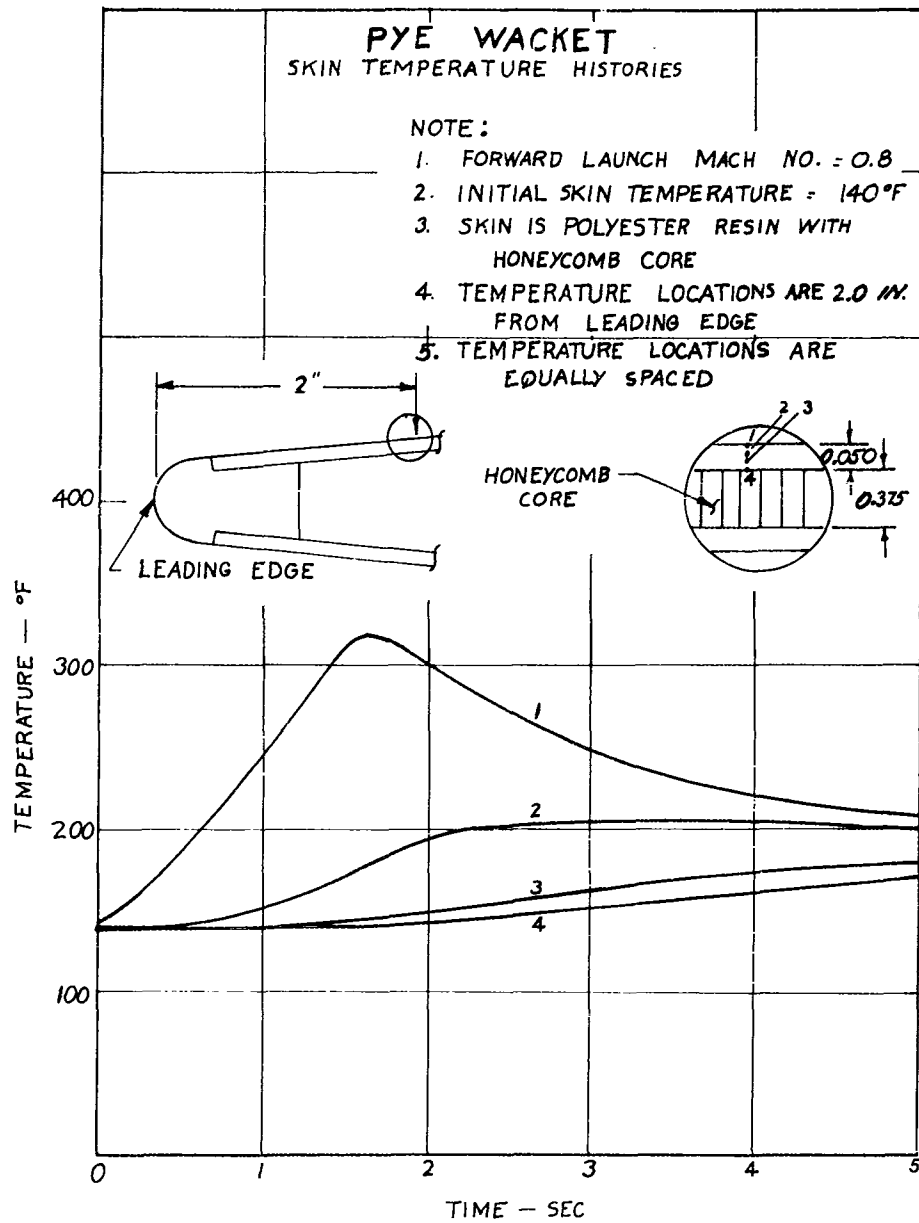
Figure 1.6.3 Temp. History - Leading edge, Plastic Sandwich Skin

1.87

PYE WACKET
SKIN TEMPERATURE HISTORIES

NOTE:
1. FORWARD LAUNCH MACH NO. = 0.8
2. INITIAL SKIN TEMPERATURE = 140°F
3. SKIN IS POLYESTER RESIN WITH
   HONEYCOMB CORE
4. TEMPERATURE LOCATIONS ARE 30 IN.
   FROM LEADING EDGE
5. TEMPERATURE LOCATIONS ARE
   EQUALLY SPACED
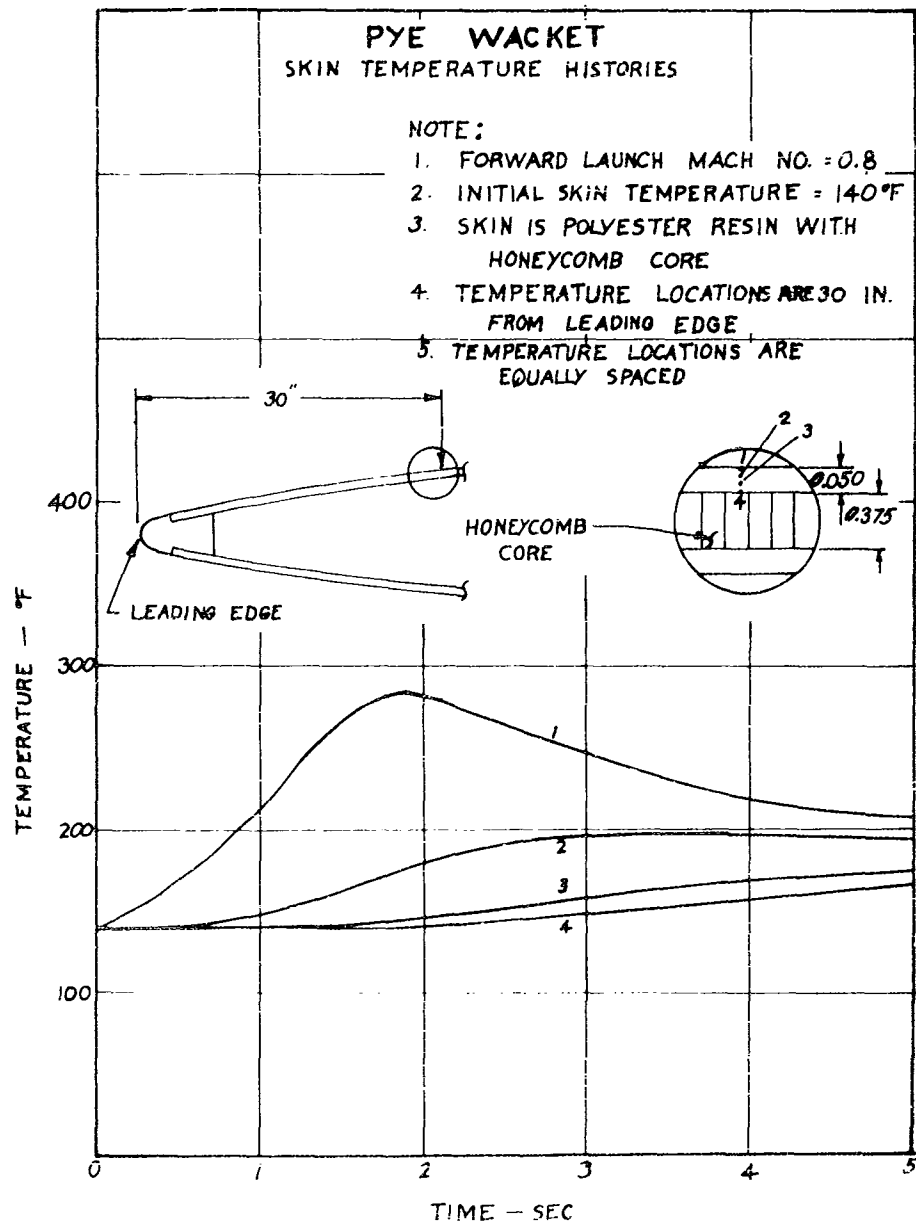
Figure 1.6.4 Temp. History - Leading edge, at Midchord, Plastic Sand. Skin

1.6.4 HEATING BY ROCKET EXHAUST When the vehicle is launched in the aft direction, it is exposed to its own rocket exhaust gases for a short period of time (an exposure of approximately 0.6 seconds if launched at Mach 0.6). An approximate study of this effect, however, indicated that only a moderate temperature ($< 300°F$) would result on the aft portions of the vehicle. Since this was the case, a more rigorous analysis of the effect was not considered necessary at this time. However, if later evidence indicates a more serious problem, a simple solution would be the application of a protective coating to the exposed areas.

Section 2.0
AUTOPILOT/CONTROL STUDIES

2.1 INTRODUCTION

The primary object of the PYE WACKET Phase II studies conducted under Contract AF 08(635)-1168, is the analysis and design, for subsequent fabrication and test, of a Feasibility Test Vehicle. It is intended that in the next phase of the program a flight test program be conducted with this vehicle to prove the feasibility of the blunted lenticular, circular planform shape as an airborne weapon. The autopilot development and the control-producing hardware are the subjects treated in this section. The background data required for the execution of this study are reported in Section 1.0, Test Vehicle Configuration Studies, (this volume), and in Volume II, Aerodynamics.

2.2 CONTROL SYSTEM DESIGN STUDIES

2.2.1 PRELIMINARY CONSIDERATIONS The PYE WACKET FTV design utilizes a reaction control system to maintain the missile attitude within specified limits under all launch and flight conditions. To accomplish this task, the control system must supply a corrective thrust in the appropriate direction in response to a command from the autopilot. With the reaction control motors offset from the vehicle center of gravity, pitch, roll, and yaw restoring moments can be produced. All conceivable reaction control systems have finite time delays between the receipt of the control signal and the application of the restoring moment; to successfully control a PYE WACKET type vehicle, it is necessary that the response time of the reaction motors be extremely short. Therefore, in order to determine the most suitable FTV control system configuration and to establish required system design criteria, a preliminary investigation was first conducted.

2.2.1.1 Control System Configuration Study The PYE WACKET reaction control system initially studied during the Phase I program consisted of a four-nozzle reaction-jet system (with the jets canted 20° from the vertical) to achieve control in the three planes of pitch, roll, and yaw (Reference 4.1). However, the short FTV development time, the FTV requirement for maximum use of off-the-shelf items, and the FTV-prototype differences in flight environment have necessitated a re-evaluation of the control system during the Phase II Program. An alternate control system configuration employing six nozzles

was investigated -- two nozzles for yaw control and four vertical
nozzles for combined pitch and roll control. A schematic of a six-
nozzle control system is shown in Figure 2.2.1. With either a four
or six-nozzle control system, combined pitch and roll commands are
directed in different combinations to the four nozzles to produce the
required pitch and/or roll moments. However, since any one of the
four nozzles might be required for both pitch and roll, the maximum
pitch and roll restoring moments cannot be applied simultaneously.
Therefore, it is necessary that each of these nozzles be capable
of part-time pitch control and part-time roll control. This situation
is further complicated in the four-nozzle system, since each nozzle
must also be capable of producing yaw control.

The reaction control system must correct for all disturbing
moments acting on the vehicle during flight and must provide maneu-
vering capability. Two critical flight conditions which the vehicle
might encounter are: 1) a called-for maximum pitch, roll, or yaw
moment, and 2) a combined correction signal of pitch, roll, and yaw
moments (because of time-sharing). To compare the performance and
design characteristics of four and six-nozzle systems, the combination
of pitch, roll, and yaw moments encountered by the vehicle at burnout
(during side launch) was selected as the initial design condition.
The method used to make this preliminary comparison of the two systems
was based on the thrust level required to control the vehicle under
the time-sharing conditions.

Root-mean-square values of angle of attack and angle of roll
were assumed, aerodynamic moments were calculated, and appropriate
misalignment moments were added to obtain the total pitch, roll,
and yaw requirements of the vehicle. Due to the time sharing require-
ment, the thrust necessary for control with the six-nozzle system
was determined by adding the pitch and roll requirements, and for
the four-nozzle system, by adding the pitch, roll, and yaw require-
ments. Four-nozzle systems with nozzle cant angles of 20°, 30°, 40°,
and 50° from the vertical were investigated. Results of the control
system comparison are shown in Figures 2.2.2 and 2.2.3 for rms angle-
of-attack and roll values equal to 1° and 2° respectively. With the
vehicle center of gravity located at the 45 percent chord, Table
2.2.1 indicates that the control thrust required of a six-nozzle
system is approximately half that of a four-nozzle system. Because
of this thrust advantage, a six-nozzle control system similar to that
shown in Figure 2.2.1 will be used in the FTV design.

2.2.1.2 <u>Parametric Relationships</u> In order to estimate the
response time and thrust required of the FTV control system, a para-
metric study of the yaw, pitch and roll characteristics of the vehicle
was conducted. The yaw analysis was restricted to a side launch
condition in which the yawing moments tend to rotate the vehicle to a

SCHEMATIC OF SIX
NOZZLE REACTION
CONTROL SYSTEM

YAW
NOZZLES
(2 PLACES)

PITCH AND
ROLL NOZZLES
(4 PLACES)

FIGURE 2.2.1

2.3
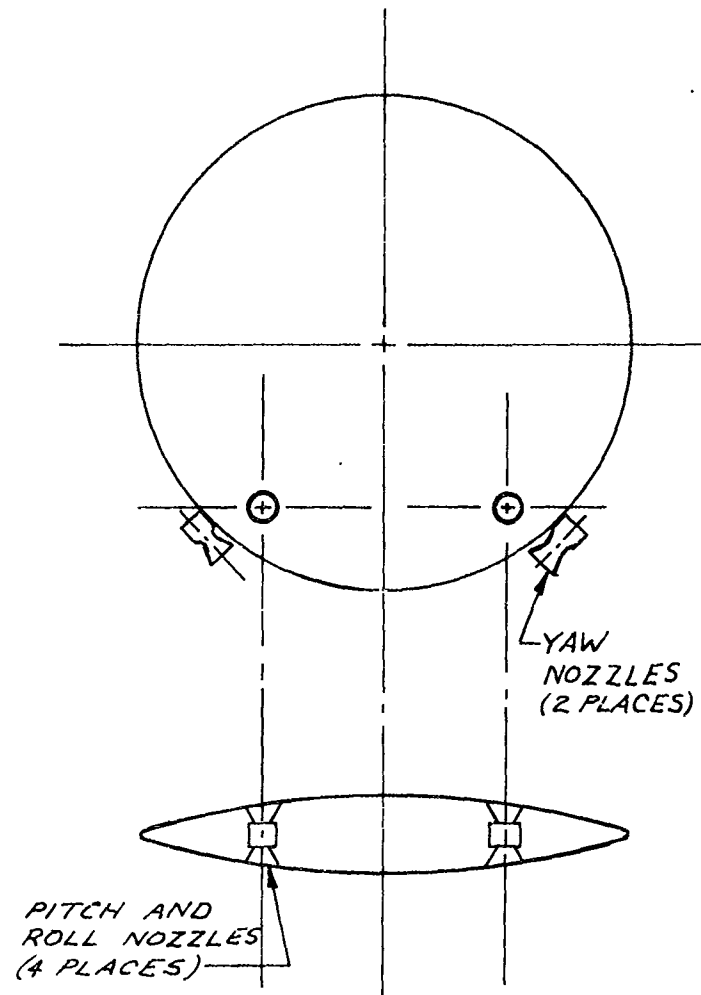
SECRET

CONTROL THRUST VS C.G.
RMS $\alpha = \phi = 1°$

CONDITIONS:
1. 60° Ω, 21% t/c, 3 MOTOR CONF.
2. EST. AERO. MOMENTS
3. SIDE LAUNCH AT M = 0.96

FOUR-NOZZLE SYSTEMS
20° CANT
50° 30°
40°

PITCH-ROLL

SIX-NOZZLE SYSTEM

YAW

CENTER OF GRAVITY ~ % CHORD
FIGURE 2.2

SECRET

CONTROL THRUST VS CG
RMS $\alpha \cdot \phi \cdot 2°$

CONDITIONS:
1. 160" D. 21'Lg., 3 MOTOR CONT
2. EST. AERO. MOMENTS
3. SIDE LAUNCH AT M=0.34

THRUST PER NOZZLE ~ LB
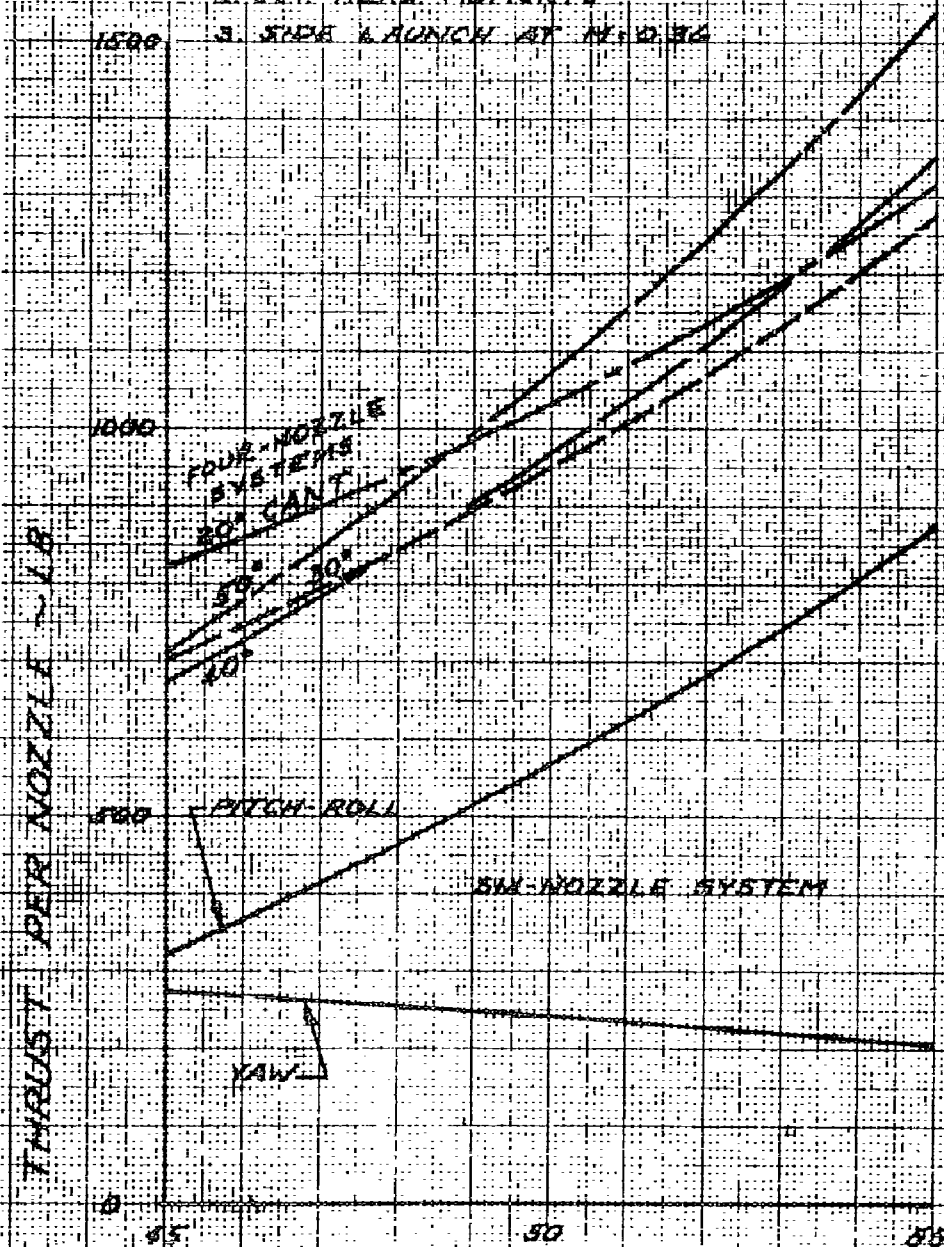
CENTER OF GRAVITY —% CHORD
FIGURE 2.2.3
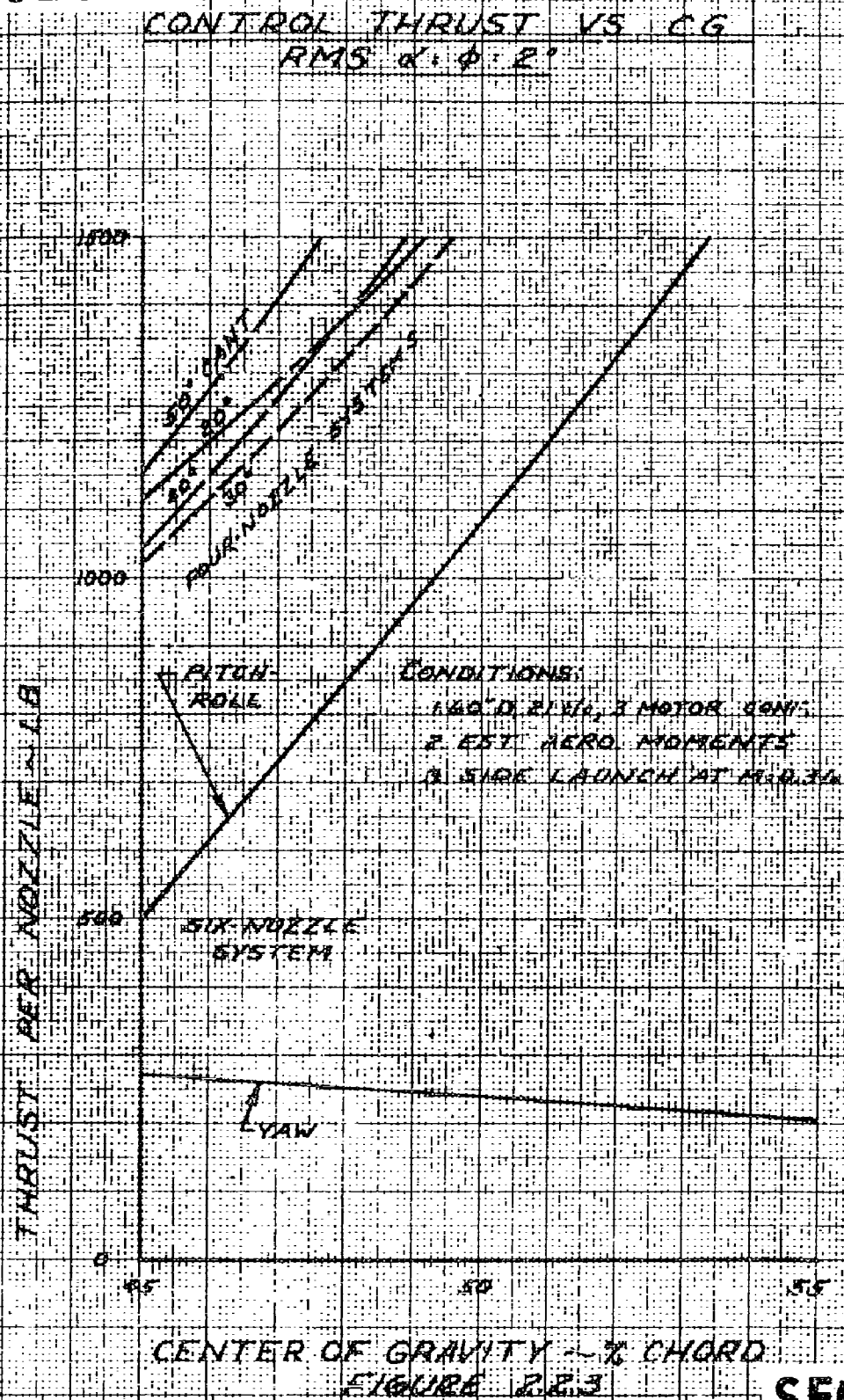
Table 2.2.1 Preliminary Thrust Requirements –
Four-Nozzle vs Six-Nozzle System

Conditions:

1. 60 inch diameter, 3 booster motor configuration

2. Launch velocity, 400 fps

3. Side launch at $\beta_0 = 90°$

4. CG. at 0.45C

RMS Angle of Attack (degrees)	Six-Nozzle	Four-Nozzle			
		20° Cant	30° Cant	40° Cant	50° Cant
1	325	820	700	675	715
2	600	1120	1025	1045	1155

zero angle of yaw. The control system is required to counteract
this rotational tendency and to maintain a constant heading with
respect to a fixed space coordinate system. The analyses of the
pitch and roll control systems were combined into a single generalized
solution. This approach was possible because the aerodynamic moment
coefficients can be linearized and because the pitch and roll control
problems are similar.

Combined Misalignment and Aerodynamic Yaw Moments   During a side
launch, aerodynamic forces and thrust misalignment forces (main pro-
pulsive system) act upon the vehicle and tend to produce a yawing
motion (a detailed study of thrust misalignment forces produced by
the FTV propulsion system is presented in Section 1.2.1.3). A counter-
acting moment greater than the additive effects of both types of
disturbing moments is then required to return the vehicle to a correct
heading. Because the configuration can be designed with a small
degree of static stability, the vehicle, for an initial launch yaw
angle, will rotate through some yaw angle during the initial time
lag of the control system. After control thrust is produced by the
yaw nozzle, the rotation of the vehicle is gradually stopped at some
maximum yaw angle (β_2). The total time consumed during this rotation,
(t_2), is the sum of the reaction control system response time (time
from actuation signal to full thrust, (t)) and the time required to
arrest the yawing motion. A continuation of the reaction control
thrust then returns the vehicle to the heading dictated by the auto-
pilot. Further disturbances of the vehicle heading would cause a
similar cycle to repeat.

Analytical relationships were developed to determine the indivi-
dual effects of control system response time and moment differential
(reaction moment minus yaw moment) on maximum yaw angle (β_2) and on
total rotation time (t_2). The total FTV yaw moment was assumed con-
stant in order to demonstrate more clearly its effect on yaw angle
and time of turning. The ratio of the time consumed in turning
through the maximum yaw angle to the reaction control response time
as a function of the reaction moment is shown in Figure 2.2.4 for
various moment differentials. The relationship that exists between
the foregoing parameters can be expressed as:

$$\frac{t_2}{\tau} = \frac{M_2}{M_2 - M_1} = \frac{1}{1 - \frac{M_1}{M_2}} \qquad (2.2.1)$$

RATIO OF TURNING TIME TO RESPONSE TIME
VS REACTION MOMENT

NOTE:
ΔM = REACTION MOMENT
     MINUS YAW MOMENT

Delta IQ - FT-LB
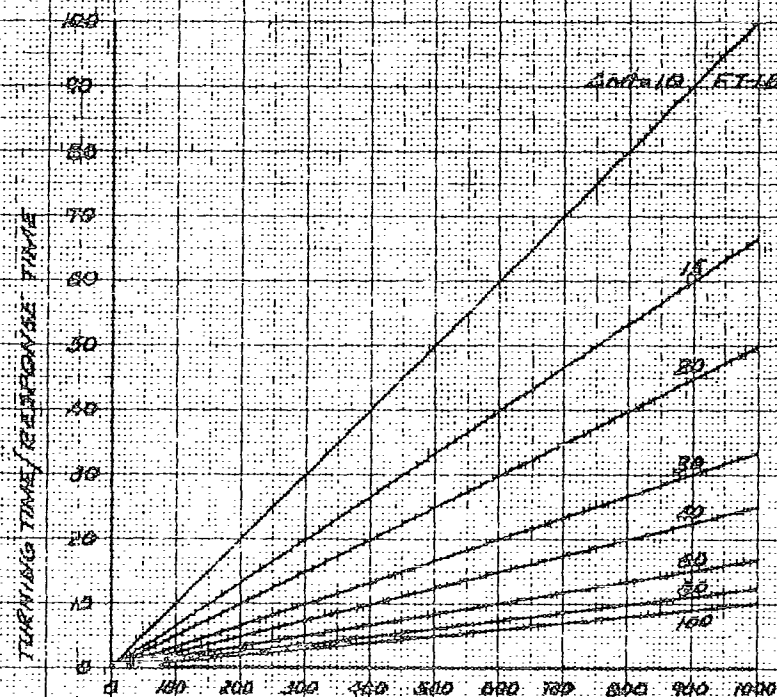
REACTION MOMENT   FT-LB
FIGURE 7.2.4

where

t₂ seconds is the time consumed in yawing to the maximum yaw angle,

$\mathcal{T}$ seconds is the reaction control system response time,

M_1 ft-lb is the sum of the aerodynamic and misalignment yaw moments, and

M_2 ft-lb is the reaction control yaw moment.

The maximum yaw angle divided by the square of the response time is shown as a function of the reaction moment in Figure 2.2.5. This figure was developed from the following equation:

$$\frac{\beta_2}{\mathcal{T}^2} = \frac{M_1}{2I}\left(\frac{M_2}{M_2 - M_1}\right) = \frac{M_1}{2I}\left(\frac{1}{1 - \frac{M_1}{M_2}}\right) \quad (2.2.2)$$

where

β_2 radians is the maximum yaw angle, and

I ft-lb-sec^2 is the moment of inertia about the vertical axis.

With the foregoing relationships for an assumed control system response time of 10 milliseconds, an estimated yaw moment of 900 ft-lb, and a control moment of 1000 ft-lb, the vehicle will turn through a maximum yaw angle of 0.8° in 100 milliseconds. With a reaction control moment of 940 ft-lb, a maximum yaw angle of 1.9° in 235 milliseconds results. Therefore, with typical flight conditions, the maximum yaw angle is not severe for excess yaw moments of 40 ft-lb or greater. However, the pulse duration (hence, the time the vehicle is off course) can be sharply reduced with a modest increase in reaction control moment.

Combined Misalignment and Aerodynamic Pitch and Roll Moments
Forward, side or aft launch of the PYE WACKET FTV from a propelled sled will undoubtedly impart an initial angle of attack and roll to the vehicle. To determine the seriousness of this condition, it was

RATIO OF ANGLE TURNED TO SQUARE OF
RESPONSE TIME vs REACTION MOMENT

NOTE:
VEHICLE POLAR MOMENT
OF INERTIA = 317 SLUG-FT²

ΔM = REACTION MOMENT
MINUS YAW MOMENT
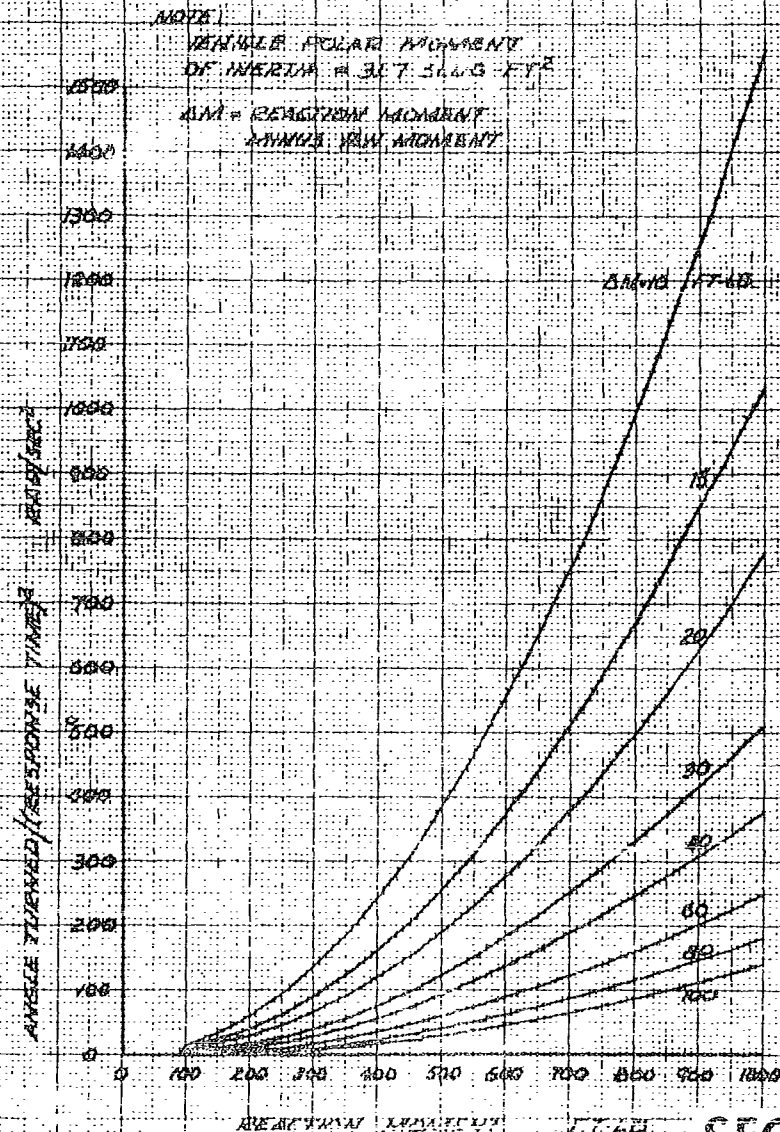
FIGURE 2.2.5

necessary to investigate the angle through which the vehicle would turn when launched at an initial angular displacement with no corrective moment. The pitching action during forward launch yields the time history of the angle of attack for various Mach numbers according to the following equation:

$$\frac{\alpha}{\alpha_o} = \left(\frac{1 + 0.00194}{M^2 \alpha_o}\right) \cosh 60.1\, Mt - \frac{0.00194}{M_2 \alpha_o} \quad (2.2.3)$$

where

    M is the freestream Mach number,

    α radians is the instantaneous angle of attack, and

    α_o radians is the initial angle of attack.

Although the above equation is rigorously accurate only in the vicinity of $\alpha_o = 5°$, the results are sufficiently accurate for general use between $\alpha_o = 3°$ and $\alpha_o = 8°$. As shown in Figure 2.2.6 (pitch versus time for various Mach numbers), a pitch ratio (α/α_o) of 1.12 would occur in 10 milliseconds during a forward launch at Mach 0.8. With an initial angle of attack of 5°, such a value would correspond to an angle of attack of 5.6° in 10 milliseconds. With a conservative value for initial angle of attack (5°) and an assumed control system corrective thrust within 10 milliseconds, it appears that a good preliminary design value for angle of attack is 6°.

The angle of attack relationship during side launch is given in the following equation:

$$\frac{\alpha}{\alpha_o} = \left(\frac{1 + 0.000269}{M^2 \alpha_o}\right) \cosh 89.5\, Mt - \frac{0.000269}{M^2 \alpha_o} \quad (2.2.4)$$

The vehicle roll angle, as a function of time, (Figure 2.2.7) indicates that during a side launch at a Mach number of 0.6, a roll (α/α_o) of 1.15 would occur in 10 milliseconds. That is, an initial roll angle of 5° would increase to 5.75° in 10 milliseconds.

PITCH vs TIME

CONDITIONS:

1. $\theta = 0°$
2. $\alpha_0 = 5°$
3. MAXIMUM ALIGN MOMENTS (NEG FT-LB)
4. $I = 2.1 \times 4$ FT-LB-SEC²
5. 0.047 0.52 C

PITCH — (rad.)

1.3

1.2

1.1

1.0

TMAX 0.8

M=0.4

TMAX 0.4

TIME — SECONDS

0   0.01   0.02
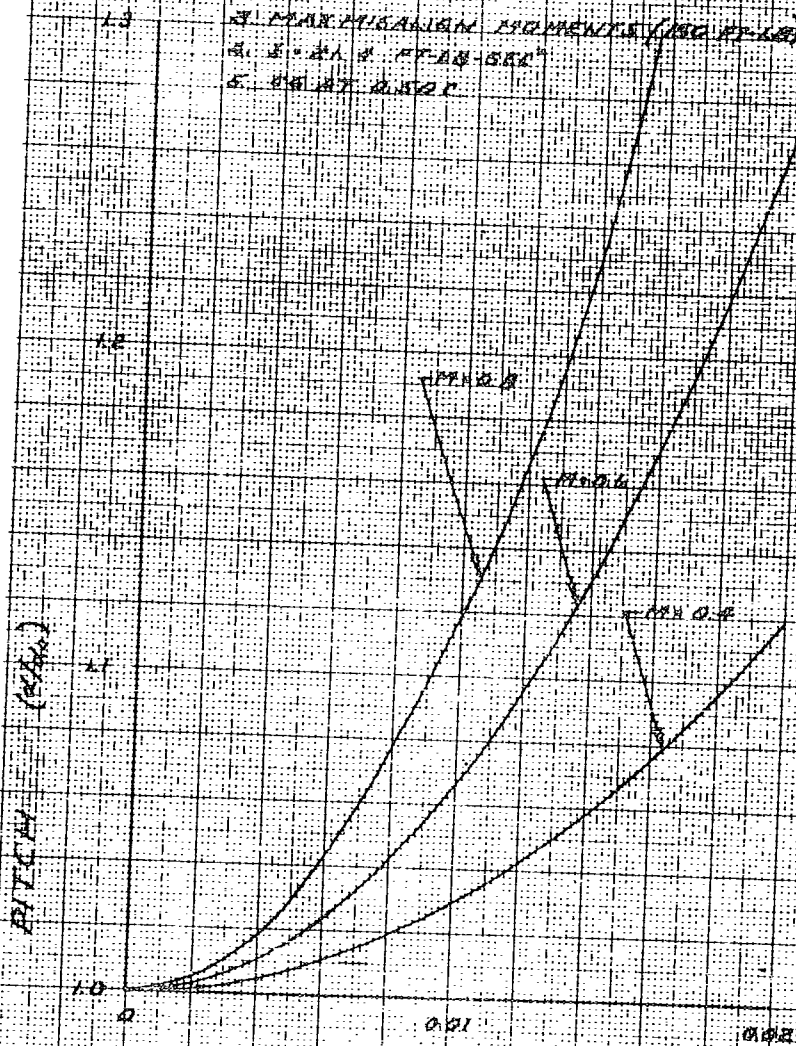
FIGURE 2.26

ROLL VS TIME

CONDITIONS:
1 MAX MISALIGN MOMENTS (30 FT-LB)
2 I = 1.6 FT-LB SEC²
3 CG AT 0.50 SPAN POS
4 β = 90°
5 α = 5°

ROLL (ω/ω₀)

M = 0.6

M = 0.8

M = 0.6

M = 0.3

ROLL

1.3

1.2

1.1

1.0

0   0.01   0.02
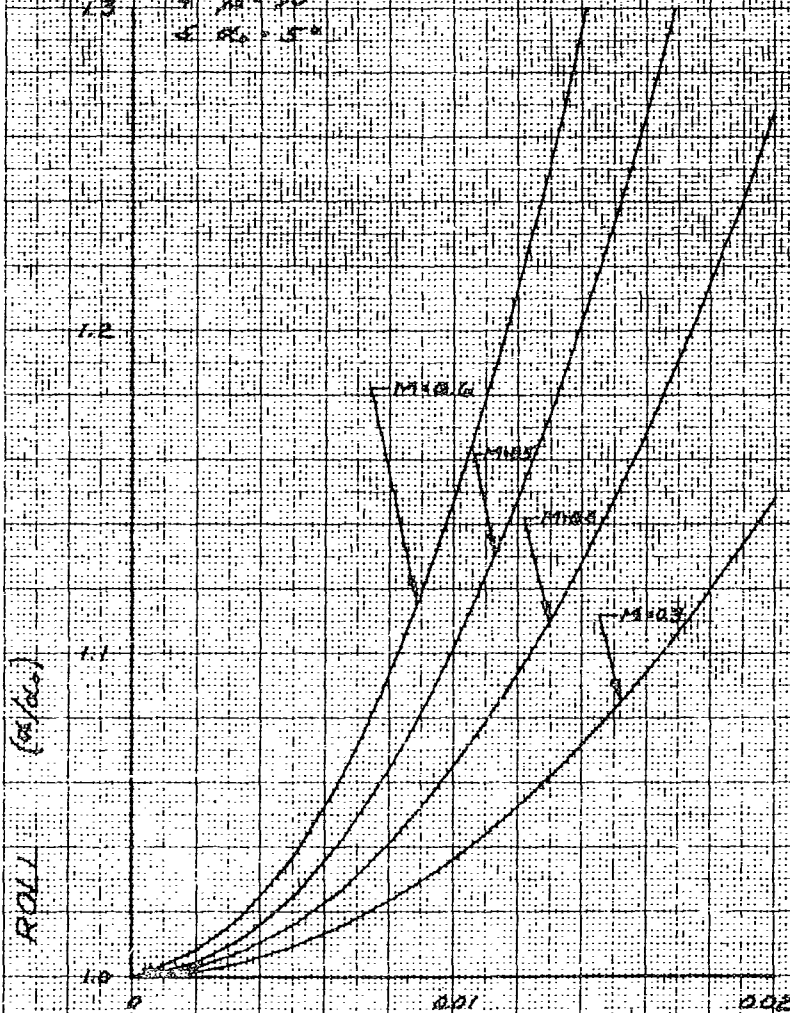
TIME ~ SECONDS

FIGURE 2.2.7

2.2.2 CONTROL SYSTEM INVESTIGATION

2.2.2.1 Restrictions and Specifications

Physical Limitations The physical configuration of the PYE
WACKET FTV imposes certain restrictions on the shape and amount of
space available for the reaction control system. Such a limitation
does not favor either a minimum weight control system or a forward
center-of-gravity location for the control system. Although minimum
weight is desirable from the standpoint of vehicle acceleration and
burnout velocity, it appears more desirable to place emphasis on
locating the center of gravity of the control system as far forward
as possible thereby increasing the pitch stability during flight. The
location of the pitch and roll nozzles however, is also governed by
the required performance of the control system. An aft location is
desirable for these items of the control system in order to house the
nozzles in a back-to-back position with collinear thrust vectors,
and also to increase the pitch control moment arm. Conversely, roll
control favors locating the nozzles at the extreme perimeter of the
vehicle again moving the location of the nozzles forward to obtain
the largest roll moment arm. From this discussion, it can be seen
that the final location of the control system pitch and roll nozzles
is a compromise between required performance, center-of-gravity lo-
cation, size and available space.

The location of the yaw control nozzles is not so much dictated
by vehicle physical limitations as by aerodynamic, propulsive, and
kinematic considerations. The nozzles should point generally aft
to obtain a greater propulsive efficiency, and should be located aft
of the vehicle 50 percent chord to reduce aerodynamic interference.
In order to obtain the maximum kinematic effect, it is also desirable
that the thrust vectors of the yaw nozzles be approximately perpendi-
cular to a line between the motor centerline and the vehicle center
of gravity. These three objectives can be accomplished by locating
the yaw nozzles approximately as shown in Figure 2.2.1.

Reaction Control System Response Limitations Although the
critical nature of the control system response time was pointed out
in Section 2.2.1.2, the vehicle stability depends not only on the
overall response time, but also on the detail dynamic characteristics
that constitute the thrust-time history. The control system response
limitations were estimated early in the program based on a typical
hypergolic bipropellant reaction jet system using solenoid operated
propellant control valves. The overall reaction control thrust delay
was subdivided into four basic elements: 1) electrical operation,
2) mechanical movement, 3) liquid transportation, and 4) gas pressure
buildup. The dynamic response of each of these elements can be con-
sidered separately with a combination of the elements forming a
mathematical model of the response characteristics of the FTV control
motors.

A cursory analysis of a mathematical model was studied for a typical bipropellant system. The electrical portion of the propellant control valve was assumed to consist of a pure resistance-inductance circuit with the time constant (L/R) limited to 0.005 seconds. The mechanical movement of the propellant control valve poppet was described by a second order differential equation of motion. The propellant transportation from the valve poppet to the point of impingement in the combustion chamber was considered to be a pure time delay, (instantaneous acceleration and translation at constant velocity) and should be a maximum of approximately 0.010 seconds. See Section 2.3 for a more detailed analysis of the mathematical model.

The thrust buildup from an output of propellant flow conforms to the solution of a first order differential equation with a maximum time constant of approximately 0.001 seconds.

Environmental Limitations   The environments which the reaction control system must withstand are classified into four operational regimes: 1) storage and transportation, 2) pre-flight, 3) launch, and 4) flight. On a conservative basis, the control system would be required to function properly during and after undergoing both the maximum individual and the combined environmental requirements. For a sled-launched missile at Edwards Air Force Base, it is anticipated that the critical environments for the reaction control system would be as shown in Table 2.2.2. There are a number of the environments (such as called out in military specification MIL-E-5272A) that are either not considered critical or are not applicable to the requirements of the PYE WACKET FTV. In the interest of economy and performance, it is also desirable to waive or relax such environments as fungus and humidity. In addition, special handling during transportation and storage will reduce the severity of the temperature, sand and dust environments. It therefore appears that the most severe environmental limitations on the control system will occur during the launch and flight phases of the vehicle. These limitations fall into the following categories:

1)   main motor exhaust effects on the control nozzles (during aft launch),
2)   acceleration loads at launch and main motor burnout,
3)   sled and vehicle vibration, and
4)   vehicle stagnation pressures as high as 20.8 psia during launch, and 107 psia during flight.

Program Scheduling Limitations   In order to meet program schedules, it will be necessary to use available off-the-shelf hardware in the control system design wherever practical. It is anticipated however, that some development work will be required even though maximum usage is made of shelf items.

SECRET

Table 2.2.2 Critical Environmental Regimes of
the Reaction Control System

Environment	Storage and Transportation	Pre-Flight	Launch	Flight
Sand and Dust	x	x	---	---
Shock	x	---	---	---
Fungus	x	---	---	---
Humidity	x	---	---	---
Temperature	x	x	x	x
Pressure	---	x	x	x
Acceleration	---	---	x	x
Vibration	---	---	x	x

2.2.2.2 Reaction Control System Analysis   Reaction control
systems can generally be categorized by the type of propulsive agent
used to provide thrust and the method used to control thrust. Cold
gas, liquid propellant(s), solid propellant(s), and various combinations
are commonly used as propulsive agents and/or as a means for pressuri-
zation or starting. The liquid or gaseous agents are adaptable to
control with either proportional or bistable propellant valves. Thrust
produced from solid propellant usually requires a pre-programmed thrust
schedule. A proportional control valve is normally utilized when the
reaction control system requires a smooth transition between various
called-for thrust levels. Otherwise, a bistable propellant valve
can be used to provide on-off thrust action. The characteristics of
the above combinations were compared with the requirements first to
establish the feasible systems and subsequently to determine the most
suitable system for the PYE WACKET FTV.

Evaluation of Propulsive Systems   Reaction control utilizing
cold gas as the propulsive agent requires that the gas be stored under
high pressure and expelled through supersonic nozzles. This type of
system is generally very reliable but relatively inefficient due to
the low energy available from the cold gas (Reference 4.10). A com-
parison of the weight and volume requirements for typical cold gas
systems producing 6600 pound-seconds of impulse is shown in Table
2.2.3. Although the comparison was based on an optimistic gas temp-
erature value of 540°F, the volume required by the gas systems considered
is in excess of 8000 cubic inches. The 2000 cubic inch space available
for the control system in the FTV negates the use of a cold gas system.

Table 2.2.3 Cold Gas System Requirements*

Gas	γ	R ft-lb$_m$/lb-°R$_f$	Isp sec	Wt. of Gas lb	Vol. of Gas cubic inches
Nitrogen	1.40	55.16	67.7	97.5	8,630
Helium	1.66	386.2	88.4	74.7	52,700
Hydrogen	1.41	766.6	147.7	44.7	60,000

* Calculations based on the requirements of a 6600 lb-sec impulse
  system. Storage pressure 4000 psia and chamber temperature 540°R.

Liquid propellant systems may be classified according to the type of pressurization used to force the propellant into the combustion chamber, the number of liquid components and the type of ignition. The three basic types of pressurization systems normally used with liquid propellants are: 1) cold gas, 2) propellant pumps, and 3) a hot gas generator. A monopropellant or a bipropellant can be used with ignition by catalytic action, by a pyrotechnic device, or by the hypergolic nature of the propellants. In order to determine the most suitable propellant, ignition system, and pressurization system that could be used for the FTV (if liquid propellant reaction control were used), a limited investigation of each of the above possibilities was conducted.

Cold gas pressurization systems generally use either nitrogen or helium. Basing the comparison on the amount of gas required to pressurize a 700 cubic inch propellant tank to 500 psia (representative system design parameters), Figures 2.2.8 and 2.2.9 show that the weight saved by using helium (less than one pound) is more than offset by its increased volume requirements. Therefore, since volume is a very important consideration in the FTV design, nitrogen gas is the preferred pressurization agent for a liquid propellant system. With nitrogen selected, the volume requirements for the pressurization system can be easily plotted in parametric form, as shown in Figure 2.2.10.

The use of a pump to force the propellant from its tank to the combustion chamber has the advantage of allowing the propellant to be stored at low pressures in the forward portion of the FTV (shifting the center of gravity forward). Such a system, however, is complex and requires a large amount of electric power. In order to determine whether the power required by this system would be excessive, a brief analysis was made for a typical monopropellant (hydrazine) with the following characteristics:

$$\text{Isp} = 180 \ lb_f\text{-sec}/lb_m \ (\text{specific impulse}),$$

$$\rho = 62.4 \ lb/ft^3 (\text{density}),$$

$$E = 30 \ \text{Volts D.C. (battery supply voltage)},$$

$$\eta = 100\% \ (\text{pump efficienty}), \text{ and}$$

$$\Delta p = 500 \ \text{psia.}$$

The results of the investigation (Figure 2.2.11) indicate that 260 amperes at 30 volts DC are required to pump the propellant for three nozzles operating at only 300 pounds of thrust. This electrical power requirement renders a propellant pumping system undesirable for the FTV control system.

VOLUME VS INITIAL PRESSURE
COLD GAS PRESSURIZATION SYSTEM

CONDITIONS:
1. GENERATOR FLOW
2. PROPELLANT VOLUME   700 CU IN
3. INITIAL TEMPERATURE 60° F
4. FUEL PRESSURE   700 PSIA

HELIUM

HYDROGEN

PRESSURIZATION TANK VOLUME ~ CUBIC INCHES

INITIAL PRESSURE ~ PSIA

Figure 2.26

WEIGHT vs INITIAL PRESSURE
COLD GAS PRESSURIZATION SYSTEM

CONDITIONS:
1. ISENTROPIC FLOW
2. PROPELLANT VOLUME 700 CU. IN.
3. INITIAL TEMPERATURE 60° F
4. FUEL PRESSURE 500 PSIA

NITROGEN

HELIUM

PRESSURIZATION TANK WEIGHT (LOADED) — POUNDS

10   8   6   4   2   0

2000   3000   4000   5000

INITIAL PRESSURE — PSIA

FIGURE 2.2.4

VOLUME VS INITIAL PRESSURE
COLD GAS PRESSURIZATION SYSTEM

CONDITIONS:
1. ISENTROPIC FLOW
2. PERFECT GAS
3. PROPELLANT VOLUME 70.0 CU. IN.
4. NITROGEN GAS

FUEL PRESSURE

1000 PSIA
750 PSIA
500 PSIA
250 PSIA

INITIAL PRESSURE - PSIA

FIGURE 2.3.02
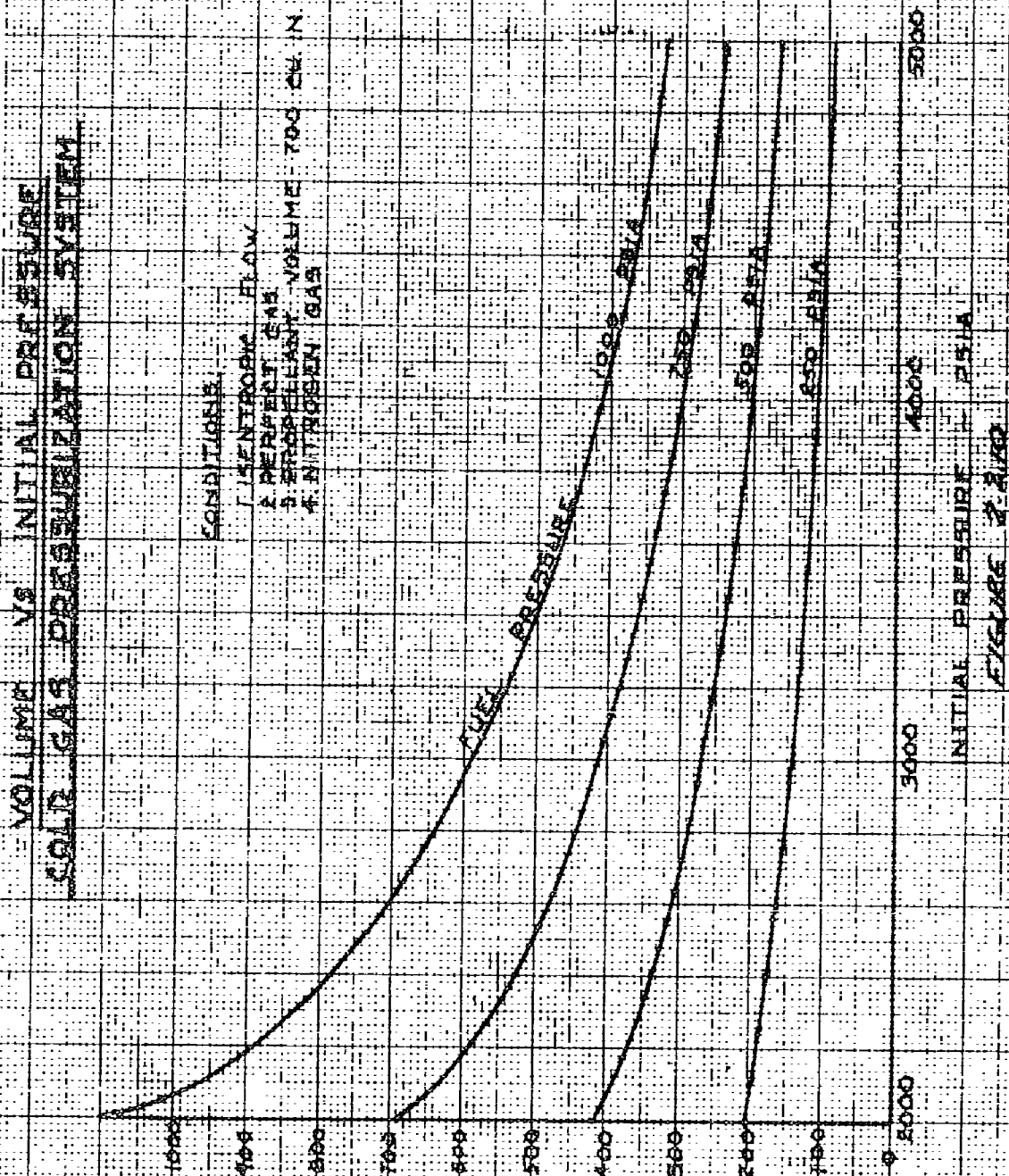
PRESSURIZATION TANK VOLUME - CUBIC INCHES

TOTAL CURRENT TO PROPELLANT PUMPS
VS.
THRUST PER NOZZLE

CONDITIONS:
1. 5 NOZZLES OPERATING
2. 30 VOLTS SUPPLY
3. $J_{sp} = 36$ LB, SEC/LB$_m$
4. EFFICIENCY = 100%
5. DENSITY = 62.4 LB /FT^3
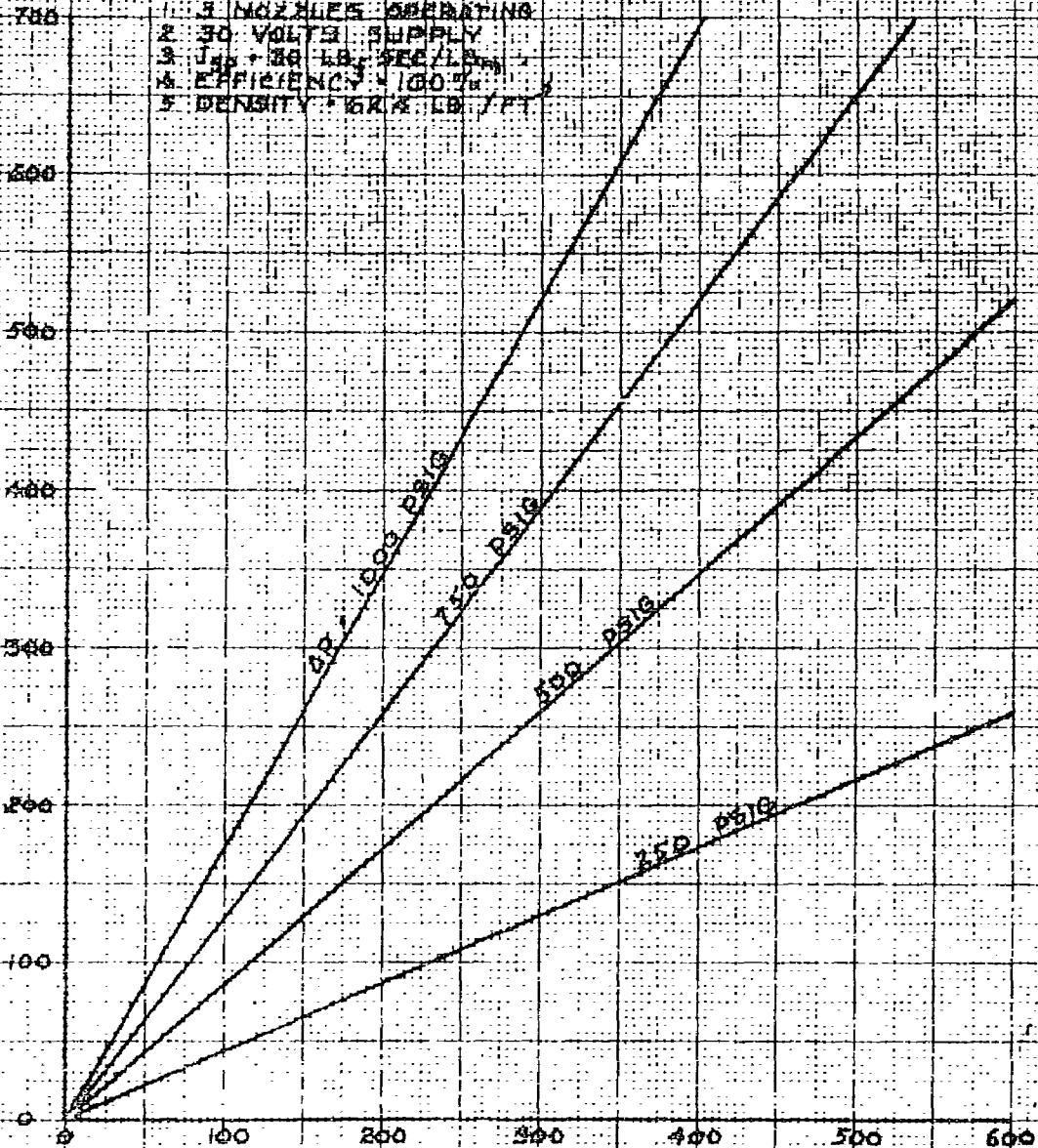
THRUST PER NOZZLE ~ LB

FIGURE 2.2.11

It is possible that a weight and/or a volume saving could be realized if either a liquid or solid propellant gas generator was used to pressurize the liquid propellant tanks. However, the hot gaseous products from the gas generator must be cooled prior to being used as 1 ·essurization agent, thereby adding complexity to the system. Considering this system (Figure 2.2.12) with a 50 cubic inch nitrogen tank at 4000 psi for cooling, only a five pound gas generator would be required (based on a gas generator mass fraction of 50 percent)*. However, the overall mission reliability (R) of this system is less than the reliability of the nitrogen pressurization system as shown in the following equation:

$$R = \left(R_{GG}\right)\left(R_{DV}\right)\left(R_{NP}\right) \qquad (2.2.5)$$

where R_{GG} = reliability of gas generator,

   R_{DV} = reliability of dump valve and circuitry, and

   R_{NP} = reliability of nitrogen pressurization system.

The effort required to develop a gas generator system poses an additional disadvantage. These two disadvantages, although partially offset by the probable reduction in pressurization system space, tend to render such a system undesirable for the FTV.

Certain combinations of the foregoing propellant feed systems with such additional components as thrust-chamber heat-exchangers, unbalanced piston cylinders (to increase pressure), and cascaded cold gas tanks provide an almost endless variety of systems (Reference 4.11). For the present application, however, these refinements are not warranted.

A reaction control system utilizing a monopropellant is shown in Figure 2.2.13. In this system, nitrogen gas pressurizes the propellant tank and six valves control the liquid propellant flow to the corresponding chambers. In addition, either a catalytic bed or a pyrotechnic igniter is required for decomposition of the propellant. (Catalytic bed chambers were assumed in this study because of their high reliability and restart capability). Although in general, mono-propellants are low specific impulse, slow reacting agents, they are used in the large majority of the operational reaction control systems (e.g., X-1B, X-15, and Scout). The experience in manufacture, handling

---

* An alternate method, using a heat exchanger to replace the nitrogen tank was considered impractical for the present application.
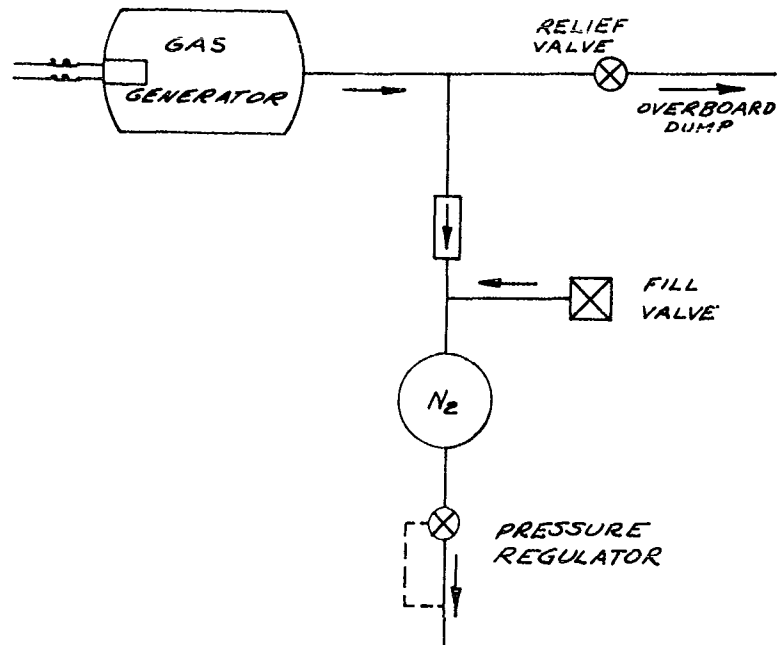
GAS GENERATOR
PRESSURIZATION SYSTEM

FIGURE 2.2.12

SCHEMATIC OF A MONOPROPELLANT
REACTION CONTROL SYSTEM

PRESSURE GAGE

SOLENOID START VALVE

FILL VALVE

N₂ TANK

PRESS. REG.

PROP. TANK

RELIEF VALVE

CONTROL VALVE

DECOMPOSITION
AND THRUST
CHAMBER

FIGURE 2.2.13

2.25
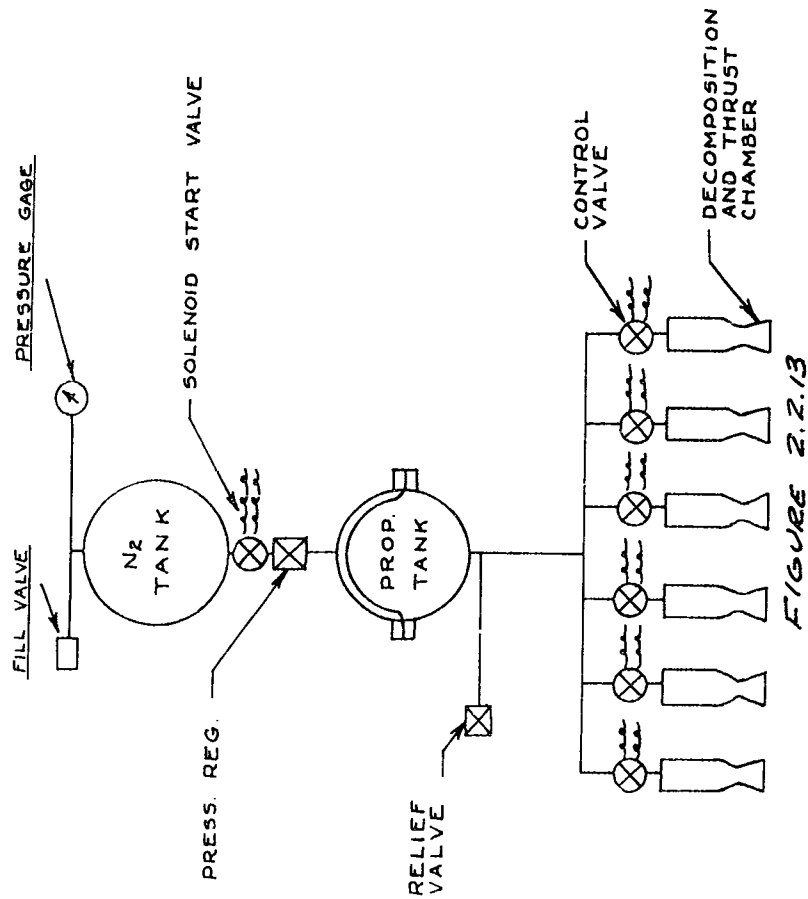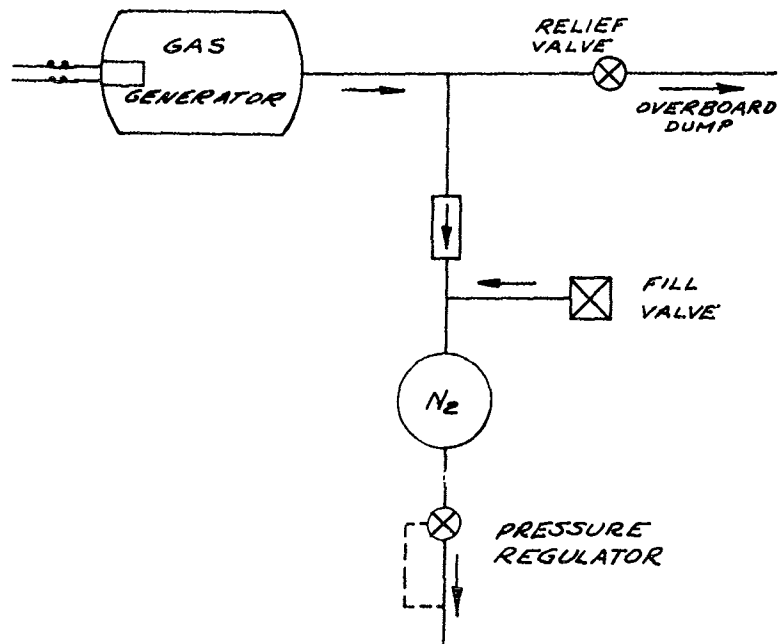
GAS GENERATOR
PRESSURIZATION SYSTEM

FIGURE 2.2.12

2.24

SCHEMATIC OF A MONOPROPELLANT
REACTION CONTROL SYSTEM

FIGURE 2.2.13
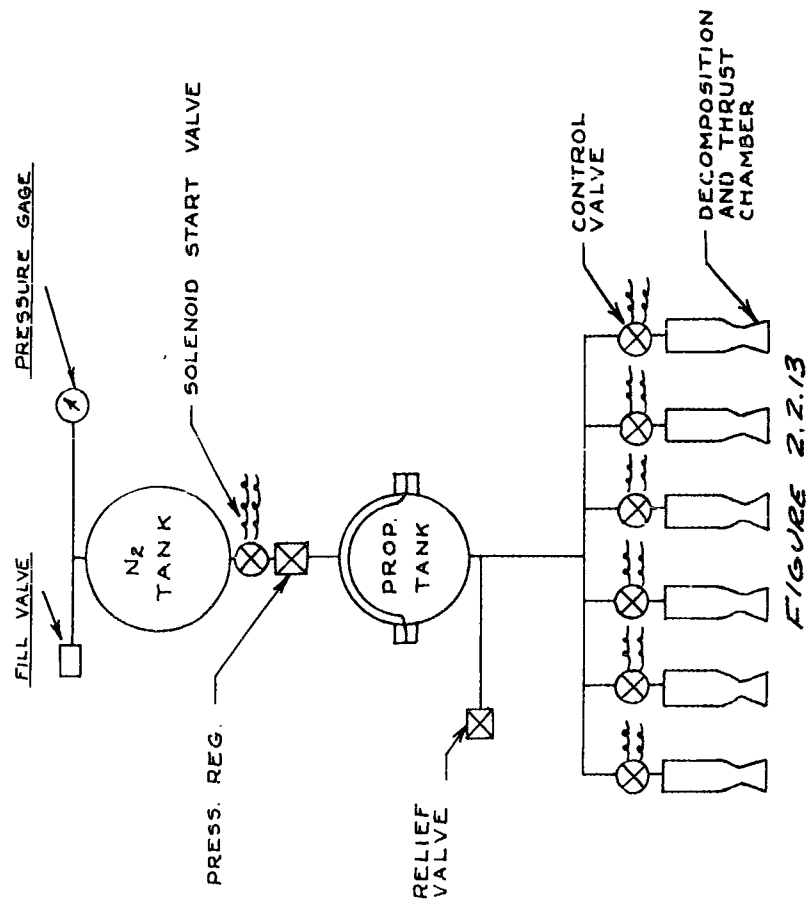
and design gives this type of system an advantage in cost, reliability, and availability over all other feasible reaction control systems. Basic properties of several of the more well known monopropellants are shown in Table 2.2.4 (References 4.12, 4.13, and 4.14).

Table 2.2.4 Monopropellant Characteristics

	Specific Impulse (Seconds)	Specific Weight	Density Impulse lb-sec/in^3	Ratio of Specific heats (γ)
90% H_2O_2	132	1.386	6.62	1.264
Ethylene Oxide	160	0.862	5.0	1.174
95% Hydrazine	180	1.006	6.55	1.289
Dyathene A5050	177	0.93	5.97	1.260
Isolde 120-A	211	1.31	10.0	1.200*

* assumed value

The three most promising monopropellants, based on density impulse (important for volume limited applications), are H_2O_2, Hydrazine, and Isolde.

A study of a control system design requiring a 6600 pounds-second impulse and a 300 pound thrust per nozzle was conducted for the latter three monopropellants assuming a nitrogen pressure of 4000 psia, a propellant tank pressure of 750 psia, and a chamber pressure of 500 psia. The results (shown in Table 2.2.5) indicate that all three monopropellant systems are feasible for the PYE WACKET FTV on the basis of total volume required (approximately 1500 cubic inches are available for propellant tanks and pressurizing gas).

Table 2.2.5 Monopropellant Systems

Propellant	Wt. of Propellant, lb	Vol. of Propellant, in^3	Vol. of Nitrogen Gas, in^3	Ratio of Specific Heats	C_F(OPT)	D_t in.	L_{NOZ} in.
90% H_2O_2	50	997	431	1.264	1.589	0.694	1.42
95% Hydrazine	36.6	1006	435	1.289	1.576	0.696	1.50
Isolde 120A	31.3	660	286	1.200*	1.625	0.685	1.66

* assumed value

The control system response characteristics using a monopropellant were next investigated. The test data shown in Figure 2.2.14 (Reference 4.15) using H_2O_2 indicate very poor response characteristics during the initial thrust cycles (0.2, 0.150, and 0.035 seconds). The data in Figure 2.2.15 give the response characteristics for a chamber with a stabilized wall temperature of 150°F, and show an overall delay of 20 milliseconds in thrust buildup. Identical thrust-time curves are produced for pulse number 1 and pulse number 100 although thrust decay times were on the order of 60-70 milliseconds. The response characteristics for a system using water and H_2O_2 (Figures 2.2.16 and 2.2.17) indicate similar results to those shown in Figure 2.2.15.

The foregoing analyses of monopropellant system response characteristics indicate that a monopropellant system will not meet the time response requirements stated in Section 2.2.2.1. In addition, the necessity for a catalytic bed to initiate decomposition results in excessive combustion chamber weight. Moreover, for any given PYE WACKET configuration, it is probable that the vehicle center of gravity will be forced aft due to the monopropellant control-system weight-space distribution.

A study was performed on a modified monopropellant system (Figure 2.2.18) in which thrust is provided by the hot gas stored in an accumulator. The analysis assumed the same design requirements as for the previous monopropellant system with the following additional assumptions:

(1) accumulator pressure will not fall below twenty-five percent of the maximum accumulator pressure,

(2) the monopropellant decomposition response time is 50 milliseconds,

(3) the response time of the control valve is 10 milliseconds,

(4) the pressure drop between propellant tank and accumulator is 100 psi (maximum),

(5) the pressure drop between the accumulator and nozzle chamber is 105 psi (maximum),

(6) the signal applied to the thrust motor control valve is also applied to valve A (Figure 2.2.18), and

(7) all reactions are step-functions, i.e., pure time delays.

The results of this analysis, shown in Figures 2.2.19 and 2.2.20, indicate that the required volume for the system exceeds 5000 cubic inches at all reasonable accumulator pressures thus rendering the system incompatible with the 2000 cubic inch space available in the FTV.
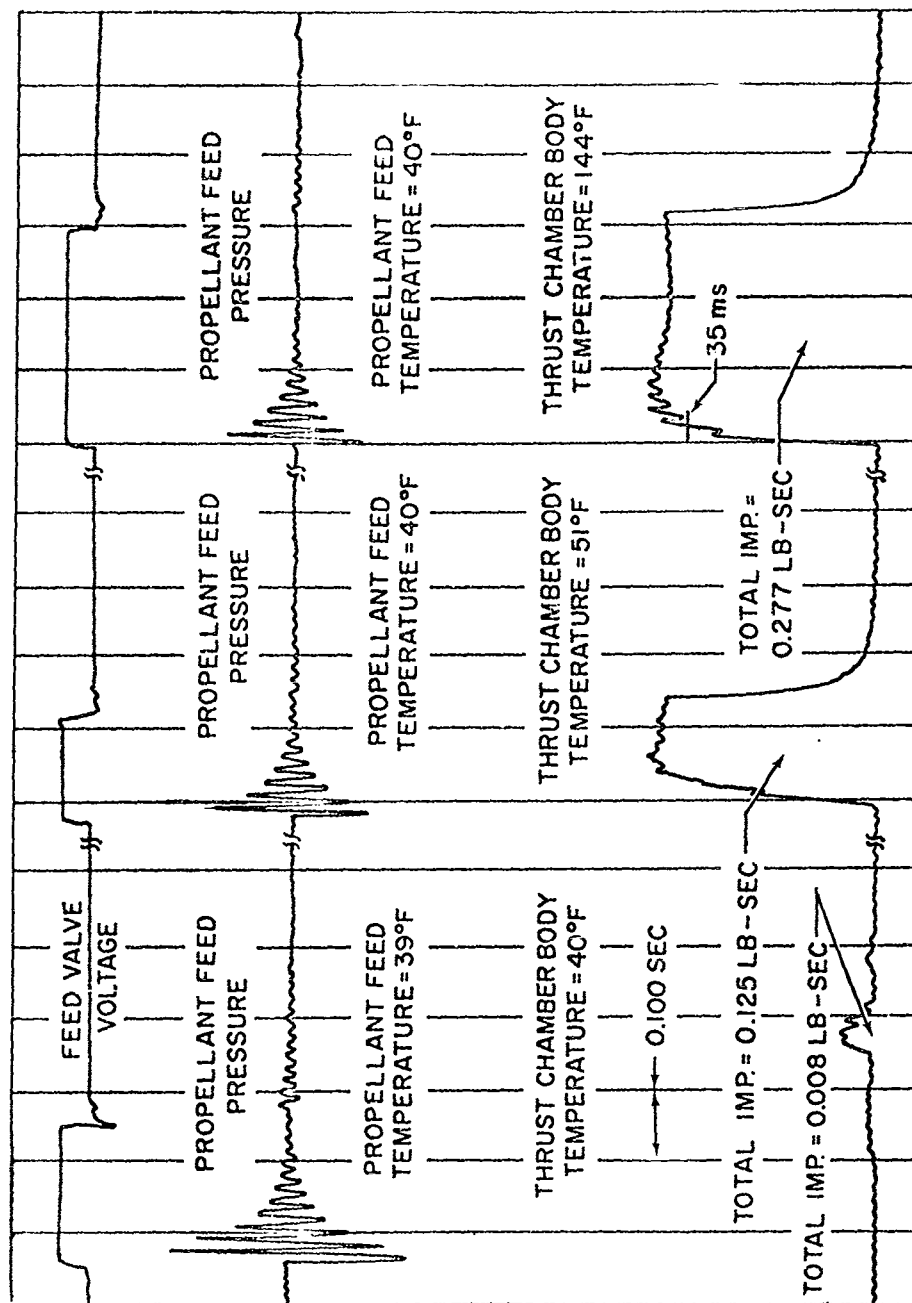
Figure 2.2.14   One-Pound Thrust Chamber Pulsing Tests
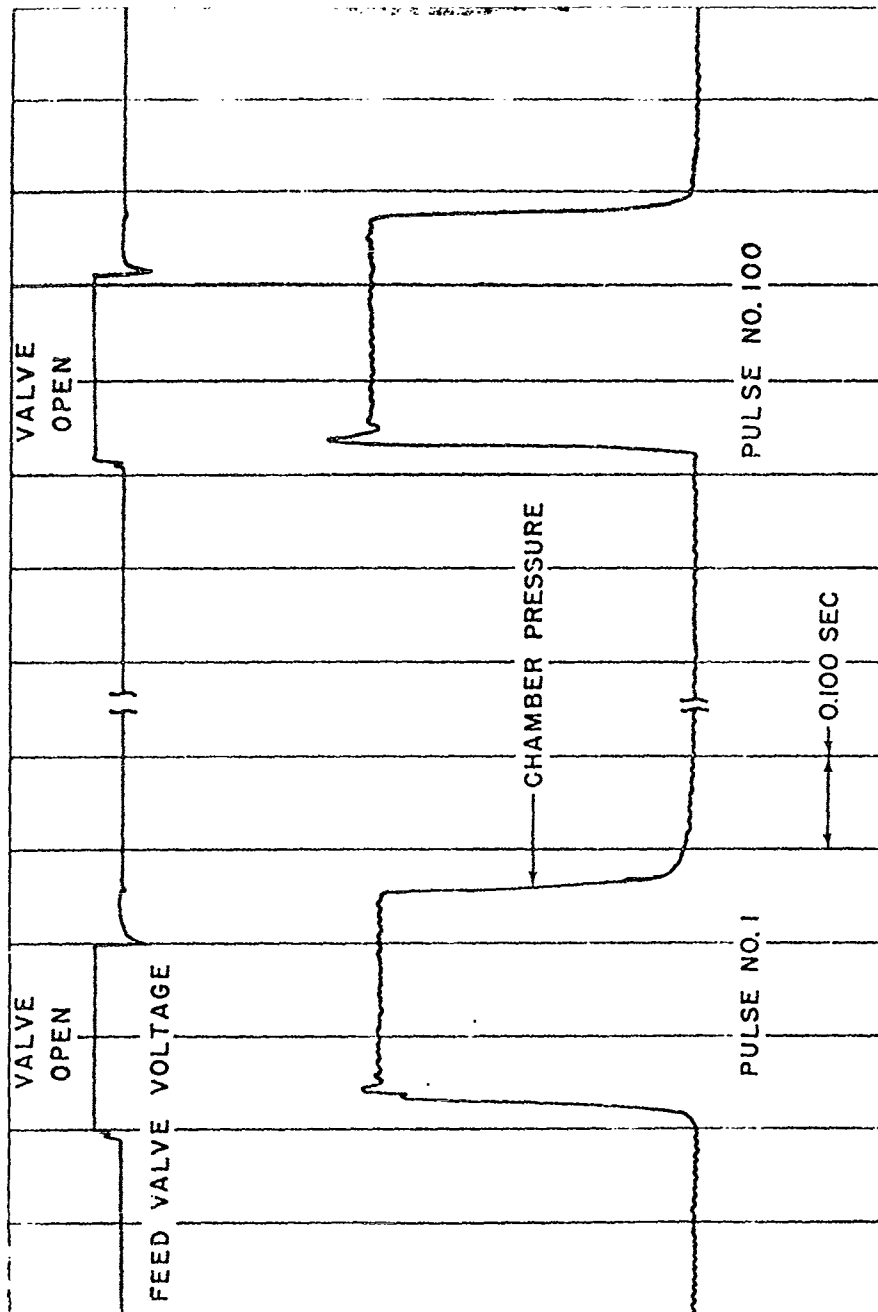
Figure 2.2.15   24-Pound Thrust Chamber Pulses

500 # VALVE
RESPONSE CHARACTERISTICS

PRESSURE	400 PSI H_2O
VOLTAGE	28 VDC
CURRENT	1 AMP
ΔP	20 PSI

10 MILLISECS

TIME

H_2O FLOW

VALVE SIGNAL

12 MILLISECS

PRESSURE

FLOW CUTOFF

VALVE DE-ENERGISED

CURRENT

VALVE CYCLED ON H_2O AFTER CYCLING ON H_2O_2 & MOTOR ASSY
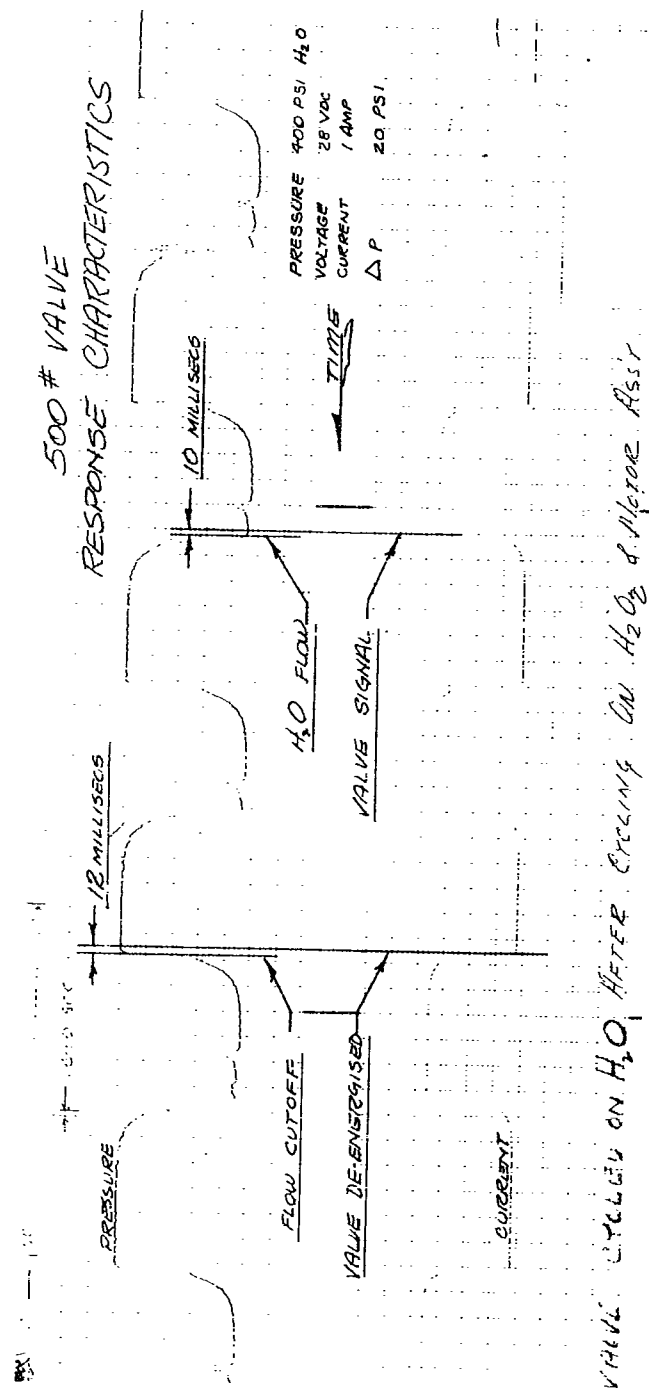
Figure 2.2.16   500-lb Thrust Motor Valve Run Record
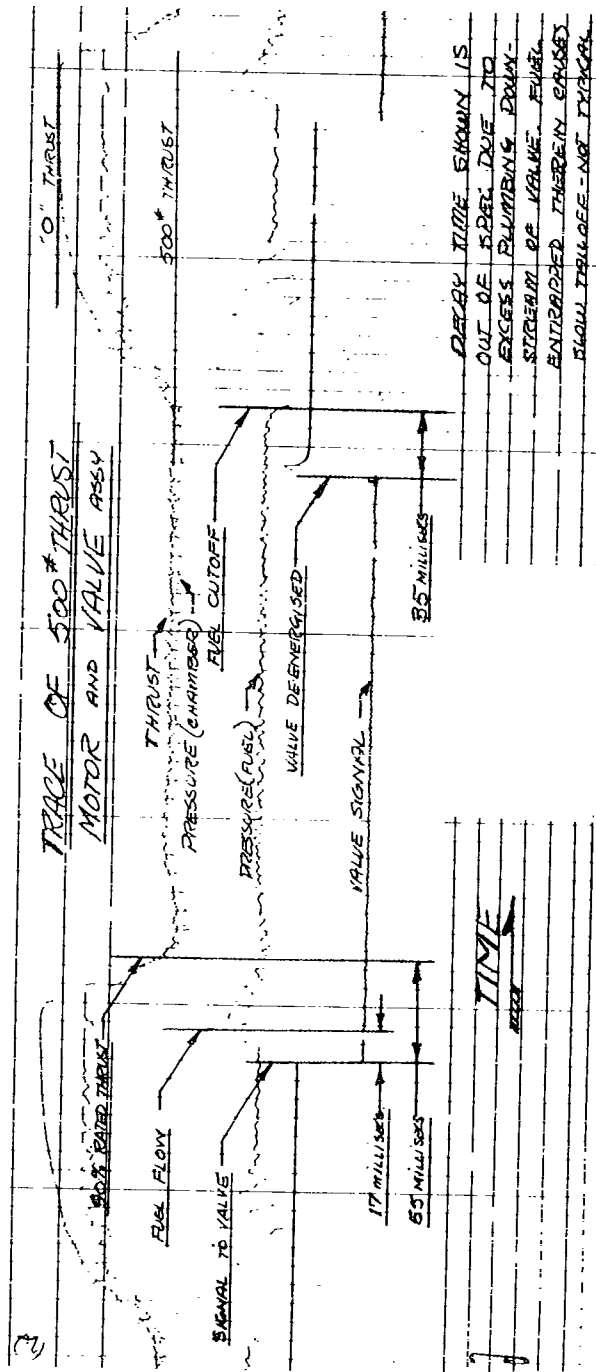
Figure 2.2.17   500 lb-Thrust Motor Run Record

2.31

HOT GAS REACTION CONTROL
SYSTEM SCHEMATIC
ACCUMULATOR TYPE

FILL VALVE

N₂ TA·

PRESSURE GAGE

PRESSURE REGULATOR

SOLENOID START VALVE

PROP TANK

PROPELLANT CONTROL VALVE `A`

RELIEF VALVE

GAS GENERATOR

HOT GAS ACCUMULATOR

CONTROL VALVE

NOZZLE CHAMBER
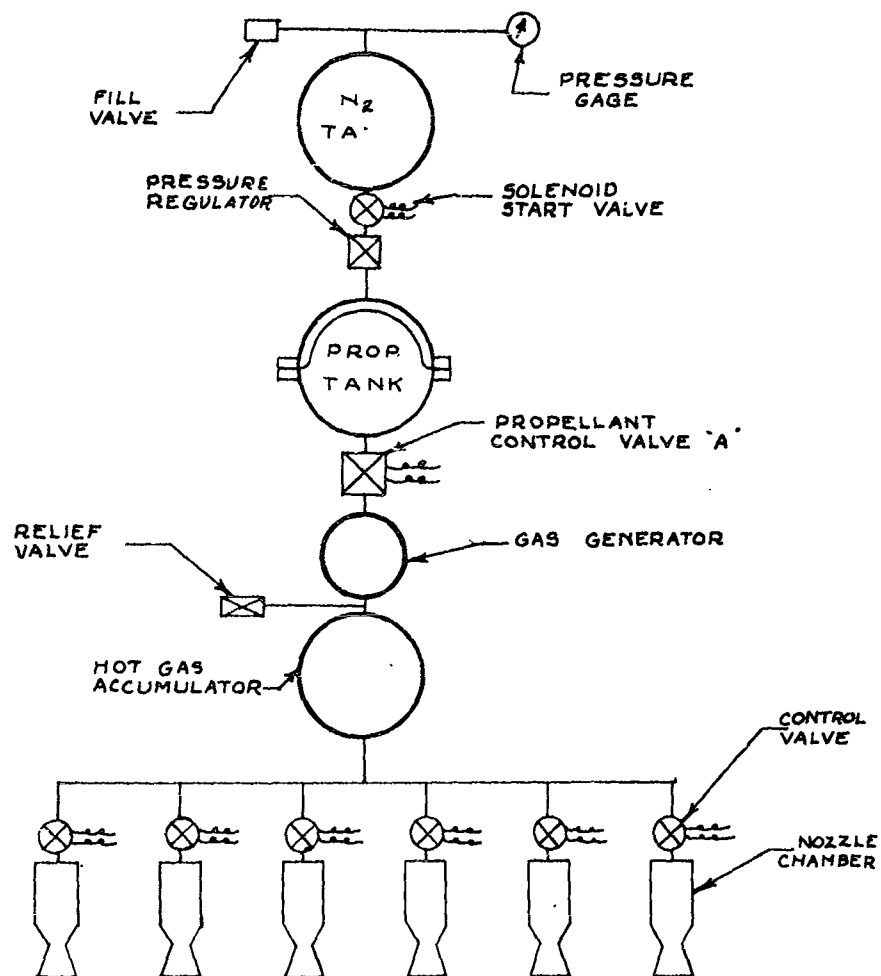
FIGURE 2.2.18

SECRET

2.32

NITROGEN AND H_2O_2 PROPELLANT
VOLUME VS ACCUMULATOR PRESSURE

CONDITIONS
1. TOTAL IMPULSE : 4600 LB-SEC
2. N_2 INITIAL PRESSURE : 4000 PSIA
3. ISENTROPIC FLOW
4. PROPELLANT : 90% H_2O_2

PROPELLANT

NITROGEN

VOLUME ~ CUBIC INCHES

2000

1000

0

0   1000   2000

ACCUMULATOR PRESSURE ~ PSIA
FIGURE 2.2.19
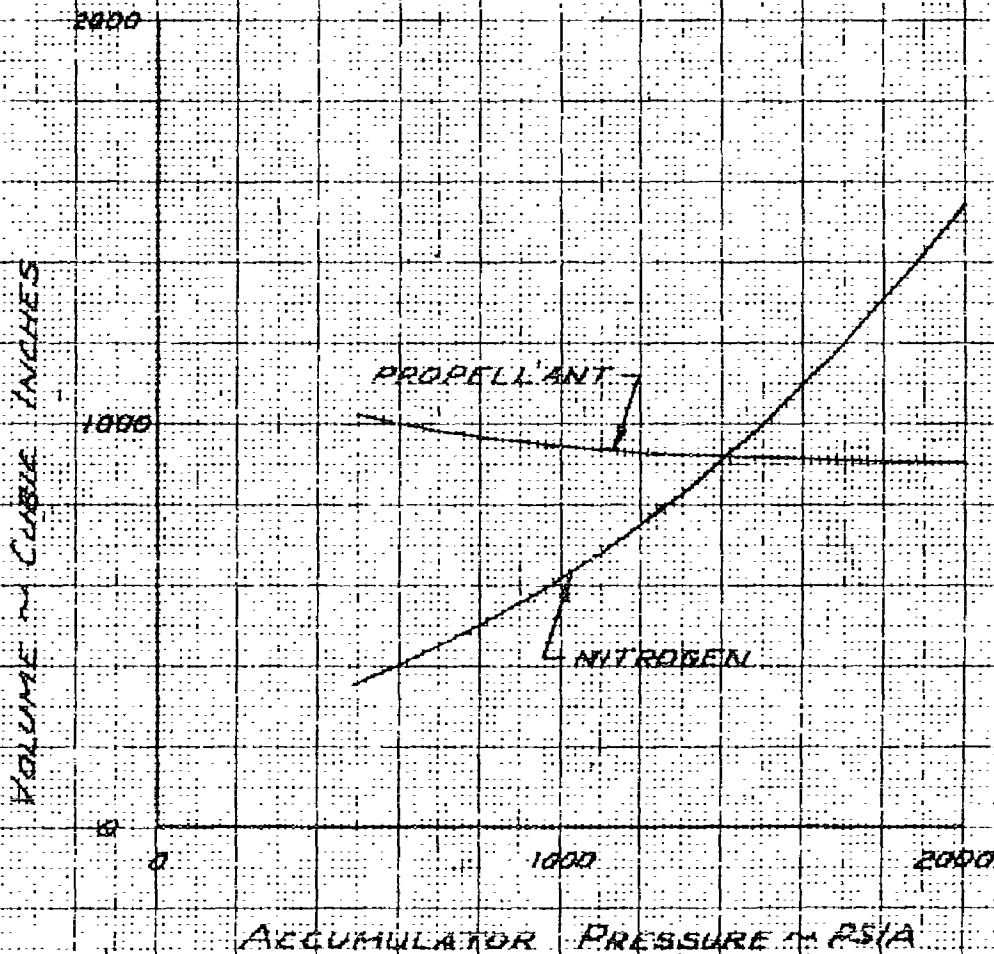
HOT GAS SYSTEM VOLUMES

CONDITIONS:
1. TOTAL IMPULSE: 6600 LB-SEC
2. N_2 INITIAL PRESSURE: 4000 PSIA
3. ISENTROPIC FLOW
4. PROPELLANT: 90% H_2O_2
5. MIN. ACCUM. PR. 25% NORMAL VALUE
6. DECOMPOSITION DELAY: 50 MS
7. THRUST RESPONSE: 10 MS
8. COMB. CHAMBER VOLUME EXCLUDED

WITH ACCUMULATOR

EXCLUDING ACCUMULATOR

VOLUME ~ CUBIC INCHES

30,000

20,000

10,000

0

ACCUMULATOR PRESSURE ~ PSIA

0   1000   2000
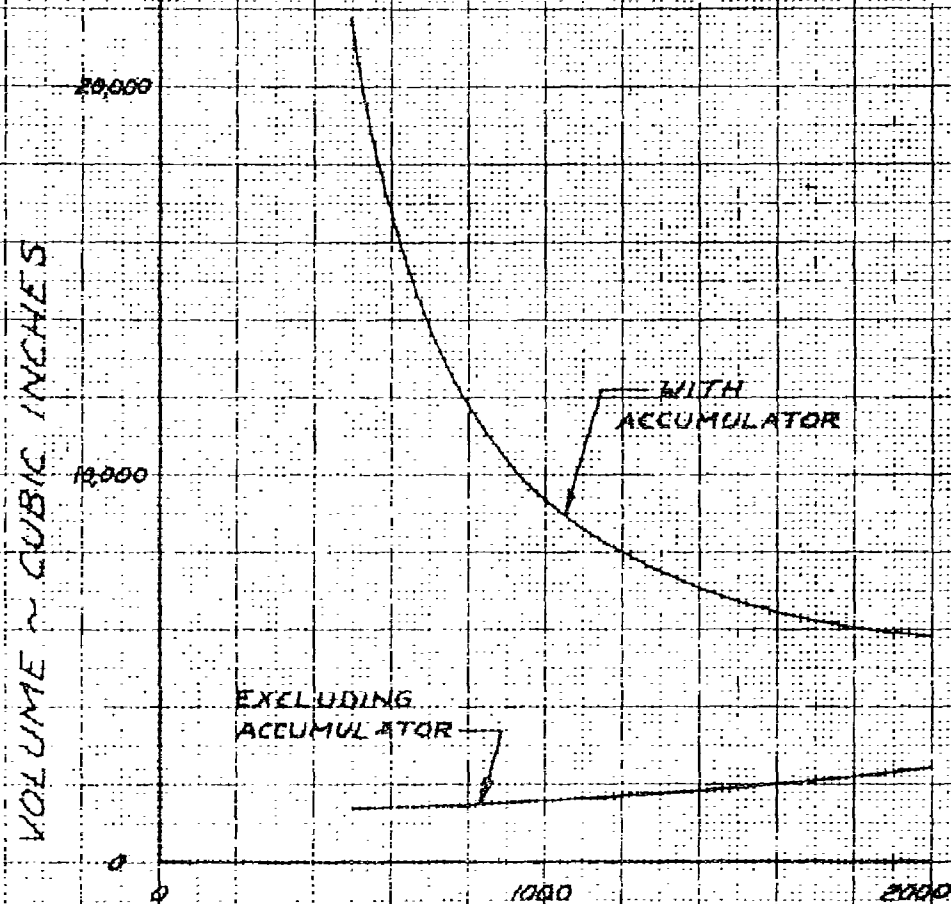
FIGURE 2.220

The third type of monopropellant system studied is a pre-programmed, hot-gas reaction control system (Figure 2.2.21). It is presupposed that the propellant control will be programmed before flight or that thrust demand will be directed to the gas generator in addition to the control valve, thereby allowing the accumulator to be reduced to a compatible size. The liquid-propellant hot-gas system would be identical to the accumulator type system with respect to propellant tank and pressurization requirements. The required volume for this system (lower curve of Figure 2.2.19) indicates that the system is feasible for the PYE WACKET FTV on the basis of weight and volume.

Response characteristics of the hot gas control systems are much faster than the liquid-controlled monopropellant system.

The major difference between a typical hypergolic bipropellant system (such as shown in Figure 2.2.22) and a monopropellant system is in the combustion chamber design. The fuel and oxidizer of a hypergolic system do not require a catalytic bed or ignition system and therefore exhibit a reduced response time for combustion. Although no bipropellant reaction control systems are currently in production (several are in development), the bipropellant systems usually exhibit a high specific impulse and low reaction time coupled with high gas temperatures. With a control system requirement for 6600 pounds-seconds of impulse, a typical bipropellant system using nitrogen tetroxide (N_2O_4) and unsymmetrical dimethylhydrazine (UDMH) would have the design conditions shown in Table 2.2.6.

Table 2.2.6 Design Conditions for N_2O_4 and UDMH System

Oxidizer	N_2O_4
Fuel	UDMH
O/F weight ratio	2.5
Ratio of Specific heats,	1.55
Specific Impulse, lb-sec/lb	262.
Oxidizer density, lb/ft^3	89.4
Fuel density, lb/ft^3	48.6
Weight of propellant, lb	25.2
Weight of fuel, lb	7.2
Weight of oxidizer, lb	18.0
Volume of fuel, in^3	256.0
Volume of nitrogen gas, in^3	348.0
Volume of nitrogen gas, in^3	260.0
Thrust coefficient (C_F)	1.612
Diameter throat, inches	1.688
Diameter exit, inches	1.562
Length of nozzle, inches	1.63

HOT GAS REACTION CONTROL
SYSTEM SCHEMATIC
PRE - PROGRAMMED
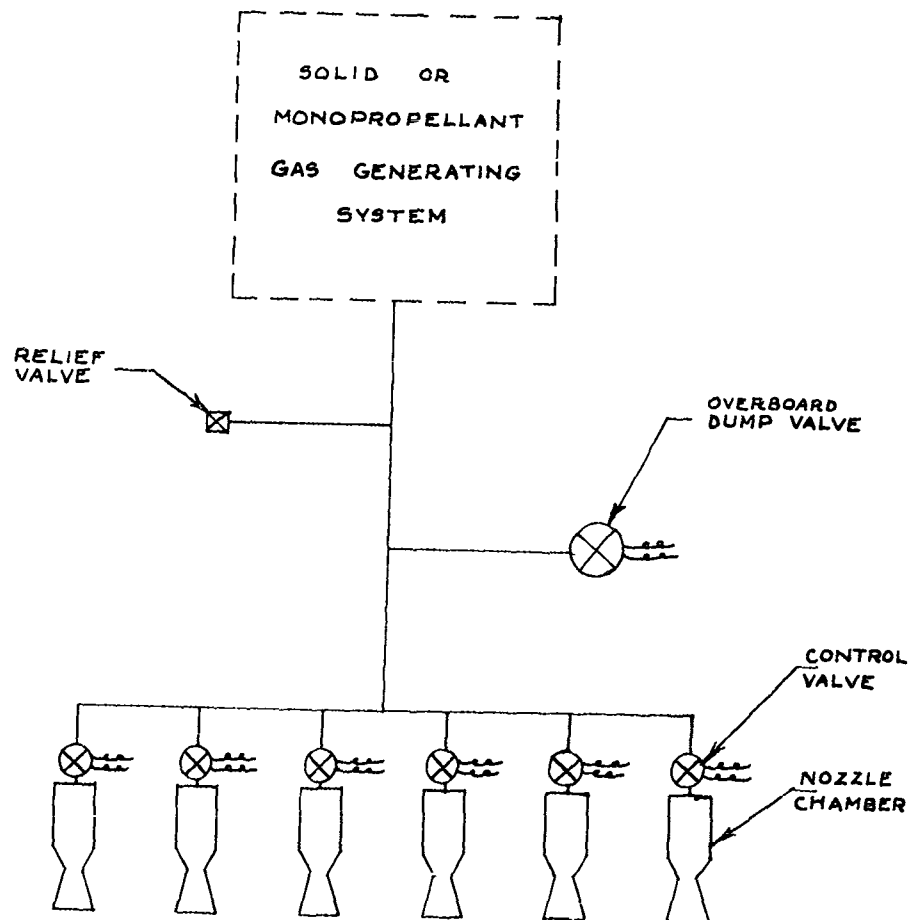
FIGURE 2.2.21

SCHEMATIC OF A BIPROPELLANT
REACTION CONTROL SYSTEM

FIGURE 2.2.22

2.37
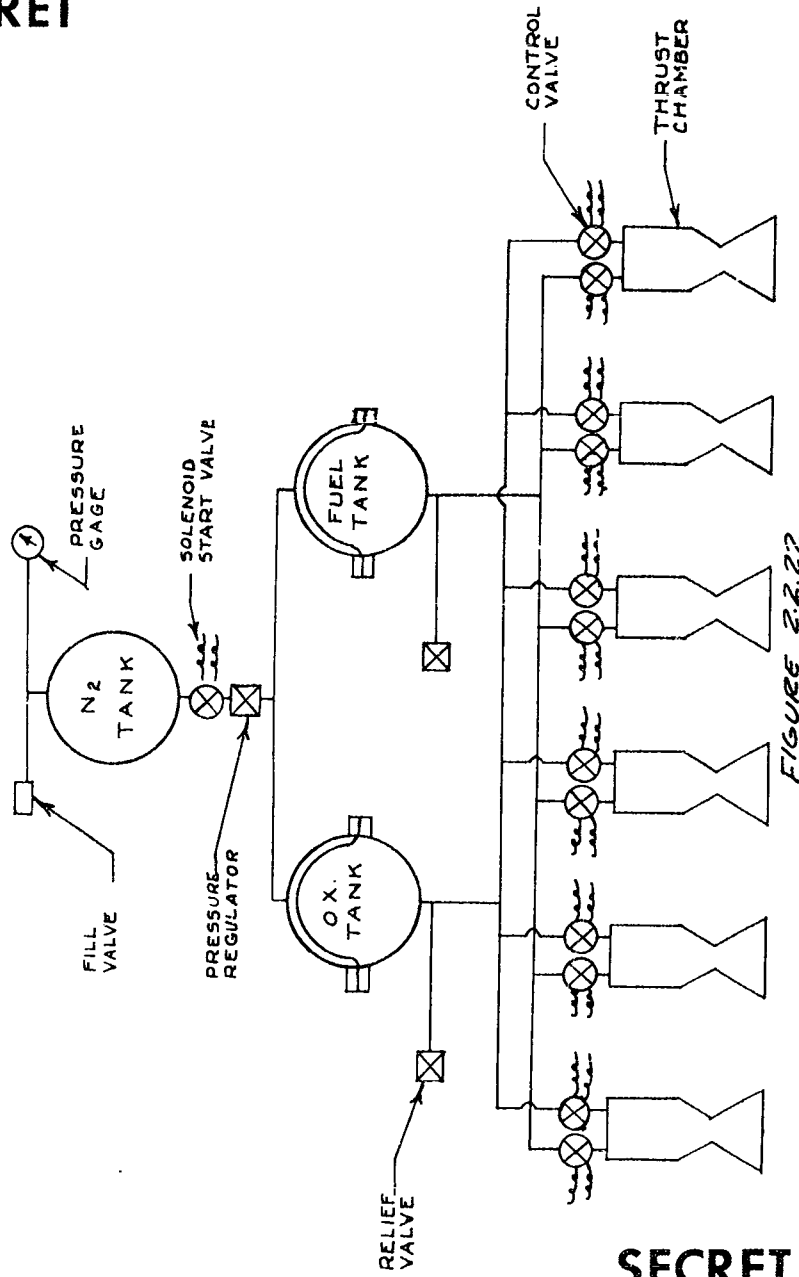
Response times of 3 to 7 milliseconds and thrust decay times of 3 to 7 milliseconds have been demonstrated in actual control motor firings. However, a more complete discussion of available bipropellant response characteristics will be given in Section 2.2.2.3.

A solid propellant could be used in the FTV reaction control system to supply hot gas to the control nozzle. Modulation of the thrust for this system would be accomplished by metering the gas through a "hot gas control valve" (in contrast to liquid metering control valves). The analysis of a typical pre-programmed, solid-propellant, hot gas control system assumed the use of low performance, low flame-temperature type of propellants (Reference 4.16) with the properties shown in Table 2.2.7

Table 2.2.7 Properties of Solid Propellants

Propellant	JPL-320	PFC-181
Isp (calc), sec.	182	177
Density, lb/in^3	0.0544	0.0535
T_p (flame temp), °R	2502	2288

The analysis of the solid propellant system was conducted with a propellant exhibiting a specific impulse of 160 lb-sec per lb and a density of 0.0544 lb per in^3. The system requires 758 cubic inches of propellant and yields response characteristics identical to the monopropellant hot-gas system previously discussed. The preliminary design also indicates that at least four gas generators and one extra booster (for the initial two seconds) would be required.

Although the solid propellant system appears feasible for the PYE WACKET FTV, the expected poor reliability of a live gas generator system in conjunction with development requirements for the gas generators and hot gas valves make this system unattractive.

<u>Evaluation of Control Valves</u>   The rapid thrust build up and decay requirements for stabilization and control of the PYE WACKET FTV necessitates the use of fast-acting control valves. The two basic types of thrust control valves considered in this study are: 1) linear, and 2) nonlinear. The linear control valve modulates the propellant flow to produce a thrust level proportional to the guidance signal. The nonlinear control valve (commonly termed "bang-bang" or bi-stable) on the other hand, provides two position operation; either full thrust or zero thrust.

SECRET

Proportional control valves are heavier and more complicated than simple bi-stable valves. Furthermore, close tolerance machining is required to attain the linear response features of the valve which in turn results in a high cost per valve. In summation, the linear valve is less desirable from the cost, reliability, and weight aspects.

Bi-stable valves are currently used in all operational reaction control systems. The two basic types of these valves are "on-off" and "positive-negative". The "on-off" bi-stable valve is either full or zero thrust and the "positive-negative" bi-stable valve provides full thrust in either the positive or negative direction. No further consideration was given to the latter valve because its configuration is not readily adaptable to PYE WACKET and because its use results in wasted fuel during conditions of zero called-for thrust.

The "on-off" bi-stable valve is considered to be the most desirable type of control for the PYE WACKET FTV. Quasi-proportional control is attainable by modulating the pulse width and/or frequency of the valve input signal. Response characteristics approaching the PYE WACKET requirements have been demonstrated. A further discussion of the present state-of-the-art of control valves is given in Section 2.2.2.3.

Summary of the Reaction Control System Analysis   Of the variety of reaction control systems studies for the PYE WACKET FTV, many systems appear feasible (see Table 2.2.8). The preferred reaction control systems are listed in Table 2.2.9.

2.2.2.3 Industry Survey   Reaction control systems are being used for attitude control of such atmospheric and space vehicles as the X-1B, X-15, Air Force Thor, and NASA Scout. These systems have performed satisfactorily for their specific applications although using (almost exclusively) monopropellants with a catalytic bed or heated chamber to initiate combustion for the reaction jet. Recent interest for advanced system applications has been in the field of extremely fast response systems. The work by various manufacturers on fast response systems is directly applicable to the PYE WACKET control requirements -- although most of the work has been done on low thrust systems.

In the attainment of a control system for the PYE WACKET FTV, two alternate methods were considered: 1) obtain the complete system from one vendor, or 2) procure components and develop the system. In order to determine which of these two possibilities was more desirable, a survey was made of vendor capability to supply entire reaction control system, in conjunction with a survey of the availability of suitable off-the-shelf components. In making the survey, the preliminary major system requirements were set forth as follows:

Table 2.2.8 Feasible Reaction Control Systems for the PYE WACKET FTV

Propellant			Pressurization		Control Effluent	Hot Gas		Control Valve Action	
Solid	Mono-	Bi-	Cold Gas	Gas Generator	Liquid	Accumulator	Demand or Pre-Programmed	Linear	Bi-Stable
X							X	X	
X							X		X
	X		X		X			X	
	X		X		X			X	X
	X			X	X			X	
	X			X	X				X
	X			X		X		X	
	X			X		X		X	X
	X		X			X			
	X		X			X			
	X		X				X	X	
	X		X				X	X	
	X			X			X	X	
	X			X			X	X	
		X	X		X			X	
		X	X		X			X	X
		X		X	X				X
		X		X	X				X

Table 2.2.9 Preferred Reaction Control Systems for the
PYE WACKET FTV

Preference	Propellant		Pressurization	Control Effluent		Control Valve Action	
	Mono-Propellant	Bi-Propellant	Cold Gas	Liquid	Pre-program or demand Hot Gas	Bi-stable	Linear
1		X	X	X		X	
2	X		X		X	X	
3		X	X				X

Total system weight 65 lb
Total system impulse 6600 lb-sec
Allowable maximum acceleration
 (all directions) 50 g's
Required maximum thrust
 level (per nozzle) 300 lb (later increased to 500
           lb)
Control valve characteristics
  cycling rate (min) 100 cps
  opening time (max) 5 ms
  closing time (max) 5 ms

  Complete Systems Proposed by vendors Several manufacturers were
invited to submit engineering data to support their approach to the
PYE WACKET FTV reaction control system and their past experience in
developing similar systems. Information from these companies has in-
dicate that three basic types of systems (monopropellant, bipro-
pellant, and solid propellant) are in various stages of development
and production. Most established systems are of the monopropellant
type.

  The large majority of operational reaction control systems utilize
monopropellants, i.e., the low response systems for the X-1B, X-15,
NASA Scout, Air Force Thor, and Air Force HETS 609A. These systems

have been qualified and are now in operational service. Also, several monopropellant reaction control systems are presently under development for the Dyna-soar, Centaur, Vega and Mercury projects. Gas generator applications using hydrogen peroxide as the propellant have been developed. An extensive background in experience and hardware is therefore available with monopropellant systems for thrust levels from fractions of a pound to 500 pounds; tankage, bladders, thrust chambers, and valving have been developed and qualified and problems involving material compatibility, heating, and system performance have been solved.

Two vendor-supplied monopropellant systems were studied for the PYE WACKET FTV reaction control system. The first of these systems (termed system A) utilizes a liquid controlled monopropellant with catalytic decomposition of hydrogen-peroxide. The system is completely qualified and hardware is available. The second system (termed system B) utilizes hot gas control with hydrazine as the propellant and nitrogen tetroxide as a hypergolic starting agent. In both systems, nitrogen gas is used for the pressurizing agent. A review of the weight breakdown of Systems A and B (shown in Table 2.2.10) and an analysis of the proposed designs, indicate the undesirable features of each to be as follows:

Table 2.2.10 Monopropellant System Weight Breakdown

	System A	System B
Pressurization System	18.6 lb	4.6 lb
Propellant System	71.7	62.8
Thrust Control System	63.7	18.7
Total System Weight (wet)	154	86.1

System A

(a) The system weight is more than twice that stated in the preliminary requirements,

(b) the thrust chambers will not fit in the present configuration, and

(c) the overall system response time is excessive;

System B

(a) the configuration will cause the vehicle center of gravity to move aft of the 50 percent chord,

(b) thrust drooping may occur for long thrust pulses, and

(c) development problems are anticipated in scaling the thrust from the present 60-lb level to the anticipated 500 lb.

Although the weight given for System B is greater than allowed, it does not pose a severe problem. System B possesses the advantages that it can be packaged into the FTV configuration and that it has operated with a response time of ten milliseconds.

Although there are no bipropellant reaction control systems currently in production, most of the companies contacted are investigating the advantages and disadvantages of such systems and are engaged in company funded development programs to resolve motor and response problems. The reason for this interest stems from the advantage of bipropellant systems in the areas of high total impulse and/or extremely fast response. The higher specific impulse of bipropellant systems usually results in a lower propellant weight. This advantage is offset by the weight of dual tankage and valving, however, these weights diminish in importance as the total system impulse increases. Also, a fast response is gained with a bipropellant system through the use of hypergolic ignition, thus eliminating the need for a catalytic bed and permitting the use of very low characteristic length chambers. The demonstrated response times of bipropellant systems far exceed that obtained with monopropellants. For example, a vendor has demonstrated an overall control system response time of the order of 3 milliseconds at a six pound thrust level, with the thrust decay essentially the same. Another vendor has demonstrated cycling rates up to 30 cps at the 300-lb thrust level, and Convair-Pomona tests (company-sponsored program) have produced an overall response time of 7 milliseconds with controlled cycling rates of 40 cps at the 500-lb thrust level. However, the use of low total impulse bipropellant systems can result in the following disadvantages:

(a) system complexity - reduced reliability,
(b) ground handling complexity, and
(c) cost for additional valves, tanks, and expensive propellant.

Three companies proposed a hypergolic nitrogen-pressurized bipropellant system for the PYE WACKET controls (see Table 2.2.11 for

weight breakdown). Details of the designs varied between companies, however, with either nitrogen tetroxide or red fuming nitric acid being proposed as oxidizers and either hydrazine or UDMH as fuels. Also, both direct solenoid and torque motor operated control valves were suggested. The proposed designs reflect a high degree of necessary development and therefore may not be realistic as far as cost and development time are concerned.

Based on the results of the industry survey, a bipropellant system appears feasible for the PYE WACKET FTV. The following problem areas exemplify the development required for the bipropellant systems:

    (a)   scaling-up design of fast response valves and injectors,

    (b)   design of a motor to be used with the high temperature propellant system, and

    (c)   design of expulsion tanks for the oxidizer system.

The Shillelagh missile currently uses eight reaction-jet nozzles located at the aft end of the vehicle to provide pitch, roll, and yaw control. A toroidal shaped solid-propellant hot-gas generator is used to supply the working fluid and four control valves distribute the hot gases among the eight nozzles. Each control valve is a solenoid operated bi-stable device that proportions the flow of hot gases between two ports. Operation of the valve is by pulse duration modulation (PDM) at a frequency of 20 cps with the pulse duration defining the flow that passes through each port. Quasi-proportional control is effected over a thrust range equivalent to 70 percent of the maximum thrust. In spite of the fairly good cycling capabilities of this system, it was not considered suitable for the PYE WACKET FTV because of the following major deficiencies:

    (a)   major development problems in designing a gas generating system are anticipated,

    (b)   the valve system is not applicable to a yaw nozzle configuration, and

    (c)   a major development effort in scaling-up the valve and ducting to the 500-lb thrust level is anticipated.

In addition, the wasteful use of propellant, even with a pre-programmed gas generator, would eliminate the normal volume advantage of a solid propellant system.

Component Survey   The most critical component of the reaction control system is the propellant control valve. Therefore, the major effort in the survey was exerted toward locating suitable control valves, with only a secondary effort on the investigation of other components.

Table 2.2.11 Bipropellant System Weight Breakdown

	System C	System D	System E
Pressurization System	6.65 lb	6.70 lb	9.1 lb
Propellant System	32.19	35.90	44.1
Thrust Control System	17.25	17.35	33.7
Total System Weight (wet)	56.09	59.95	86.9

Control valves are generally categorized by method of valve action and the physical state of the effluent. Since there are two basic methods of valve action (proportional and bi-stable) and the effluent may be in either the liquid or gaseous state, four basic valves are conceivable:

(a) proportional control of liquid propellant,
(b) proportional control of hot gas,
(c) bi-stable control of liquid propellant, and
(d) bi-stable control of hot gas.

In addition, two types of bi-stable action are available: 1) flow can be turned "on and off", or 2) flow can be diverted to the "positive or negative" direction.

Only one proportional control valve was located with response characteristics similar to the FTV requirements. This valve meters both fuel and oxidizer in the liquid state by means of a torque motor controlling a two-stage hydraulic amplifier. The overall envelope of the valve is a 3.5-inch diameter cylinder 5.4 inches long, with a weight per valve of 5.5 lb. Successful operation of this valve at 40 cps (while driven with a bi-stable element) has been accomplished at Convair-Pomona (Reference Figure 2.2.23). From weight and packaging considerations, however, the valve would require some modification for use on the PYE WACKET FTV.

One "positive-negative" bi-stable control valve with extremely fast response characteristics is presently available. This valve is used in the Shillelagh solid propellant, hot-gas control system, but as already mentioned, is not considered suitable for the PYE WACKET FTV.

TYPICAL 300 LB MOTOR RESPONSE
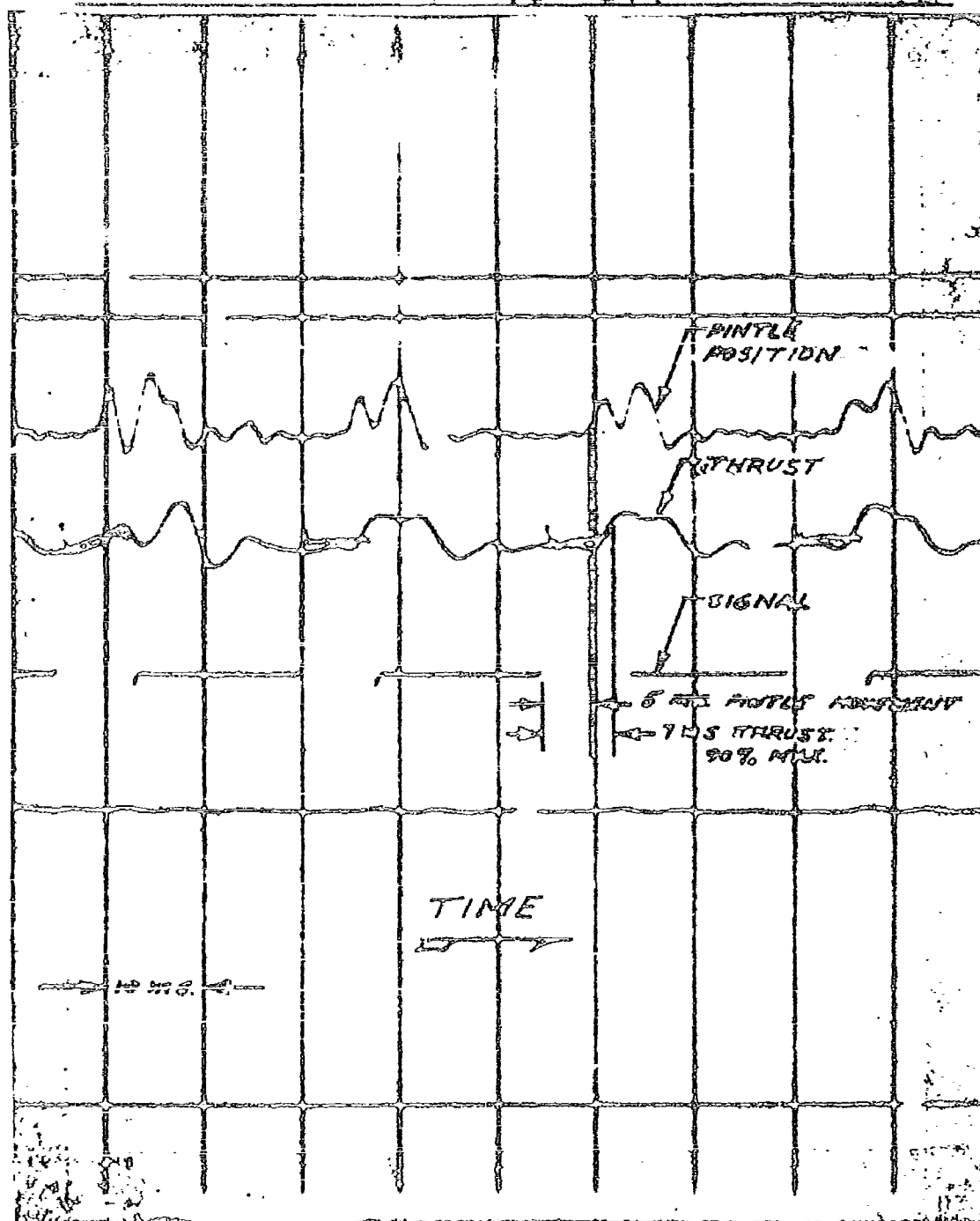
FIGURE 2.2.23

The most suitable hot-gas, "on-off" control valve located in the survey was developed for the Boeing Dyna-soar. This system incorporates a solenoid actuated poppet-type thrust control valve. The operation of the valve consists of three steps:

(a) energizing the solenoid moves a pilot poppet to the exhaust position,

(b) the dome pressure holding the valve closed is reduced as the gases flow by the pilot poppet to the atmosphere, and

(c) system pressure overcomes dome pressure and opens the valve.

The Dyna-soar valve is completely developed and has a demonstrated response time, from signal input to 90% thrust, of approximately 10 milliseconds. A modification of the valve was proposed for the PYE WACKET FTV which included a balanced-pressure poppet-valve of the required thrust level. Such a modification would allow the use of a smaller solenoid and thereby reduce weight, electrical transients, and power requirements. It is estimated that a valve of this type could be developed within the required time period to give an overall response time between 3 and 5 milliseconds.

A torque motor actuated, bi-stable valve has been developed for a hypergolic bipropellant reaction control system. Operation of this valve consists of energizing the torque motor which directly actuates the main valve poppet. The valve also forms a part of the combustion chamber thus eliminating the transportation delays downstream of the control valve. Experimental verification of a 3 millisecond overall response time at the 6-pound thrust level is available. Since it is anticipated that the FTV will require a 500-pound thrust level, a modified valve with multiple balanced-pressure poppets and a new propellant impingement concept was suggested. Although 300 pounds of thrust was estimated as the upper limit of this valve configuration, the valve is still considered feasible for the PYE WACKET FTV if necessary development effort was considered worthwhile.

A bistable control valve using a solenoid operated pilot-poppet to admit or exhaust nitrogen gas, was proposed. The nitrogen gas pressure acts on one side of the main poppet with oxidizer or fuel pressure acting on the opposite side. When the pilot-poppet admits nitrogen, the main poppet moves to stop the propellant flow; when the pilot-poppet exhausts nitrogen, the main poppet moves to allow propellant flow. Although the valve has not been tested as yet, the vendor predicts a 4 millisecond valve response time will be obtained with this design. Envelope dimensions of the valve are given as 2" x 2" x 4-1/2", with a weight per valve of 1.97 lb.

Another proposal incorporated a bistable liquid control valve using a solenoid control pilot-stage with separate valves for fuel

and oxidizer. Operation of the valve requires the solenoid to open the pilot poppet to bleed the pressure from behind the main poppet thereby allowing propellant pressure to open the main poppet. Tests have not been made with this valve as yet. The envelope dimensions of the valve were given as 1-1/2" x 2-1/2" x 3-1/2" and the weight per valve as 0.82 lb.

In addition to information on propellant control valves, the availability of other components of the anticipated system was investigated. Although off-the-shelf equipment was located for most of the valving and filters, it was found that the propellant tankage will probably be a developmental item. Compatibility considerations will undoubtedly limit the tank bladder material to Teflon TFE and FEP or Fluorosilicone elastomer for the nitrogen tetroxide oxidizer. In addition, a program will be necessary to develop two basic tank configurations--with expulsion, vibration, acceleration, and sloshing tests required. It also can be concluded from the survey that development effort may be required on the control motor itself.

2.2.2.4 <u>Reaction Control System Selection</u> The most promising reaction control systems for the FTV were selected on the basis of a system analysis for the following considerations:

    (a)   overall system response time,
    (b)   control valve response time,
    (c)   control system volume,
    (d)   control system weight,
    (e)   vehicle center of gravity,
    (f)   availability of components,
    (g)   industry experience with system concept,
    (h)   vehicle performance,
    (i)   extent and intricacy of development, and
    (j)   program cost.

The three most promising systems, in order of preference, are as follows:

    (a)   pressurization: high pressure nitrogen,
           propellant: hypergolic bipropellant (N_2O_4/UDMH-N_2H_4),
           control: bistable, on-off, liquid control.

    (b)   pressurization: high pressure nitrogen,
           propellant: monopropellant hydrazine with hypergolic start,
           control: bistable, on-off, hot-gas control.

    (c)   pressurization: high pressure nitrogen,
           propellant: hypergolic bipropellant (N_2O_4/UDMH-N_2H_4),
           control: proportional, liquid control.

A schematic of a bipropellant system is shown in Figure 2.2.24.

2.2.3 CONTROL SYSTEM CAPABILITIES

2.2.3.1 Interaction Effects   The interaction effect between the pitch and roll control jet exhaust and the external aerodynamic flow field around the vehicle was studied extensively. This investigation was conducted because the jets tend to create an abrupt change in the flow direction of the vehicle freestream and, in general, cause separated flow and a complicated shock pattern (Reference 4.17). The resulting variation in the external pressure field is then reflected in a variation of the forces and moments acting on the vehicle airframe. The typical flow pattern that could exist in the region of the control jet is depicted in Figure 2.2.25. It is important to note that all of the interaction studies were conducted for steady-state flight conditions with the control motor thrust output held constant. The results are applicable to the control system only when the effects of pulsed thrust and time varying aerodynamics are evaluated (Section 2.3.1.6).

Theoretical and Analytical Discussion   The interaction effects between the free stream and the control jets are caused by a combination of parameters both external and internal to the vehicle. Externally, the interaction is a function of the freestream Mach number (M_∞), the specific heat ratio (γ_∞), the static ambient pressure (P_∞), and the geometry and flight aspect of the vehicle. Internally, the interaction is a function of the control jet exit Mach number (M_j), the jet exhaust specific heat ratio (γ_j), and the control motor chamber pressure (P_c). Other external parameters, such as the type of flow (laminar or turbulent) over the missile surface, seem to have little effect. The majority of previous studies (References 4.18, 4.19, and 4.20) indicate that the interaction effect was independent of Reynold's Number. It was reasoned that a laminar boundary layer separation covers a larger area than a turbulent separation, but the pressure rise at separation is greater for a turbulent boundary layer than for a laminar boundary layer.

A consequence of the interaction effects and the accompanying normal force variation is a magnification (or demagnification) of the control moment produced by the reaction jet. This problem has been studied by H. P. Liepman and colleagues (References 4.19, 4.21, 4.22, 4.23 and 4.24), from the viewpoint of a normal force magnification factor (K_N). An equation was developed to determine this factor using two-dimensional flow based on the assumption that the exhaust gas expands isentropically to P_∞ and the jet flows along the surface of the missile immediately upon leaving the sonic nozzle exit. The equation derived by Liepman is:

BIPROPELLANT REACTION CONTROL SYSTEM SCHEMATIC
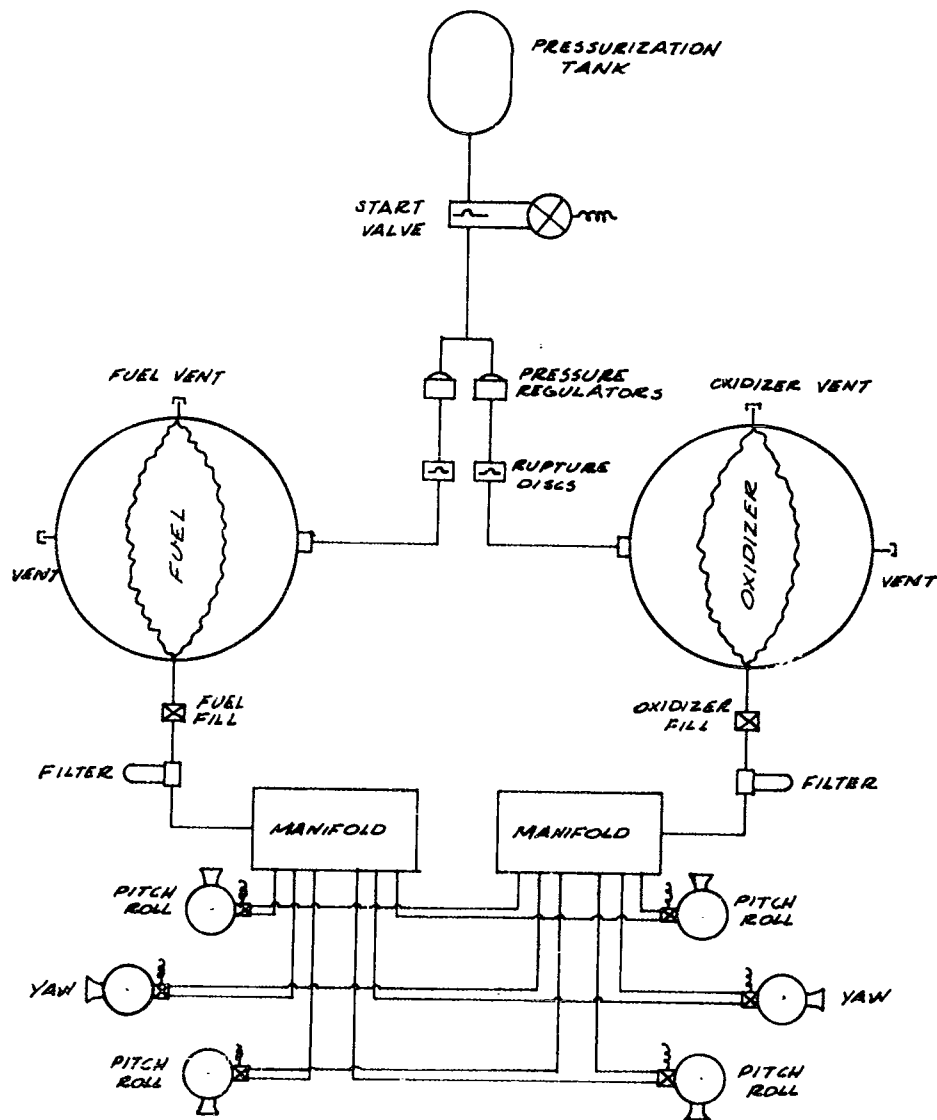
FIGURE 2.2.24

TYPICAL CONTROL JET FLOW PATTERN IN
SUPERSONIC STREAM

PRIMARY SHOCK

JET PENETRATION

JET SHOCK

JET EXIT

HIGH PRESSURE REGION

EXPANSION REGION

HIGH PRESSURE REGION

SECTION A-A

PRIMARY SHOCK

HIGH PRESSURE REGION

JET PENETRATION

$M_\infty > 1$

A

A

COMPRESSION WAVES

HIGH PRESSURE REGION

BOUNDARY LAYER SEPARATION

EXPANSION REGION

JET

FIGURE 2.2.25

2.51
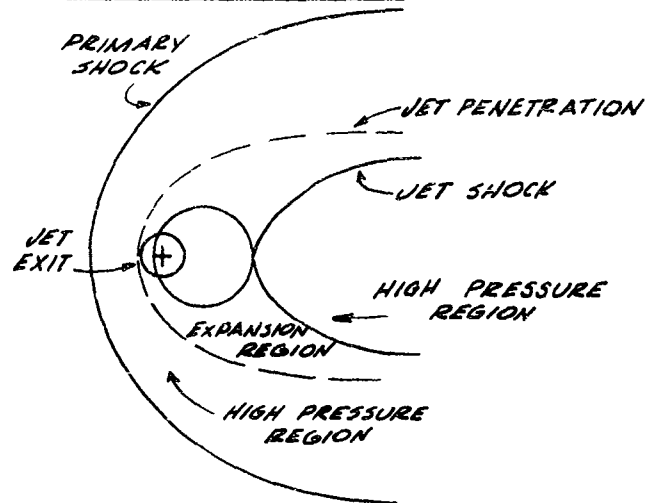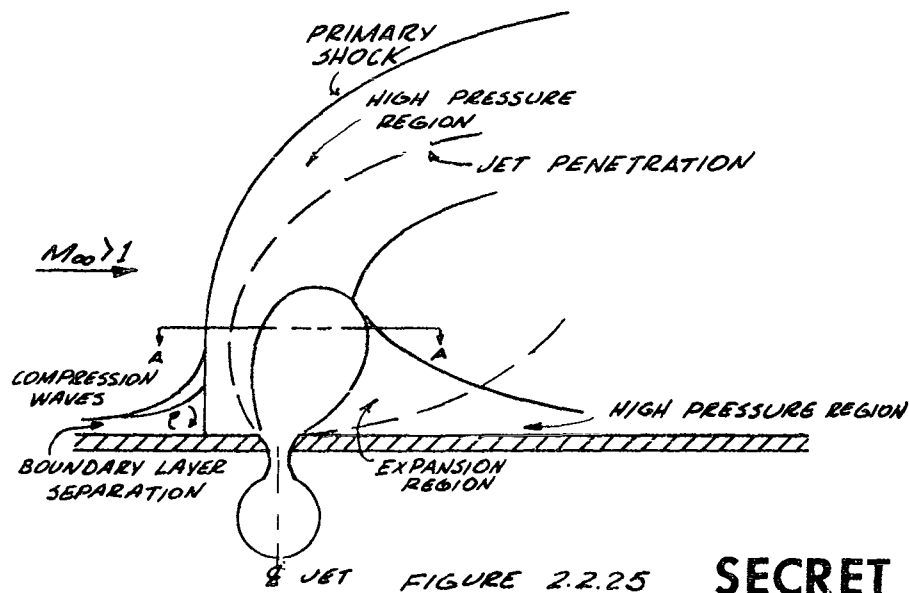
$$K_N = 1 + \frac{N_I}{N_V} \quad , \text{or} \qquad (2.2.6)$$

$$K_N = 1 + \frac{\gamma_\infty M_\infty^2}{2\sqrt{\frac{\gamma_j+1}{\gamma_j-1}\left(M_\infty^2-1\right)\left[\left(\frac{P_c}{P_\infty}\right)^{\frac{\gamma_j-1}{\gamma_j}}-1\right]}\left(\frac{P_c}{P_\infty}\right)^{\frac{\gamma_j-1}{\gamma_j}}} - 2\left(\frac{2}{\gamma_j+1}\right)^{\frac{1}{\gamma_j-1}}\left(\frac{P_c}{P_\infty}\right) \qquad (2.2.7)$$

where N_I is the interaction normal force and N_V is the normal force
in a vacuum. Using the foregoing equation, normal force magnifi-
cation as a function of pressure ratio was determined (see Figure
2.2.26). These results show that the interaction magnification factor,
as defined by the equation, decreases with increasing jet pressure
ratio. Also, it is shown that the lower limit of thrust magnifica-
tion is reached at a Mach number of $\sqrt{2}$, the minimum point of the curve

$$M_\infty^2 \Big/ \sqrt{M_\infty^2-1} \; .$$

Experimental Results   In the wind tunnel tests conducted at
AEDC, the change in aerodynamic moments caused by the reaction jets
was investigated by use of a pressure model of the vehicle. This
model was a 1/3 scale PYE WACKET FTV vehicle with 86 pressure taps
distributed over the airframe surface. By machine integration of the
data obtained during the tests, normal force coefficients (C_N), pitching
moment coefficients (C_m), and rolling moment coefficients (C_l), for
various simulated flight conditions, were determined. The freestream
(air) specific heat ratio, the reaction jet (air) exit Mach number
and specific heat ratio were held constant for the various runs made
to investigate the effect on magnification factor of angle of attack,
angle of sideslip, freestream Mach number, reaction jet chamber pres-
sure, and freestream static pressure.

The correlation of the wind-tunnel test-results with actual ve-
hicle control characteristics was based upon the previous theoreti-
cal studies and the experimental work on the jets. The normal force
magnification factor (K_n) for this correlation was defined as the
ratio of the actual normal force on the vehicle (due to the reaction
jets) to the theoretical force of the reaction jets. In order to

NORMAL FORCE MAGNIFICATION FACTOR VS PRESSURE RATIO
(THEORETICAL)

CONDITIONS:
1. SONIC JET
2. $\gamma_\infty = 1.4$
3. $\gamma_j = 1.2$
4. STATIC FLIGHT CONDITIONS
5. CONSTANT CONTROL THRUST

$\frac{M_\infty}{P_c}$
2.0

$\frac{1.6}{1.2}$

SYMBOLS:
M_∞ = FREE STREAM MACH NO.
P_c = CHAMBER PRESSURE
P_∞ = FREE STREAM STATIC PRESS.
γ_j = JET SP. HEAT RATIO
γ_∞ = FREE STREAM SP. HT. RATIO

PRESSURE RATIO - P_c/P_∞
FIGURE 2.2.26

MAGNIFICATION FACTOR - K_N
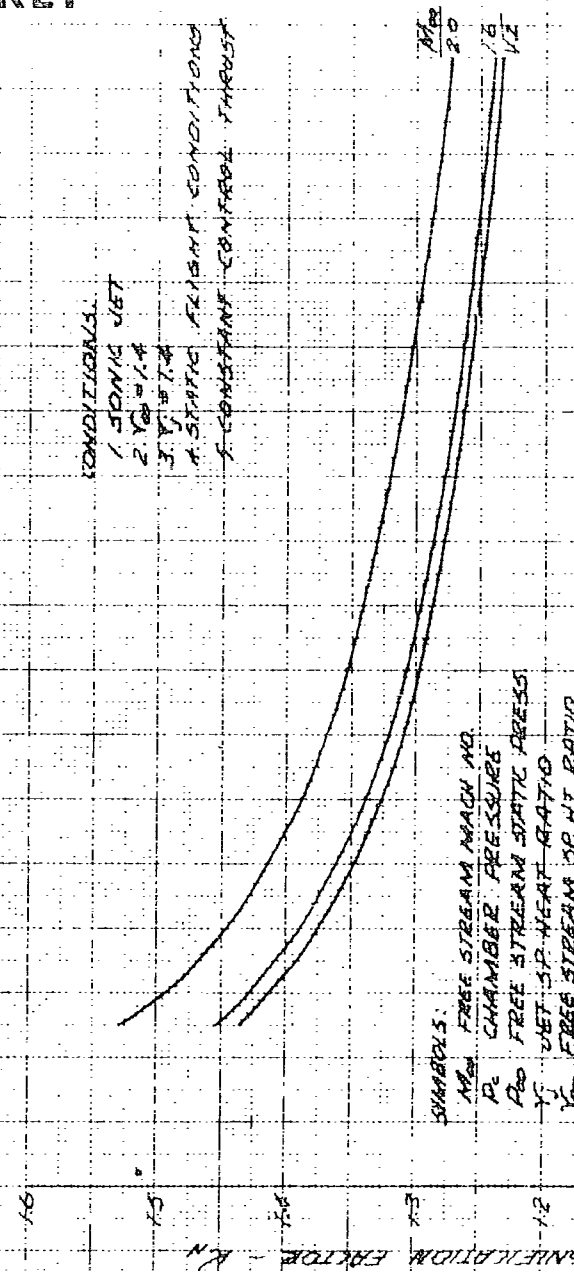
obtain values of K_n however, it was necessary to perform the following operations:

(a) calculate the thrust (N_v) of the reaction jet based on nozzle calibration tests, test procedures, and temperature readings,

(b) determine the interaction force (N_I) from the wind tunnel tests using the difference in aerodynamic normal force coefficient between jet-on and jet-off (ΔC_n),

$$N_I = \Delta C_n \, q \, S \qquad (2.2.8)$$

where

q = the dynamic pressure psf, and

S = the model planform area, sq ft,

(c) determine the actual normal force by adding the calculated thrust (N_v) to the interaction force (N_I), and

(d) determine normal force magnification factor from

$$K_N = \frac{N_V + N_I}{N_V} \qquad (2.2.9)$$

Similarly, the moment magnification factor (K_m) was defined as the ratio of the actual moment on the vehicle (due to the reaction jets) to the theoretical moment caused by the reaction jets. The interaction moment was calculated from

$$M_I = \Delta C_m \, q \, S d \qquad (2.2.10)$$

where ΔC_m is the aerodynamic moment coefficient between jet-off and jet-on conditions as determined from the wind tunnel results, and d is the moment arm between the jet exit and the vehicle center of gravity. The actual moment was determined from the calibration force data and the measured moment arm. The moment magnification factor was then expressed as follows:

$$K_M = \frac{M_V + M_I}{M_V} \qquad (2.2.11)$$

Effect of Chamber Pressure on Magnification Factor The effect of chamber pressure on magnification factor (see Figure 2.2.27) was studied during the wind tunnel tests over a pressure range of 500 to 1300 psia. In order to ascertain this chamber pressure effect, the free stream Mach number was held constant at 1.2, the free stream static pressure was constant at 3.7 psia, and the model was maintained at zero angle of attack ($\alpha = 0$) and zero sideslip angle ($\beta = 0$). The data indicate the same trend as was established in the theoretical investigation, although the actual values are different. This difference is a result of model geometry, since Liepman utilized an ogive-cylinder with the jet orifice located very close to the base; whereas the PYE WACKET model is much flatter and has considerably more projected area forward of the orifice (where the greatest increase in pressure takes place). Also, Liepman's jet was choked, whereas the PYE WACKET model has supersonic jets.

Effect of Sideslip Angle on Magnification Factor In the majority of the wind tunnel runs, the chamber pressure was held constant at 900 psia while the free stream Mach number, vehicle angle of attack, and vehicle angle of sideslip were varied. In Figures 2.2.28, 2.2.29, and 2.2.30, the magnification factors that develop from the interaction effects are plotted as functions of the free stream Mach number. Runs at 900 psia chamber pressure were made for simulated forward ($\beta = 0°$), aft ($\beta = 180°$), and side ($\beta = 90°$) launched vehicles. The data are presented for vehicle center-of-gravity locations at 43% and 50% chord (wind tunnel data were recorded on a model with a 50% chord center-of-gravity location).

Figures 2.2.28, 2.2.29, and 2.2.30 all show a demagnification in the low Mach number fixed flight regime, with a positive slope occurring at approximately Mach 0.5. In the forward launch case (Figure 2.2.28), for a launch Mach number of 0.8 or greater, the interaction effect is
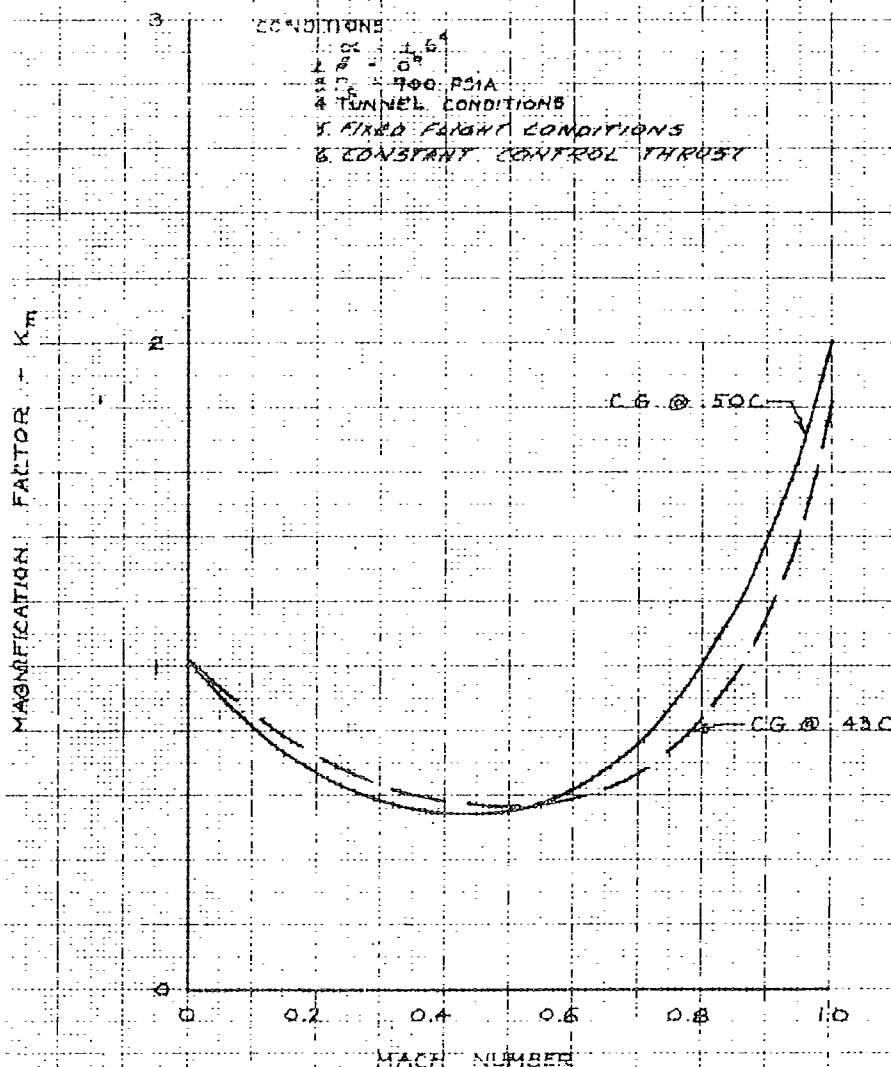
MAGNIFICATION FACTOR VS. CHAMBER PRESSURE
(EXPERIMENTAL)

CONDITIONS:-
$M_{des} = 1.2$
$\alpha_L = 0°$
$\beta = 0°$
$q_1 = 5400 \ psf$
$q_{des} = 3.72 \ psia$
$N_y = 2 \ c.G.$

STATIC FLIGHT CONDITIONS
(CONSTANT CONTROL THRUST)

K_{α} (measured)

K_{α} (measured)

K_{m} (measured)

CHAMBER PRESSURE $P_c - PSIA$
STATIC FLIGHT $M = 2.2.12$

MAGNIFICATION FACTOR K_{α}/K_{m}

MAGNIFICATION FACTOR VS MACH NUMBER

$$\beta = 0°$$

CONDITIONS
1. $\alpha = \pm 6°$
2. $\beta = 0°$
3. $P_c = 700$ PSIA
4. TUNNEL CONDITIONS
5. FIXED FLIGHT CONDITIONS
6. CONSTANT CONTROL THRUST

C.G. @ .50 C

C.G. @ .43 C

MAGNIFICATION FACTOR - K_m

MACH NUMBER

FIGURE 7.2.28

MAGNIFICATION FACTOR VS MACH NUMBER

$\beta = 180°$

CONDITIONS:
1. $\alpha = \pm 3°$
2. $\beta = 180°$
3. $P_o = 100$ PSIA
4. TUNNEL CONDITIONS
5. POWER OFF
6. FIXED FLIGHT CONDITIONS
7. CONSTANT COMMAND THRUST

$C.G. = 43 C$

$C.G. = 50 C$

MAGNIFICATION FACTOR - K_m
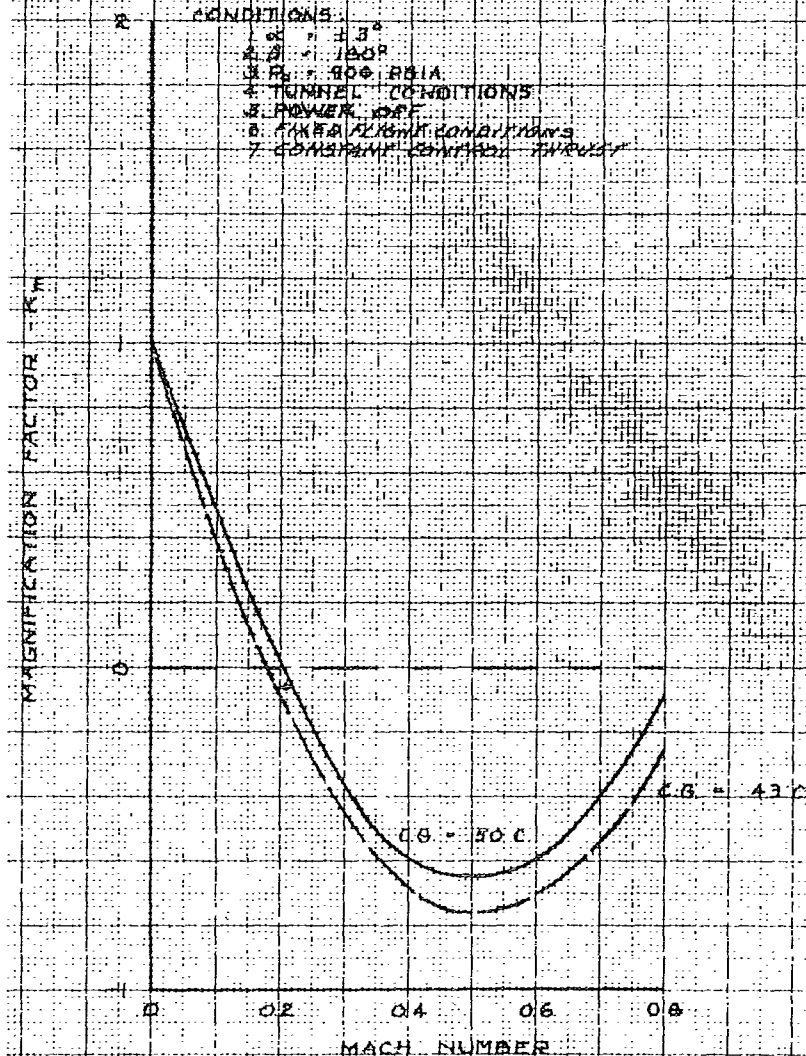
MACH NUMBER

FIGURE 2.2.29

MAGNIFICATION FACTOR
vs.
MACH NUMBER
$\beta = 90°$

CONDITIONS:
1. $\beta = 90°$
2. $\alpha = 56°$
3. $P_c = 900\ psia$
4. TUNNEL CONDITIONS
5. FIXED FLIGHT CONDITIONS
6. CONSTANT CONTROL THRUST

MAGNIFICATION FACTOR K_2

MACH NUMBER

FIGURE 2.2.30

aiding the reaction jets (a magnification factor greater than unity). In aft launch (Figure 2.2.29), an adverse situation exists in that the magnification factor is negative when the launch velocity is between Mach 0.2 and Mach 0.8 -- indicating that the reaction jet interaction force is greater than the vacuum thrust of the jet and is in fact opposite in sense. However, it is important to note that the values shown in these figures apply only to the conditions of steady-state operation with main booster motors off. This situation will not be duplicated in actuality, since the only time the vehicle will be moving in an aft direction is immediately following an aft launch. In addition, the control system is pulse-modulated so that steady-state effects normally will not be realized.

Figure 2.2.30 illustrates the effect of Mach number on the rolling moment magnification factor (K_l) for a side-launch vehicle. This factor was developed in the same manner as K_m except that the change in rolling moment coefficient (C_l) was used instead of C_m. Since the center of gravity is located at the mid-span of the vehicle, only one curve is shown.

<u>Effect of Freestream Static Pressure Magnification Factor</u> The effect of freestream static pressure on the rolling moment magnification factor is indicated by Figure 2.2.31. The exponential shape of the curve confirms theoretical reasoning. The magnification factor is a function of $P_\infty^{\frac{\gamma-1}{\gamma}}$ and must be unity at zero ambient pressure since the absence of air precludes flow and, hence, interaction.

<u>Pitch-Roll Cross Coupling</u> At a flight attitude wherein the angle of yaw or sideslip is other than zero or 180°, the external aerodynamic flow field is asymmetric with respect to the vehicle longitudinal axis. Due to possible differences in the flow fields around the reaction jets, the flow interaction existing at one jet is not necessarily equal to the interaction at the other jet. Hence, when two jets are operating for pitch control, a roll moment may be induced. This cross-coupling effect can also occur during roll correction when the difference in interaction existing about opposite jets can cause an induced pitching moment. In addition, angle of attack can be a contributing factor in both roll-inducing and pitch-inducing moments.

From the wind tunnel results, the severity of cross-coupling was determined as a function of an induced roll coefficient, λ_l where λ_l is defined as:

$$\lambda_l \triangleq \frac{\text{Actual induced roll moment}}{\text{Theoretical pitch moment.}} \tag{2.2.12}$$

THRUST MAGNIFICATION VS FREE STREAM STATIC PRESSURE

$\beta = 90°$
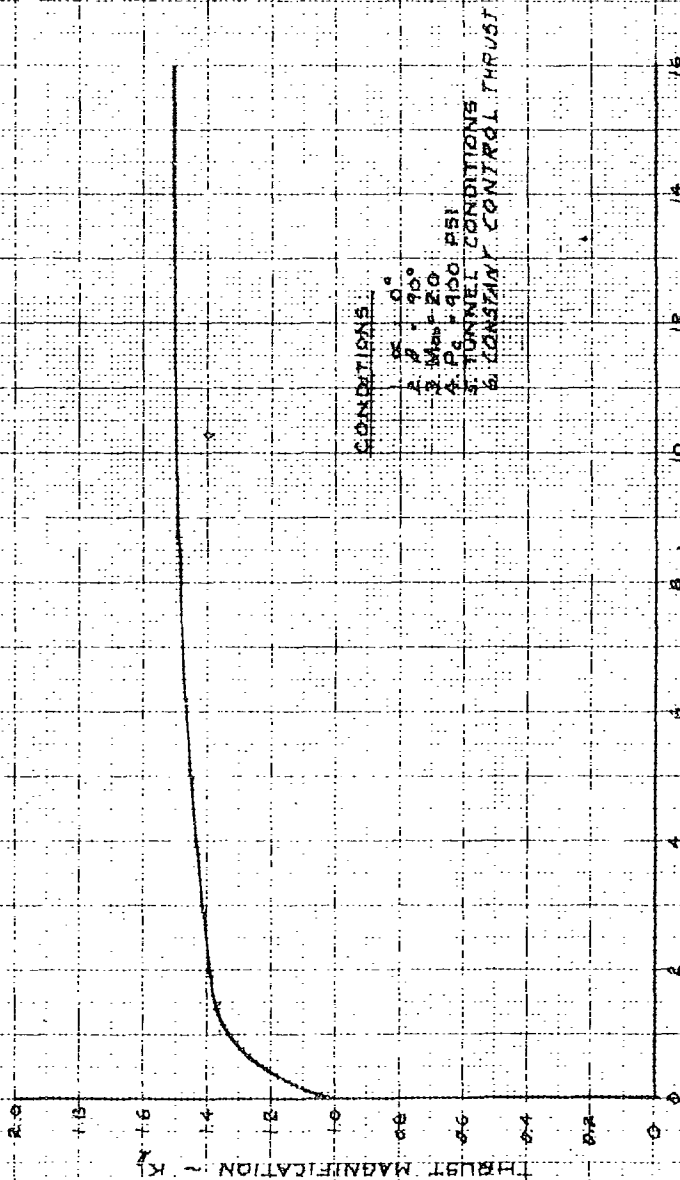
CONDITIONS
1. $\alpha = 0°$
2. $\beta = 90°$
3. $M_\infty = 2.0$
4. $P_G = 400$ PSI
5. TUNNEL CONDITIONS
6. CONSTANT CONTROL THRUST

THRUST MAGNIFICATION ~ K_1

2.0 1.8 1.6 1.4 1.2 1.0 0.8 0.6 0.4 0.2 0

FREE STREAM STATIC PRESSURE ~ P_∞ ~ PSIA

0 2 4 6 8 10 12 14 16

FREE STREAM STATIC PRESSURE ~ P_∞ ~ PSIA

FIGURE 2.2.31

For various freestream Mach numbers, the pitching moment magnification factor (K_m) was determined as a function of sideslip angle (see Figure 2.2.32). The corresponding induced roll moment coefficient resulting from the pitch correction thrust was also determined (see Figure 2.2.33).

2.2.3.2 <u>Correlation with FTV System</u> The magnification factors that were developed in the preceding section are only applicable to the wind tunnel test conditions. In order to expand their range of applicability, difference factors must be applied before equating the results to actual fixed flight conditions. These factors convert to the use of: 1) hot exhaust gas instead of cold air as the reaction jet medium, 2) an estimated nominal chamber pressure of 500 psia as opposed to the 900 psia used in the model, and 3) an ambient pressure of 13.66 psia (2000 ft altitude at the test range) instead of the various ambient pressures used in the tunnel. These differences must be applied utilizing the wind tunnel magnification factor data in the design of the FTV control system.

<u>Hot Exhaust Gas Correction</u> It is theorized that the interaction effect of the reaction jet on an external aerodynamic field can be simulated by duplicating the external plume of the jet. The most significant parameter in developing this plume is the initial jet mixing boundary angle (δ), with a secondary effect arising from the variation in jet momentum due to variations in the reaction jet chamber pressure.

The initial jet mixing boundary angle is a function of the ratio of specific heats (γ) of the jet gas, the ratio of reaction jet chamber pressure to the ambient pressure (P_c/P_∞), and the jet exit Mach number. Based on the work reported in References 4.22, 4.25, and 4.26, however, a difference in the ratio of specific heats can be corrected by the proper selection of an equivalent pressure ratio (assuming the nozzle configuration remains the same). Using the results of Love (Reference 4.25), the pressure ratios, in conjunction with a γ of 1.2, required to simulate the same external effects as a gas with a γ of 1.4 are reported in Figure 2.2.34. This figure provides a means to transfer the reaction jet air of the wind tunnel model to the reaction jet characteristics of the FTV. The data were formulated by utilizing plots of δ versus the jet stagnation pressure ratio for various γ's as reported by Love, although he generally assumed an ideal fluid jet boundary and used the characteristic theory in his calculations. A less rigorous, more approximate method for determining the mixing boundary (developed by Adamson and Nicholls, Reference 4.27) was compared to the characteristic solutions of Love. However, since this method was mainly applicable to low nozzle pressure ratios, and was based upon the change in Prandtl-Meyer angle from the nozzle lip to atmospheric, the comparison indicated that the Adamson-Nicholls method was adequate only when the angle between the jet boundary and

MAGNIFICATION FACTOR VS SIDE SLIP ANGLE

CONDITIONS:
1. $\alpha = 2°$
2. C.G. = .50 C
3. P.S. = 400 PSI
4. TUNNEL CONDITIONS
5. FIXED FLIGHT CONDITIONS
6. CONSTANT CONTROL THRUST

FREE STREAM
MACH NUMBER

1.0

.8

.6

MAGNIFICATION FACTOR ~ K_m

SIDE SLIP ANGLE ~ β ~ DEGREES
FIGURE 22.82

ROLL COEFFICIENT VS SIDE SLIP ANGLE
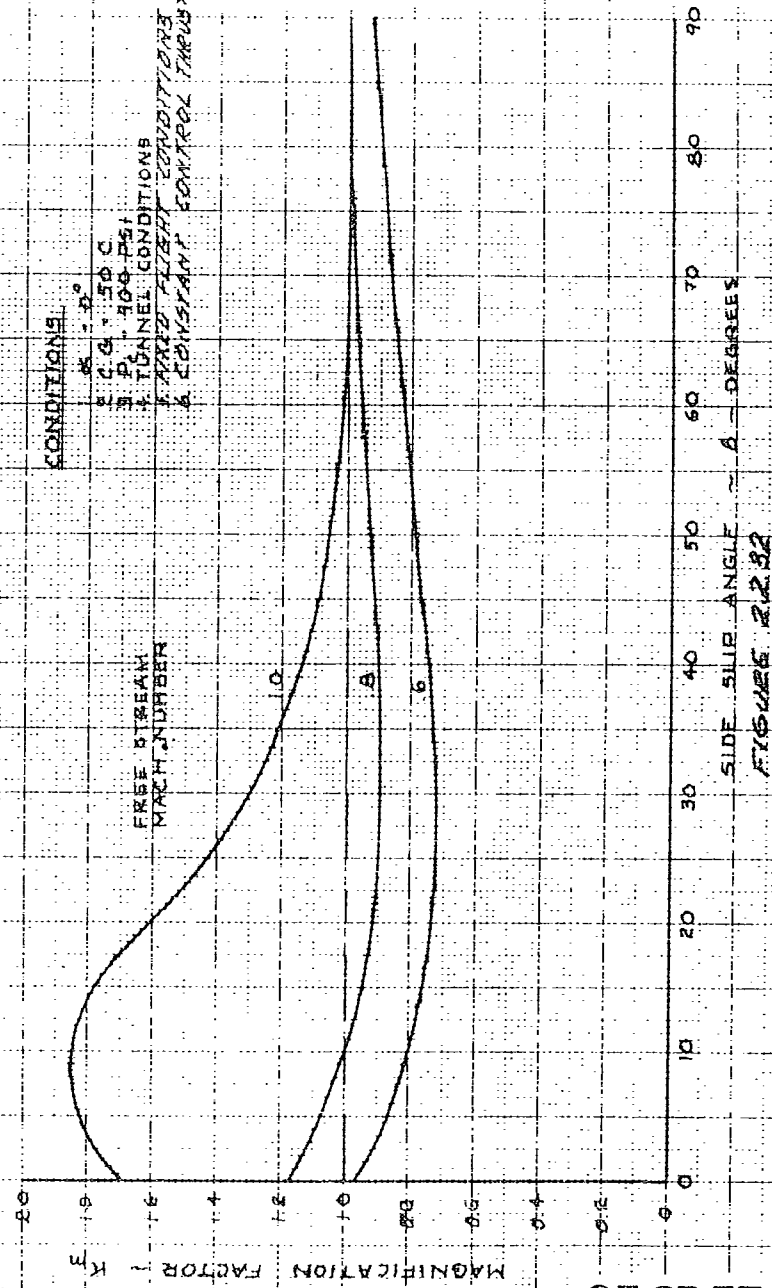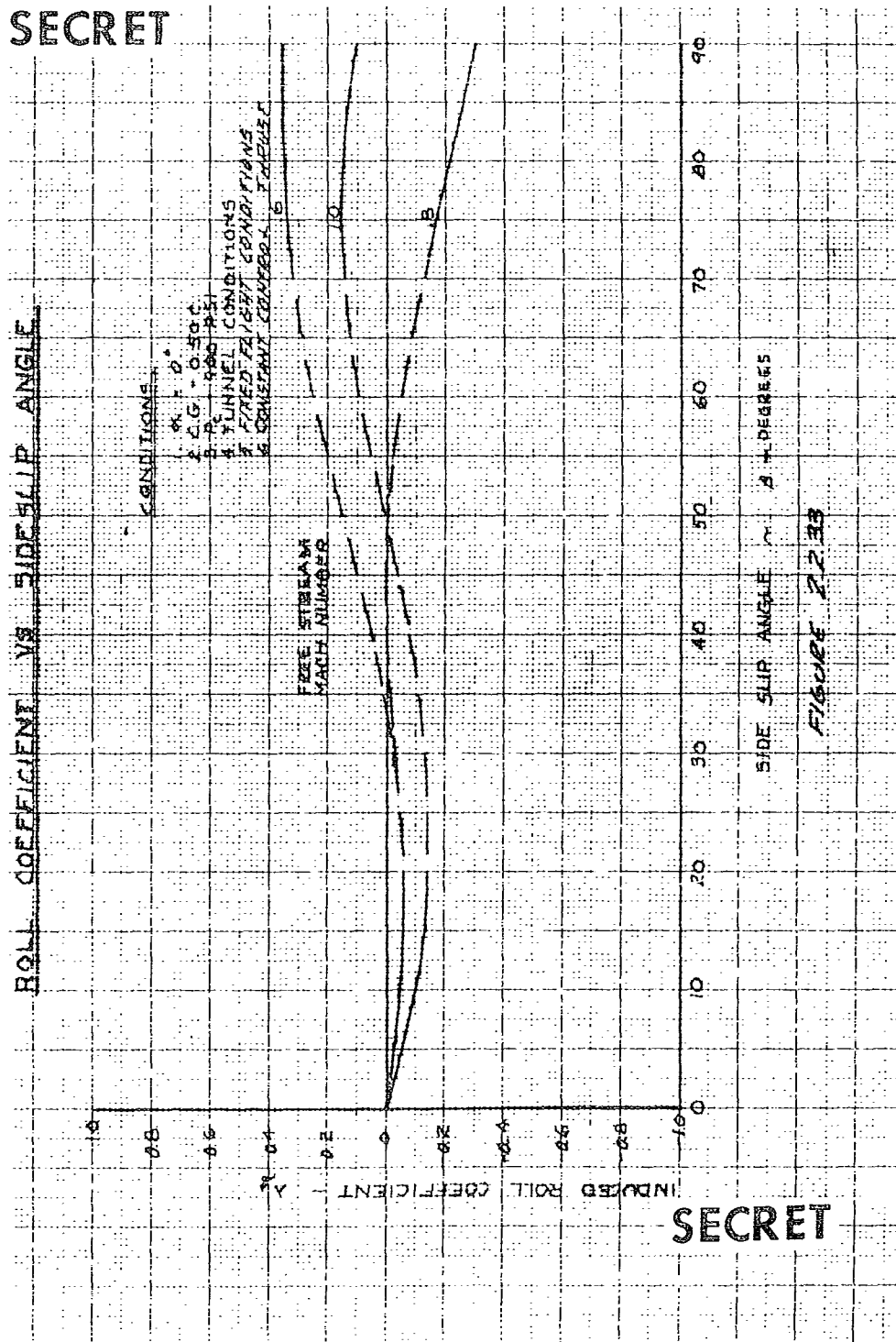
FIGURE 22.33

PRESSURE RATIO CONVERSION

M RANGE 2.0 - 3.0

FIGURE 2.2.34

2.65
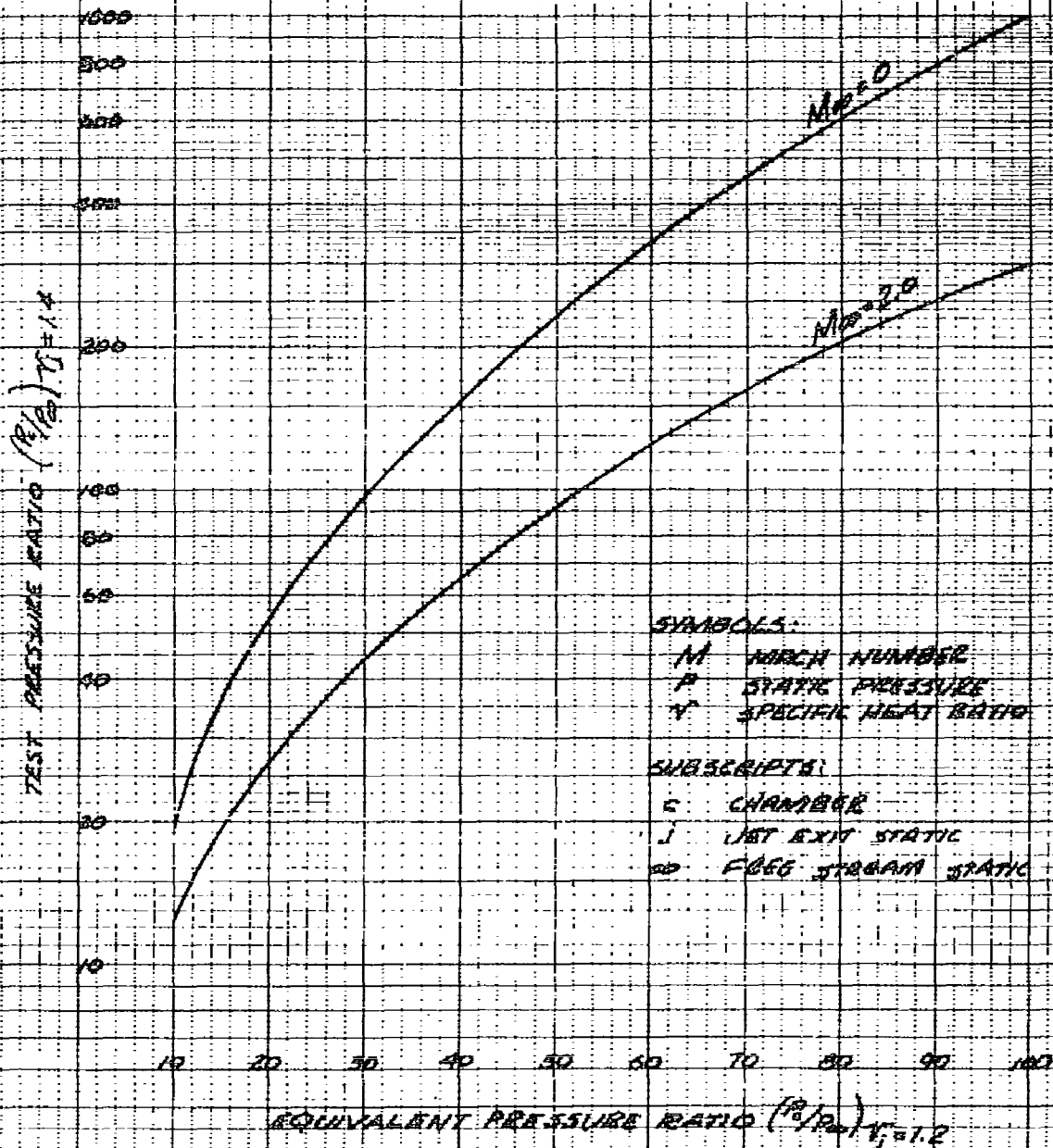
the nozzle was small. On the other hand, the comparison of the methods did show that the simulated pressure ratios must vary considerably before an appreciable change in δ occurs. The curves of Figure 2.2.34 adequately represent the jet pressure ratio equivalency between the wind tunnel conditions and the FTV.

Chamber Pressure Correction   Since the anticipated chamber pressure of the FTV reaction jets will be approximately 500 psia, all force and moment magnification factors determined from wind tunnel data must be corrected. Using the wind tunnel test results of Figure 2.2.27, the ratio of the magnification factor at 500 psia chamber pressure to the magnification factor at any given chamber pressure was determined as a function of chamber pressure and reported in Figure 2.2.35.

Ambient Pressure Correction   Assuming that the FTV sled tests are to be conducted at an altitude of 2000 feet (13.66 psia), a multiplication correction factor for ambient pressure (Figure 2.2.36) was determined from the information given in Figure 2.2.31.

Vacuum-to-Flight Conditions Correction   The magnification factors were originally based on reaction jet thrust under vacuum conditions in order to compare experimental results with theoretical values and to keep the factors in their most general form. Since the flight of the FTV will not be under vacuum conditions, it is necessary to correct the magnification factors by converting vacuum thrust to actual thrust.

Since thrust is proportional to thrust coefficient (C_f) when the chamber pressure and nozzle throat area are constant, the magnification factor can be corrected by determining optimum thrust coefficients for the vacuum and flight conditions. Using an optimum expansion of the nozzle and an exhaust gas with a ratio of specific heats of 1.2, the vacuum thrust coefficient was found to be 1.66 and the optimum flight thrust coefficient was 1.51 (chamber pressure of 500 psia and nozzle exit pressure 13.66 psia). The corrected thrust magnification factor was then determined from the following equation:

$$ K_f = 1 + \frac{1.66}{1.51}(K-1) \qquad (2.2.13) $$

where the magnification factors K_f and K correspond to true flight conditions and vacuum conditions, respectively. The correction factor is shown in Figure 2.2.37 over a range of vacuum conditions.

MAGNIFICATION FACTOR RATIO VS. CHAMBER PRESSURE

MAGNIFICATION FACTOR RATIO = $\dfrac{K @ 500 \text{ PSIA}}{K @ P_c}$
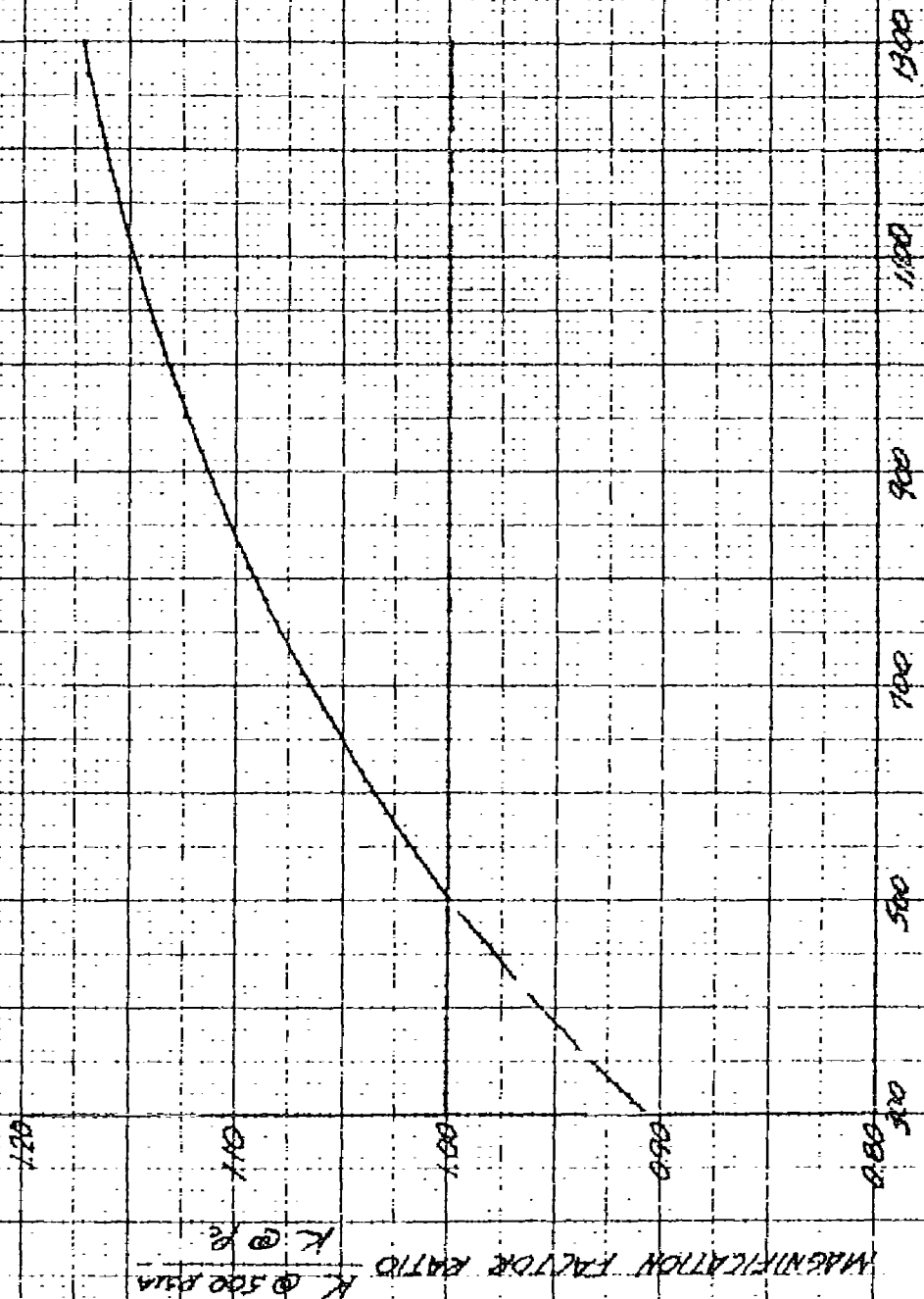
CHAMBER PRESSURE, P_c PSIA

FIGURE 2.2.35

MAGNIFICATION FACTOR RATIO

vs. Free Stream Static Pressure

MAGNIFICATION FACTOR RATIO $\dfrac{k_{\varnothing}/1.44\ psia}{k_{\varnothing}/P_{\varnothing}}$

FREE STREAM STATIC PRESSURE $P_{\varnothing\varnothing}$ PSIA

FIGURE 12.2.2.4
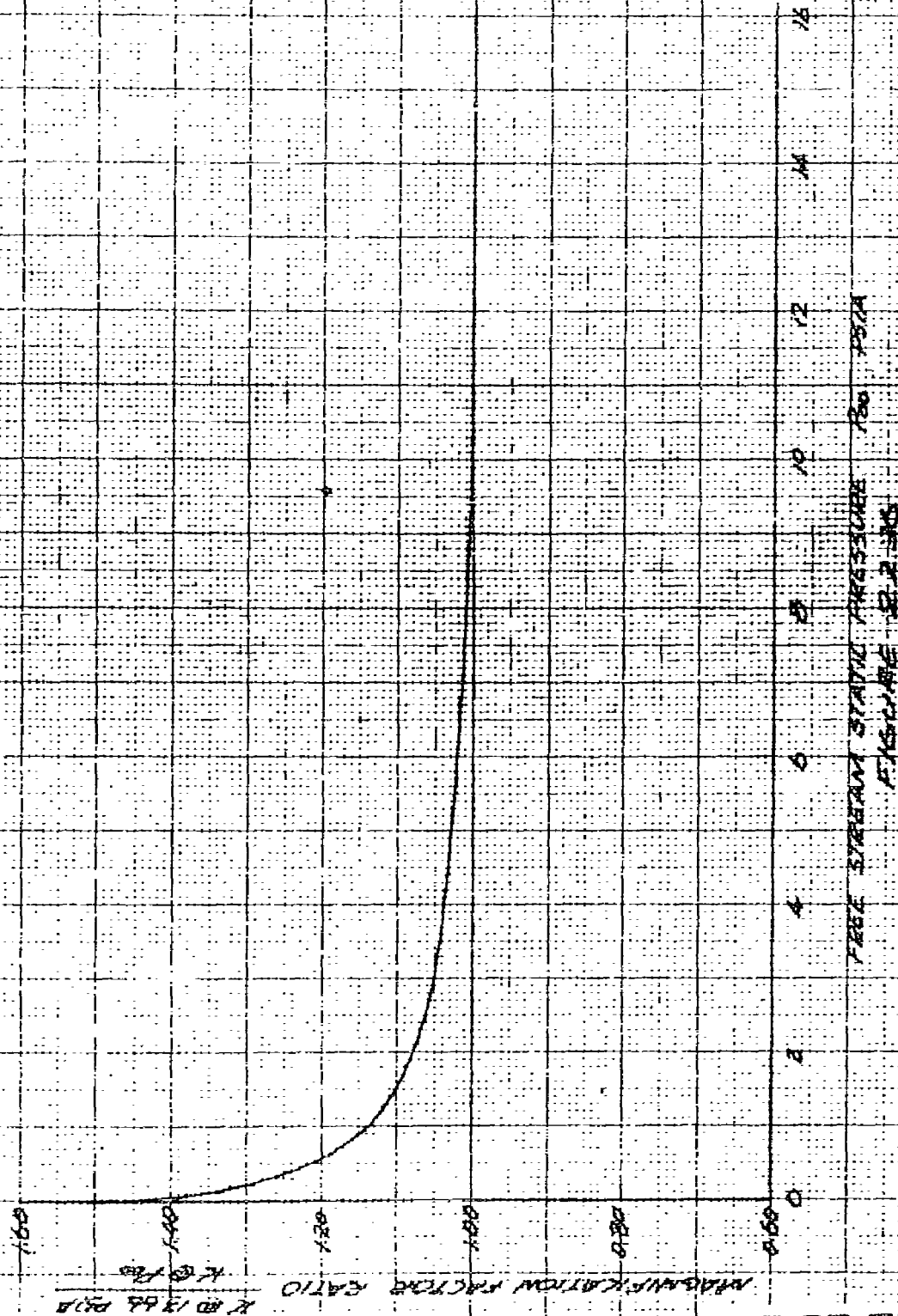
MAGNIFICATION FACTOR CORRECTION

VACUUM TO FLIGHT
CONDITIONS

RANGE: -1.0 - 0

-1.0 -0.9 -0.8 -0.7 -0.6 -0.5 -0.4 -0.3 -0.2 -0.1 0

MAGNIFICATION FACTOR BASED ON FLIGHT CONDITIONS

K_f

FLIGHT CONDITIONS:
$\gamma = 1.2$
$P_c = 500$ PSIA
$P_{ao} = 13.64$ PSIA @ 2000 FT ALT

FIGURE 2.2.37a

MAGNIFICATION FACTOR CORRECTION

VACUUM TO FLIGHT
CONDITIONS

RANGE: 0 - 1.0

FLIGHT CONDITIONS:
γ = 1.2
P_c = 300 PSIA
P_∞ = 13.66 PSIA @ 2000 FT ALT

MAGNIFICATION FACTOR BASED ON VACUUM CONDITIONS
K
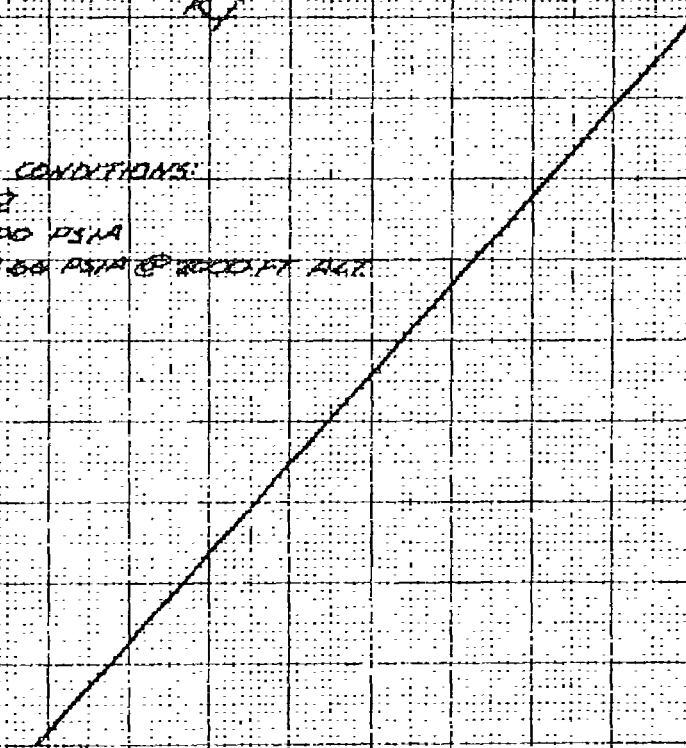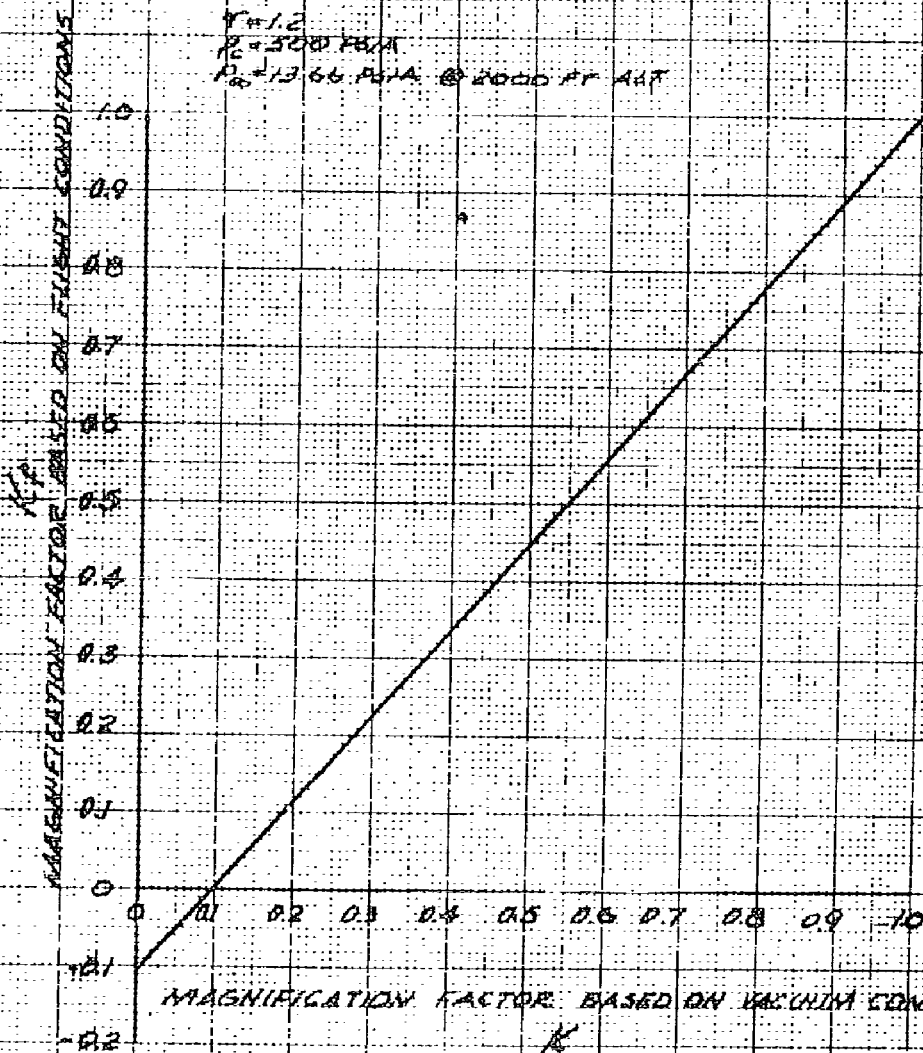
FIGURE 2.2.37b

SECRET

MAGNIFICATION FACTOR CORRECTION

Vacuum to Flight Conditions

Range 1.0-2.0

FLIGHT CONDITIONS:
γ = 1.2
P_c = 500 PSIA
P_a = 1.366 PSIA @ 2000 FT. ALT

FIGURE 2.2.37a

SECRET

Transient Aerodynamic and Booster Exhaust Effects As mentioned previously, the wind tunnel magnification factors must also be compensated for transient aerodynamic effects and the enveloping nature of the propulsion system exhaust during aft launch of the prototype vehicle. Transient aerodynamic effects occur during all launch conditions and tend to lessen the reaction jet interaction when the pulse-width of the reaction thrust on-time decreases. The envelopment of the vehicle in the main propulsion exhaust is important during aft launch since it tends to decrease the effective boundary layer Mach number in the vicinity of the reaction controls, thus appreciably reducing the interaction effect. Both of these situations are examined parametrically in Section 2.2.3.3.

Correction Summation The application of the correction factors discussed in the preceding paragraphs yields the magnification factors for FTV flight conditions (Figures 2.2.38, 2.2.39, and 2.2.40). A comparison of these results with the wind tunnel factors (Figures 2.2.28, 2.2.29, 2.2.30) indicates that the adverse effect of the negative magnification factor is generally intensified by the corrections. The trend in the corrections is also consistent since magnifications (factors greater than unity) are increased by the corrections, while demagnifications (factors less than unity) are decreased.

2.2.3.3 Aft Launch Performance Study The most important unknowns encountered during the control study were the effect of transient aerodynamics and the effect of propulsion exhaust on aft launch vehicle performance. In order to clarify this situation to some extent, a brief study was made to analytically account for these effects.

Transient Aerodynamics The transient aerodynamic field on the vehicle was assumed to occur according to the following equation:

$$\frac{C - C_1}{C_2 - C_1} = 1 - e^{-t/\tau} \qquad (2.2.14)$$

where C is the aerodynamic coefficient (i.e., C_m, C_ℓ, or C_n),

τ is the time constant, seconds,
subscript 1 is the original steady state value, and
subscript 2 is the final steady state value.

An example of the use of the above equation shows the aerodynamic pitching moment coefficient varying as:

$$C_m = C_{m1} + \left(C_{m2} - C_{m1}\right)\left[1 - e^{-t/\tau}\right] \qquad (2.2.15)$$

MAGNIFICATION FACTOR
vs
MACH NUMBER

$\beta = 0°$

CONDITIONS:
1. $\beta = 0°$
2. $\alpha = \pm 6°$
3. $R = 500$ psia
4. FIXED CONDITIONS
5. FIXED FLIGHT CONDITIONS
6. CONSTANT CONTROL THRUST

MAGNIFICATION FACTOR

MACH NUMBER

FIGURE 22.28

MAGNIFICATION FACTOR
vs
MACH NUMBER
β = 180°

Conditions:
1. β = 180°
2. α = 6°
3. h = 100,000
4. RTV CONDITIONS
5. POWER OFF
6. FIXED FLIGHT CONDITIONS
7. CONSTANT CONTROL TORQUE
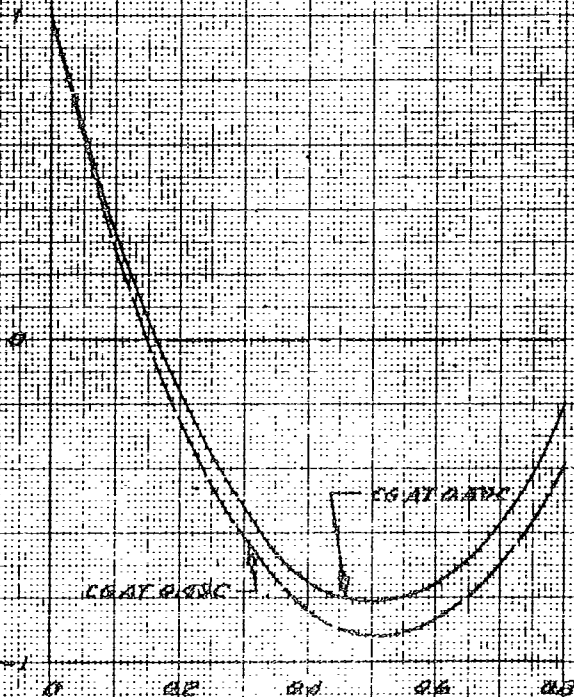
MAGNIFICATION FACTOR — K.F.

CG AT 0.69C

CG AT 0.60C

MACH NUMBER

FIGURE 3.2.39

MAGNIFICATION FACTOR
vs
MACH NUMBER
$\beta = 90°$

CONDITIONS:
1. $\alpha = 90°$
2. $\alpha = \pm 2°$
3. $p = 700$ mm
4. STP CONDITIONS
5. FIXED FLIGHT CONDITIONS
6. CONSTANT CONTROL THRUST

MAGNIFICATION FACTOR ~ M

MACH NUMBER
FIGURE 22.40

The aerodynamic interaction moment then varies as:

$$M_I \equiv \left(C_m - C_{m1}\right) \, q \, Sd, \tag{2.2.16}$$

$$M_I = \left(C_{m2} - C_{m1}\right) q \, Sd \left[1 - e^{-t/\tau}\right], \tag{2.2.17}$$

and the total moment on the vehicle as a result of the reaction jets (sum of aerodynamic interaction moment (M_I) and reaction jet moment (M_V) would be represented by:

$$M = M_V + M_I, \ or \tag{2.2.18}$$

$$M = M_V + C_m \, q \, Sd \left[1 - e^{-t/\tau}\right]. \tag{2.2.19}$$

The moment magnification factor (K_m) for steady state conditions, discussed in previous sections, was:

$$K_m = \frac{M_V + M_I}{M_V} \tag{2.2.20}$$

which can also be written as follows:

$$K_m = 1 + \frac{\Delta C_m q S d}{M_V} \tag{2.2.21}$$

Under transient condition, the moment magnification factor can be expressed as:

$$K_m(t) = \frac{M_V + M_I}{M_V}, \text{ or} \tag{2.2.22}$$

$$K_m(t) = 1 + \frac{\Delta C_m q S d}{M_V} \left[1 - e^{-t/\tau} \right] \tag{2.2.23}$$

where $K_m(t)$ is the moment magnification factor as a function of time. Substituting Equation (2.2.21) into Equation (2.2.23) yields:

$$K_m(t) = 1 + \left(K_m - 1 \right) \left[1 - e^{-t/\tau} \right] \tag{2.2.24}$$

and integrating between zero and T (the duration of the thrust pulse from the control jet), the mean moment magnification factor ($\bar{K}_m$) is:

$$\bar{K}_m = 1 + \left(K_m - 1 \right) \left[1 + \frac{\tau}{T} \left(e^{-T/\tau} - 1 \right) \right], \tag{2.2.25}$$

where K_m is defined by the equation:

$$\bar{K}_m = \frac{1}{T} \int_0^T K_m(t) \, dt . \tag{2.2.26}$$

2.77

Using various control thrust pulse durations in the above equation, the modified moment magnification factor was then determined as a function of Mach number (see Figure 2.2.41).

Propulsion Exhaust During aft launch of the vehicle, the propulsion system exhaust gas will surround the vehicle and temporarily create an artificial environment for the reaction jets. The superposition of this exhaust flow field in the area of the reaction jets will then tend to reduce the effective free-stream velocity near the surface of the vehicle. If the ratio of the effective boundary layer Mach number under the two conditions (power off- - -no exhaust gas/power on- - -exhaust gas) is defined by the sumbol   , a means is established to effectively correct the moment magnification factor and thereby take into account propulsion exhaust effects on vehicle aft launch. Based on the conservation of momentum, values of   are always greater than unity; values from 1.0 to 4.0 were therefore investigated. Modification of the magnification factor was accomplished by correcting the factors obtained at wind tunnel Mach numbers. That is, if   = 2.0, the factor obtained at a wind tunnel Mach number of, for example, 0.2 would correspond to a flight condition Mach number of 0.4. On this basis, values of moment magnification, for various values of   , were determined as shown in Figure 2.2.42.

It must be emphasized that the foregoing study on transient aerodynamic and propulsion exhaust effects is an analytical effort and should be supported by future experimental work. However, the analysis does show that results obtained from the power-off wind tunnel tests are extremely conservative for aft launch of the vehicle.

2.3 AUTOPILOT SYNTHESIS

The development studies conducted on the autopilot are a continuation of the work performed during the initial feasibility studies (Reference 4.1). The analysis performed during the preceding contract dealt with the generalized concept; e.g., in the controls section, reaction jets were recommended in place of aerodynamic surfaces to best exploit the full potential of the circular planform, blunted lenticular shape. The study efforts conducted for the present program utilized detailed representations of the body aerodynamic characteristics, thrust-producing hardware, and the proposed autopilot electronics.

The principal objective of these studies is the development of an autopilot design which will provide stabilization and control of the PYE WACKET vehicle. The most stringent environment for the FTV is that which results from an omnidirectional launch from a high speed rocket sled at or near sea level. The design endeavors to use sensing instruments and electronics which require little or no development work, i.e., components fully developed and readily available.

2.78

MAGNIFICATION FACTOR vs MACH NUMBER

FOR VARIOUS PULSE DURATIONS

$\beta = 180°$

CONDITIONS:
1. $\beta = 180°$
2. $\alpha = 76°$
3. $P_0 = 300$ PSIA
4. FTV CONDITIONS
5. POWER OFF
6. C.G. AT 0.43C

PULSE DURATION

T

10 ms

20 ms

30 ms

40 ms

50 ms

∞

MAGNIFICATION FACTOR = $\frac{T_m}{T_g}$

2

0

1

0   0.2   0.4   0.6   0.8

MACH NUMBER

FIGURE 3.2.4!

MAGNIFICATION FACTOR VS MACH NUMBER
FOR VARIOUS EFFECTIVE BOUNDARY
LAYER MACH NUMBER RATIOS

$\beta = 180°$

CONDITIONS:
1. $\beta = 180°$
2. $\alpha = 16°$
3. $P_c = 500$ PSIA
4. DRY CONDITIONS
5. $C\Delta$ AT $0.43C$

FIGURE 2.2.42
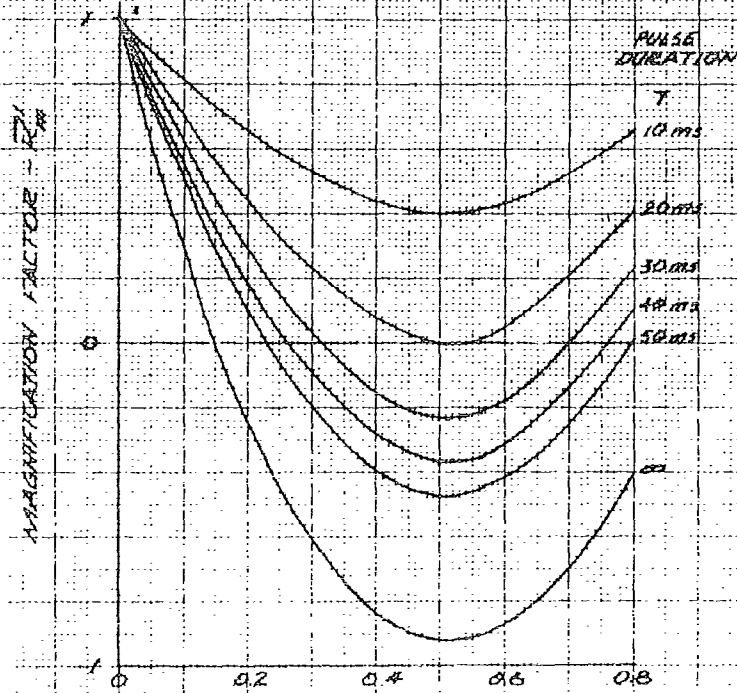
Boundary conditions are determined for the initial conditions resulting from forward and crosswind launches from a moving platform. These limits are reasonably broad to permit some latitude for the unknowns within the environment. It is anticipated that a more accurate determination will be made in Phase III.

Although the four control-motor arrangements discussed in the Phase I report will produce control moments about all three axes, the Feasibility Test Vehicle will utilize a six-motor configuration, four to produce pitch and roll control and two to produce yaw control. The time and cost limitation of the Phase II program imposed several restrictions on the studies required to effectively integrate the control signals from three planes into four common reaction jets. Since the development work is simplified by separating the control for one plane from the remaining two and since the employment of two additional jets does not affect the overall purpose of the Feasibility Test Vehicle, the design incorporates a separate autopilot and controls section for the yaw plane.

The main motivation for studying a nonlinear control system was provided by the necessity that the FTV hardware requires a minimum of development effort. The design of a proportional valve and reaction motor appeared remote because of the variable orifice area requirement to control the fluid propellant. However a solenoid or torque-motor operated bistable valve is conceivable with response times in the order of milliseconds. If the response times are small, a nonlinear control system oscillating at a relatively high frequency and low amplitude can be achieved.

With the control philosophy established, attention was directed toward the selection of the guidance elements which are compatible with the system and its associated flight test objectives. An accelerometer reference was chosen to provide normal acceleration control in the pitch plane. The roll and yaw systems employ angular references.

The tactical missile, to be launched from an airborne platform, is envisioned to be directed by an inertial reference in a pre-computed trajectory through the boost phase. This inertial phase will be sustained (or supplemented by a command system) until target acquisition occurs for the homing guidance phase. The instrumentation in the FTV pitch system is applicable for the autopilot during the homing phase. The yaw alignment with the velocity vector also matches the guidance concept for this final phase. The roll system for either the inertial or homing phase would receive signals corresponding to an attitude control. In the tactical missile, the homing guidance electronics would provide the signal for the roll-pitch autopilot while the yaw control would depend on the aerodynamic stability of the vehicle about the yaw axis.

2.81

The development of the closed loop system for control about each of the three axes was conducted with both analytical and analog computer techniques. A linear control equation was chosen because its simplicity facilitated analysis and manipulation. The electronics which simulate this equation will shape the signals being fed to the nonlinear control hardware. Although linear equations are not optimum, they do provide adequate response for the FTV. Further studies in this area would be conducted during the initial phases of a prototype development program.

The initial autopilot studies were conducted on the individual systems (pitch, roll and yaw) using preliminary aerodynamics and fixed flight conditions. During this phase, the parameters were established for each system, to satisfy these conditions. The roll and pitch systems were then electronically integrated thus ensuring that both systems could operate effectively through common reaction jets.

A three dimensional analog simulation was the final step in verifying the control system computations. The aerodynamics from the wind tunnel tests conducted within this contract, were simulated continuously as a function of the magnitude and direction of the velocity vector. The final autopilot parameters were established, which in turn specified the launch and flight boundary conditions. Following this process the single plane systems were then re-examined with both analytical and computer techniques to validate the conclusions established with the three-dimensional simulation.

2.3.1 PITCH AUTOPILOT SYNTHESIS   The single plane studies were conducted at several fixed flight conditions (constant missile velocity) in order to gain insight into the system stability and response. Although a single plane analysis of the pitch autopilot is applicable only during a zero sideslip condition, the complicated parametric variations of time varying three-dimensional simulation limit its use to finalizing a previously established design.

2.3.1.1 Airframe Transfer Function   The initial autopilot design may be simplified to a single plane analysis with three degrees of freedom, i.e., missile c.g. translation normal to the body in the pitch plane, missile rotation in pitch, and reaction motor thrust-produced motion in the pitch plane parallel to the x-axis of the missile.

Figure 2.3.1 defines the missile angles in this single plane analysis.

2.82
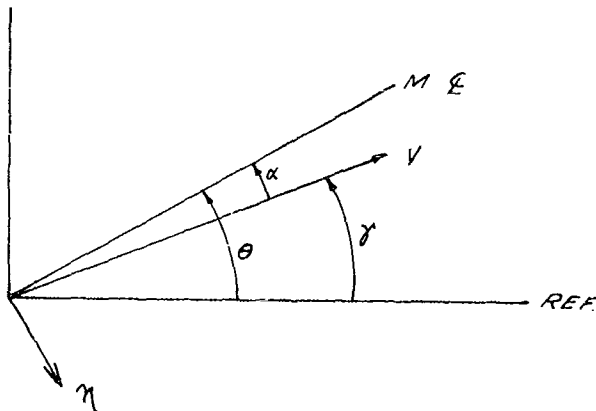
Figure 2.3.1 Missile Motion Geometry

α = angle of attack, i.e., the angle between missile planform and the velocity vector,

n = acceleration in g's perpendicular to the missile planform,

γ = angle between the velocity vector and the reference, and

θ = angle between the missile centerline and the reference.

The force and moment equations may be written as:

$$-n = A\alpha - B f_p \tag{2.3.1}$$

$$\theta = C\alpha + E f_p \tag{2.3.2}$$

For small angles of attack (α),

$$\frac{V \dot{\gamma}}{32.2} = -n \ (57.3)$$

or

$$\dot{\gamma} = -\frac{1845}{V} n \tag{2.3.3}$$

where

$$A = \frac{1481 \lambda S M^2}{W} C_{N\alpha}$$

$$B = \frac{1}{W} \ .$$

2.83

$$C = \frac{57.3 \ (1481) \ \lambda \ M^2 \ Sd}{I_p} \ C_{m\alpha}$$

$$E = \frac{57.3}{I_p} \ k_p, \ and$$

$$G = \frac{1845}{V} \ .$$

The above symbols are defined as follows:

η = acceleration, in "g's" (positive downward),

M = mach number,

V = velocity, ft per sec,

W = weight, (330 lb empty),

I_p = pitch moment of inertia, slug-ft^2 (19.8 empty),

λ = static pressure ratio,

S = reference area, 19.63 ft^2,

d = reference length, 5 ft,

k_p = pitch moment arm (1.792 ft for c.g. located at the 0.43 chord), and

f_p = control motor thrust which contributes to missile rotation in pitch.

Rearranging Equations (2.3.1), (2.3.2) and 2.3.3) yields:

$$-n \ (1 + \frac{A \ G}{S}) - \frac{A}{S} \ \dot{\theta} = -Bf_p, \qquad (2.3.4)$$

$$-n \ \frac{C}{S} \quad G\eta + (S - \frac{C}{S} \ )\dot{\theta} = Ef_p. (2.3.5)$$

That is,

$$\left(\frac{-n}{f_p}\right) = \frac{\begin{vmatrix} -B & -\frac{A}{S} \\ E & \left(S - \frac{C}{S}\right) \end{vmatrix}}{\begin{vmatrix} 1 + \frac{AG}{S} & -\frac{A}{S} \\ \frac{CG}{S} & \left(S - \frac{C}{S}\right) \end{vmatrix}} = \frac{AE + BC - Bs^2}{S^2 + AGs - C},$$

$$\qquad (2.3.6)$$

$$\frac{\dot{\theta}}{f_p} = \frac{\begin{vmatrix} 1 + \frac{AG}{S} & -B \\ \frac{CG}{S} & E \end{vmatrix}}{\left(S^2 + AGs - C\right)\, 1/s} = \frac{G(AE + BC) + Es}{S^2 + AGs - C}.$$

$$\qquad (2.3.7)$$

and,

$$-\frac{\dot{\theta}}{n} = \frac{G(AE + BC) + Es}{(AE + BC) - Bs^2} \qquad (2.3.8)$$

2.3.1.2 <u>Control Equations</u>   The pitch control equation is given by

$$\mathcal{E}_p = -(n_c - n)\, K_1 - K_2\, \dot{\theta} - K_3\, \ddot{\theta}. \qquad (2.3.9)$$

2.85

Figure 2.3.2 shows the system block diagram.
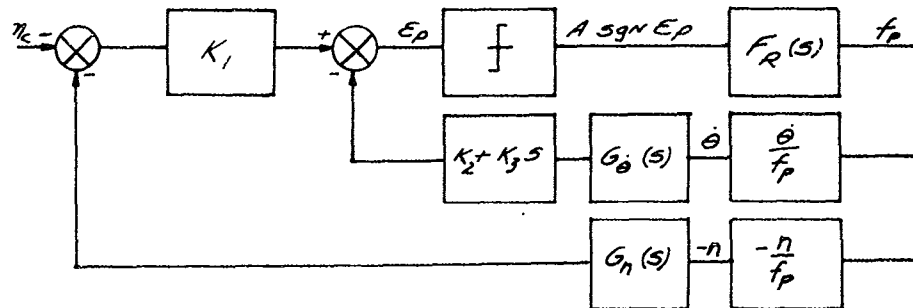
Figure 2.3.2 Pitch Autopilot Block Diagram

where

n_c is the called-for acceleration,

$G_{\dot\theta}$ (s) represents the pitch rate gyro response,

G_n (s) represents the accelerometer response,

A sgn ε_p = A $\left[\text{sign of } \varepsilon_p \right]$ = A $\dfrac{|\varepsilon_p|}{\varepsilon_p}$, and

F_R(s) = control reaction motor transfer function.

A detailed description of the reaction motor is given in Section 2.3.1.7
For simplicity, the reaction motor is approximately represented by the
mathematical expression

$$\frac{e^{-\tau_1 s}}{1 + \tau_2 s} \qquad\qquad (2.3.10)$$

where

τ_1 = 3 milliseconds and

τ_2 = 2.17 milliseconds.

2.86   **SECRET**

2.3.1.3 <u>Steady State Behavior (zero input)</u> With the system in a steady state oscillation mode, $A \, Sgn \, \epsilon_p$ (square wave) can be expanded into a Fourier series. The ratio of the first harmonic to the input is then defined as

$$N = \frac{4 \, \Gamma}{\pi}$$

where

$$\Gamma = \frac{A}{\text{input amplitude}} \, (x)$$

For the loop opened at f_p , examine the equation

$$\frac{-f_o}{f_i} = F_R(s) N \left\{ \left(\frac{-n}{f_p}\right) K_1 G_n(s) + \left(K_2 + K_3 \, s\right) G_{\dot\theta}(s) \left(\frac{\dot\phi}{f_p}\right) \right\} = -1 \qquad (2.3.11)$$

The points (x_1 , w_1), (x_2 , w_2), are defined by the intersection of

$$f(s) = F_R(s) \left[\left(\frac{-n}{f_p}\right) K_1 G_n(s) + \left(K_2 + K_3 s\right) G_{\dot\theta}(s) \left(\frac{\dot\phi}{f_p}\right) \right] \quad and \quad (2.3.12a)$$

$$f(s) = -\frac{1}{N} \qquad (2.3.12b)$$

For the loop opened at n, examine the equation

$$\frac{K_1 N F_R(s) G_n(s) \left(\frac{-n}{f_p}\right)}{1 + \left(K_2 + K_3 s\right) G_{\dot\theta}(s) \left(\frac{\dot\phi}{f_p}\right) N F_R(s)} = -1 \qquad (2.3.13)$$

where Equation (2.3.13) is essentially the same term as Equation (2.3.12). It is therefore sufficient to examine the system steady state behavior from Equation (2.3.12). Neglecting the instruments and the reaction motors, Equation (2.3.12) becomes,

2.87

$$\frac{1}{s^2 + AGs - C}\left\{K_1\left[(AE+BC)-Bs^2\right]+(K_2+K_3 s)\left[G(AE+BC)+Es\right]\right\} = -\frac{1}{N}$$

(2.3.14)

or

$$\frac{(AE+BC)(K_1+K_2 G)\left(\frac{s}{z_1}+1\right)\left(\frac{s}{z_2}+1\right)}{s^2 + AGs - C} = -\frac{1}{N}$$

(2.3.15)

where

$$z_1, z_2 = \frac{K_2 E + K_3 G(AE+BC) \pm \sqrt{\left[K_2 E + K_3 G(AE+BC)\right]^2 + 4\left[K_1 B - K_3 E\right]\left[K_1 + K_2 G\right]\left[AE+BC\right]}}{2(K_3 E - K_1 B)}$$

If z_1, and z_2 in Equation (2.3.15) are in the right half plane and are of the order of magnitude of the roots of $s^2 + AGs - C = 0$, the system steady state dither frequency is completely determined by system imperfections. It should be noted that in most cases $C^{-1/2} \gg$ instrument periods or reaction motor time constants and therefore the effect of a variation in C is negligible at the high frequencies at which the system dithers. This can be seen from the plots of Equation (2.3.12) at various flight conditions (Figure 2.3.3). The pitch autopilot parameters and dither frequency are presented in Table 2.3.1.
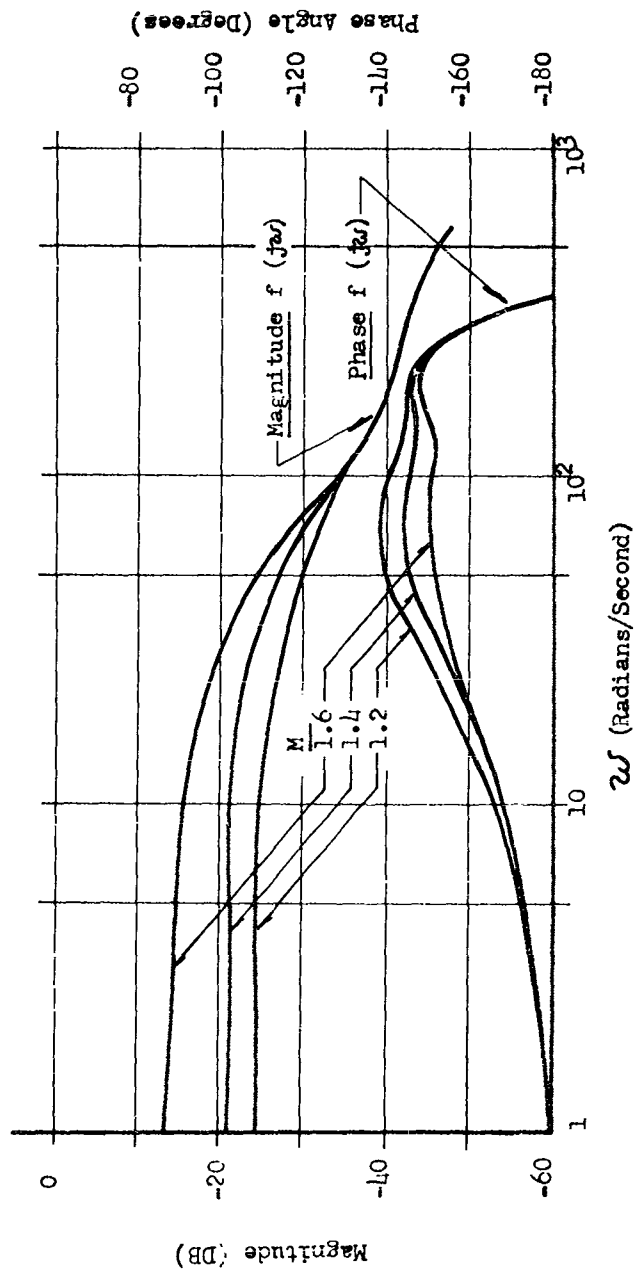
Figure 2.3.3   Pitch Autopilot Frequency Response

Table 2.3.1 Pitch Autopilot Parameters

Flight Cond.	Mach No.	I_p	W lt	c.g.% of chord	A	B	C	E	G	Dither Freq. r/s
1	1.6	19.8	330	0.409	9.0	0.00303	601	5.19	2.52	314
2	1.4	19.8	330	0.409	6.91	0.00303	1120	5.19	2.2	314
3	1.2	19.8	330	0.409	5.27	0.00303	1345	5.19	1.89	314
4	1.0	19.8	330	0.409	3.79	0.00303	1472	5.19	1.58	314
5	0.8	19.8	330	0.409	2.14	0.00303	1570	5.19	1.26	314
6	0.6	19.8	330	0.409	1.14	0.00303	680	5.19	0.95	314

2.3.1.4 Stability   An examination of the system for positive

values of C, indicates that:

(1) the airframe alone is divergently unstable,

(2) the system may exhibit one or more points of oscillation (stable and/or unstable).

If the transport delay ($e^{-s\tau}$), other than that contributed from the reaction motors, is added to Equation (2.3.12), a value of τ is reached at which the system become divergently unstable for zero input. (see Figure 2.3.4). As the time delay increases, the dither frequency decreases. The assumption that higher harmonics are negligible is not valid at low dither frequencies and, hence, the describing function technique is no longer applicable. Figure 2.3.5 compares the analog results to the approximate describing function technique results. Note that a value of τ definitely exists for which the system is unstable.
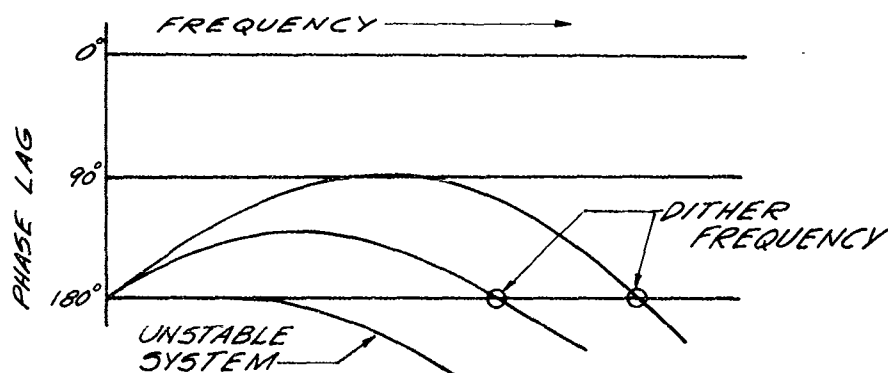
Figure 2.3.4 Effect of Time Delay on Pitch Autopilot Dither Frequency

Figure 2.3.5 presents the oscillation frequency as a function of the added time delay. The discrepancy is due in part to the approximation of the reaction motor transfer function and to the inaccuracy of the describing function technique when the higher harmonics become significant.

Re-examining Equation (2.3.6), (rewritten here for convenience),

$$-n = \frac{[(AE + BC) - Bs^2]}{s^2 + AGs - C} f_p, \qquad (2.3.6)$$

for steady state conditions indicates that

$$f_p \cong F_p \sin \omega_D t \qquad \text{for } \omega_D \gtrsim 250r/s \text{ sinusoidal waveform}$$

$$f_p \cong \frac{4}{\pi} F_p \sin \omega_D t \qquad \text{for } \omega_D < 250r/s \text{ waveform bears more resemblance to a square wave}$$

where ω_D is the frequency of oscillation.

2.91
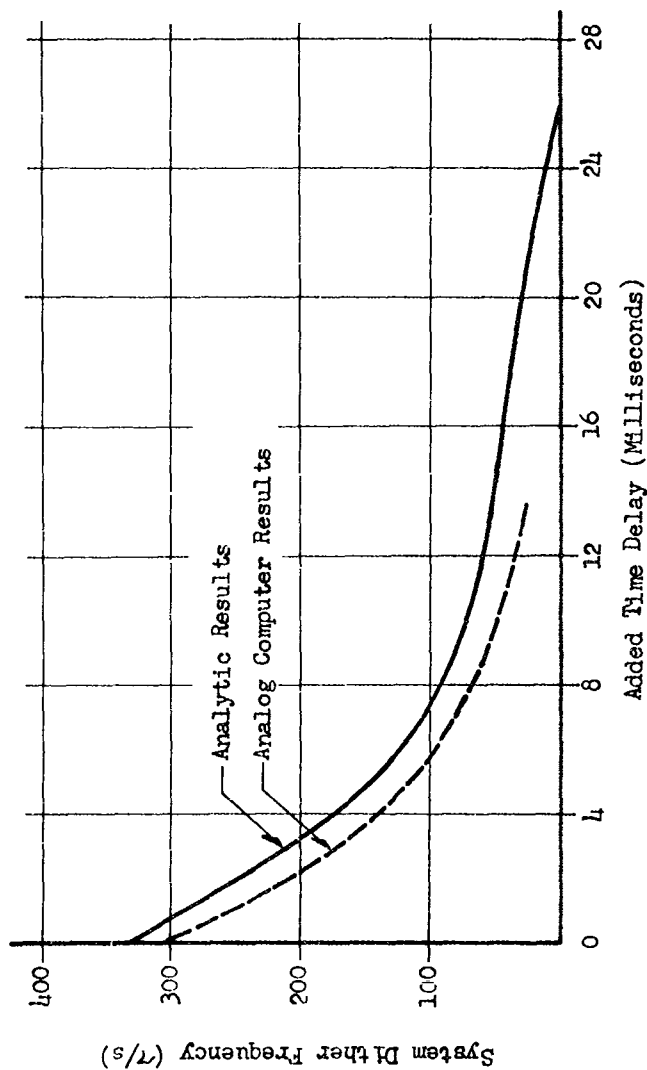
Figure 2.3.5 Pitch Autopilot Dither Frequency
Sea Level, Fixed Flight Conditions, M=1.2

2.92

The roots of Equation (2.3.6) are:

numerator $\quad Z_1, Z_2 = \pm\sqrt{\dfrac{(AE+BC)}{B}} \cong \sqrt{\dfrac{AE}{B}} \quad FOR\ AE \gg BC$

denominator $\quad P_1, P_2 = \dfrac{-AG \pm \sqrt{(AG)^2 + 4C}}{2}$

or for $AG \ll C$

$$P_1,\ P_2 \cong \pm\sqrt{C}$$

Table 2.3.2 presents P_1, P_2 & $Z_1 Z_2$ for different flight conditions.

Table 2.3.2 Critical Frequencies from Equation (2.3.6)

F_G.	Mach No.	Weight lb	n_{min} $g\,s$	max degrees	P_1 rad/sec	P_2 rad/sec	$Z_1 Z_2$ rad/sec^2
2	1.4	330	.3.0	4.62°	29.8	37.6	114
3	1.2	330	3.0	3.85°	33.4	40.3	102
5	0.8	330	3.0	3.31°	38.6	40.7	72.3
6	0.6	330	3.0	7.64°	25.5	26.6	51.3

At large dither frequencies the form of Equation (2.3.6) is:

$$n \simeq \beta f = \frac{f}{w} \qquad (2.3.16)$$

i.e., the amplitude of the oscillation is entirely determined by the thrust-to-weight ratio. If the frequency of oscillation is equal to or less than

$$\sqrt{\frac{AE}{B}}$$

the amplitude of oscillation in "g's" increases rapidly. This is verified by the computer results shown in Figure 2.3.6 where the peak amplitude in "g's" is plotted against the added time delay for various Mach numbers and in Figure 2.3.7 where amplitude is plotted against frequency.

Table 2.3.2 also presents the angle of attack which will produce an aerodynamic moment equal to the maximum missile pitch restoring moment for steady state condition.

2.3.1.5 Effect of Instruments For the steady state behavior, it is desirable, as indicated in the previous section, to have the oscillation frequency greater than $\sqrt{C}$.

Equation (2.3.15) indicates that for $w > 250$ rad per sec the lag contributed from the left hand side of the equation is approximately 90°. By adding the effect due to the reaction motors, the oscillation frequency can be expressed by,

$$\text{arc tan } \frac{w_0}{460} + 3(10^{-3}) w_0 = \frac{\pi}{2} \qquad (2.3.17)$$

or

$$w_0 = 300 \text{ rad/sec}$$

During steady state, the instruments should essentially contribute no lag at this frequency. This dictates a high natural frequency in both the accelerometer and the rate gyro. The upper part of the spectrum is dictated by noise considerations. Certain combinations of gain, instrument characteristics and added time delay stabilize the system at either of two oscillation modes in steady state. This is shown in Figure 2.3.8. The system initially oscillates at the higher dither frequency but if disturbed by a transient command will immediately fall into the lower dither frequency mode, a mode in which the missile response is detrimental to maneuverability.
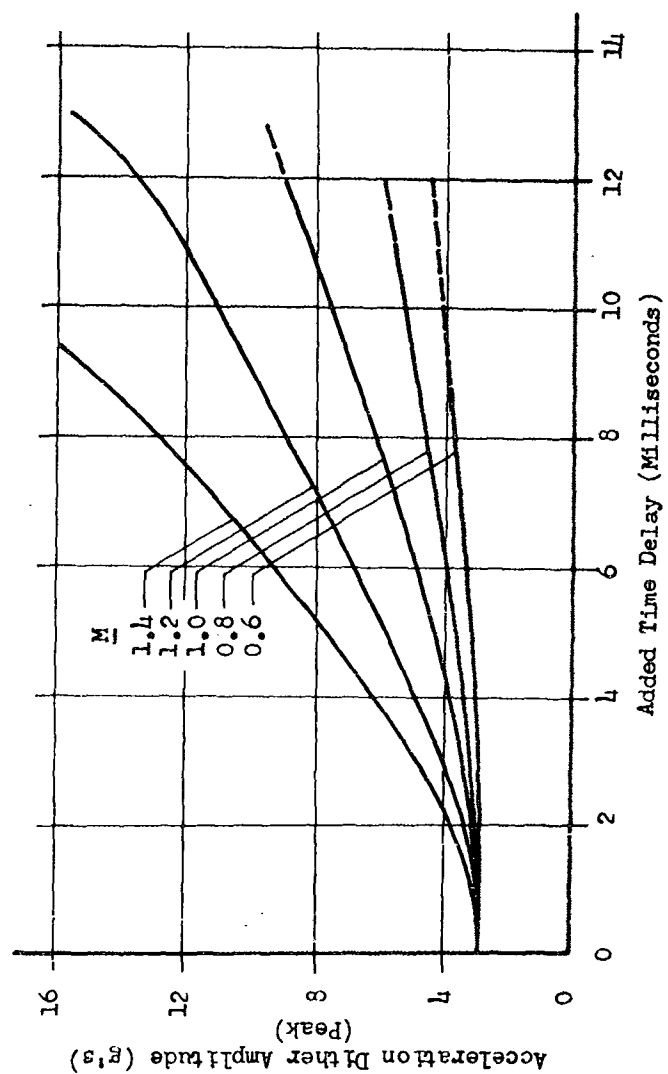
Figure 2.3.6 Pitch Autopilot Dither Amplitude
Sea Level, Fixed Flight Conditions, Analog Results

$$\eta = \left[\frac{(AE+BC)-BS^2}{S^2+AGS-C}\right] f$$

Frequency (Radians/Second)
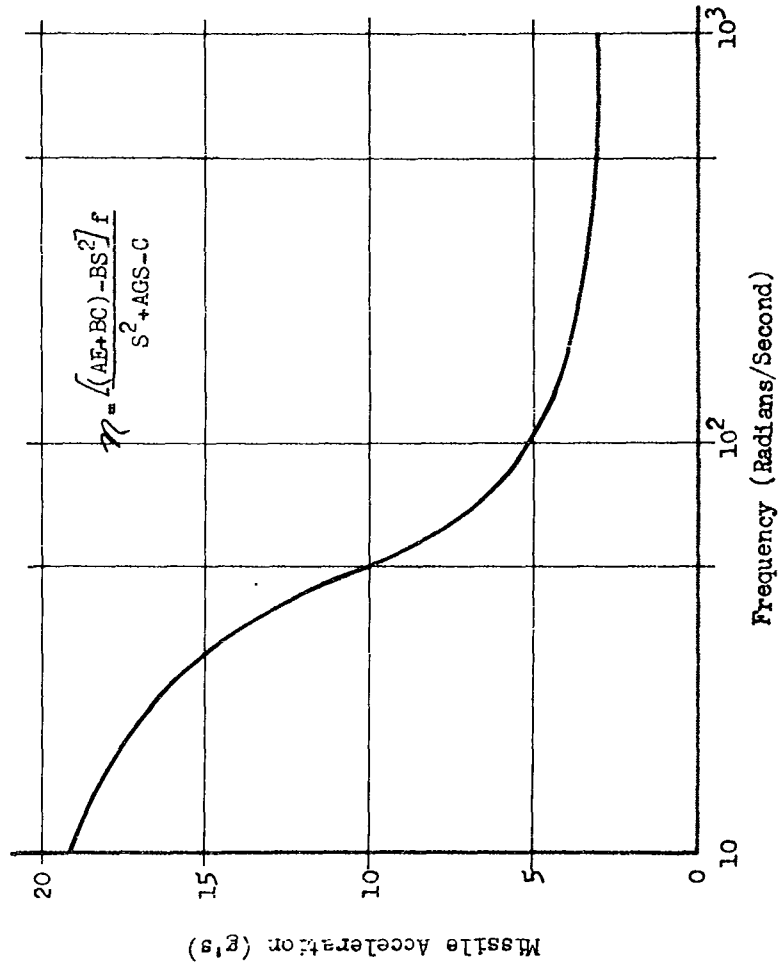
Figure 2.3.7 Pitch Autopilot Dither Amplitude
Sea Level, Fixed Flight Conditions, M=1.2.

Missile Acceleration (g's)

2.96

Phase Angle (Degrees)

○ Stable Point
☐ Unstable Point

Phase $e^{-j\omega\tau}$ $\begin{cases} \mathcal{T}'=5.00 \text{ Milliseconds} \\ \mathcal{T}'=2.37 \text{ Milliseconds} \end{cases}$

Magnitude $f(j\omega)$

Phase $f(j\omega)$

ω (Radians/Second)

Magnitude (DB)
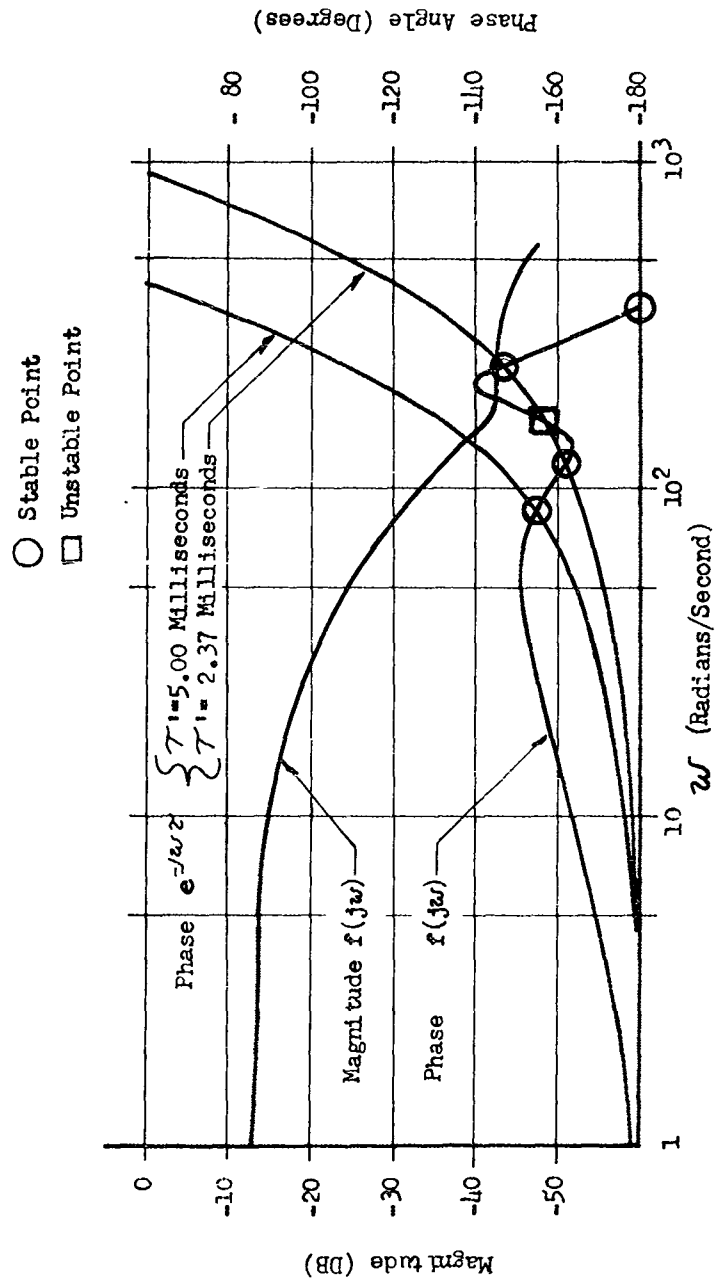
Figure 2.3.8 Pitch Autopilot Frequency Response

2.97

It has been determined on the analog computer and verified analytically that the instrument characteristics should be:

	natural frequency	damping	max. amplitude
accelerometer	26-35 cps	0.75-0.85	15 g's
pitch rate gyro	120	0.5	250°/sec
roll rate gyro	120	0.5	500°/sec

A lower natural frequency for the accelerometer limits the response time for a command maneuver in the pitch plane while a higher natural frequency allows a jump transition to occur to the lower frequency dither mode. A lowering of the rate gyro natural frequency rapidly degenerates the response times and stability of the missile. The natural frequency of the roll rate gyro is critical for the side launch condition and, as such, dictates the use of the same natural frequency as the pitch rate gyro. Omnidirectional launch considerations require that the roll rate gyro displays an accuracy at zero degrees to within 0.5 degree for maximum stability in side launch.

2.3.1.6 Steady State Effects of Magnification Factor   The magnification factor has a build-up time which can be represented as a first order system with a time constant varying from large values (100 milliseconds or more) at low Mach numbers to approximately 10 milliseconds for supersonic Mach numbers. This lag can be represented as illustrated in Figure 2.3.9a or as approximated in Figure 2.3.9b.

(a)   k · K-1   (b)
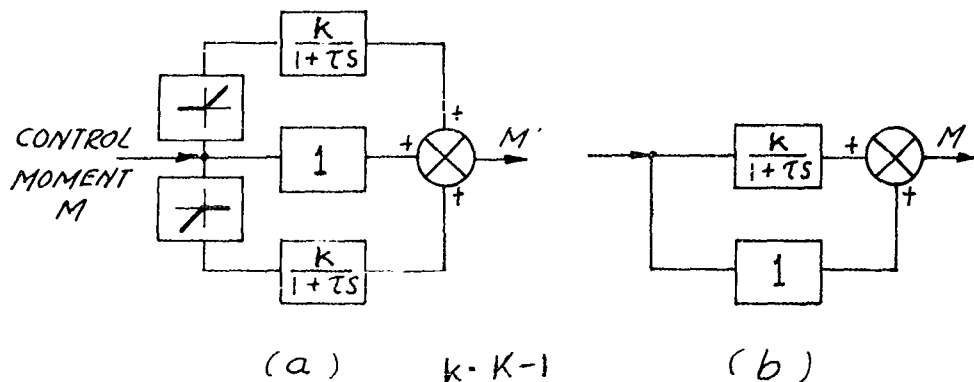
Figure 2.3.9 Magnification Schematic

2.98

Incorporating this lag into Equation (2.3.17) yields,

$$f(s) = \frac{F_\rho(s)(1+k+\tau s)}{1+\tau s}\left\{\left(-\frac{\eta}{f}\right)K_1 G_\eta(s) + (K_2 + K_3 s)G_{\dot{\theta}}(s)\left(\frac{\dot{\theta}}{f}\right)\right\}$$

$$(2.3.18)$$

From the aerodynamic data for forward launch,

$$0.5 \leq (1+k) \leq 2.0$$

then, for τ = 0.01 seconds,

$$k=1, \qquad \frac{1+k+\tau_3}{1+\tau_3} = \frac{2\left(1+\frac{s}{200}\right)}{1+\frac{s}{100}} \qquad (2.3.19a)$$

$$k=-0.5, \qquad \frac{1+k+\tau_3}{1+\tau_3} = \frac{0.5\left(1+\frac{s}{50}\right)}{\left(1+\frac{s}{100}\right)} \qquad (2.3.19b)$$

The oscillation frequency would vary from a low of 290 rad per sec to a high of 365 rad per sec. The oscillation amplitude would vary with $(1+k$ as:

$$|-\eta| = \frac{\left[(BC+AE)+B\omega_D^2\right](1+k)f}{\sqrt{(\omega_D^2+C)^2+(\omega_D AG)^2}}$$

2.3.1.7 Valve and Reaction Motor   The analog simulation and resultant simplified transfer function of valve and torque motor were determined from the characteristics of a modified commercial valve and from the test data on reaction motors. A schematic of the valve and motor is given below:
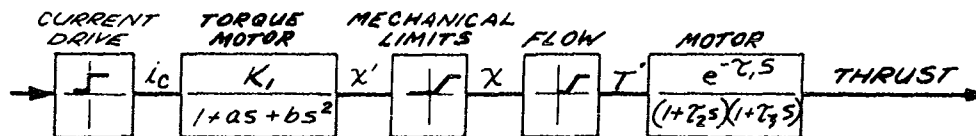
It was assumed that a solenoid action similar to that of the commercial model could control a greater propellant flow without significant degradation in the response time.

In order to obtain a minimum response time it is desirable that a bistable flip-flop control provide a two-value "constant current" output to drive this solenoid. Thus, to the degree that a "step" constant-current output can be produced (solenoid load), the valve step response can be shortened over that obtainable with a voltage drive (2 millisecond advantage). A ten second flight would require about 500 openings and closings.

The equation used for operating with a constant current source is:

$$ i_c = \frac{K_E}{K_{IF}} \left(\frac{m}{K_E} S^2 + \frac{B}{K_E} S + 1 \right) x \quad \text{for unrestrained motion,} $$

and with a constant voltage source the response would be governed by a further equation

$$ V = i \frac{d i_c}{dt} + R i_c + g\left(i_c, \dot{x} \right) $$

The symbols used in the latter two equations are:

$\dot{i}_c$ = the solenoid current in amperes,

K_{IF} = the electromagnetic coefficient in $\dfrac{\text{lb force}}{\text{amp}}$,

K_E = the spring coefficient in $\dfrac{\text{lb force}}{\text{in.}}$,

m = the mass coefficient in $\dfrac{\text{lb force}}{\text{in/sec}^2}$,

B = the damping coefficient in $\dfrac{\text{lb force}}{\text{in./sec}}$,

K_{IF}/K_E = 0.043 in/amp,

$$m/K_E = 6.69 \times 10^{-6} \text{ sec}^2,$$

$$B/K_E = 1.24 \times 10^{-4} \text{ sec},$$

V = applied voltage,

L = solenoid inductance in henries,

R = coil resistance in ohms, and

$g(i_c, \dot{x})$ = term due to core motion.

The equation of motion was subjected to the mechanical restrictions shown in Figure 2.3.10.
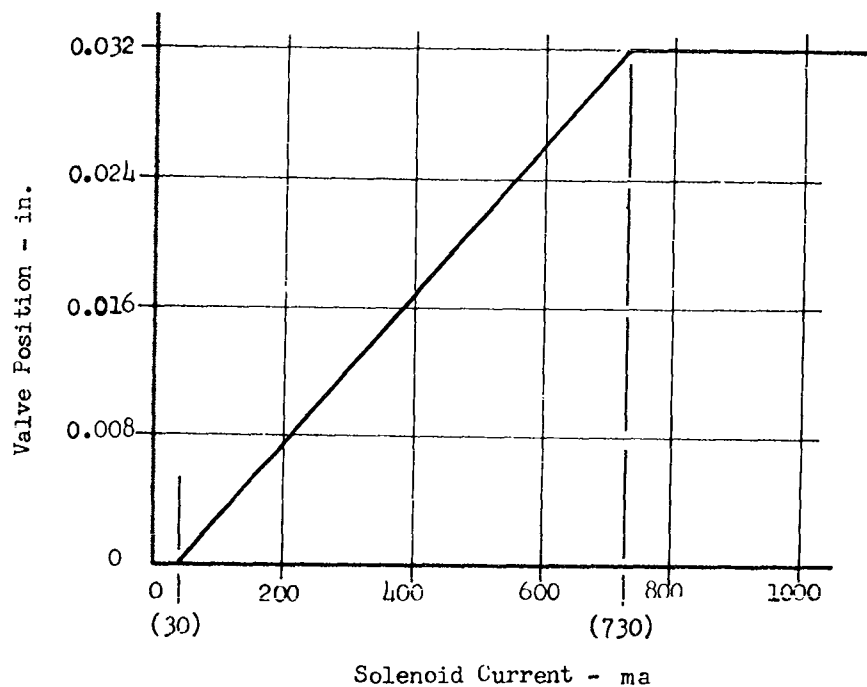
Figure 2.3.10 Valve Position versus Solenoid Current

The spring restrains the solenoid thus preloading it against the bottom (closed) stop. Thirty ma is required to overcome the preload. The valve is driven by a current of 1000 ma.

The thrust from the propellant flow was assumed linear over the region shown in Figure 2.3.11 below (propellant flow being a linear function of position between 0.003 and 0.032 in.). For an I_{sp} of 250 sec., a 500-lb thrust motor requires a propellant flow of 2 lb per sec.
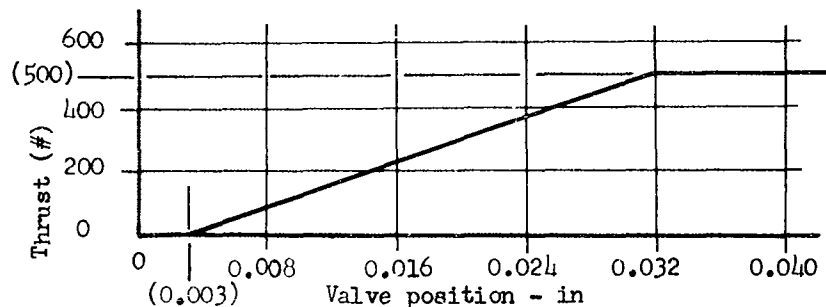
Figure 2.3.11 Thrust Versus Valve Position

For the bang-bang controller, the time that the piston position x is between 0.003 and 0.032 inches is very small compared to the time spent at zero or at full open. That is, the linear approximation for thrust versus x is of little importance.

The expression describing the dynamic relationship of fluid flow and thrust may be written as

$$\frac{e^{-0.002s}}{(1+0.0005s)(1+0.0007s)}$$

These terms include fluid transport delay, reaction time and pressure build-up. The above delays are approximations obtained by applying a degradation factor to the results of experimental measurements. From inspection of the analog computer runs the entire transfer function for thrust versus input current i_c, can be approximated by

$$\frac{A \ e^{-0.003s}}{1+0.0022s}$$

where A is a magnitude term.

Analog measurements of control stability and missile maneuverability (verified by analysis) indicated that it would be desirable to achieve an overall delay of 5 milliseconds or less.

2.3.2 ROLL AUTOPILOT SYNTHESIS   As in the case of the pitch autopilot, a single plane analysis was conducted for the roll system. This work was initially accomplished to obtain a general understanding of the roll autopilot and the associated airframe response prior to electronically combining the pitch and roll autopilots and finally to incorporating the combined system into the three-dimensional simulation.

2.3.2.1 <u>Control Equation</u>   The control equation chosen for the roll autopilot is given by

$$\mathcal{E}_r = K_4 \left(\phi_c - \phi \right) - K_5 \dot{\phi} \left(1 + \mathcal{T}_R S \right)$$

A block diagram which simulates this equation and incorporates it into the roll system is illustrated in Figure 2.3.12.
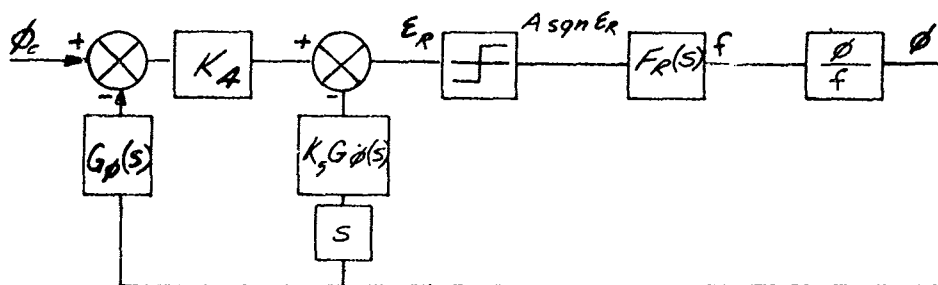
Figure 2.3.12   Block Diagram of the Roll Autopilot

The nomenclature utilized in the block diagram follows:

ϕ_c =   "called-for" rotation,

$G\dot{\phi}(S)$ =   rate gyro response,

$G\phi(S)$ =   free gyro response,

$F_R(S)$ =   reaction motor transfer function, and

$\mathcal{T}_R$ =   autopilot gains.

The simplified transfer function for the reaction motors is

$$\frac{e^{-\tau_1 s}}{1 + \tau_1 s} \qquad\qquad (2.3.21)$$

where

τ_1 = 3 milliseconds and

τ_2 = 2.17 milliseconds.

The roll system perturbations may be classified into the following three catagories:

1. initial roll and roll rate conditions,

2. command roll, and

3. extraneous roll torque ($\ddot{\phi}_T$).

2.3.2.2 <u>Airframe Transfer Function</u>   The following is a listing of the nomenclature used throughout the discussion of the airframe transfer function.

f_r = total thrust of the reaction motors contributing to a roll moment,

I_r = moment of inertia, slug-ft^2 (11.59 full and 9.79 empty),

C_ℓ = roll moment derivative,

ℓ_r = roll moment arm (1.71 ft), and

ϕ = rotation about the missile centerline

The roll moment equation is,

$$\ddot{\phi} + F\dot{\phi} = K_r f ,$$

where,

$$F = \frac{1481 \lambda \, S d M^2 C_\ell}{\left(\frac{2V}{b}\right) I_r}$$

$$K_r = \frac{57.3 \, k_r}{I_r}$$

For a roll moment arm,

$$\frac{\phi}{f} = \frac{K_r}{s(s+F)}$$

Neglecting instruments,

$$- (K_4 \, \phi + K_5 \, \dot{\phi}) = 0$$

represents the switching line.

2.3.2.3 <u>Steady State Behavior</u>   The steady state behavior for zero input may be described by the solution of

$$\frac{K_r}{s(s+F)}\left[K_4 + K_5 \, S(1+\tau_R \, S) \, G_\phi(S) \right] \frac{e^{-\tau_1 S}}{1+\tau_2 S} = \frac{-1}{N(r)} \qquad (2.3.23)$$

Figure 2.3.13 presents the solution of Equation (2.3.23) for F = 0

2.3.3   COMBINED ROLL AND PITCH AUTOPILOT   The roll and pitch systems were combined to minimize the number of components and the required thrust level of the jets. The indirect effects resulting from this philosophy are a minimum of development work, minimum cost, minimum missile weight, maximum reliability, etc. This coupling introduces certain restrictions on the control demands. The control time is shared, that is, only a pure roll or a pure pitch moment is possible at one time. Thus, to insure stability, it is essential that the system controlling the motion about the unstable aerodynamic axis exercise the dominant control. For forward motion the pitch system should dominate the roll system, hence, the control equation is weighted heavily in favor of pitch demands. For side motion at 90° launch, the roll system should be predominant; therefore the co-efficients of the roll control equation are raised so that roll control demands take precedence.
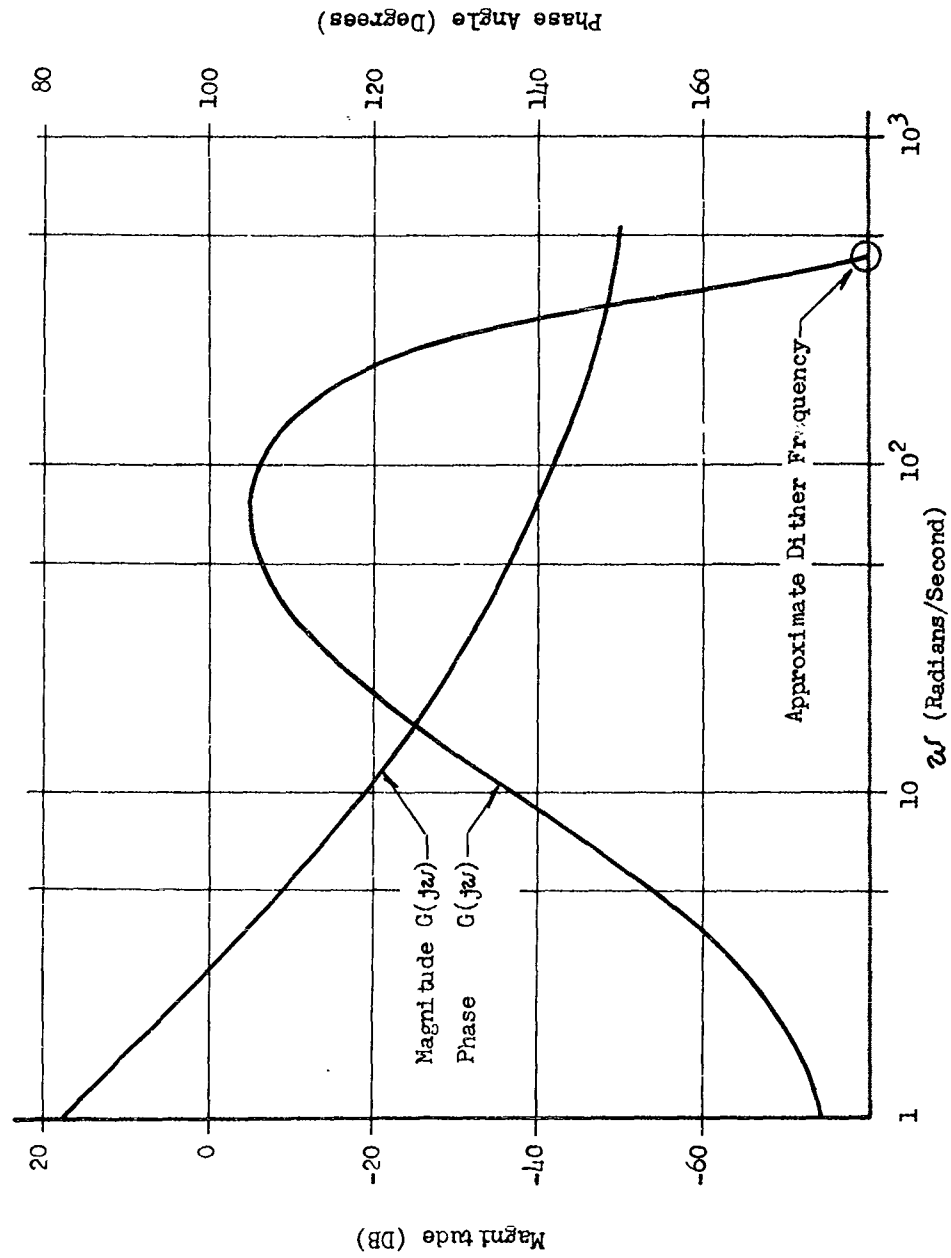
Figure 2.3.13   Roll Autopilot Frequency Response

This combination of pitch and roll requires a switch in dominant systems if the missile is to possess omnidirectional launch capability. Since the major portion of the flight is in the forward direction, the roll control equation for normal flight has relatively small coefficients in comparison to the pitch equation. The switch-over is planned for a side slip angle, β, of less than 20°.

2.3.3.1 Reaction Motor Logic   Figure 2.3.14 presents the missile reaction motor configuration in two views.
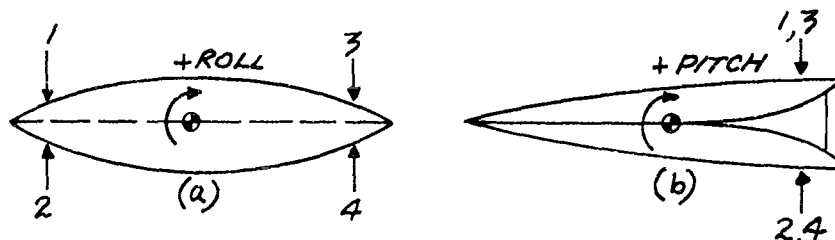
Figure 2.3.14   Reaction Motor Configuration

The system reacts to roll and pitch errors as follows:

+ ε_r will activate reaction motors 2 and 3 resulting in + f_r,

+ ε_p will activate reaction motors 1 and 3 resulting in + f_p,

- ε_r will activate reaction motors 1 and 4 resulting in - f_r,

- ε_p will activate reaction motors 2 and 4 resulting in - f_p.

Figure 2.3.15 presents one method of mechanizing the system. The signals being applied to the valves can be expressed as,

$$A_1 = L \operatorname{sgn} (-\varepsilon_r + \varepsilon_p), \text{ and}$$

$$A_2 = L \operatorname{sgn} (+\varepsilon_r + \varepsilon_p).$$

If $|\varepsilon_r| > |\varepsilon_p|$ there will be only a roll moment generated and if $|\varepsilon_p| > |\varepsilon_r|$ there will be only a pitch moment generated. Since either ε_p or ε_r is generally in a steady state oscillation, two average moments can be generated over a period by time sharing.
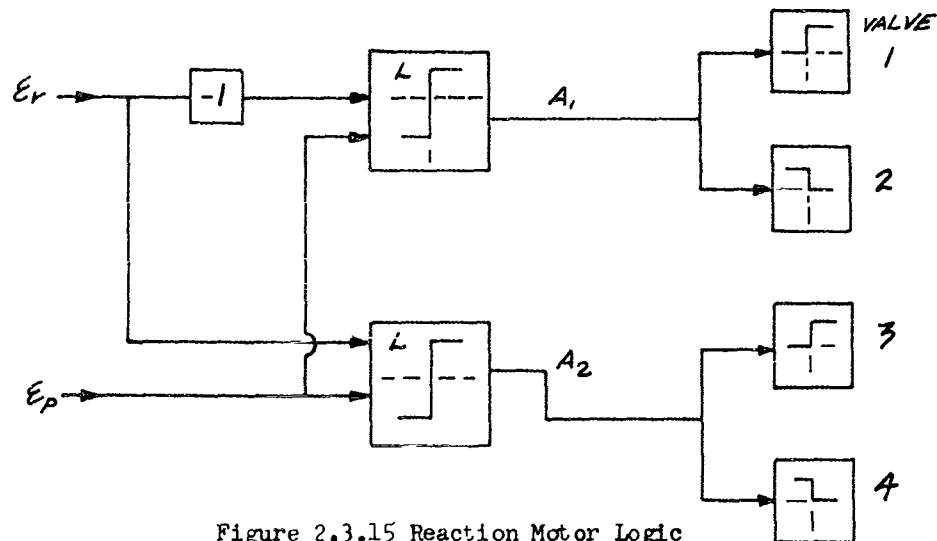
Figure 2.3.15 Reaction Motor Logic

During steady state, zero command operation, the oscillation frequency may be dictated by either the

    (1)   pitch loop alone,

    (2)   roll loop alone, or

    (3)   bimodal operation, where the oscillations may either be in one mode or the other for small disturbances.

The form of the open loop transfer functions and their relative gains determine the oscillation frequency for zero input, steady state conditions. The analysis of the modes of operation of this type of nonlinear-coupled systems has been conducted using the describing function technique. The method establishes the existence of these modes of operation and specifies its operating conditions.

When one system predominates, the other system will not oscillate, in fact, under ideal conditions of symmetry, the instantaneous error will remain zero. Asymmetry will tend to produce small oscillations in this channel. Small errors due to inputs or disturbances in the dependent channel will tend to be nulled out by means of thrust pulses of varying widths. Figure 2.3.16 presents the pulses in roll thrust (f_r) forming an average roll restoring moment due to constant roll error (pitch system predominating). It is evident that during a small roll maneuver, the amplitude of the oscillations in pitch will be temporarily reduced. A steady state error in the pitch channel ($\mathcal{E}_p = A + B \sin \omega_o t$) with no error in the roll channel will result only in an average pitch restoring moment.

                        SECRET

Figure 2.3.16   Reaction Motor Sequence for Combined Roll-Pitch Error Signals

When a condition such as $|\mathcal{E}_r| > |\mathcal{E}_p|$ arises, the dependent system is essentially in an open loop state. Since the pitch system is unst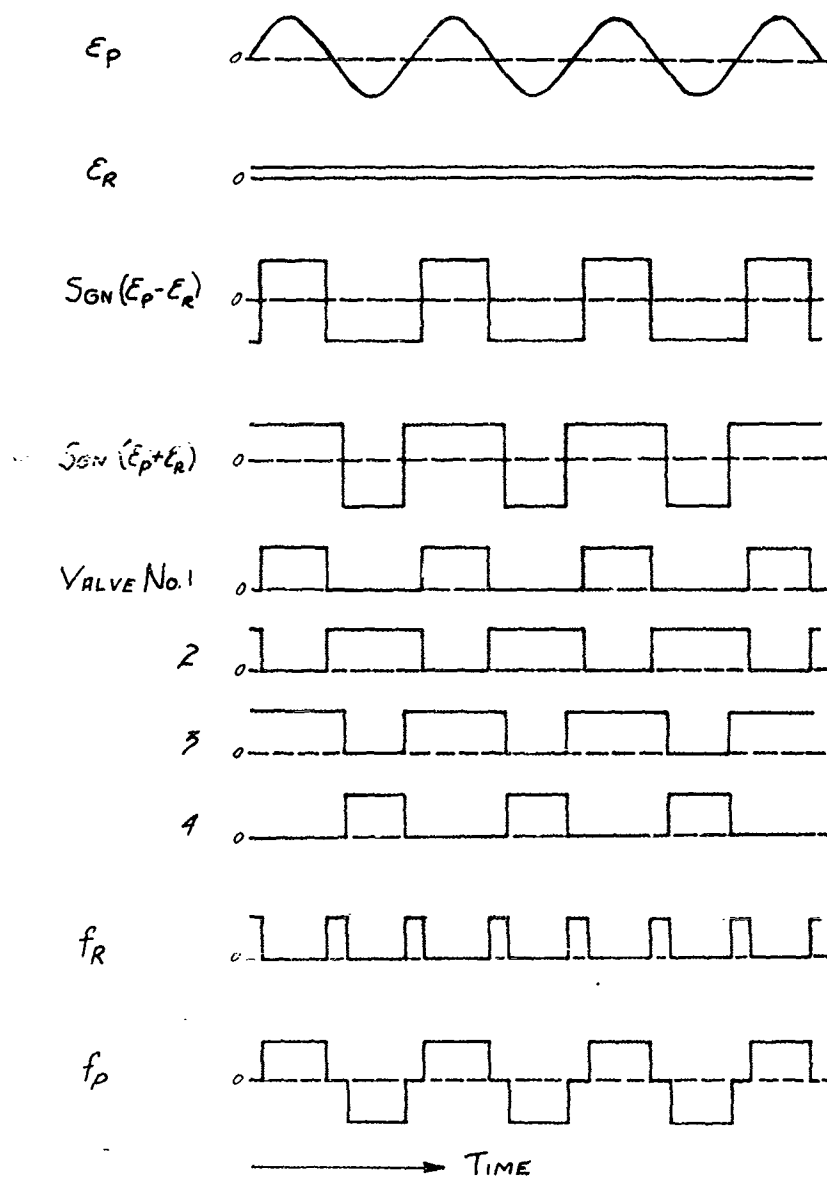able alone, it will diverge until $|\mathcal{E}_p| > |\mathcal{E}_r|$. If at the time this condition is reached, the body rate and aerodynamic moment are beyond the stability boundaries, the system will not recover. The relative magnitude of the roll input is normally small compared to the pitch input if the pitch system is initially at some body rate and angle of attack. Thus, there are boundaries in pitch and roll body rates, and in the angle of attack for various flight conditions and system parameters. The gains are chosen to optimize these boundary conditions. The synthesis was conducted on the analog computer. For all regimes except the initial stage of side launch, optimum boundaries were obtained when the pitch autopilot dictated the mode of oscillation.

2.3.3.2　Forward Launch　The operation in forward launch is similar to normal flight with the exception that the gain coefficient of the normal acceleration (K_1) is increased so that errors arising from initial conditions may be rapidly reduced. This higher gain is not suitable for the region of peak Mach numbers ($>$ M 1.4) during the flight. The control equations during forward launch are:

$$\mathcal{E}_p = 5\,(n - n_c) - 0.55\,\dot{\theta}\,(1 + 0.0015s), \text{ and } \quad (2.3.24)$$

$$\mathcal{E}_r = -0.3\,(\phi - \phi_c) - 0.08\,\dot{\phi}\,(1 + 0.005s) \quad (2.3.25)$$

The switch to the flight gain takes place at approximately 0.5 ± 0.25 seconds after launch.

2.3.3.3　Side Launch　The airframe is unstable about the roll axis when the missile is launched perpendicular to the direction of travel of the sled. In order to maintain loop stability, the compensation must be changed. As the missile accelerates along its own axis, the side slip angle, β, shifts rapidly from $90°$ down to approximately arc tan $\left(\dfrac{\text{sled velocity}}{\text{max missile vel}}\right)$.

At this point the missile is allowed to weathercock, reducing β to zero (damping being provided by the yaw autopilot).

An idealized linear system was synthesized analytically for a fixed flight condition and $90°$ attitude in yaw. The time varying case was then analyzed on the computer for stability. The synthesis proceeded to the more detailed nonlinear system during which the control equation was optimized to give ideal boundary conditions.

Since the initial conditions imposed upon the roll autopilot during a side launch are similar to those imposed upon the pitch autopilot during forward launch, a cursory analysis was conducted to determine if acceleration control in the roll autopilot would be advantageous during the initial phase of a side launch. The stability equation for this condition indicates that, for acceleration control in the roll autopilot, polarity reversal would be required for the initial condition of $\beta = +90°$ if the pitch accelerometer were used, i.e., positive roll would produce acceleration in the downward direction because of the negative angle of attack. At $\beta = -90°$, positive roll would produce acceleration in the upward direction as does positive ϕ in forward flight. This polarity reversal would increase the complexity of the control system. The method, however, was investigated on the analog computer to prove that it could be used if necessary.

A preferable method requires close control of the roll angle (ϕ) during the acceleration period. If, prior to launch, ϕ is caged to the launch platform reference, then the angle of attack, α, and the roll angle, ϕ, would be essentially the same during the initial launch period. Control of ϕ would keep α small. As the missile accelerates, the plane of the angle of attack shifts around towards the longitudinal axis of the missile and roll control becomes less critical; at the same time pitch control becomes more critical. The control philosophy requires a gain change at this crossover point. This point is influenced by the weighting of the control equation coefficients; i.e., during normal forward flight the coefficients of ϕ, $\dot{\phi}$, and $\ddot{\phi}$ in the equation for ξ_r, are small so that pitch control will always predominate; a roll maneuver during this mode will be developed by a sequence of short control bursts rather than one long pulse which would interrupt the pitch control. During side launch the roll equation coefficients are larger and the corrective maneuvers about the pitch axis will be effected by several short pulses of pitch thrust. The weighting between pitch and roll control for side launch is such that stability is controlled down to $\beta < 20°$, for the forward flight the weighting factor is changed such that stability is maintained for $+20° > \beta > -20°$. It is not desirable however to command extreme maneuvers during the launch phase (the first 1.5 seconds for $\beta = 90°$ at launch).

A simulated missile flight was programmed on the analog computer using noise inputs of 2 volts rms on ξ_r and ξ_p. The system maintained very good control with no degradation in the programmed trajectory. Figures 2.3.17 and 2.3.18 are short portions of the recordings taken during a simulated flight, a flight similar to that illustrated in Section 2.3.6. These noise levels with the initial autopilot gains are equivalent of $0.25°$ rms in roll and 0.4 g's rms in pitch. With flight gains, the same noise voltages are equivalent to $2.5°$ rms in roll and 1 g rms in pitch. The results indicate that the system could withstand a much larger proportion of noise in roll. Further study will determine
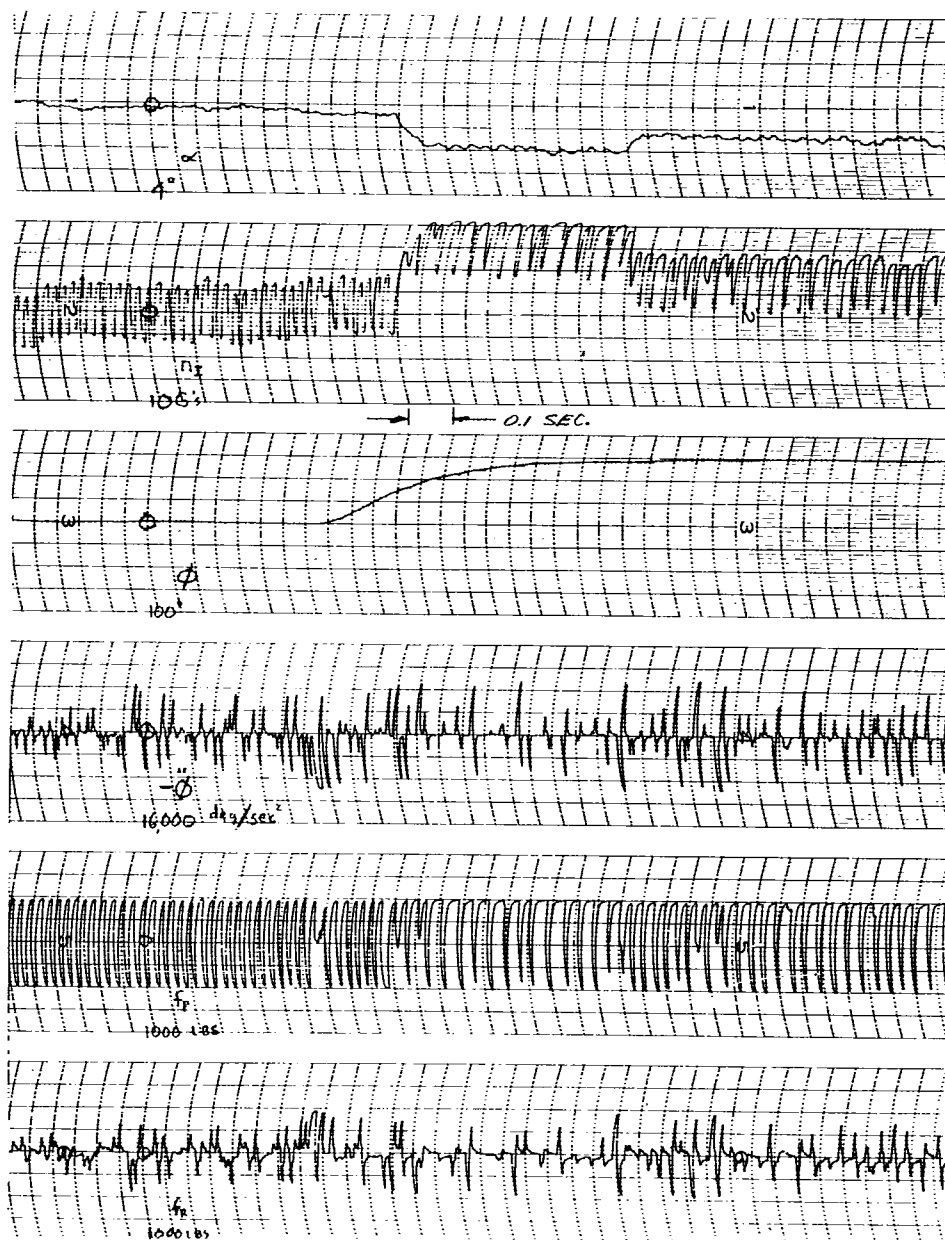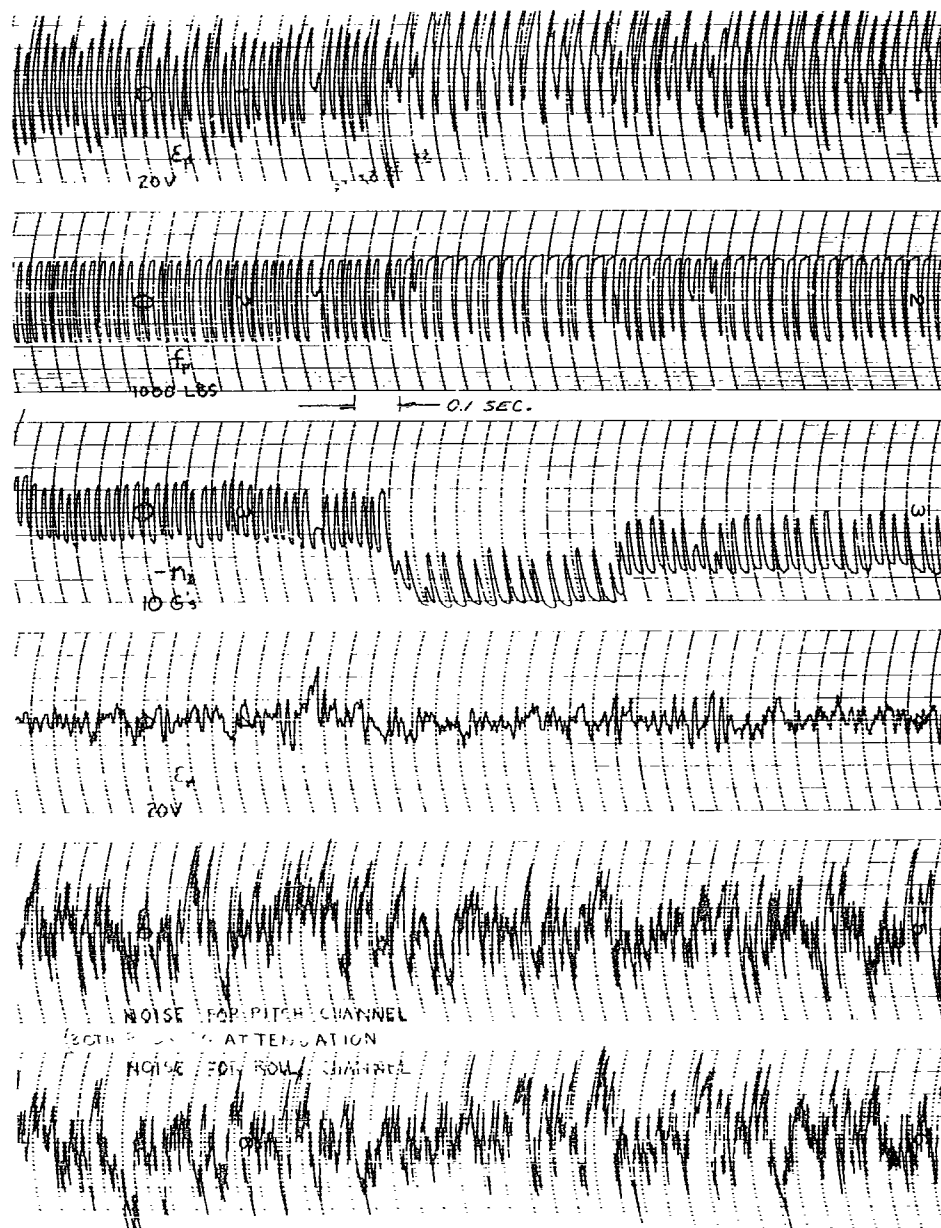
Figure 2.3.17   Effect Of Noise In Pitch And Roll Channels

Figure 2.3.18   Effect Of Noise In Pitch And Roll Channels

the maximum allowable noise; however, the levels tested were of adequate magnitude, being as large, or larger than any noise expected in practice.

The pitch and roll control equations for side launch are:

$$\mathcal{E}_p = 5(\eta - \eta_c) - 0.55\,\dot{\theta}\,(1 + 0.0015\,s), \text{ and } (2.3.26)$$

$$\mathcal{E}_r = -8(\phi - \phi_c) - 0.375\,\dot{\phi}\,(1 + 0.005\,s). \quad (2.3.27)$$

The system analysis indicates that a minimum of one gain change will be required during flight. The switching time will be determined by the missile side slip angle at launch and the launcher velocity. A relatively small number of possible switching times would be feasible. The guidance computer could enter the appropriate switching time in the missile immediately prior to launch.

The initial studies were simplified by assuming missile symmetry for yaw attitude angles from 0° to 90°, constant missile velocity, and fixed flight attitude of 90° yaw. If the error and its derivatives are simultaneously reduced to some equilibrium state about zero, the same could be assumed to occur when the missile is launched. The approach in utilizing a fixed condition is approximate since the problem is time varying.

For the 90° yaw condition, the aerodynamic coefficients are analogous to those of pitch for the 0° yaw condition.

Pitch Autopilot $(\beta = 90°)$ In the 90° attitude, the moment equation is defined as

$$\ddot{\theta} + F'\,\dot{\theta} = K_p\,f_r, \quad (F' \cong 0), \quad (2.3.28)$$

where,

$$F' = \frac{1481\,\lambda\,s\,d\,M^2\,C_l'}{\left(\frac{2V}{b}\right)I_p}, \text{ and}$$

$$K_p = \frac{57.3}{I_p}\,k_p.$$

The control equation is

$$\mathcal{E}_p = -\dot{\theta} K_2 - \ddot{\theta} K_3 + K_1 n \qquad (2.3.29)$$

The block diagram is shown in Figure 2.3.19
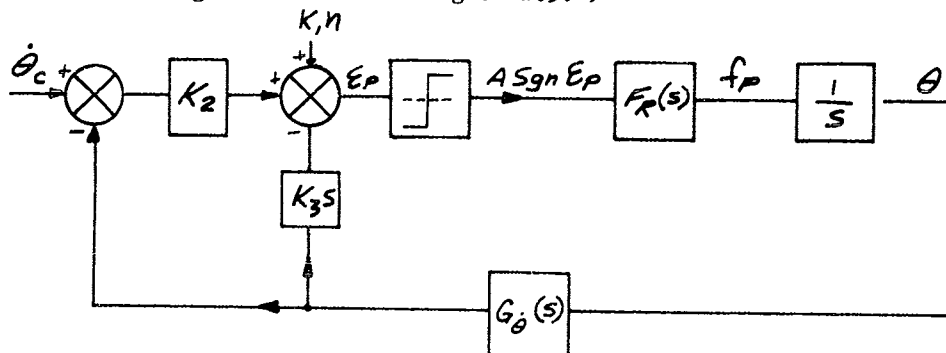
Figure 2.3.19 Block Diagram of the Pitch Autopilot ($\beta = 90$)

Assuming $K_1 n$ zero, the steady state behavior is described by the solution of

$$\left[\frac{K_p f_r(s)\ G_{\dot{\theta}}(s)\ (K_2 + K_3 s)}{s} \right] = \frac{1}{N(\Gamma)} \qquad (2.3.30)$$

where

n is acceleration in the downward direction,

$\dot{\theta}_c$ is the called-for body rate,

$G_{\dot{\theta}}(s)$ is the rate gyro response,

$F_r(s)$ is the approximate expression for the reaction motor,

$N(\Gamma)$ is the describing function for the simple contactor, and

f_p is the jet pitch thrust contributing to a pitch restoring moment.

2.115

The form of Equation (2.3.30) is shown in Figure 2.3.20.

From the block diagram in Figure 2.3.19, K_{1n} acts as a disturbance input to the system.

<u>Roll Autopilot ($\beta = 90^\circ$)</u> The moment and force equations are stated respectively as follows:

$$\ddot{\phi} = C'\alpha + f_r E', \tag{2.3.31}$$

$$-\eta = A'\alpha - \frac{f_p}{W}. \tag{2.3.32}$$

The roll autopilot gains are increased relative to the pitch autopilot gains in order to optimize the stability boundaries. This condition allows the roll autopilot to control the system dither frequency.

Assuming the pitch error, $\mathcal{E}p$, is initially zero the force equation becomes

$$-\dot{\eta} = A'\alpha. \tag{2.3.33}$$

then

$$-\left(\frac{\eta}{f_r}\right) = \frac{A'E'}{s^2 + AGs - C}, \tag{2.3.34}$$

and

$$\frac{\dot{\phi}}{f_r} = \frac{E'(G'A' + s)}{s^2 + A'G's - C} \tag{2.3.35}$$

where,

$$A' = \frac{1481 \lambda S M^2 C' N\alpha}{W},$$

$$C' = \frac{57.3(1481) \lambda SdM^2 Cm\alpha}{I_r},$$

$$E' = \frac{57.3 k_r}{I_r}$$

2.116

SECRET

Phase Angle (Degrees)

-60

-100

-140

-180

10^3

Phase G(jω)

10^2

10

Magnitude G(jω)

ω (Radians/Second)
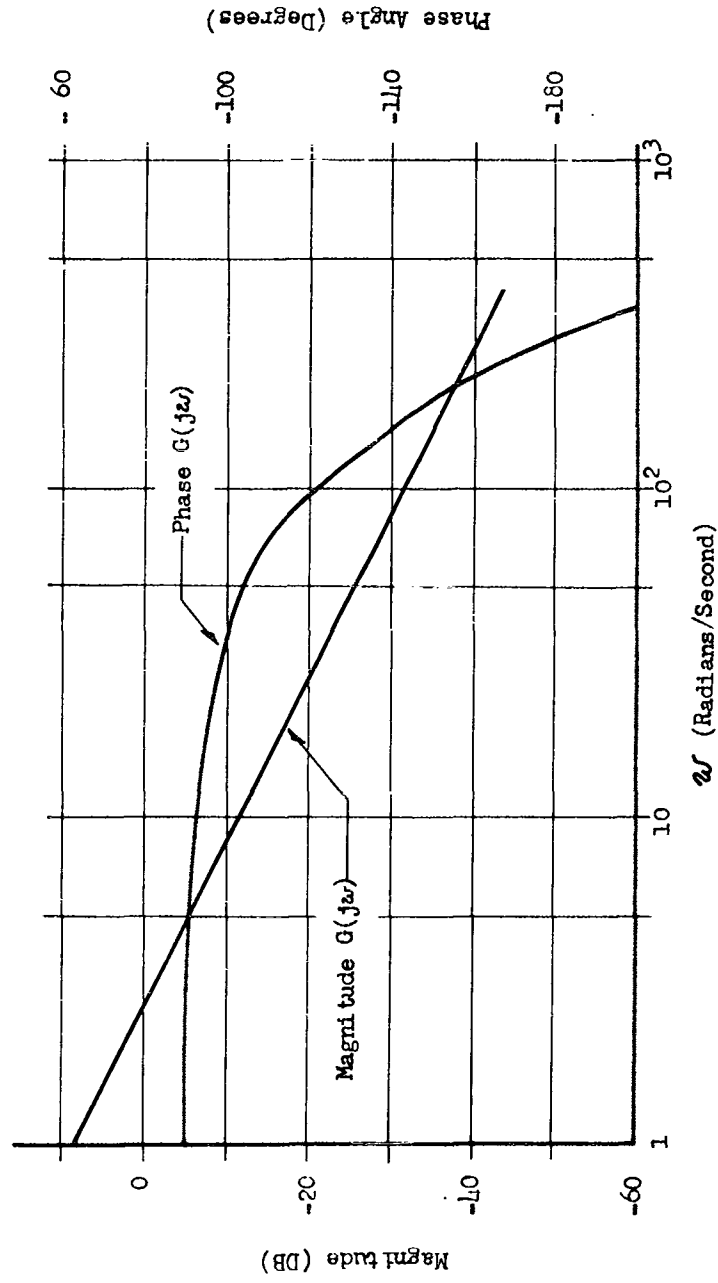
Figure 2.3.20   Pitch Autopilot Frequency Response
Side Launch Gains

0

-20

-40

-60

Magnitude (DB)

1

2.117

SECRET

$$G = \frac{1845}{V} \qquad , \text{ and}$$

$$\gamma ' = \phi - \alpha \quad .$$

Here, $C'_{N\alpha}$ and $C_{m\alpha}'$ are analogous to $C_{N\alpha}$ and $C_{m\alpha}$.

The control equation is

$$\mathcal{E}_r = \left(\phi_c - \phi\right) K_4 - K_5 \left(1 + \tau_r s\right) \dot{\phi} \qquad (2.3.36)$$

The block diagram of the roll autopilot for $\beta = 90°$ is illustrated in Figure 2.3.21.
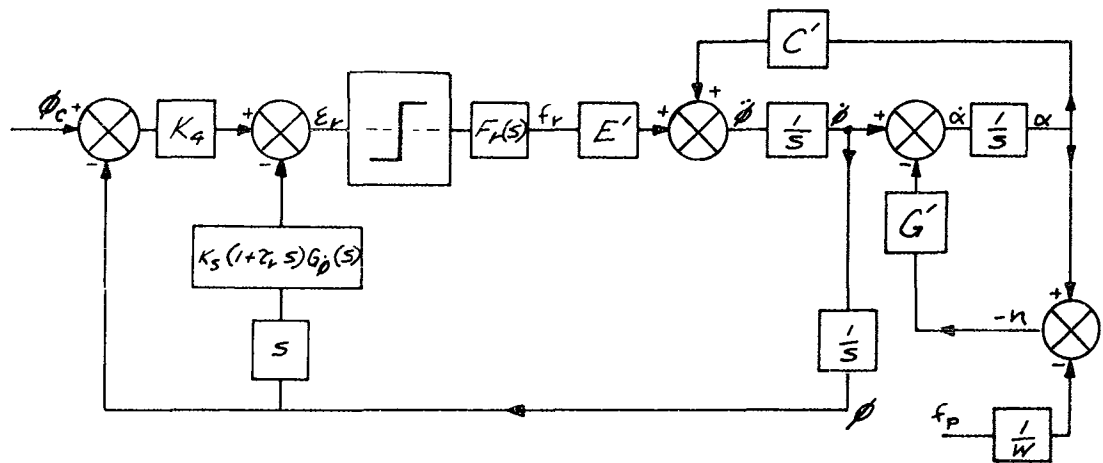
Figure 2.3.21 Block Diagram of the Roll Autopilot for $\beta = 90°$

The steady state behavior is described by the solution of

$$\frac{\left(A'E'G' + E's\right)\left[K_4 + K_5 \left(1 + \tau_r s\right)s\right]F_r(s)}{s\left(s^2 + A'G's - C\right)} = \frac{-1}{N(r)} \qquad (2.3.37)$$

The form of Equation (2.3.37) is shown in Figure 2.3.22.

An examination of Figure 2.3.22 indicates the existence of both an unstable and a stable point of oscillation. The system, when started initially from zero, will increase its oscillations until a stable point is reached. The unstable point essentially represents the approximate stability boundaries of the system. For finite values of ε_p, f_p/W acts as an input disturbance to the system.

2.3.3.4 **Aft Launch** A detailed study of the aft launch controls problem is not possible without the power-on aerodynamic data.

If the predicted jet demagnification effects for power-on aft launch (the only relevant case) are moderate, there is no doubt that the missile can be controlled. The predominately low velocity environment increases the ratio of jet control force to aerodynamic force. Control has already been demonstrated for simulated flights with zero launch velocity.

The problem is essentially dependent on the polarity of $C_{N\alpha}$ for velocity, $V < 0$. If $C_{N\alpha}$ is negative for $V < 0$ (i.e., aft end down gives upward lift in backward flight), the vertical accelerometer will remain beneficial to pitch control. If $C_{N\alpha}$ is positive for $V < 0$, then it would be advantageous to eliminate the accelerometer from the control system until $V > 0$. In the latter case the missile would be stabilized by pitch rate alone.

Roll control in either case in unaffected. $C_{m\alpha}$ may be positive or negative; at present $C_{m\alpha}$ is positive for forward flight and control has been demonstrated; a negative $C_{m\alpha}$ would be more desirable.

For omnidirectional launch considerations it would be advisable to have a timer switching function coupled with the launch angle to switch the accelerometer (if necessary). The contour is illustrated in Figure 2.3.23.

Inside the cross hatched area there would be no pitch accelerometer in the control system ($C_{N\alpha}$ positive, $V < 0$).

The suitability of the present gains would be entirely dependent on the magnitude and polarity of the aerodynamic forces and moments.

2.3.3.5 **Post Launch** At approximately 0.5 seconds for a forward launch and 1.1 seconds for a side launch, the missile control is switched to flight gains and the following control equations become effective:

$$\varepsilon_p = +2\left(n - n_c\right)_A - 0.55\ \dot{\theta}_A\left(1 + 0.0015\ s\right) \quad (2.3.38)$$
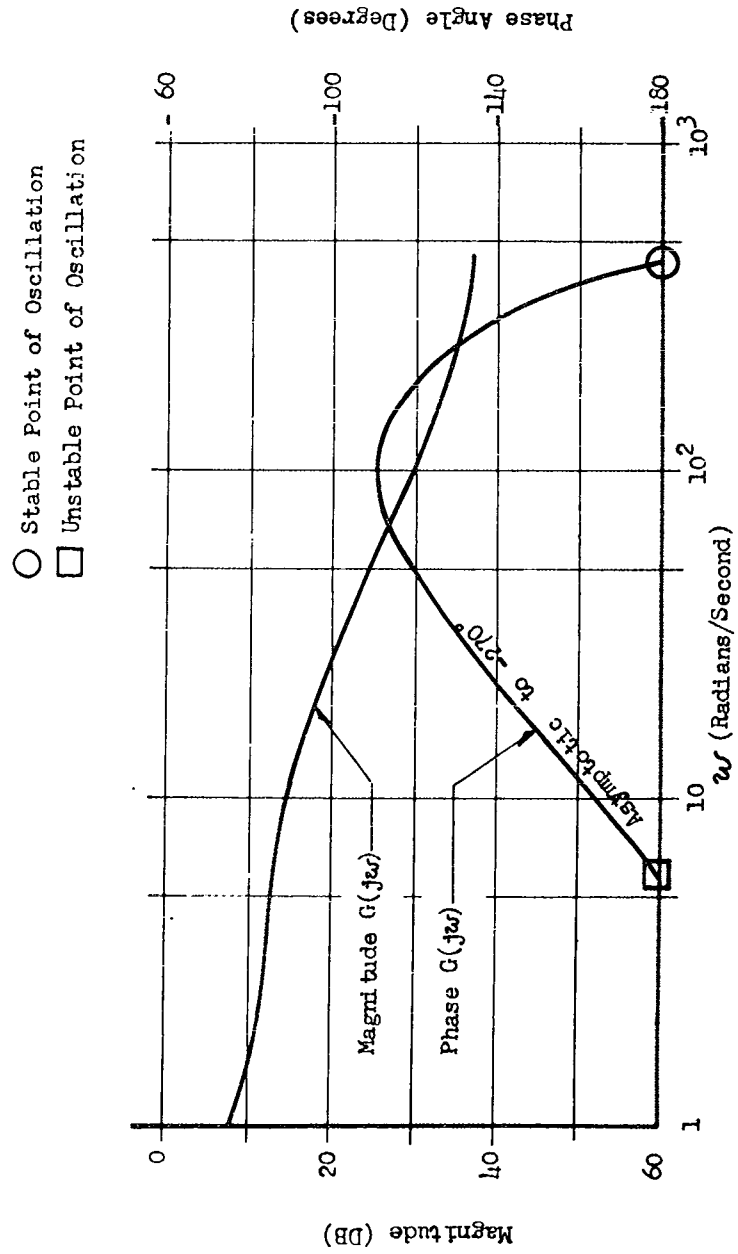
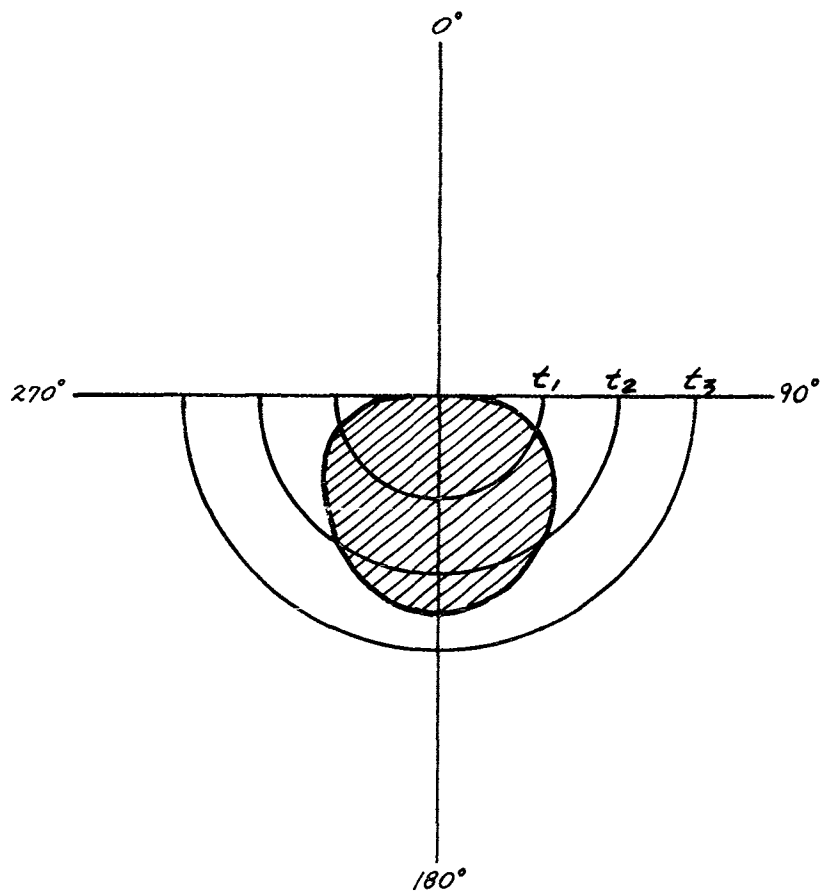Figure 2.3.22 Combined Roll Autopilot Frequency Response

Figure 2.3.23

Time-Angle Regime, Pitch Control, No Accelerometer, Aft Launch

$$\mathcal{E}_r = -0.8 \left(\phi - \phi_c\right)_A - 0.08\,\dot{\phi}_A \left(1 + 0.005\,s\right) \quad (2.3.39)$$

The pitch system is predominant with the roll maneuver being accomplished by unbalancing the pitch control pulses.

A turn is accomplished by a roll-pitch maneuver, i.e., the missile is rolled until the command change of direction is perpendicular to the missile planform. The missile is then pitched in the desired direction. The symmetrical shape of the missile allows it to fly at any roll attitude, thus allowing "turns" in any direction in space.

The post-launch pitch gains were chosen to maintain maximum maneuverability, coincident with stability, over the velocity range of Mach 0.4 to Mach 1.8. The roll gains were chosen high enough to allow control for β ranging from $0°$ to $20°$, as occurs in the last stages of launch, but low enough to provide minimum interference with pitch during roll maneuvers.

2.3.3.6 <u>Initial Conditions at Launch</u> During a forward launch the major factors are α and $\dot{\theta}$. The roll rate $\dot{\phi}$ is considered minor for this condition. Figure 2.3.24 illustrates the initial boundary conditions for the forward launch. The boundaries were computed for the most stringent conditions, i.e., for α and $\dot{\theta}$ of the same sign.

For a side launch, as previously discussed, the roll system predominates. However, because of the transitory nature of the side launch conditions, the roll system does not dominate the control to the same extent as does the pitch system during a forward launch. The initial boundary conditions were computed, again for the most stringent conditions, and are illustrated in Figure 2.3.25.

The recordings (Figures 2.3.26 and 2.3.27) illustrate the recovery from arbitrary initial conditions in forward and in side launch.

2.3.4 YAW CONTROL SYSTEM A symmetrical lenticular object is conditionally stable and extremely underdamped in its yaw plane. However, when the basic lenticular form was modified for aerodynamic and packaging considerations, the missile became aerodynamically stable in the yaw plane for small angles of sideslip.

For a side launch ($\beta = 90°$ initially), the yaw aspects of the missile flight can be divided into three successive modes:

2.122

FORWARD LAUNCH
$M_o = 0.6$
$M_o = 0.4$

$\alpha_o = 0°$

$\alpha_o = 0°$

$\alpha_o = 5°$

$\alpha_o = 3°$

$\alpha_o = 0°$ $\alpha_o = 5°$

ROLL RATE (°/SEC)

PITCH RATE (°/SEC)

Figure 2.3.24

SIDE LAUNCH
$M_o = 0.4$

$\alpha_o = 0°$

$\alpha_o = 3°$

$\alpha_o = 5°$

ROLL RATE (°/SEC)
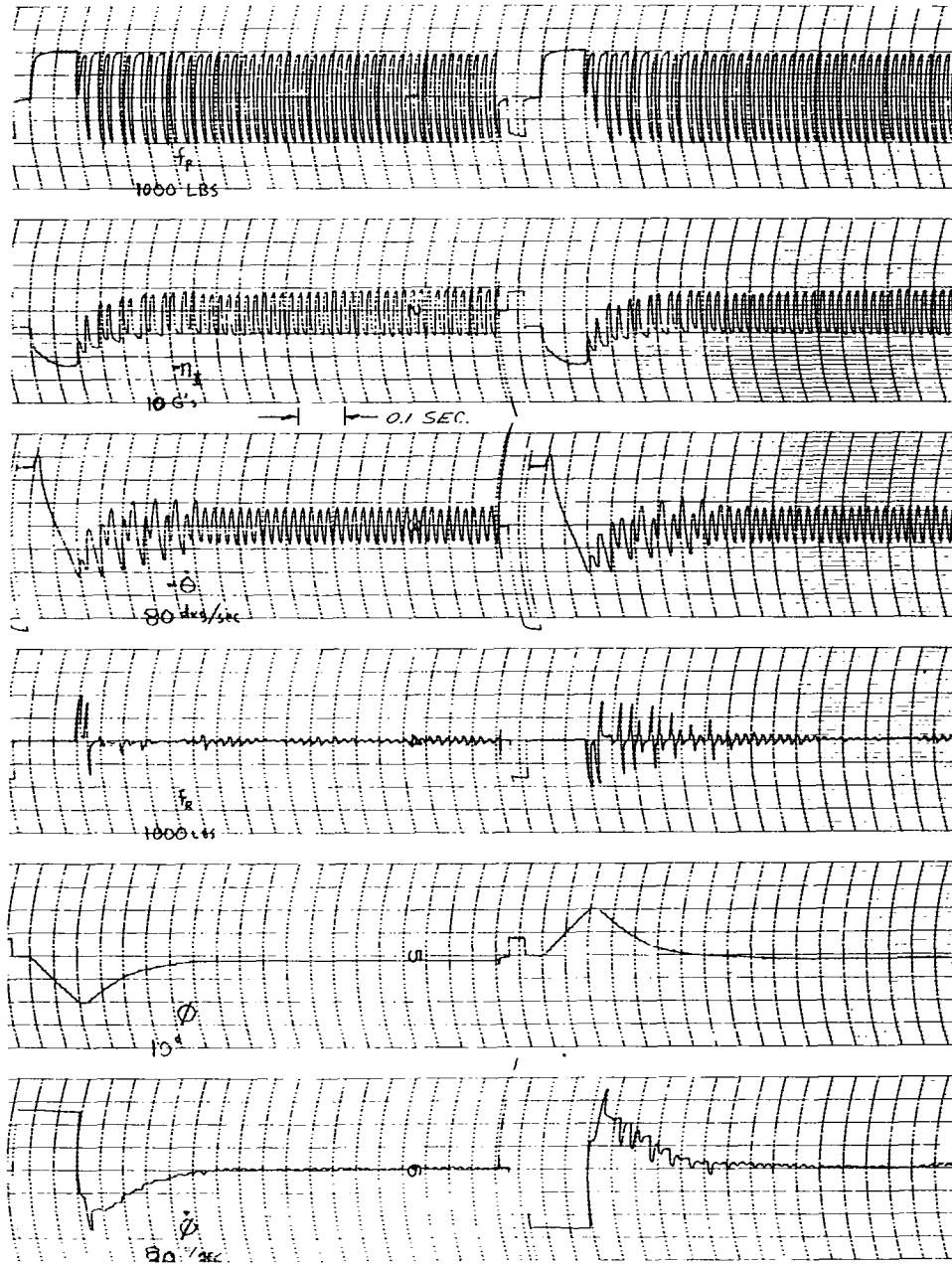
PITCH RATE (°/SEC)
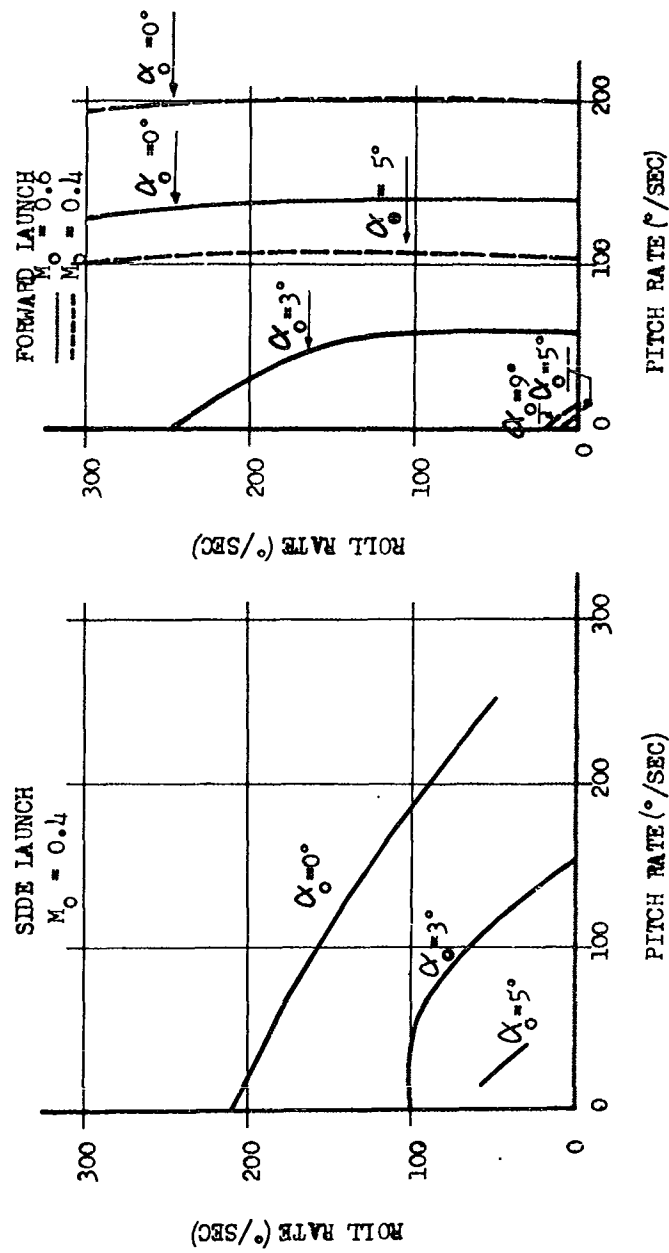
Figure 2.3.25

Initial Boundary Conditions
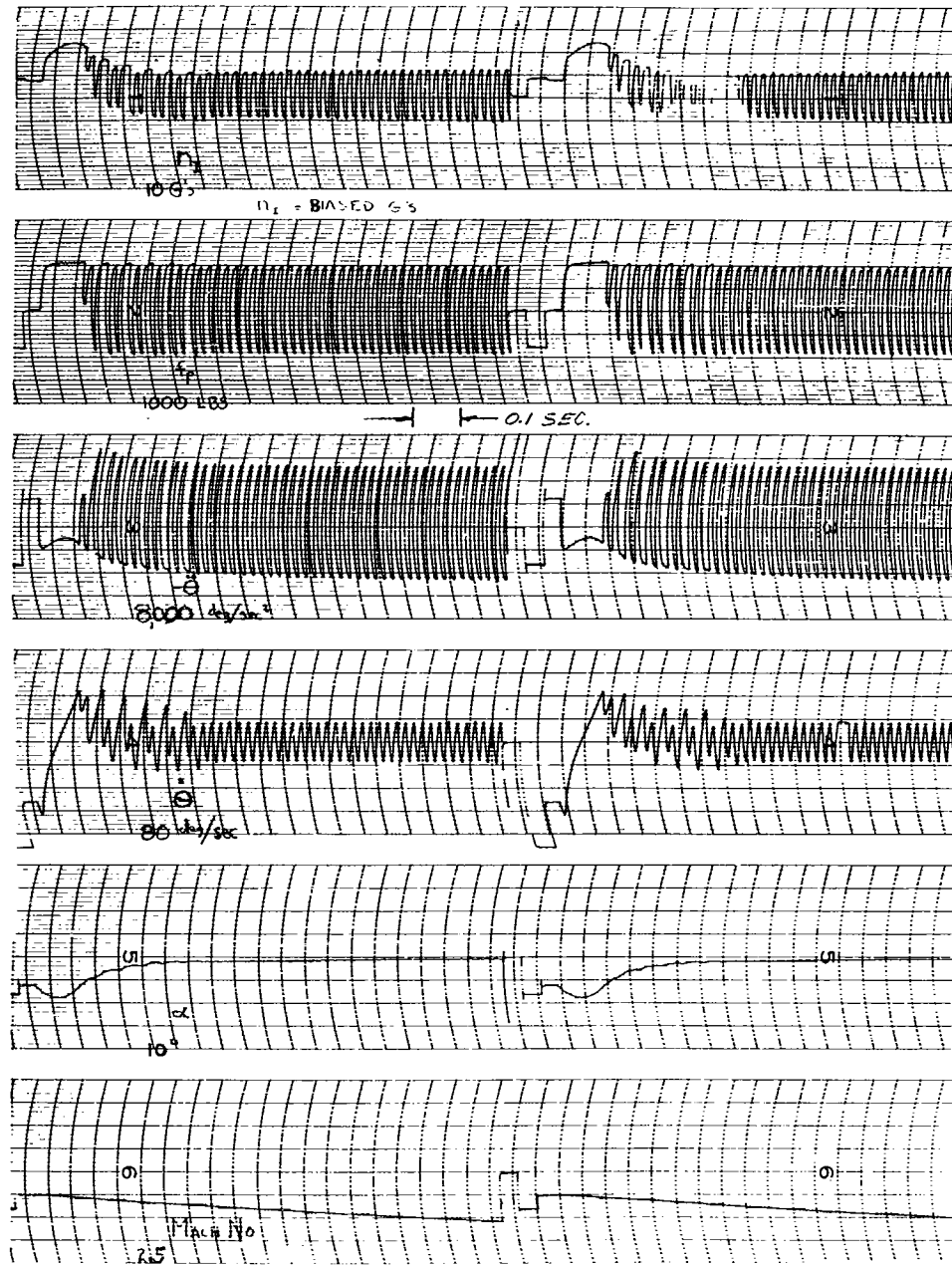
2.123

Figure 2.3.26a   Recovery From Initial Conditions, Forward Launch

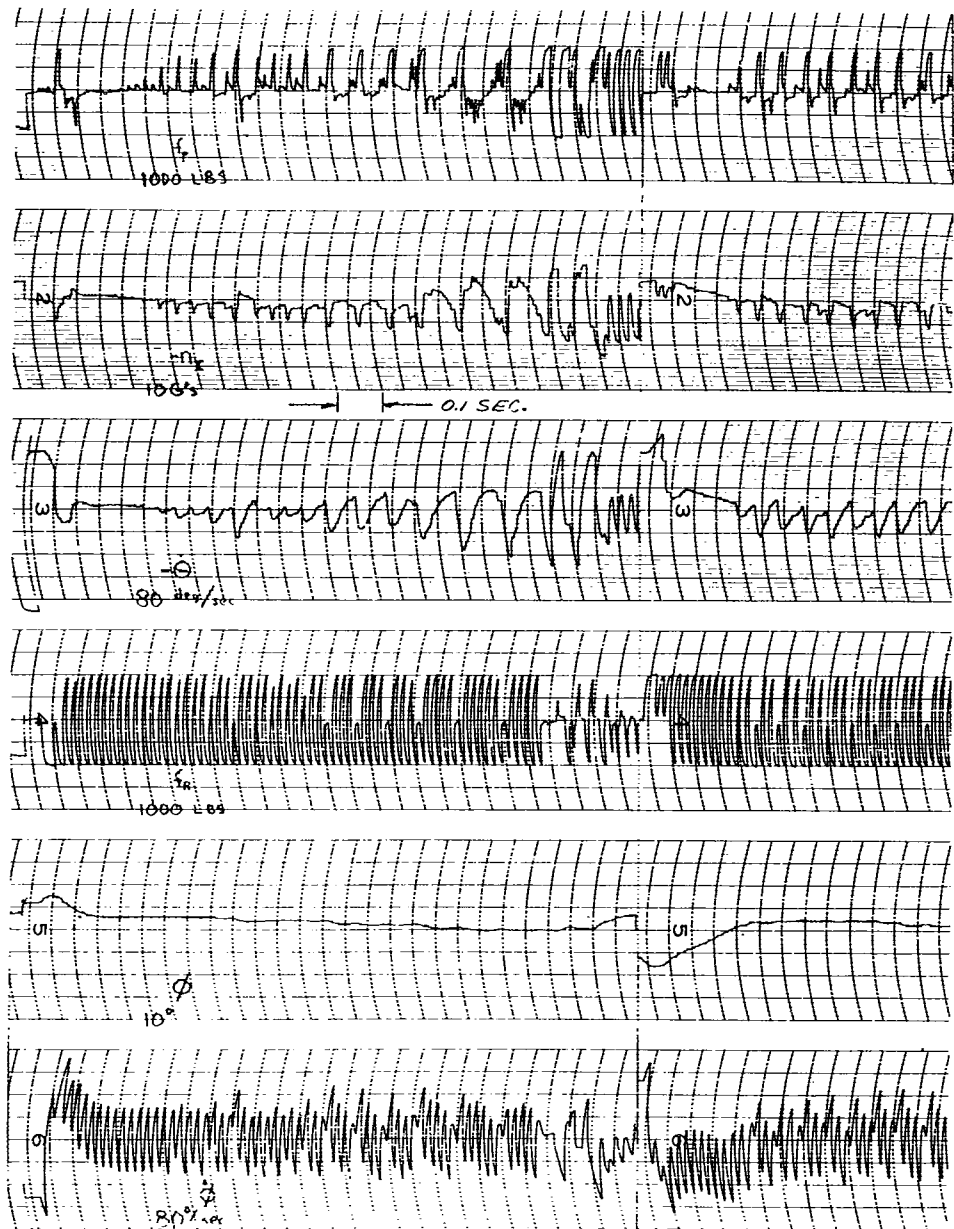Figure 2.3.26b   Recovery From Initial Conditions, Forward Launch

Figure 2.3.27a   Recovery From Initial Conditions, Side Launch
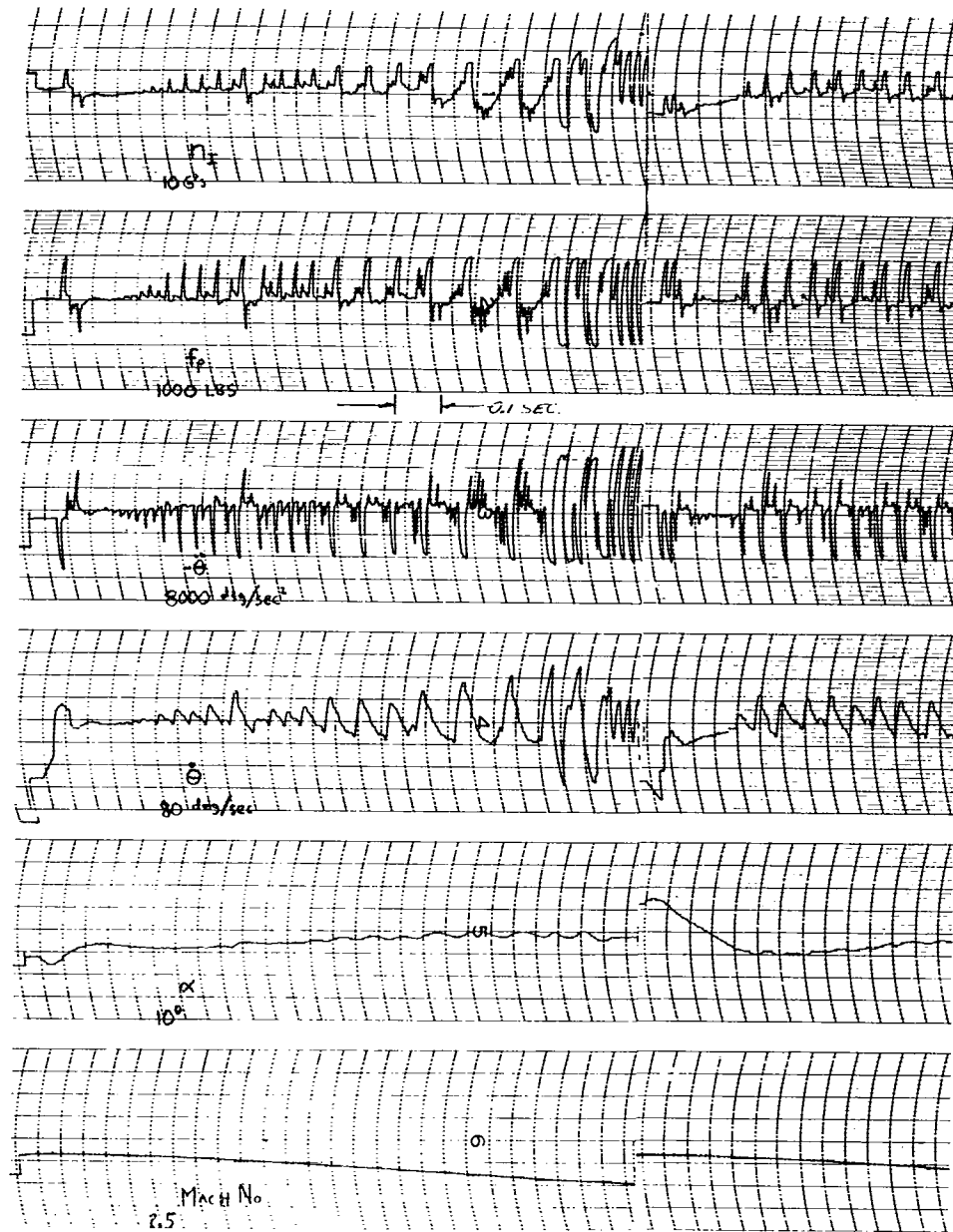
Figure 2.3.27b   Recovery From Initial Conditions, Side Launch

2.127

1. from the time of launch until the sideslip angle is reduced to the region in which the missile exhibits a restoring yaw moment,
2. from the end of mode 1 until the sideslip angle is zero, and
3. the remainder of the flight after the sideslip angle is zero.

For a discussion of the yaw autopilot, the distinction must be made between the yaw or sideslip angle (β) and the heading angle (ψ). The yaw angle (β) is that angle between the velocity vector and missile longitudinal axis. The heading angle (ψ) is that angle between the missile centerline and the desired direction of missile travel. The yaw autopilot must initially maintain the angle (ψ) as near zero as possible.

The yaw autopilot was designed considering each mode as a separate problem.

2.3.4.1 System Transfer Functions To satisfy the requirements of the side launch conditions, the missile longitudinal axis must maintain its initial direction. Yaw control is required here regardless of the stable or unstable properties of the aerodynamics. The direction of missile flight during mode 1 operation for a side launch is the vectorial sum of the initial launch velocity and the missile longitudinal velocity (due to the main propulsion). When the missile longitudinal velocity reaches a maximum, the sideslip angle (β) reaches a steady state value (primarily dependent upon launch velocity, thrust and drag) and the angular rate ($\dot{\beta}$) has decreased significantly. At this point, the reference angular position control is removed and β is reduced to zero by the restoring aerodynamic moment (mode 2 operation). Since the missile is inherently underdamped in the yaw plane, a rate control is required throughout the flight. The minimum instrument requirements for effective yaw control are tabulated below for each mode of operation.

mode 1	mode 2	mode 3
yaw angle	---	---
yaw angular rate	yaw angular rate	yaw angular rate

The yaw autopilot must maintain the initial launch heading (ψ) in the presence of the disturbing aerodynamic moment. This perturbation is a function of Mach number and sideslip angle. From the preliminary trajectory studies, this torque input (Figure 2.3.29) was determined as a function of time and included in the analog simulation as such. The block diagram of the yaw autopilot for the mode 1 operation is illustrated in Figure 2.3.28. During this portion of the flight (side launch), the yaw autopilot functions to regulate the heading angle ψ.

2.128
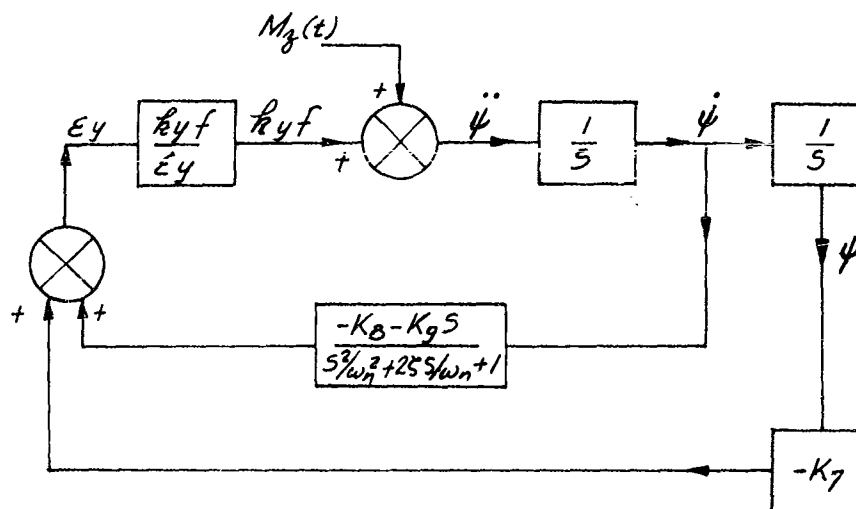
Figure 2.3.28 Yaw Autopilot for Mode 1 Operation (ψ Controller)

The equations which describe the mode 1 control system are

$$\varepsilon y = \frac{(-K_8 - K_9 S)\dot{\psi}}{S^2/\omega_n{}^2 + 2\zeta S/\omega_n + 1} - K_7 \psi \quad , \text{ and} \qquad (2.3.40)$$

$$\ddot{\psi} = k_y f + M_{\mathfrak{z}}(t) \qquad (2.3.41)$$

where

εy = control error,
ψ = heading angle, degrees,
f = reaction motor thrust,
k_y = proportionality constant,
$M_{\mathfrak{z}}(t)$ = torque disturbance,
β = sideslip angle, and

$$\frac{1}{S^2/\omega_n{}^2 + 2\zeta S/\omega_n + 1}$$ = rate gyro transfer function.

2.129
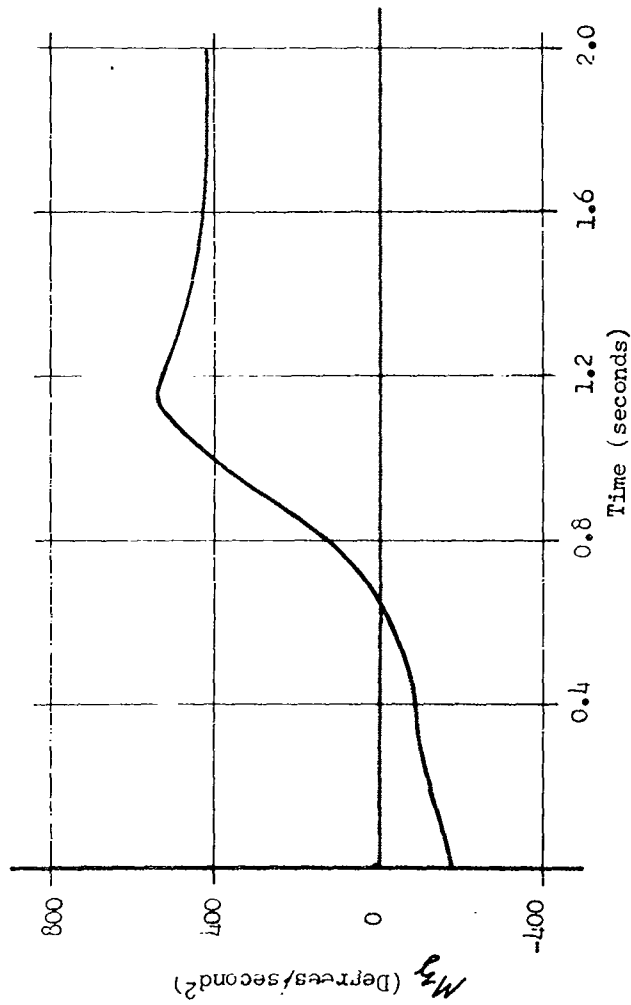
Figure 2.3.29 Equivalent Yaw Acceleration from Disturbance Torque (M_z)

2.130

$$\omega_n = 628 \text{ radians/sec.}$$
$$\zeta = 0.5$$

During mode 2 operation the position feedback is opened and the reference angular position is allowed to seek a value corresponding to $\beta = 0$. The system then becomes a β controller since the aerodynamic moment is restoring. Also, the value of acceleration feedback gain (K_9) is increased. The autopilot block diagram for the mode 2 operation is illustrated in Figure 2.3.30.
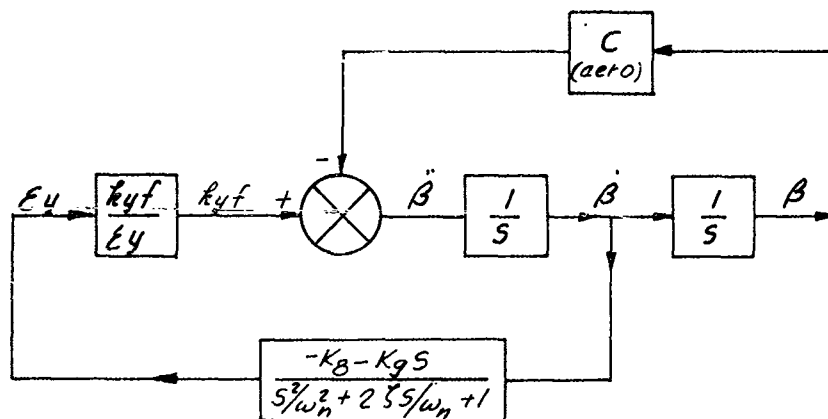
Figure 2.3.30 Yaw Autopilot for Mode 2 Operation (β Controller)

The equations which describe the mode 2 control system are:

$$\mathcal{E}y = \frac{-K_8 - K_9 S}{S^2/\omega_n^2 + 2\zeta/\omega_n + 1} \, \dot{\beta} \qquad\qquad (2.3.42)$$

$$\ddot{\beta} = k_y f - C\beta \qquad\qquad (2.3.43)$$

$$\text{where} \quad C = \frac{1481\lambda M^2 Sd \, C_{n\beta} \, (57.3)}{I_y}$$

I_y = yaw moment of inertia (31.7 slug-ft^2) full,

$C_{n\beta}$ = yaw moment coefficient $\approx$ 0.00014, and

β_0 = 20° (initial).

For the preliminary studies the yaw moment stability derivative $C_{n\beta}$, was considered to be linear with respect to β over the range $0° < \beta < 20°$. For the fixed flight conditions considered, (Mach 1.0) the approximation is sufficiently accurate. During all three modes the missile yaw aerodynamic damping was assumed negligible.

During the third mode, the controlled variable β is maintained at a minimum. The acceleration feedback is detrimental in this case and is therefore eliminated at the initiation of this phase of flight.

The autopilot schematic is the same as in the second mode above with the exception that K_9 is zero. Therefore,

$$\mathcal{E}_y = \frac{-K_\beta}{(S/\omega_n)^2 + 2\zeta S/\omega_n + 1} \tag{2.3.44}$$

During the preliminary studies a linear yaw autopilot was synthesized. This system, with assumed linear reaction control motors, resulted in adequate control of the airframe in the yaw plane. However, since non-linear reaction control motors are physically more feasible, very little effort was applied toward this preliminary investigation. The continued analyses utilized the performance specifications of the valve in accordance with the expectations of industry. The simulations considered the valve to be operated with a voltage driven torque motor. The use of a voltage source in place of the current source utilized in the pitch system added some additional time lag to the yaw system. However, this is not critical and additional hardware and electrical power is conserved.

The non-linear closed loop control system is represented by Figure 2.3.31. The dashed lines indicate electronic components utilized to conserve fuel. These additional components control the duty cycle of the reaction motor and can be adjusted to a compromise of fuel consumption and steady state oscillation of the controlled parameter. The electronic components (non-linear filters) can best be described by the sketches shown in Figure 2.3.32. The duration of control thrust is a function of the time $\mathcal{E}_y$ remains one sided, the relative magnitude of b/L and the time constant, $\mathcal{T}$.

2.3.4.2 <u>Yaw System Synthesis</u> The autopilot gains were first optimized for the model flight condition with $\mathcal{T}_0$ = 0.01 sec. During the initial computer studies, only angular rate and position feedback control was considered, (i.e., K_9 = 0). The propellant consumption,
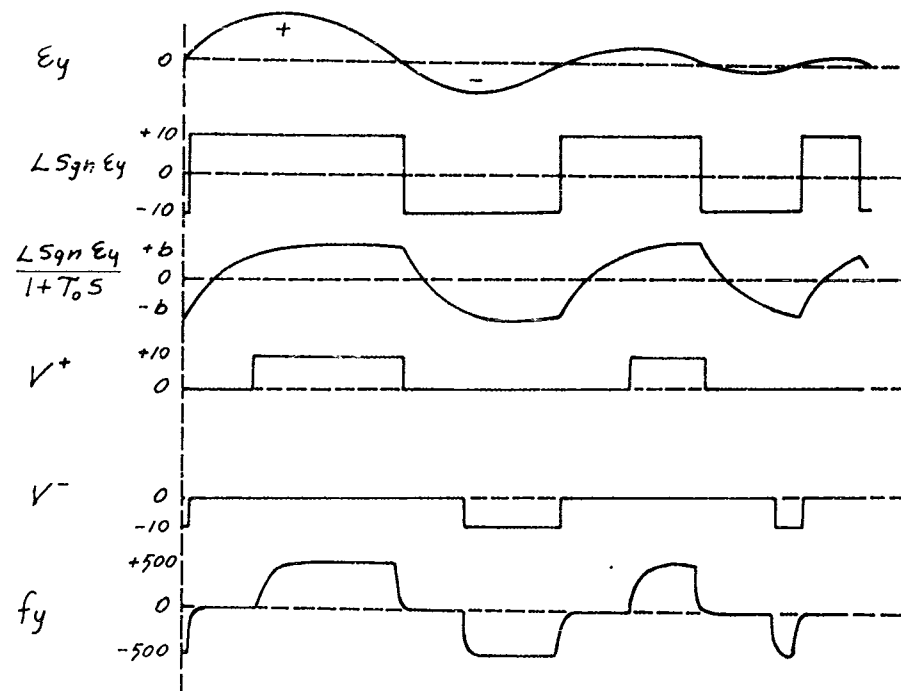
Figure 2.3.31   Yaw Autopilot Block Diagram

Figure 2.3.32   Effects of Non-Linear Filter

Table 2.3.3   Switching Logic for Yaw Autopilot

Mode	Parameter	Relay Position
1	ψ	B
2	β	A --K_7 = 0
3	β	A --K_7 = 0 K_9 = 0

maximum excursion and the peak-to-peak ψ oscillations were studied for various ratios of the feedback gains (K_8/K_7). The results are illustrated in Figure 2.3.33. The cross hatched area in the left side of the graph indicates those feedback ratios which cause unstable oscillations in ψ, (note the rapid increase of the peak-to-peak values of steady-state oscillations as the feedback ratio approaches the critical area).

Further studies were conducted to determine the effect of utilizing acceleration feedback in addition to the rate and position feedback terms. The propellant consumption and maximum ψ excursions were evaluated for varying feedback ratios. However, for these studies, the ratios of K_8 to K_7 were held fixed while the ratio of K_9 to K_7 was varied. The fixed ratios ($K_8/K_7 = 0.15$) are illustrated in Figure 2.3.34. The addition of the acceleration feedback resulted in a considerable decrease in both the propellant consumption and the maximum ψ excursion.

A $K_8/K_7 = 0.025$ D $K_8/K_7 = 0.15$

B $K_8/K_7 = 0.50$ E $K_9/K_7 = 0.20$

C $K_8/K_7 = 0.10$ F $K_8/K_7 = 0.25$

The rapidity with which the ψ response approaches a steady-state condition was studied next. The evaluation was conducted for a range of K_9/K_7 values at each of the K_8/K_7 values tabulated above. These results are presented in Figure 2.3.35. The range of acceptable feedback gain ratios are listed in Table 2.3.4. The gain ratios associated with run code D were selected for the mode 1 operation. Since the ratio of the feedback gains governs the control, the selection of the individual values will be dictated only by the desired voltage levels in the autopilot.

Table 2.3.4 Acceptable Feedback Gain Ratios for Mode 1 Operation

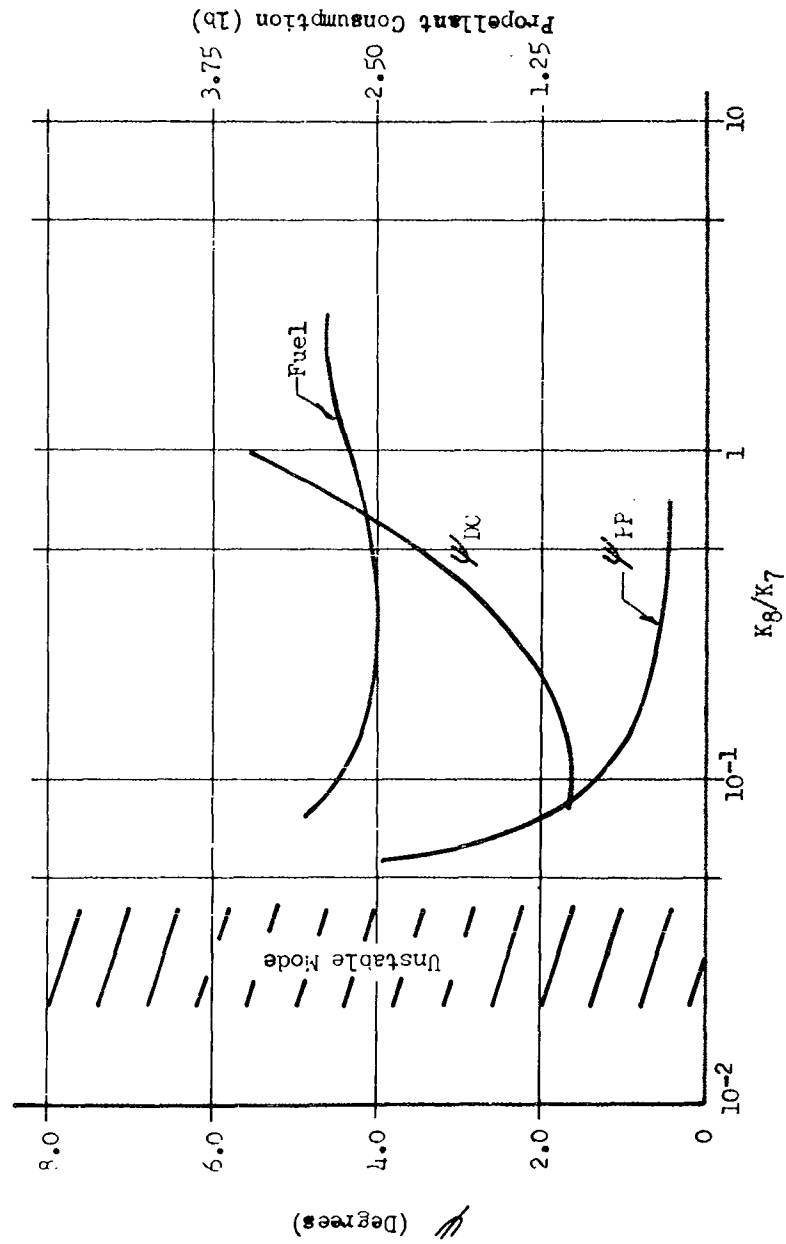| Run Code	K_8/K_7	K_9/K_7	Remarks
A	0.025	7.5 (10^{-4})	Marginally acceptable, however unstable if K_9 is lost
B	0.05	7.5 (10^{-4})	marginal stability if K_9 is lost
C	0.10	1.25 (10^{-3})	acceptable
D	0.15	1.70 (10^{-3})	acceptable
E	0.20	2.25 (10^{-3})	acceptable
F	0.25	3.5 (10^{-3})	steady-state error excessive if K_9 is lost

Figure 2.3.33   Effect of Feedback Ratios on Heading
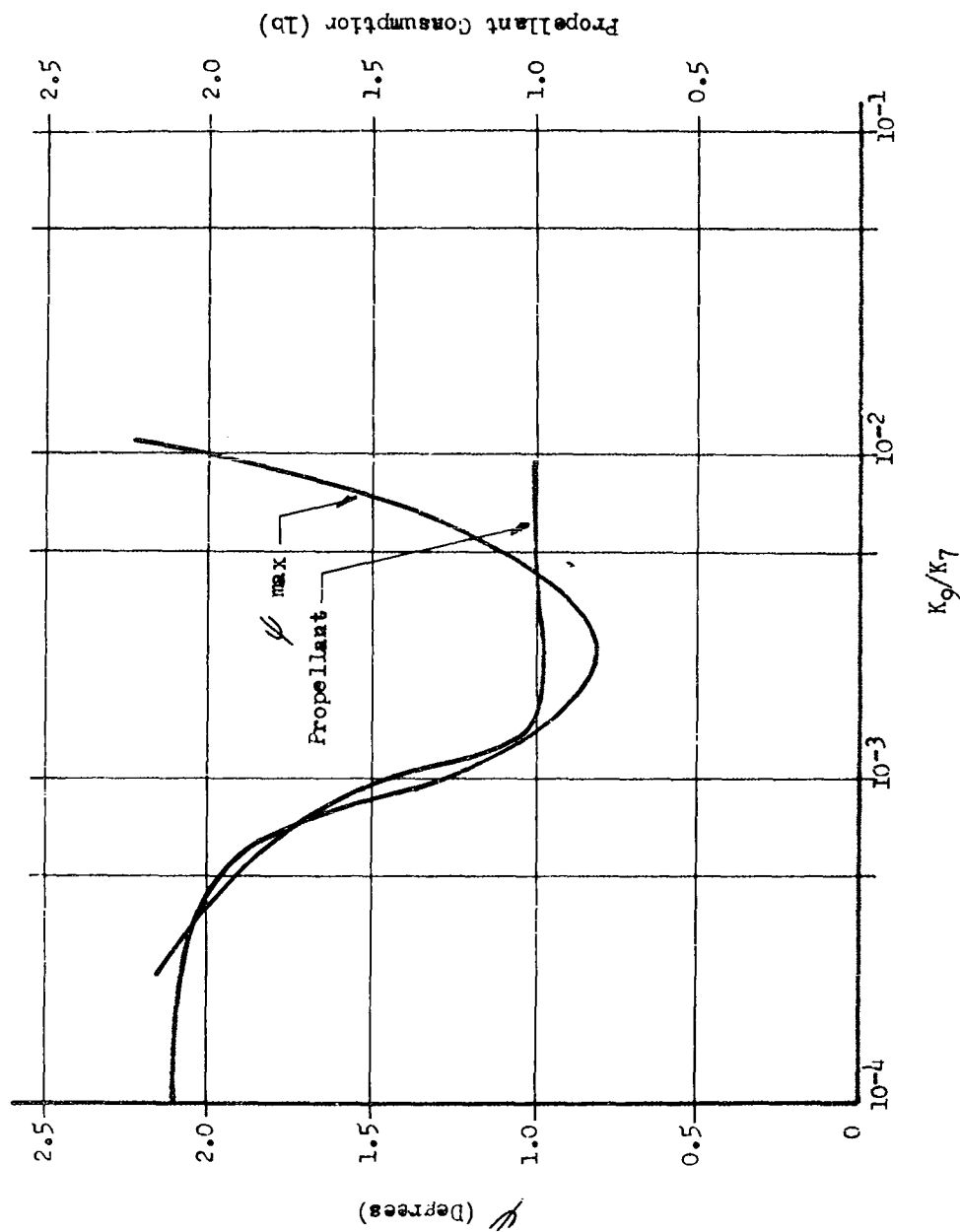Angle Excursion and Propellant Consumption

Figure 2.3.34 Effect of Acceleration Feedback on Heading Angle
Excursion and Propellant Consumption

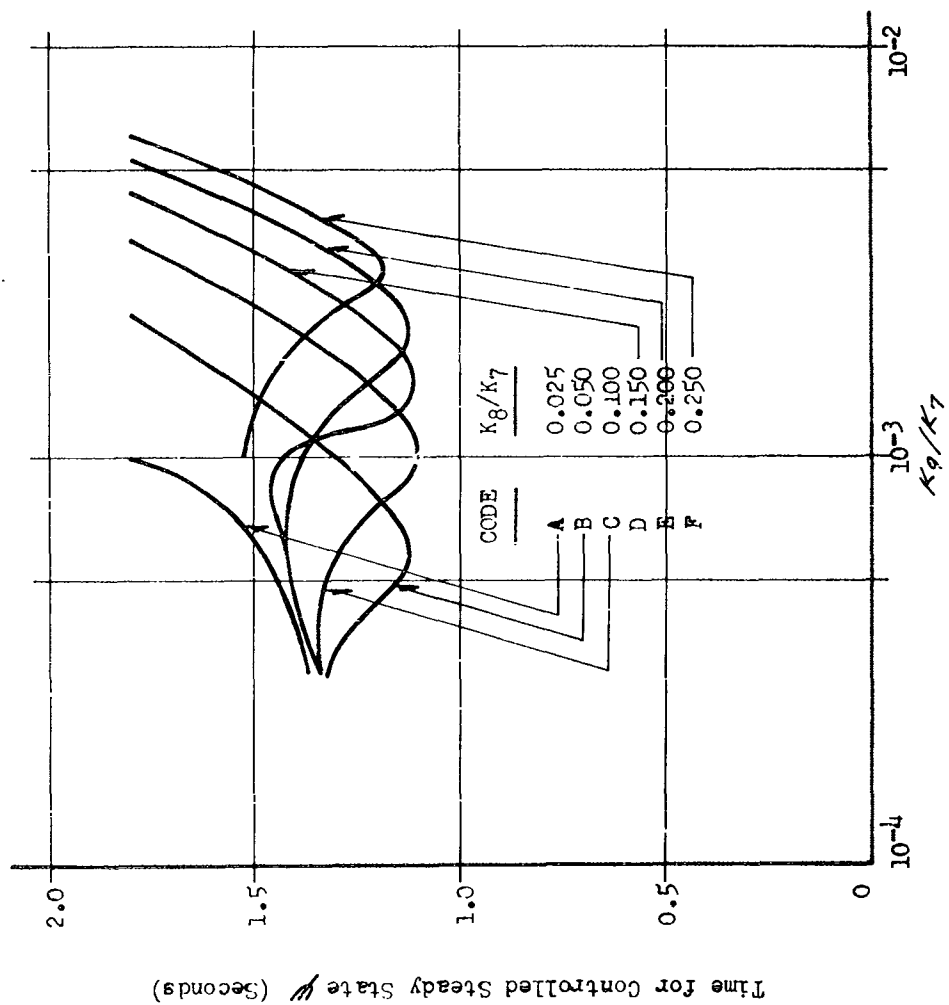Flight Duration = 2 sec   Mode 1 Code D $K_8/K_7 = 0.15$

Figure 2.3.35 Effect of Acceleration Feedback on Heading Angle
Response Time Mode I

2.138

The time constant (T_o) of the non-linear filter (duty cycle electronics), was doubled and halved and the effects were noted as changes in propellant consumption and ψ excursion for a two-second flight. These results are tabulated below.

Table 2.3.5 Effect of T_o on ψ Excursion and Fuel Consumption for Mode 1

Code	K_8/K_7	K_9/K_7	$T_o = 0.005$ sec		Final Design Value $T_o = 0.010$ sec		$T_o = 0.02$ sec	
			ψ	Fuel(lb)	ψ	Fuel(lb)	ψ	Fuel(lb)
A	0.025	7.5 (10^{-4})	0.3°	1.4	0.85°	1.0	2.3°	1.0
B	0.05	7.5 (10^{-4})	0.3°	1.6	0.6°	1.0	1.6°	0.9
C	0.10	1.25 (10^{-3})	0.5°	1.7	0.6°	0.95	1.6°	0.75
D	0.15	1.50 (10^{-3})	0.6°	1.8	0.9°	1.0	1.7°	0.8
D	0.15	1.75 (10^{-3})	0.7°	1.9	0.85°	1.0	2.0°	0.8
E	0.20	3.00 (10^{-3})	0.7°	2.0	0.9°	1.0	3.3°	0.75
F	0.25	4.6 (10^{-3})	0.6°	1.8	1.0°	1.0	4.4°	0.6

The primary objective of the autopilot design during Mode 2 operation is that β be brought to a minimum steady state in the least possible time. Since the control equation utilizes rate and acceleration feedback with no position control, it is only necessary to investigate ratios of K_9 to K_8. Therefore the autopilot rate gain remained unchanged while K_9 was adjusted for minimum response time. Two time intervals were recorded during the computer studies; the time required for β to decrease to 2°, and the time required for β to decrease to 5°. The computer results are shown in Figure 2.3.36. For optimum control K_9 must be increased by at least a factor of 4 times its mode 1 value.

Since a minimum number of gain changes is desired, the transition from mode 2 to mode 3 was considered before finalizing the mode 2 value of K_9. For this study, β was allowed to assume a steady state value during the mode 2 computer runs. Figure 2.3.37 illustrates the maximum excursion of β as a function of K_9 for the mode 3 operation. These results indicate that a value of K_9 can be chosen which is compatible with both modes of operation. The extreme gradient on either side of the minimum (see Figure 2.3.37) becomes critical when noise levels and gain tolerances are considered. One solution to this
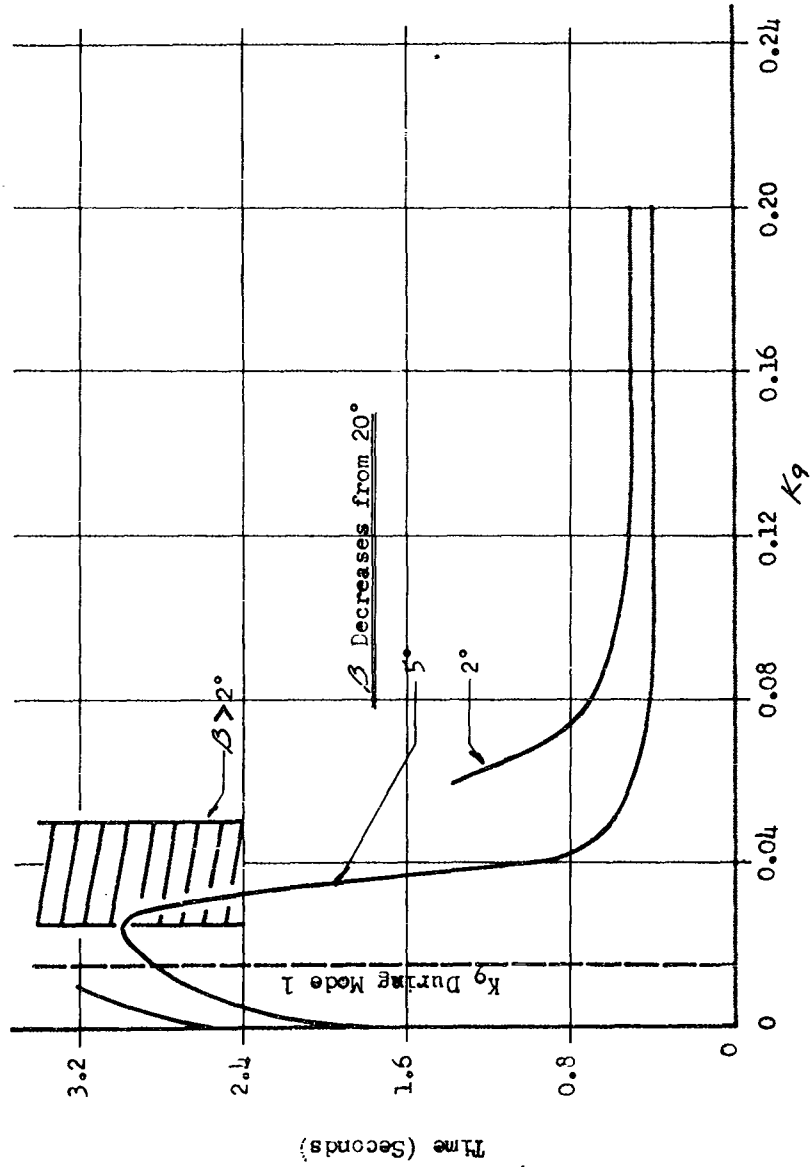
Figure 2.3.36 Effect of Acceleration Feedback on Yaw Angle
Response time

Mode 2 $K_8 = 1.5$
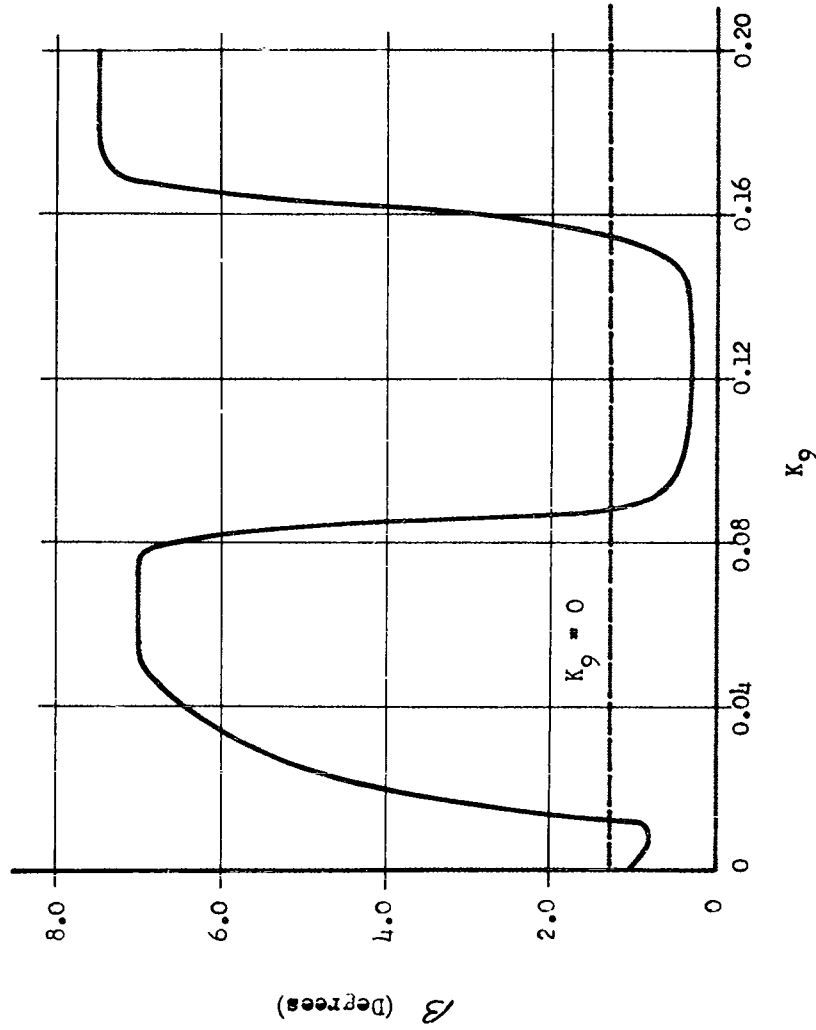
Figure 2.3.37 Effect of Acceleration Feedback on Yaw
Angle Excursion

Flight Duration = 2.0 sec   Mode 3 $K_8 = 1.5$

problem results from eliminating the acceleration feedback term for both mode 2 and mode 3. However with no acceleration feedback in mode 2, β requires a relatively long time to reach zero. The preferable alternate solution results from eliminating the K_9 factor for the mode 3 phase. If the transition occurs before β reaches zero degrees, the angle will still seek zero regardless of a reasonable rate gyro noise and missile gain tolerances. The propellant consumption for a two second portion of the flight (during mode 2 and mode 3) is illustrated in Figure 2.3.38.

The mode 1 duration and the switching time will be compatible with the roll-pitch gain change. At this time β is approximately 20° and the missile velocity is approximately Mach 1.0. The duration of mode 2 is approximately 0.50 seconds.

Switching the time constant of the non-linear filter is necessary during the transition from mode 1 to mode 2. The capacitor is changed from 0.01 uf to 0.025 uf. Table 2.3.6 shows the effect of this switch on the time required to decrease β from 20° to 5° and from 20° to 2°.

Table 2.3.6 The Effect of τ_0 on Mode 2 β Response

K_9	$\tau_0 = 0.01$ sec		$\tau_0 = 0.025$ sec		$\tau_0 = 0.05$ sec	
	t_5 sec	t_2 sec	t_5 sec	t_2 sec	t_5 sec	t_2 sec
0.0625	never	never	0.5	never	0.35	2.0
0.080	never	never	0.42	0.7	0.35	1.5
0.100	never	never	0.40	0.60	0.70	1.2
0.125	never	never	0.40	0.50	0.75	1.2
.0.15	never	never	0.40	0.50	0.75	1.2
0.18	never	never	0.40	0.50	0.70	1.2

t_5 time in seconds for β to decrease from 20° to 5°
t_2 time in seconds for β to decrease from 20° to 2°

Mode 3 operation is comparable to the forward launch case. The yaw autopilot can control the missile during forward launch with rate control alone.

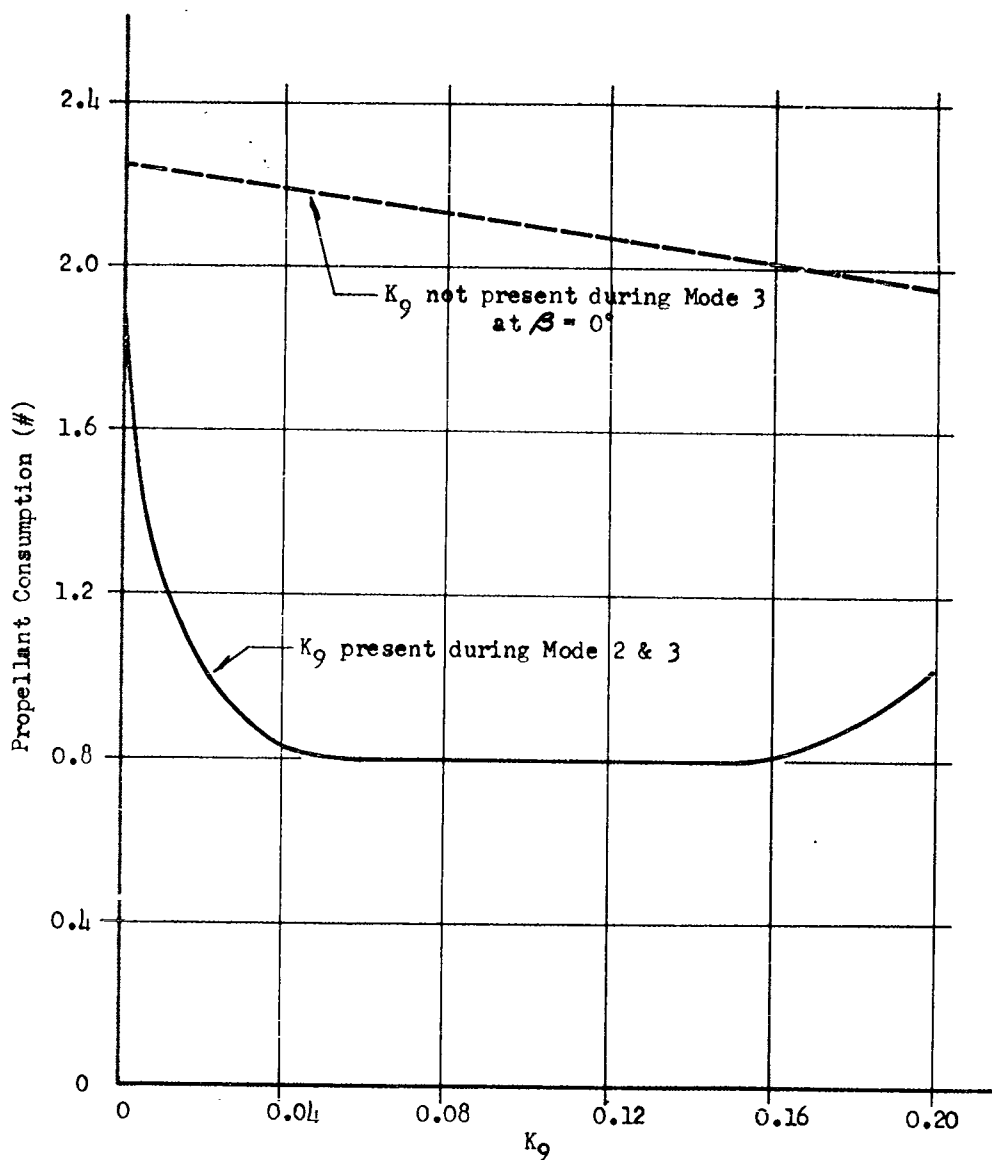A summary of the switching and gains is given in Table 2.3.7 below.

Figure 2.3.38 Effect of Acceleration Feedback on
Propellant Consumption

Flight Duration = 2 sec   Mode 2 & 3   K_8 = 1.5

Table 2.3.7 Final Yaw Autopilot Gains, τ_0 and Switching Times

time, seconds	K_7	K_8	K_9	τ_0	Capacitor
0	10	1.5	0.015	0.010	μf
1.1	0.0	1.5	0.15	0.025	μf
1.6	0.0	1.5	0.0	0.025	μf

The steady state (mode 3) dither frequency was determined analytically by the describing function technique (see Figure 2.3.39) as 4.95 cps compared with the dither of 5.1 cps determined experimentally.

This yaw autopilot was incorporated into the simulated three-dimensional time-varying system for verification of the design. The yaw control results compared closely with the results of this section. During a ten second flight (side launch) simulated on the combined system, the yaw reaction motors used 5 lb of propellant.

The system responded acceptably with 2 volts rms of noise (rate gyro noise comparable to 13.3°/sec (rms value). In fact, the noise influenced the duty-cycle such as to improve the propellant consumption. This improvement is verified by Figure 2.3.40.

2.3.5 THREE-DIMENSIONAL SIMULATION With the exception of an actual flight test, the most reliable method of checking a missile system lies in a simulated flight using the complete parametric description of a time-varying three-dimensional (3-D) simulation. The unique launch capabilities of FYE WACKET dictated an exacting approach to the 3-D simulation problem, i.e., the approximations valid for the simulation of more conventional missiles are inadequate. The 3-D simulation, essential to the final autopilot/control studies of a lenticular missile, is described in this section.

2.3.5.1 General Description of the 3-D Simulation The missile is simulated with six degrees of freedom on an analog computer. Flights are simulated from both a forward and side launch position for a Mach number range of zero to two and for an angle of attack variation of zero to ten degrees. The primary inputs are the booster rocket-motor thrust and the command signals for pitch and roll maneuvers. From the numerous available outputs, studies can be conducted on the autopilot design, response characteristics, propellant consumption, missile launch problems, trajectories, etc.

2.144

$$G(s) = \frac{K s e^{-0.005 s}}{(s^2/_{37}+1)(0.0045+1)(s^2/(628)^2 + s/_{628}+1)}\left(1+e^{\pi/_2 \omega}\right)$$

$$\underline{/N(\alpha)} = -\pi + \frac{\omega \tau}{2} \ln\frac{1}{4}\left(1-\frac{b^?}{L^2}\right)\left(1+e^{\pi/_2 \omega}\right)$$

$$\tau = 0.025 \quad b = 9 \quad L = 10$$

$/G(s)$

$-\left(/N(\alpha)\right)^{-1}$

Frequency (Radians/Second)
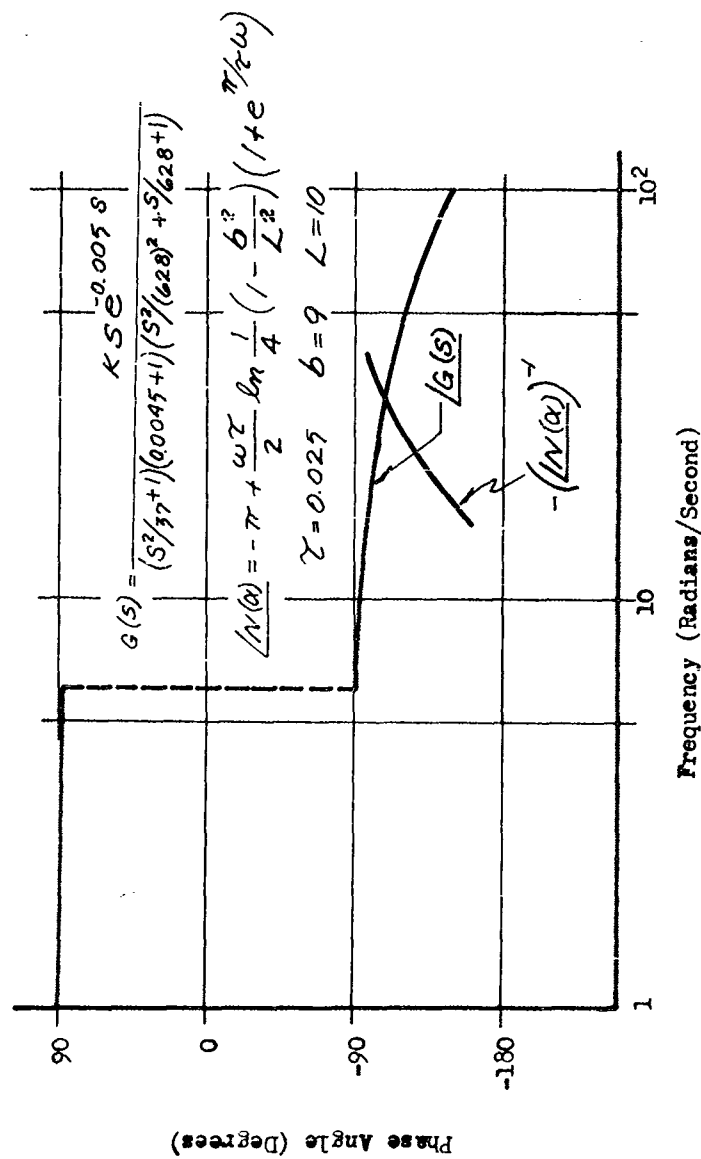
Figure 2.3.39 Mode 3 Dither Frequency
(Describing Function Technique)

Phase Angle (Degrees)

2.145
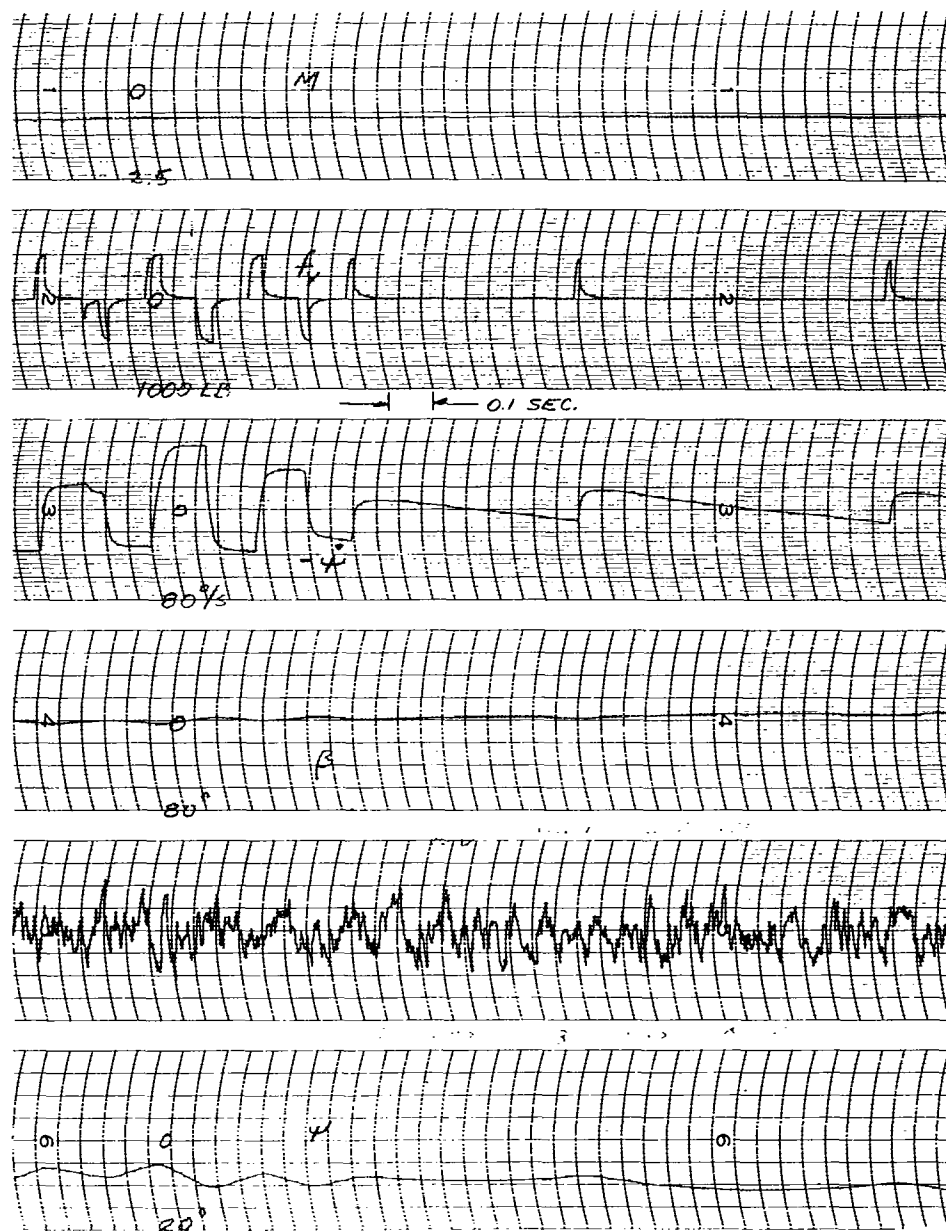
Figure 2.3.40   Effect Of Noise In Yaw Channel

To completely simulate the missile it was necessary to utilize circuits employing five rectangular coordinate resolvers, ten servo-multipliers, over 100 operational amplifiers, and a variety of auxiliary equipment for read-out and simulation check-out purposes. The auto-pilot loops for pitch, roll and yaw plus the response characteristics of all six reaction motors are completely simulated. The variations in missile weight, moment of inertia, and center-of-gravity location are also included.

The 3-D simulation was utilized to study the complete control prob-lem and to select the final autopilot parameters. A high degree of confidence was attained for the selection of autopilot parameters when successful simulated flights were run on the analog computer. These simulated flights were conducted in the presence of all of the cross coupling terms (especially those resulting from the pitch and roll systems utilizing common reaction motors) and all of the parameter variations.

Detailed analyses were also conducted for the launch phase to establish the autopilot parameters and to determine the operating boun-dary conditions for the finalized autopilot. The efforts were next directed toward the post burn-out phase to study the maneuvering capa-bilities of the FTV. The studies, analyses and tests all culminated into the final computer runs during which the missile trajectories were established for the future flight test program.

2.3.5.2 Coordinate Systems and Equations of Motion   The coordinate systems and the equations of motion were developed by first considering the relationships between the missile-body fixed-coordinates and the velocity vector. Euler transformations were established between the body axes, the wind axes and the earth axes. The preliminary studies for the 3-D simulation included a detailed analysis of the functions to be simulated and axis system most suited to the particular function. For example, the translational equations of motion are most conveniently solved in the axis system affixed to the wind vector. These wind axes translational equations are derived from those of the body axes. The angle of sideslip and the angle of attack are computed as the integrated difference between the angular rates of the body and wind axes.

The body coordinate system is illustrated in Figure 2.3.41. The arrows attached to the x, y and z axes denote the positive direction as defined by the right hand rule. The origin for all coordinate systems is located at the missile center of gravity. The velocity vector is related to the body axes through the angles β (sideslip) and α (angle of attack). The velocity vector is expressed in the body axes by the components u, v and w directed along the x, y and z axes respectively. The missile angular rates are resolved along the x, y and z axes by the rates p, q and r. The positive direction of the rates is also defined

Figure 2.3.41   Body and Wind Axes Systems

by the right hand rule and shown in Figure 2.3.41. The moments of inertia of the missile, expressed about the x, y and z axes, are I_R, I_P and I_Y, respectively. The body axes of the PYE WACKET configuration are a principal axis system and therefore the products of inertia are zero.

Utilizing the above definitions, the missile equations of motion, expressed as the total force and moment exerted on the missile, are:
the body axis translational equations,

$$\Sigma F_X = m\left[\dot{u} + wq - vr\right], \tag{2.3.45}$$

$$\Sigma F_Y = m\left[\dot{v} + ur - wp\right], \tag{2.3.46}$$

$$\Sigma F_Z = m\left[\dot{w} + vp - uq\right]; \text{ and} \tag{2.3.47}$$

the body axis rotational equations,

$$\Sigma M_X = I_R\dot{p} + (I_P - I_Y)qr, \tag{2.3.48}$$

$$\Sigma M_Y = I_P\dot{q} + (I_Y - I_R)pr, \text{ and} \tag{2.3.49}$$

$$\Sigma M_Z = I_Y\dot{r} + (I_R - I_P)pq. \tag{2.3.50}$$

A derivation of these equations is given in Reference 4.28. The outputs or computed functions from these equations are u, v, w, p, q and r and the inputs are the forces F and the moments M. The inputs are composed of the control forces F, the aerodynamic forces A, the weight W, the control moments T, and the aerodynamic moments M. A computer solution is possible here since there are six non-linear equations and six unknowns. The weight W acts through the missile c.g., however, the body axes orthogonal components of W can be determined only by relating the body axes to the earth axes.

From the computed values, u, v and w, the total velocity, V, can be determined and the angles α and β defined. From the geometry of Figure 2.3.41,

$$\mathcal{U} = V \cos \beta \cos \alpha,$$

$$\mathcal{N} = V \sin \beta \cos \alpha, \text{ and}$$

$$\omega = V \sin \alpha.$$

A solution of these equations yields,

$$V = \sqrt{\mathcal{U}^2 + \mathcal{N}^2 + \omega^2}$$

$$\alpha = ARC\,SIN\,\frac{\omega}{V} \qquad , \text{ and}$$

$$\beta = ARCTAN\,\frac{\mathcal{N}}{W} .$$

The quantities V, α and β are now used to compute the aerodynamic forces (A) and moments (M).

The control forces and moments are generated by the booster motor and the reaction control motors. The force along the x-axis, P_x, is simply the thrust from the booster motor. The forces along the y and z axes, P_y and P_z, and the moments T_x, T_y and T_z result from the control thrust produced on command from the autopilot.

Specifying the relationship of the body to earth axes, the autopilot control equations and the aerodynamic force and moment characteristics would complete the requirements for the 3-D simulation of the PYE WACKET missile. However, since the equations are solved by an analog computer, there are several objections to simulating the equations in their present form. Some of these problem areas are precipitated by the unique characteristics of the PYE WACKET missile.

For studies of the conventional cylindrical type missile, the approximation is normally valid that the angles α and β are small and hence

$$u = V,$$

$$\beta = \frac{\mathcal{N}}{V} \quad , \text{ and}$$

$$\alpha = \frac{\omega}{V} .$$

This approximation results in a considerable simplification of the translational equations of motion. However considering the omnidirectional launch capability of PYE WACKET, it is axiomatic that β is not always small. Therefore the body axes translational equations of

motion remain complex by virtue of all of the cross products. Since V, α and β are inputs for the aerodynamic computations, it is absolutely essential that they be accurately simulated.

The computation of the missile coordinates in the earth axes from the body axes components of rates and angular velocities is rather complex and requires at least twelve multiplications. The objections are twofold: multipliers are at a premium because of their demand for aerodynamic computation and many multiplications reduce the accuracy of computation.

If the simulation is developed in the body axes then it is also desirable to compute the aerodynamic forces and moments in the same axis system. It was estimated prior to the wind tunnel tests that the aerodynamic coefficients C_l, C_M, C_A, and C_Y would exhibit sinusoidal characteristics as a function of sideslip angle, β, to about 90°. It was also assumed that the coefficients C_N and C_n would be relatively insensitive to variations in sideslip angle. The preferable procedure would be to specify the aerodynamic coefficients in an axes system affixed to the velocity vector since for constant Mach numbers and angle of attack all coefficients should be relatively constant with varying β. However the remaining difficulty arises from the transformation from wind axes to body axes. A compromise was made for the final simulation.

The stability axis system, used for the final simulation, is obtained by rotating the xy body axes about the z-axis through the angle β (see Figure 2.3.41). The angular rates are denoted as p_s, q_s and r_s with the positive direction of each defined by the right hand rule. The transformation of an arbitrary vector $\overline{H}$ from the body axes to the stability axes is computed from:

$$\begin{bmatrix} H_{xs} \\ H_{ys} \\ H_{zs} \end{bmatrix} = \begin{bmatrix} \cos\beta & \sin\beta & 0 \\ -\sin\beta & \cos\beta & 0 \\ 0 & 0 & 1 \end{bmatrix} \begin{bmatrix} H_x \\ H_y \\ H_z \end{bmatrix} \qquad (2.3.51)$$

The inverse is computed from:

$$\begin{bmatrix} H_X \\ H_Y \\ H_{\ell} \end{bmatrix} = \begin{bmatrix} \cos\beta & -\sin\beta & 0 \\ \sin\beta & \cos\beta & 0 \\ 0 & 0 & 1 \end{bmatrix} \begin{bmatrix} H_{XS} \\ H_{YS} \\ H_{\ell S} \end{bmatrix} \quad (2.3.52)$$

The wind axes system is obtained by rotating the x_S z_S axes about the y_S axis through an angle $-\alpha$. Since the new x_w axis coincides with the velocity vector, the component velocities are $u_w = V$, $v_w = 0$ and $w_w = 0$. The wind-axis system contains the angular rates p_w, q_w and r_w with the positive directions again defined by the right hand rule. The transformation matrix from a vector in the body axes to the equivalent in the wind axes is stated below.

$$\begin{bmatrix} H_{x_w} \\ H_{y_\omega} \\ H_{\ell_\omega} \end{bmatrix} = \begin{bmatrix} \cos\beta\cos\alpha & \sin\beta\cos\alpha & \sin\alpha \\ -\sin\beta & \cos\beta & 0 \\ -\sin\alpha\cos\beta & -\sin\alpha\sin\beta & \cos\alpha \end{bmatrix} \begin{bmatrix} H_x \\ H_y \\ H_{\ell} \end{bmatrix} \quad (2.3.53)$$

The translational equations of motion in the wind axes are expressed by the following:

$$\Sigma F_{x_W} = m\dot{V},$$

$$\Sigma F_{y_W} = mVr_W \quad , \text{ and}$$

$$\Sigma F_{\ell_W} = -mVq_W .$$

The equations are much simpler than their counterparts in the body axes. Expressing the rotational equations of motion in the wind axes does not result in a simplification. Furthermore, since the wind axes do not represent a principal axis system, the moments of inertia are functions of α and β and the products of inertia are not zero. Therefore, the rotational equations are best solved in the body axes.

The computation of the angles α and β is greatly simplified if knowledge of q_w and r_w is available. The equations relating these

functions are developed in the following sequence:

$$\dot{\alpha} = q_s - q_w$$

By substituting for q_s from the stability to body transformation,

$$\dot{\alpha} = -p \, SIN \, \beta + q \, COS \, \beta - q_w . \qquad (2.3.54)$$

Equation (2.3.54) is an exact representation of $\dot{\alpha}$. The equation for β is developed in a similar manner starting with

$$\dot{\beta} = r_s - r.$$

But

$$r_s = r_w \, COS \, \alpha + p_w \, SIN \, \alpha$$

Hence

$$\dot{\beta} = r_w \, COS \, \alpha + p_w \, SIN \, \alpha - r . \qquad (2.3.55)$$

Equation (2.3.55) is an exact representation of $\dot{\beta}$.

To complete the simulation of the $\dot{\beta}$ equation, the wind axis rate p_w must be computed. The angular rate about the velocity vector is related to the stability and body axes components as follows:

$$p_s = p_w \, COS \, \alpha - r_w \, SIN \, \alpha = p \, COS \, \beta + q \, SIN \, \beta ,$$

from which,

$$p_w = \frac{r_w \, SIN \, \alpha + p \, COS \, \beta + q \, SIN \, \beta}{COS \, \alpha} \qquad (2.3.56)$$

Equation (2.3.56) presents no simulation difficulty because α is a small angle.

The earth axis system (**XYZ**) is a set of right-handed orthogonal coordinates with the XY plane tangent to the earth's surface (see Figure 2.3.42). The missile weight vector is always parallel to the Z-axis. The missile velocity components along the earth axes are v_X, v_Y and v_Z and the position coordinates are S_X, S_Y and S_Z (downrange, off range and altitude respectively, the altitude above sea level being $-S_Z$). The earth axes are related to the missile wind axes through three successive rotations. Initially the earth XY plane is rotated about Z axis through an angle ψ_W to form an X' Y' Z' system (Z and Z' coincide). The new X'Z' plane is next rotated about the Y' axis through an angle θ_W to form X" Y" Z" system (Y' and Y" coincide). Finally the Y"Z" plane is rotated about the X" axis through an angle ϕ_W to form the wind axis system (x_W y_W z_W). Once the Euler angles ψ_W, θ_W and ϕ_W are defined and the transformation matrix established, the order of rotation cannot be interchanged. The transformation matrix from earth axes to wind axes follows:

$$
\begin{bmatrix} H_{X_W} \\ H_{Y_W} \\ H_{Z_W} \end{bmatrix} = \begin{bmatrix} \cos\theta_W \cos\psi_W & \cos\theta_W \sin\psi_W & -\sin\theta_W \\ \begin{matrix} -\cos\phi_W \sin\psi_W \\ +\cos\psi_W \sin\theta_W \sin\phi_W \end{matrix} & \begin{matrix} \cos\phi_W \cos\psi_W \\ +\sin\phi_W \sin\theta_W \sin\psi_W \end{matrix} & \sin\phi_W \cos\theta_W \\ \begin{matrix} \sin\phi_W \sin\psi_W \\ +\cos\phi_W \sin\theta_W \cos\psi_W \end{matrix} & \begin{matrix} -\sin\phi_W \cos\psi_W \\ +\cos\phi_W \sin\theta_W \sin\psi_W \end{matrix} & \cos\phi_W \cos\theta_W \end{bmatrix} \begin{bmatrix} H_X \\ H_Y \\ H_Z \end{bmatrix}
$$

$$(2.3.57)$$

The inverse transformation matrix, i.e., the wind to earth axes, follows:

$$
\begin{bmatrix} H_X \\ H_Y \\ H_Z \end{bmatrix} = \begin{bmatrix} \cos\theta_W \cos\psi_W & \begin{matrix} -\cos\phi_W \sin\psi_W \\ +\sin\phi_W \sin\theta_W \cos\psi_W \end{matrix} & \begin{matrix} \sin\phi_W \sin\psi_W \\ +\cos\phi_W \sin\theta_W \cos\psi_W \end{matrix} \\ \cos\theta_W \sin\psi_W & \begin{matrix} \cos\phi_W \cos\psi_W \\ +\sin\phi_W \sin\theta_W \sin\psi_W \end{matrix} & \begin{matrix} -\sin\phi_W \cos\psi_W \\ +\cos\phi_W \sin\theta_W \sin\psi_W \end{matrix} \\ -\sin\theta_W & \sin\phi_W \cos\theta_W & \cos\phi_W \cos\theta_W \end{bmatrix} \begin{bmatrix} H_{X_W} \\ H_{Y_W} \\ H_{Z_W} \end{bmatrix}
$$

$$(2.3.58)$$

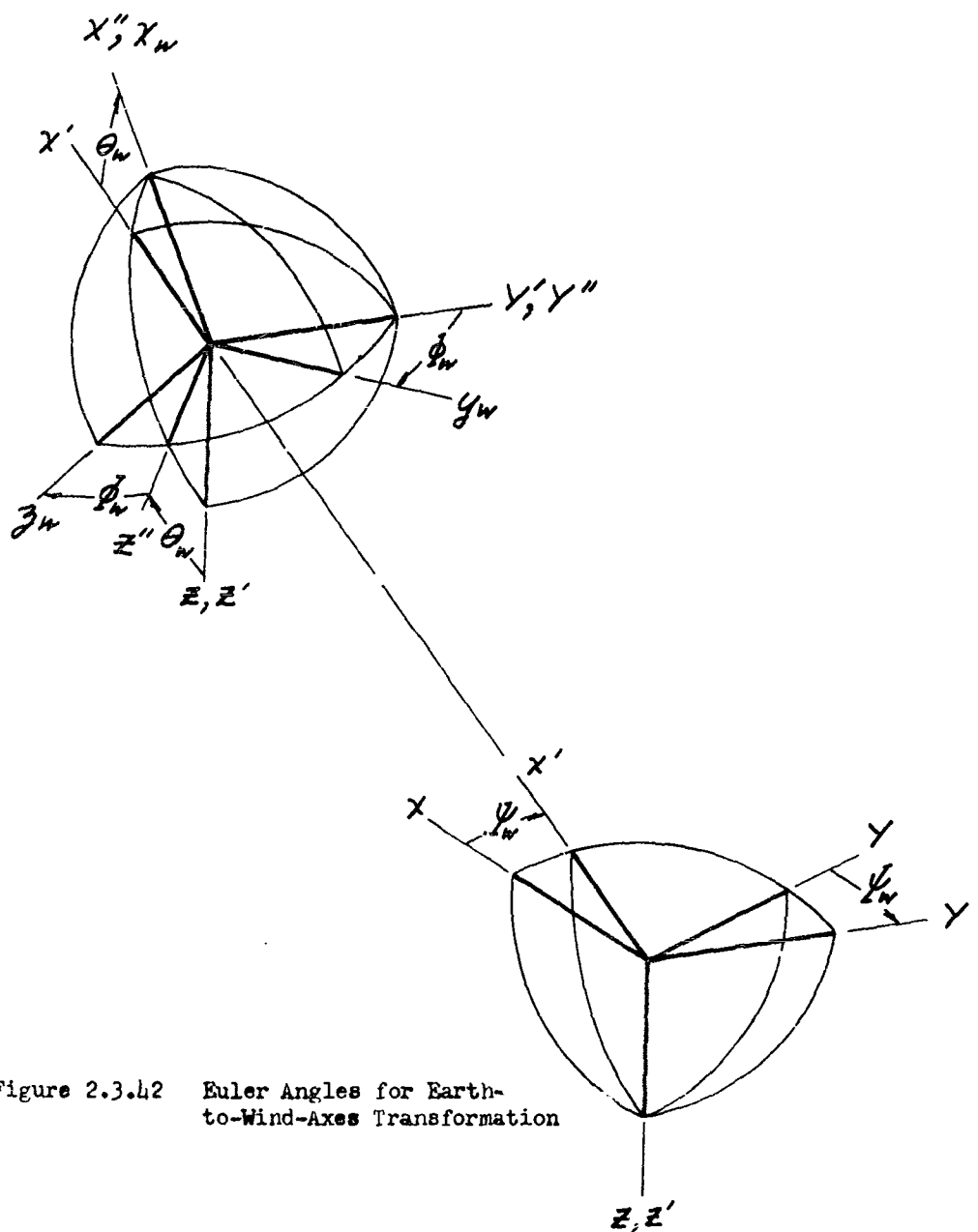Figure 2.3.42   Euler Angles for Earth-
to-Wind-Axes Transformation

The relationship between the wind axes angular rates (p_W, q_W and r_W) and the Euler angles (ψ_W, θ_W and ϕ_W) is developed in a piecemeal manner with the aid of superposition. That is, the contributions of each Euler angle rate to p_W, q_W and r_W is calculated separately then appropriately grouped to form the following equations:

$$p_W = \dot{\phi}_\omega - \dot{\psi}_\omega \sin\theta_\omega$$

$$q_W = \dot{\theta}_\omega \cos\phi_\omega + \dot{\psi} \cos\theta_\omega \sin\phi_\omega, \text{ and}$$

$$r_W = -\dot{\theta} \sin\phi_\omega + \dot{\psi} \cos\theta_\omega \cos\phi_\omega .$$

The computer solution for the Euler angles is conducted on the following relationships developed by rearranging the latter equations:

$$\dot{\phi}_\omega = p_\omega + \dot{\psi}_\omega \sin\theta_\omega, \tag{2.3.59}$$

$$\dot{\theta}_\omega = q_\omega \cos\phi_\omega - r_\omega \sin\phi_\omega, \text{ and} \tag{2.3.60}$$

$$\dot{\psi}_\omega = \left[r_\omega \cos\phi + q_\omega \sin\phi_\omega \right] \frac{1}{\cos\theta_\omega} . \tag{2.3.61}$$

From the knowledge of these Euler angles, the missile weight vector components are computed in the wind axes, and the velocity vector components in the earth axes.

The following list is a summary of the equations or matrices in the 3-D simulation:

1. Euler angle transformation from wind to earth axes,
2. translational equations in the wind axes,
3. rotational equations in the body axes,
4. aerodynamic forces and moments in the stability axes,
5. computation of α, β and p_W, and
6. associated transformations between the body and wind axes.

2.3.5.3 <u>Simulation</u> A block diagram of the 3-D simulation is presented in Figure 2.3.43. The error associated with the aerodynamic computations is $< 4\%$ for $0.2 \leq M \leq 2.0$.
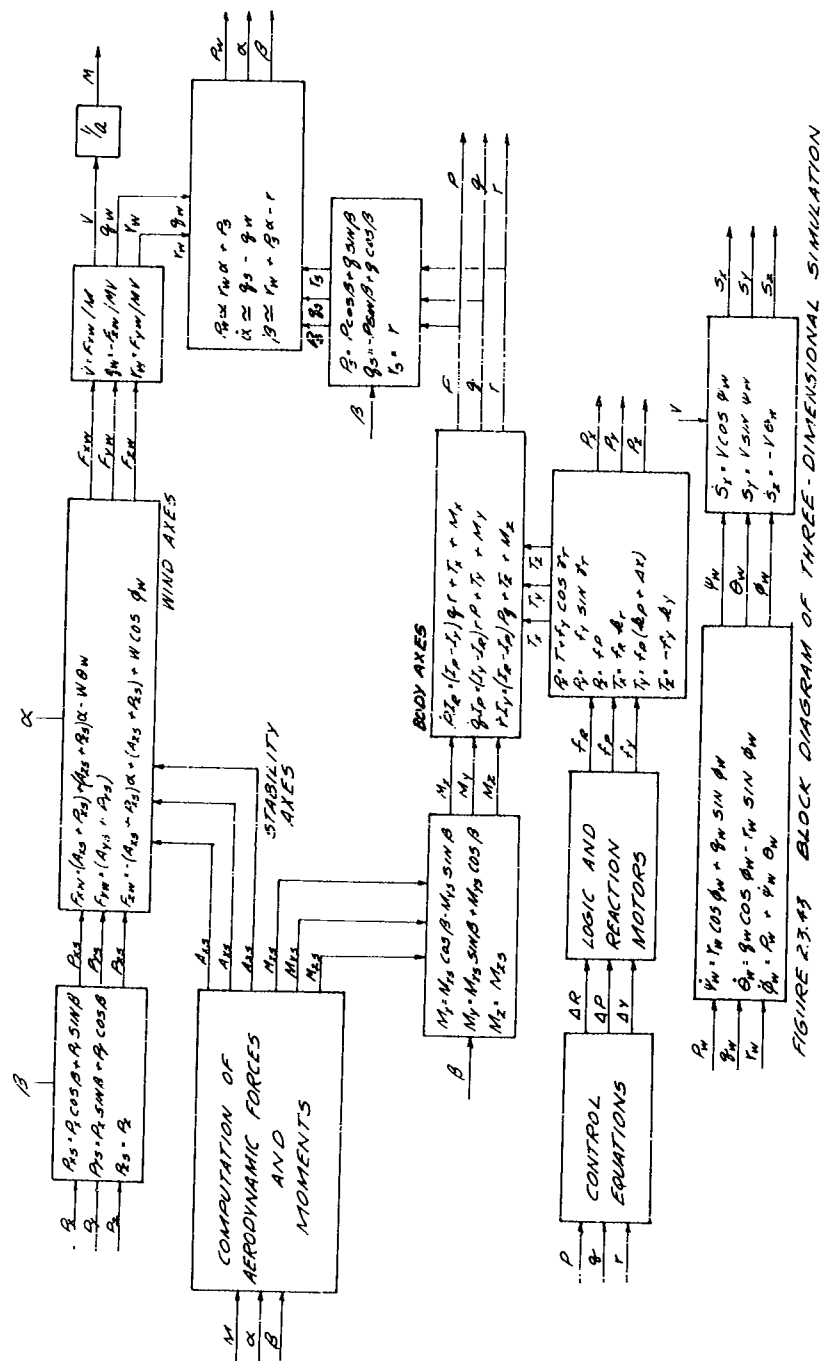
FIGURE 2.3.43 BLOCK DIAGRAM OF THREE-DIMENSIONAL SIMULATION

Figure 2.3.43 Block Diagram of Three-Dimensional Simulation

The aerodynamic coefficients were initially plotted from wind tunnel data in the stability axes. In Figure 2.3.43, the block labeled "Computation of Aerodynamic Forces and Moments" contains the following equations:

$$A_{x_S} = -1481 \lambda S M^2 C_{A_S} \quad lb, \tag{2.3.62}$$

$$A_{y_S} = 1481 \lambda S M^2 C_{y_S} \quad lb, \tag{2.3.63}$$

$$A_{z_S} = -1481 \lambda S M^2 C_{N_S} \quad lb \tag{2.3.64}$$

$$M_{x_S} = 1481 \lambda S d M^2 C_{\ell_S} \quad ft\text{-}lb \tag{2.3.65}$$

$$M_{y_S} = 1481 \lambda S d M^2 C_{m_S} \quad ft\text{-}lb, \text{ and} \tag{2.3.66}$$

$$M_{z_S} = 1481 \lambda S d M^2 C_{n_S} \quad ft\text{-}lb, \tag{2.3.67}$$

where

S = reference area of 19.6 ft^2,
d = reference length of 5 ft, and
λ = static pressure ratio.

The change in aerodynamic coefficients due to c.g. shift was computed by the following equations:

$$C_{\ell_S} = C_{\ell_{S_o}} - \frac{\Delta x}{d} \sin\beta \, C_{N_S} ,$$

$$C_{m_S} = C_{m_{S_o}} - \frac{\Delta x}{d} \cos\beta \, C_{N_S} , \text{ and}$$

$$C_{n_S} = C_{n_{S_o}} + \frac{\Delta x}{d} \sin\beta \, C_{A_S} - \frac{\Delta x}{d} \cos\beta \, C_{y_S} ,$$

where subscript o indicates the coefficient for the reference c.g. location, and Δx is the difference between the reference c.g. and actual c.p. locations.

The minor differences between the axial drag coefficients for the

control jet power-on and power-off modes were not simulated. This data obtained during the wind-tunnel tests and presented in Volume II Section 2.4.5 of this report indicates that the differences are small for subsonic flight regimes and negligible for supersonic flight regimes (reference Volume II, Figure 2.4.25).

The following notes apply to the simulation of the aerodynamic coefficients in equations (2.3.62) through (2.3.67) inclusive:

1. C_{A_S} - simulated as a function of M only. The variation with respect to α and β were considered negligible.

2. C_{Y_S} - simulated as a non-linear function of M and a linear function of β and considered independent of α. This coefficient is small when evaluated in the stability axes.

3. C_{ℓ_S} - simulated as a non-linear function of M and a linear function of α (up to 10°) and considered independent of β.

4. $C_{l_{S_o}}$ - simulated as a linear function of β only. This approximation is poor but conservative. The resulting error is negligible since this coefficient is very small when referred to the stability axes.

5. $C_{n_{S_o}}$ - simulated as a non-linear function of M and a linear function of α and β. Since this coefficient is important it was simulated very accurately.

6. $C_{n_{S_o}}$ - simulated as a function of M and β. Below Mach 1.0,

$$M^2 C_{n_{S_o}} = f_1 (\beta) \times g_1 (M) + f_2 (\beta) \times g_2 (M)$$

and above Mach 1.0, $C_{n_{S_o}} = C_{n_{S_o}} (M) \times \beta$. F and g are non-linear functions of β and M respectively. The simulation switch at Mach 1.0 has caused a "glitch" to appear on many of the computer traces.

The physical characteristics of the missile utilized in the simulations are listed in Table 2.3.8.

2.3.6 TRAJECTORIES For final verification of the flight capability of the EYE WACKET design, the missile was "flown" on the 3-D simulation. Flights were simulated for both forward and side launch conditions at several initial Mach numbers. In each case, a trajectory was chosen to demonstrate the post-burnout maneuverability of the missile. All of the control functions for pitch, roll and yaw were recorded throughout the computer runs.

2.3.6.1 Side Launch Two side launch trajectories are illustrated by the XY and YZ plots from the analog computer (Figure 2.3.44). The computer strip recordings of Figures 2.3.45, 2.3.46, and 2.3.47 and 2.3.48 display the detailed system information of that trajectory in Figure 2.3.44 which illustrates a roll-pitch maneuver to the left. Table 2.3.9 provides additional information to simplify the interpretation of the computer recordings.

Table 2.3.8 Physical Characteristics
Used In Simulation

	Wt.(lb)	C.G. (% Chord)	I_R (slug-ft^2)	I_R (slug-ft^2)	Iy (slug-Arm(in.))	Roll Moment Arm(in)	Pitch Moment Arm(in)	Yaw Moment Arm(in)
Full	424	43.0	11.59	21.39	31.68	20.5	21.5	34
Burncut	330	40.9	10.09	19.81	28.70	20.5	22.8	34
Empty	290	42.2	9.79	18.89	26.72	20.5	22.1	34

Table 2.3.9 Additional Information for Computer Recordings

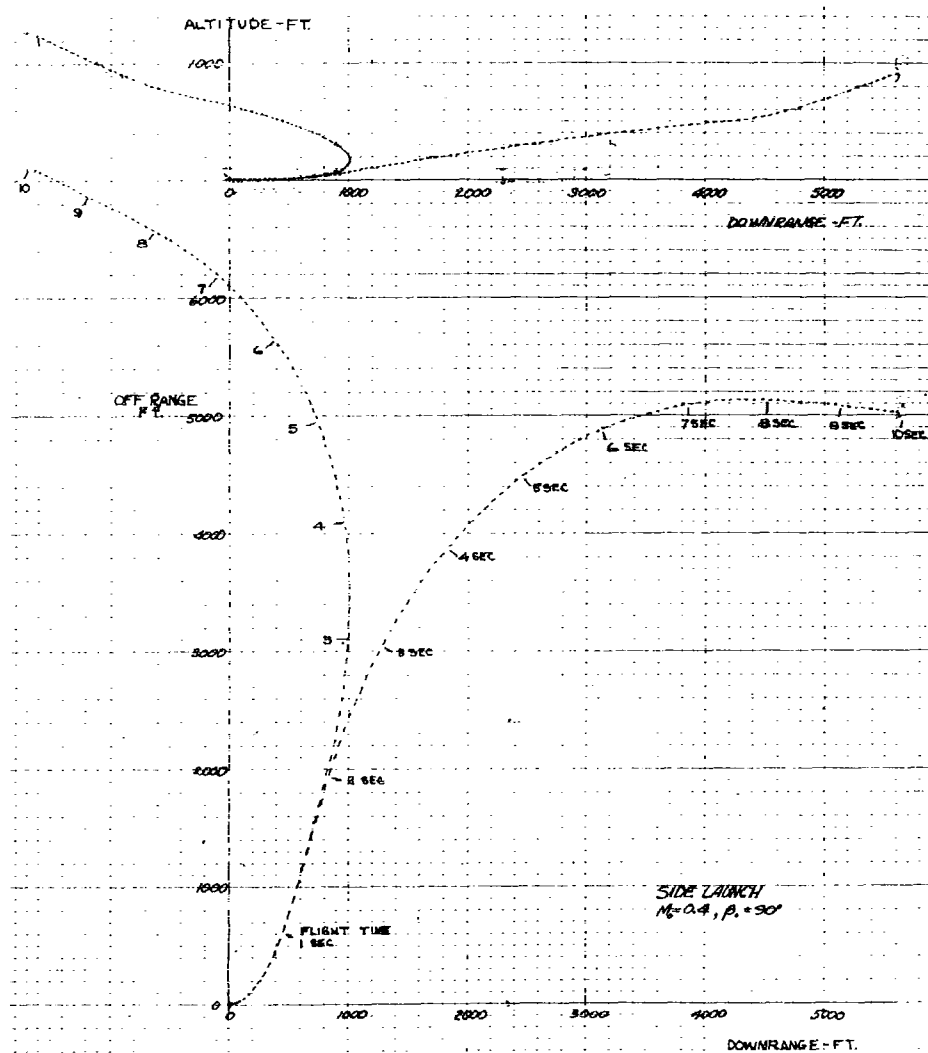| Time	Approximate Missile Velocity	Description
0-1.2 sec	M 0.4 (sled)	β varies from 90° to 20°. Autopilot uses side launch gains. Note sporadic pitch activity to correct disturbances due to roll-pitch coupling and gravity. Roll angle ϕ and heading angle ψ are controlled within 1° of zero.
1.1-1.2 sec	M 1.0	Yaw system switches to $\dot{\beta}$ control. ψ increase toward 15°. β reduces toward zero. Autopilot switches to flight gains; therefore the pitch system becomes predominant.
1.7 sec		Yaw autopilot switched to low duty cycle.
1.9 sec	M 1.25	Missile rolls to -75°. An 0.15 second time constant is used to filter the large roll demand to prevent amplifier overloading in the simulation. For the missile, a time constant of 0.05 seconds is advised to ensure minimum pitch disturbance during large roll demands. Note that roll control thrust is present as a series of short bursts so as to cause a minimum pitch interference.
2.6 sec	M 1.1	Midway through the roll maneuver a 10 g pitch command is imposed on the missile
2.6 sec	M 1.1	Command pitch maneuver is decreased to 5 g's.
7.4 sec	M 0.62	Missile rolls to 0°.
8.4 sec	M 0.57	Command pitch maneuver is decreased to zero g's.

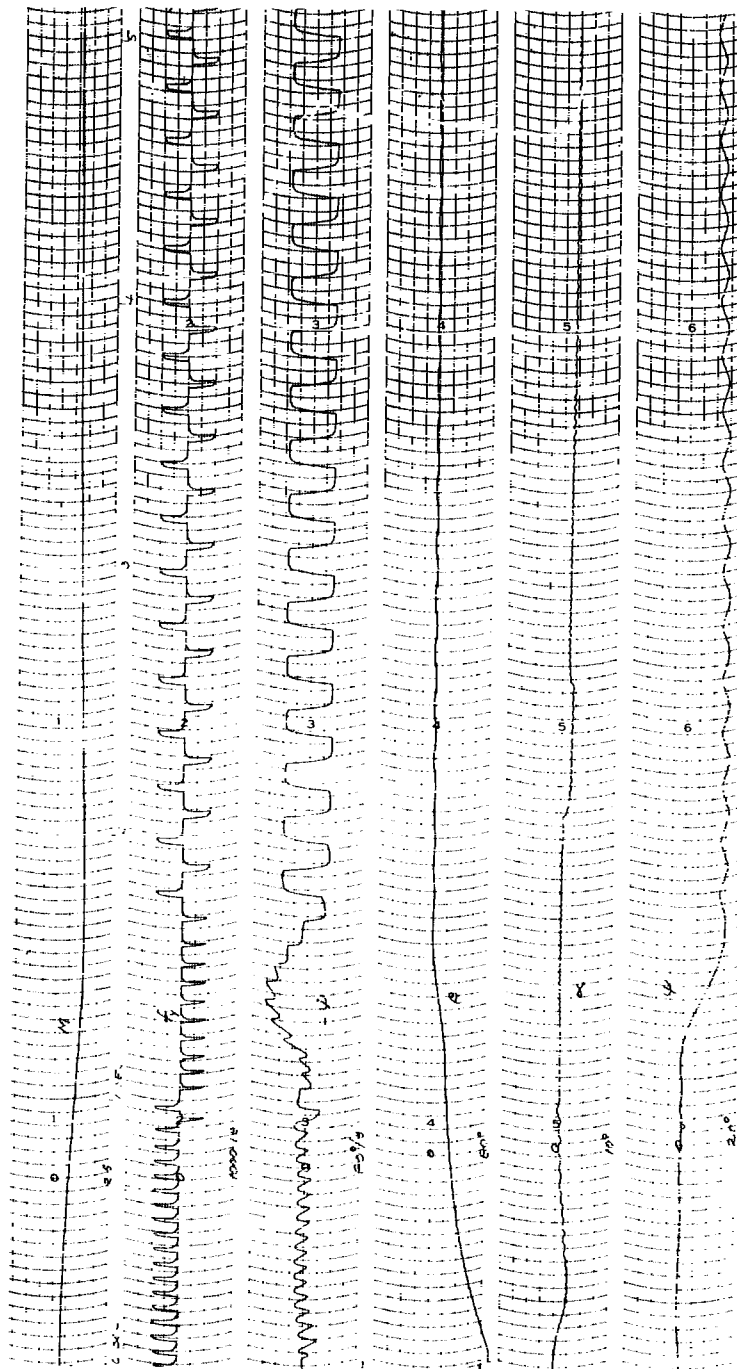Figure 2.3.44   Side Launch Trajectories, $M_o = 0.4$, $\beta_o = 90°$
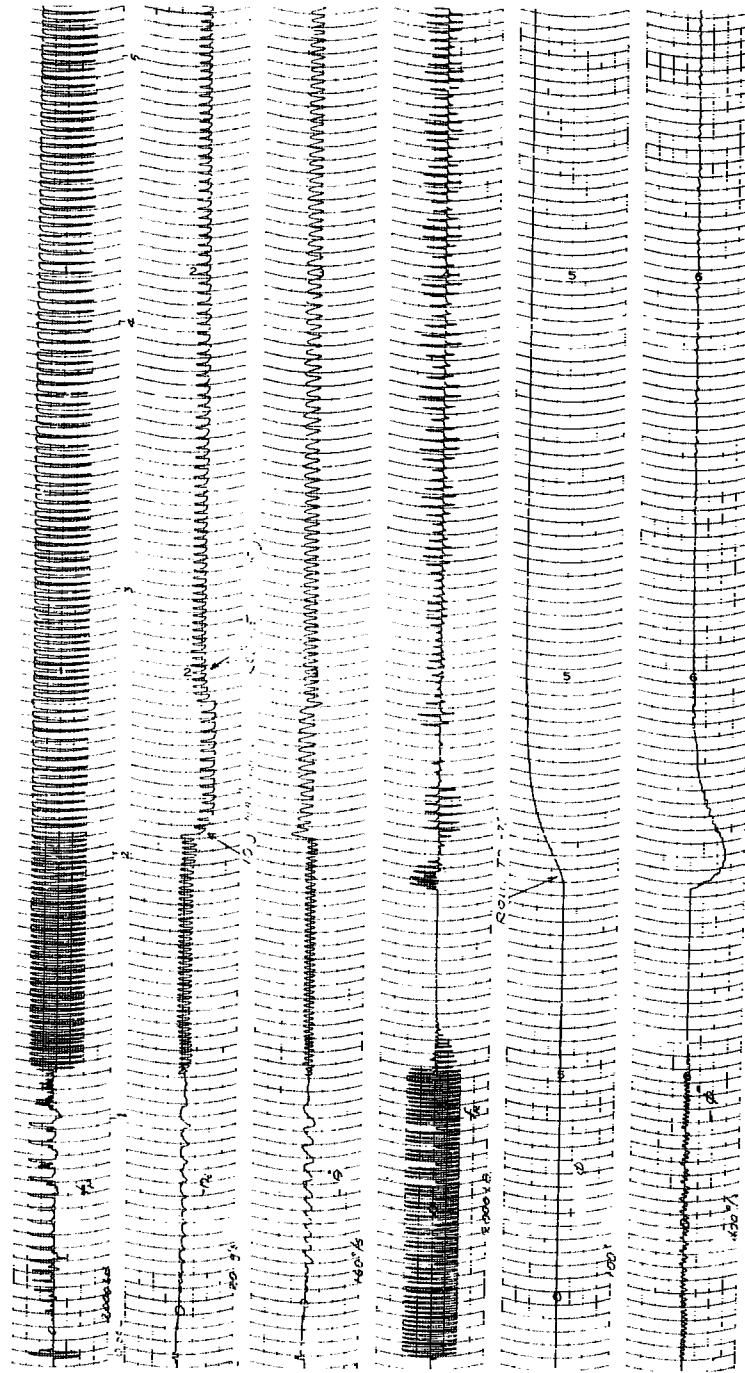
Figure 2.3.45 Missile Functions, Side Launch (0 - 5 Seconds)

Figure 2.3.46 Additional Missile Functions, Side Launch (0 - 5 Seconds)
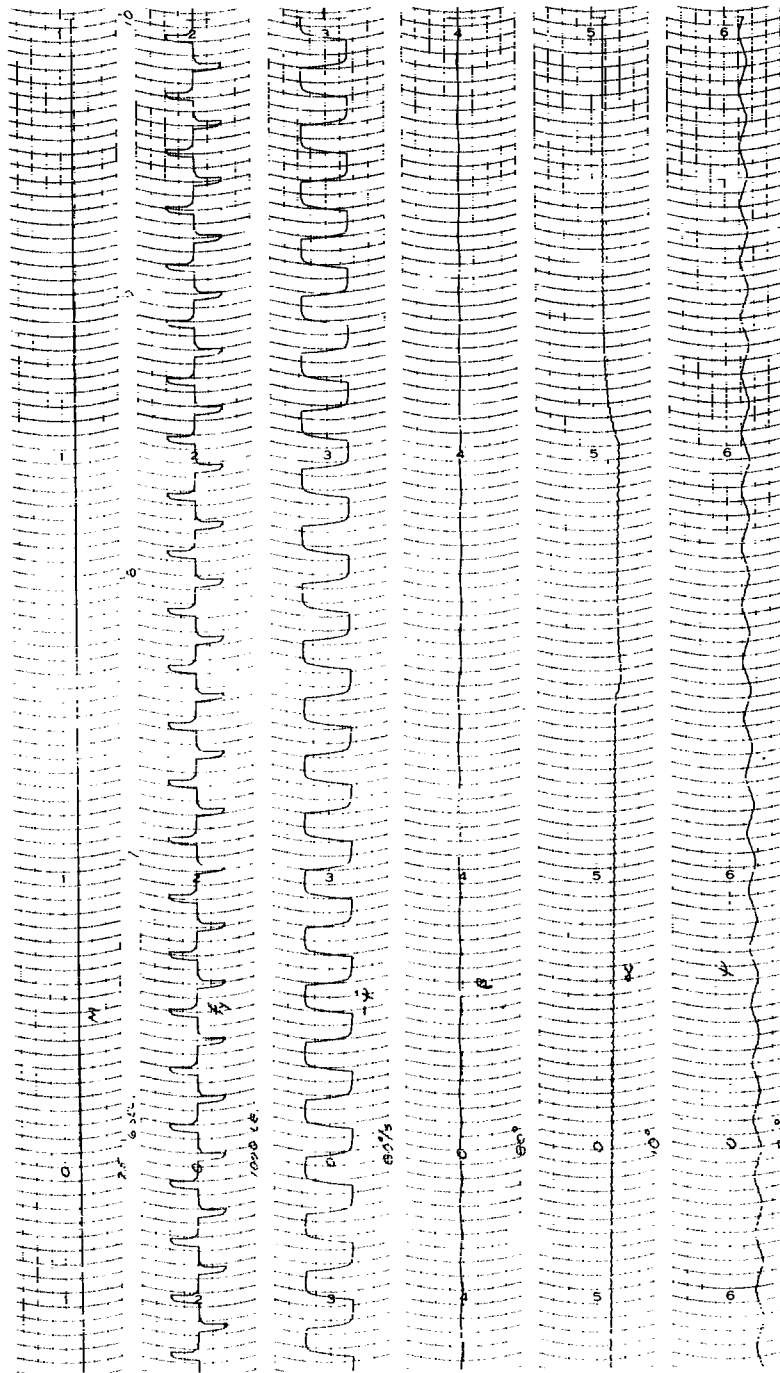
Figure 2.3.47 Missile Functions, Side Launch (5-10 Seconds)

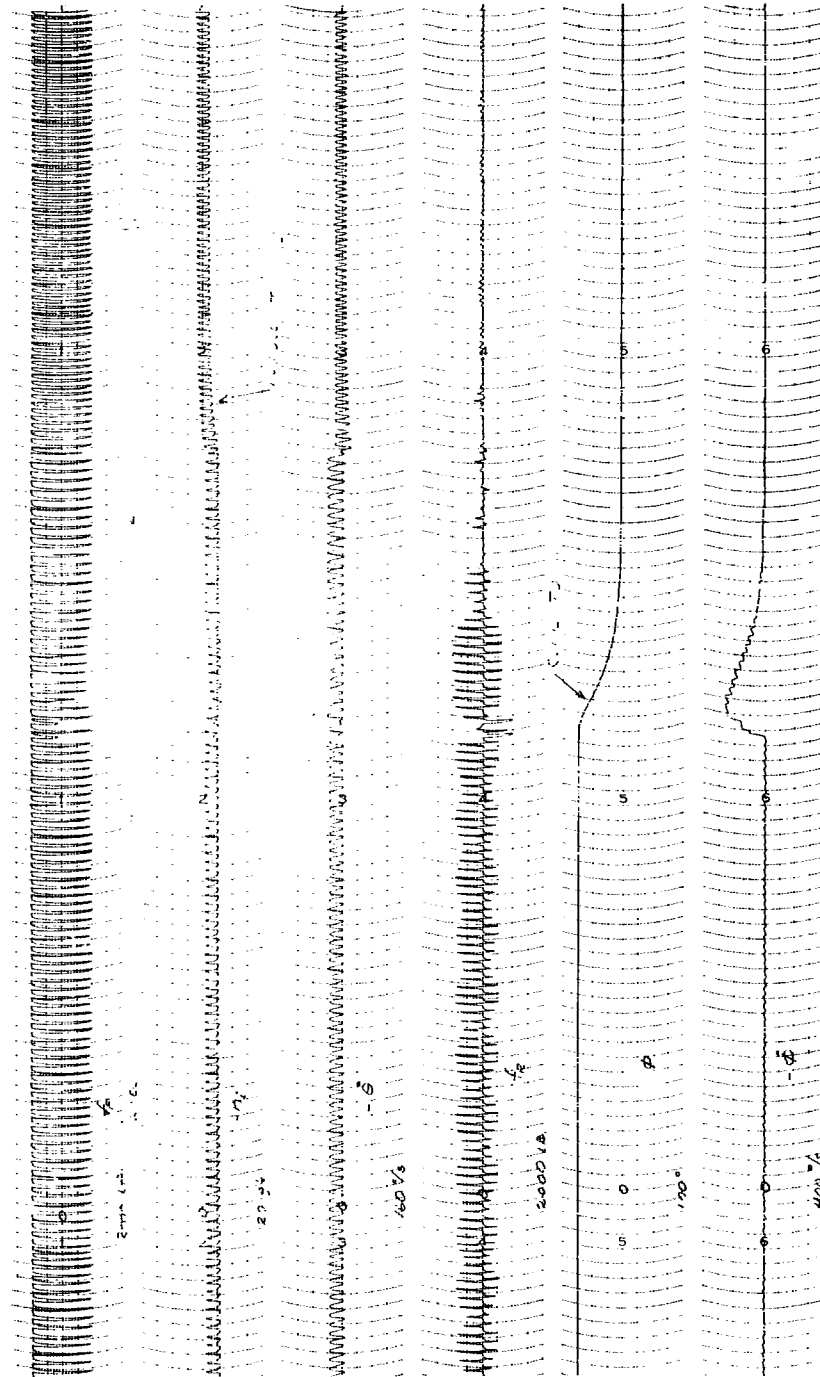Figure 2.3.48 Additional Missile Functions Side Launch (5-10 Seconds)

Figure 2.3.44 illustrates a typical test trajectory in which no attempt was made to approach the maximum of maneuverability. The missile displayed normal behavior.

2.3.6.2 <u>Forward Launch</u> A typical trajectory for a forward launch is not included in the report because it would display little information not contained in the trajectory for the more stringent conditions of the side launch. However a typical forward launch capture was illustrated in Figure 2.3.26. Typical Mach number time histories are presented for three initial velocities (see Figure 2.3.49). The sharp increase and decrease of velocity occurring during the early phase of flight is clearly illustrated.

2.3.6.3 <u>Nomenclature for Analog Computer Variables</u>

f_p = pitch thrust in lb,

n_i = acceleration output in g's, biased 1 g to allow level flight in the presence of gravity,

$\dot{\theta}$ = pitch rate in degree per second,

f_r = roll thrust in lb,

ϕ = roll angle in degree,

$\dot{\phi}$ = roll rate in degree per second,

M = Mach number

f_y = yaw thrust in lb,

$\dot{\psi}$ = heading angle rate in degree per second,

β = sideslip angle in degree,

α = angle of attack in degree, and
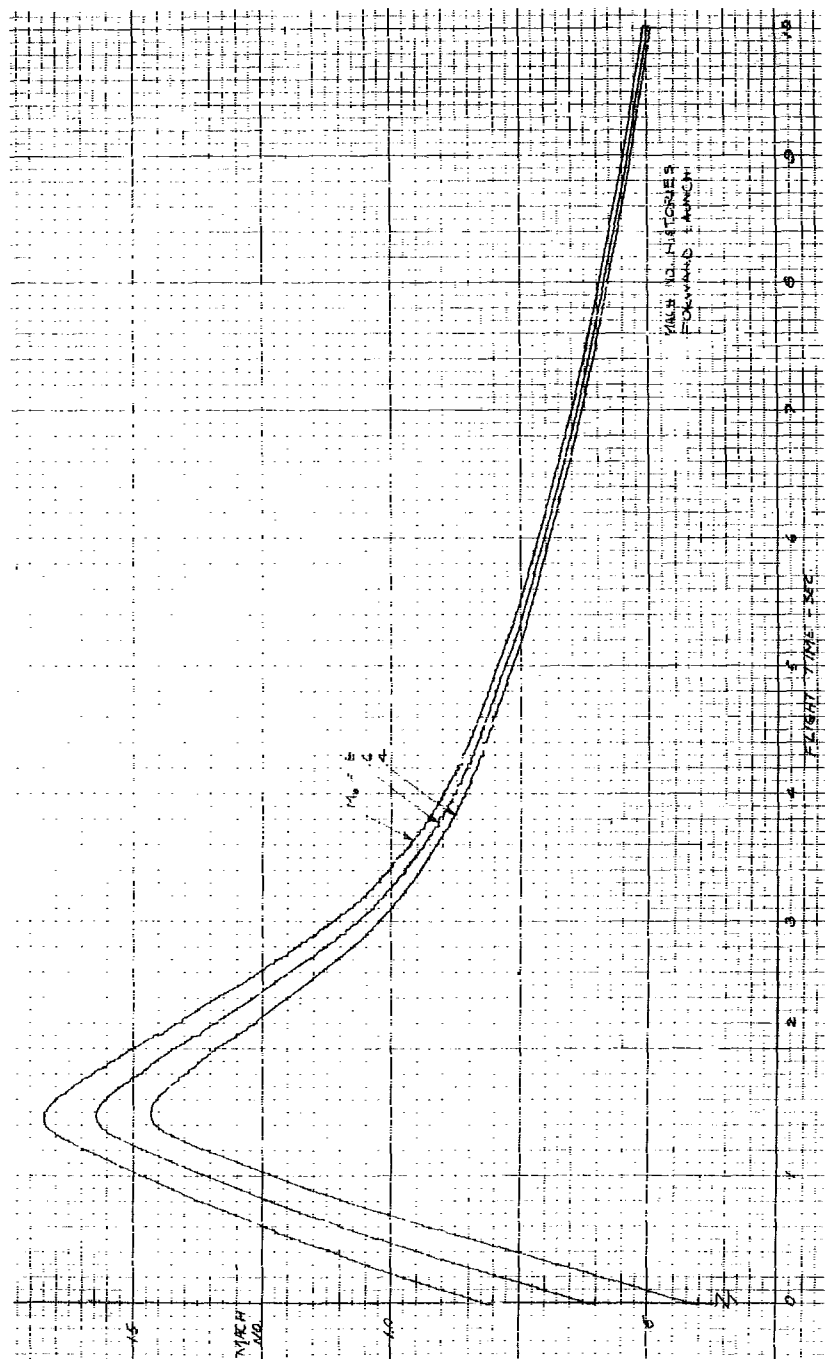
ψ = heading angle in degrees

Figure 2.3.49   Mach Number Histories, Forward Launch

Section 3.0
CONCLUSIONS AND RECOMMENDATIONS

3.1 CONCLUSIONS

The studies reported in this document were concerned with the analysis and design of a Feasibility Test Vehicle. The preliminary designs are directed toward the subsequent implementation and flight testing of the vehicle to prove that the configuration possesses the unique characteristics deemed necessary for a bomber defense missile. The conduct of these analyses has resulted in a large degree of optimism in the ability of the missile to successfully demonstrate the desired operational characteristics.

The Feasibility Test Vehicle is a 60-inch diameter with a 21% thickness-to-chord ratio. The main structure consists of four magnesium alloy (AZ 31B) channels criss-crossing the missile planform. The shroud is a magnesium alloy integral-rib configuration. The studies indicated that the honeycomb-sandwich construction constitutes a possible second-choice skin configuration. The main propulsion for the FTV will be provided by a three-motor (M58A2) booster configuration. The study results conclude that the structure will adequately withstand the aerodynamic, aeroelastic, handling, launching and propulsive perturbations expected during a flight test program.

The control moments will be provided by six reaction jet nozzles, four for pitch-roll control and two for yaw control. In each case the control motors will be driven by a nonlinear element. Hypergolic bipropellants will develop the required thrust on command from the autopilot. The control philosophy was demonstrated on time varying three-dimensional simulation employing a complete parametric description of the missile. These latter studies culminated in the successful establishment of flight trajectories for the PYE WACKET Feasibility Test Vehicles.

3.2 RECOMMENDATIONS

The recommendations stem not only from the work accomplished under the auspices of this contract (AF C8(635)-1168) but also from several company sponsored studies of the wide range of applications open to the basic lenticular configuration. The work has progressed successfully to date but has consisted solely of paper studies, i.e., there have been no hardware programs. In order to fully establish the feasibility of the circular planform, blunted lenticular configuration, it is imperative that flight data be obtained. It is recommended

SECRET

that, at the earliest possible time, a program be initiated to build, test and fly the Feasibility Test Vehicle. During this flight test program, the plans should be formulated and implemented for the development of an operational unit. The latter is justified by the survivability studies for both the B-52 and B-70 bombers during a penetration mission.

The continuation of the PYE WACKET studies will also result in several significant advances in the state-of-the-art of missile control. The electronics planned for this vehicle include the use of the microminiature packaging, a concept important to both atmospheric and space vehicles because of its compactness and lightness. The fast-acting reaction controls, necessary for the omnidirectional launch, are imperative for space application whether the vehicle be manned or unmanned. It is also axiomatic that before this configuration can be utilized in any applications, its aerodynamics must be verified by actual flight test.

Section 4.0
LIST OF REFERENCES

4.1   PYE WACKET Lenticular Rocket Feasibility Study, APGC-TR-60-
      25, May 1960, Secret

4.2   Jato Manual - SPIA/M., Volume II, APL/JHU, August 1960, CONFI-
      DENTIAL

4.3   Model Specification - Solid Propellant Rocket Engine - M58A2,
      Report No. SP-83B, Thiokol Chemical Corp., May 1958, CONFIDEN-
      TIAL

4.4   Roark, Raymond J., Formulae for Stress and Strain, third
      edition, New York, McGraw-Hill Book Company, Inc., 1954

4.5   Kordes, E. E., Tuovila, W. J., and Guy, L. P., "Flutter
      Research on Skin Panels", Joint Conference on Lifting Manned
      Hypervelocity and Re-entry Vehicles, Part I, Langely Research
      Center, April 1960, CONFIDENTIAL

4.6   Theiss, E. C., Proposed Standard Cold and Hot Atmosphere for
      Aeronautical Design, Technical Memorandum Report WCSE 141,
      Wright Air Development Center, USAF, June 1952

4.7   Colburn, A. P., "A Method of Correlating Forced Convection
      Heat Transfer Data and Comparison with Fluid Friction",
      Transactions AICHE, Volume 29, 1933

4.8   Chauvin, L. T., and DeMoraies, C. A., Correlation of Supersonic
      Convection Heat Transfer Coefficients from Measurements of the
      Skin Temperatures of a Parabolic Body of Revolution (NACA RM 10)
      NACA TN 3623, March 1956

4.9   Sibulkin, N., "Heat Transfer Near the Forward Stagnation Point
      of a Body of Revolution", Journal of Aeronautical Sciences,
      August 1952

4.10 Sutton, G. P., Rocket Propulsion Elements, second edition,
      New York, John Wiley & Sons, Inc., 1956

4.11 Kaplan, D. J., "Selection of a Pressurization System for a
      Storable Liquid Propellant Rocket Engine", American Rocket
      Society Report No. 1250-60, July 1960

4.12　Liquid Propellants Handbook, Battelle Memorial Institute, October 1958, CONFIDENTIAL

4.13　Clark, John D., Development and Properties, the New Monopropellant "ISOLDE 120-A", U.S.N.A.R.T.S. Report No. 93, November 1956, CONFIDENTIAL

4.14　High Energy Liquid Monopropellant, Quarterly Progress Report No. 5, Phillips Petroleum Company, July 1958, CONFIDENTIAL

4.15　Sanscrainte, W.,"Hydrogen Peroxide Attitude Control Systems", Fourth Symposium on Ballistic Missiles and Space Technology, Los Angeles, August 1959

4.16　Propellant Powder Manual - SPIA/M2, APL/JHU, Solid Propellant Information Agency, CONFIDENTIAL

4.17　Falanga, R. A. and Janos, J. J., Pressure Loads Produced on a Flat Plate Wing by Rocket Jets Exhausting in a Spanwise Direction Below the Wing and Perpendicular to a Free-Stream Flow of Mach Number 2.0, NACA RM-L-58D09, June 1958, CONFIDENTIAL

4.18　Ferrari, C., Interference Between a Jet Issuing Laterally From a Body and the Enveloping Supersonic Stream, Bumblebee Series Report No. 286, APL/JHU, April 1959

4.19　Liepman, H. P., "Experimental Jet Interference", Minutes of 40th Meeting of Bumblebee Aerodynamics Panel, APL/JHU TG-14-37A, May 1959, CONFIDENTIAL

4.20　Vinson, P. W., Amick, J. L., and Liepman, H. P., Interaction Effects Produced by Jet Exhausting Laterally Near Base of Ogive - Cylinder Model in Supersonic Main Stream, NASA Memo 12-5-58W, February 1959

4.21　Amick, J. L., Carvalho, G. F. and Liepman, H. P., "Interaction Experiments of Lateral Jets with Supersonic Streams", Minutes of 39th Meeting of Bumblebee Aerodynamics Panel, APL/JHU TG-14-36, Sept. 30-Oct. 1, 1958, SECRET

4.22　Cortwright, E. M. and Kochendorfer, F. D., Jet Effects on Flow Over Afterbodies in Supersonic Stream, NACA RM-E-53H25, November 1953

4.23　Liepman, H. P., "Experimental Jet Interference", Minutes of 38th Meeting of Bumblebee Aerodynamics Panel, APL/JHU TG-14-35, March 1958, CONFIDENTIAL

4.24   Liepman, H. P., "On the Use of Side-Jets as Control Devices",
       ARS Journal, June 1959

4.25   Love, E. S., et.al., Experimental and Theoretical Studies of
       axisymmetric Free Jets, NASA TR R-6, 1959

4.26   Pitts, W. C. and Wiggins, L. E., Axial-Force Reduction by
       Interference Between Jet and Neighboring Afterbody, NASA
       TN D-332, September 1960

4.27   Adamson, T. C. and Nicholls, J. A., "On the Structure of
       Jets From Highly Underexpanded Nozzles Into Still Air",
       Journal of the Aero/Space Sciences, Volume 26, January 1959

4.28   Etkin, Bernard, Dynamics of Flight - Stability and Control,
       New York, John Wiley and Sons, Inc., 1959

INITIAL DISTRIBUTION

1	Wpns Sys Eval Gp	2	NASA, Space Task Gp
3	Hq USAF (AFDAP)	1	NASA - Ames Aeronautical Lab
3	Hq USAF (AFOOP)	3	NASA - Ames Aeronautical Lab
1	Hq USAF (AFPTR)		Ames Rsch Cen, Lib
4	Hq USAF (AFDRT)	1	Arnold Engineering Dev Cen,
3	Hq USAF (AFORQ)		PWT
2	Hq USAF (AFCOA)	1	Arnold Engineering Dev Cen
1	AFSC (SCGS)		von Karman Facility
2	AFSC (SCL)	3	Convair Div
3	AFSC (SCR)	15	ASTIA (TIPCR)
1	DOD DDR & E,		APGC
	Ofc of Asst Dir of Fuels,	1	ASQ
	Materials and Ord	2	ASQW
2	Asst Sec of AF (Rsch & Dev)	6	ASQP
1	AU (Lib)	3	PGEH
1	AF Ofc of Scientific Rsch	2	PGTRI
1	SAC (DO)		
5	SAC (OA)		
5	SAC (DORQ)		
1	TAC (TOD)		
1	TAC (TMD)		
1	TAC (TPL)		
3	ADC (ADO)		
1	Ofc of Aerospace Rsch		
1	Inst of Air Wpns Rsch (Lib)		
1	PACAF (PFOOP-RQ)		
3	Ballistic Sys Div		
3	Space Sys Div		
1	USAFE (OA)		
1	USAFE (OTREQ)		
2	ASD (ASAT)		
4	ASD (ASL)		
1	ASD (ASO)		
7	ASD (ASZ)		
1	Dir, USAF Proj RAND		
1	Ofc of Ord Rsch		
2	Bu of Naval Wpns, R		
1	Bu of Naval Wpns, Conv Air		
	Wpns Sys Code RM-377		
1	Bu of Naval Wpns, OP-07		
1	Bu of Naval Wpns, OP-03		
1	Naval Air R & D Act Comd		

AD

Convair/Pomona, Convair Division of General Dynamics Corporation, Pomona, California, PYE WACKET Feasibility Test Vehicle Study (Configuration and Autopilot/Control), UNCLASSIFIED TITLE), June 1961. 261p. incl. illus. 28 refs. (AFSC Project 3811; ASD-TR-61-34 - Volume III) (Contract AF 08(635)-1168)   Secret NF report

This report, consisting of three volumes contains the results of a series of studies conducted to form the basis for the design of PYE WACKET Feasibility Test Vehicles. Detailed studies (including wind tunnel tests), were conducted in the areas of aerodynamics, control system structures and test vehicle performance. All studies were based on sea level flight environment. The complete task is reported in three volumes: Volume I - Summary, Volume II -- Aerodynamics, and Volume III -- Configuration and Autopilot/Control.

1. Test vehicles
2. Hypersonic test vehicles
I. Det 4, Hq ASD
II. Contract AF 08(635)-1168
III. Project 3811
IV. PYE WACKET

AD

Convair/Pomona, Convair Division of General Dynamics Corporation, Pomona, California, PYE WACKET Feasibility Test Vehicle Study (Configuration and Autopilot/Control), UNCLASSIFIED TITLE), June 1961. 261p. incl. illus. 28 refs. (AFSC Project 3811; ASD-TR-61-34 - Volume III) (Contract AF 08(635)-1168)   Secret NF report

This report, consisting of three volumes contains the results of a series of studies conducted to form the basis for the design of PYE WACKET Feasibility Test Vehicles. Detailed studies (including wind tunnel tests), were conducted in the areas of aerodynamics, control system structures and test vehicle performance. All studies were based on sea level flight environment. The complete task is reported in three volumes: Volume I - Summary, Volume II -- Aerodynamics, and Volume III -- Configuration and Autopilot/Control.

1. Test vehicles
2. Hypersonic test vehicles
I. Det 4, Hq ASD
II. Contract AF 08(635)-1168
III. Project 3811
IV. PYE WACKET